STRUCTURAL ELUCIDATION OF GUANOSINE SELF-ASSEMBLIES USING SPECTROSCOPIC AND COMPUTATIONAL METHODS

by

Irene Ching Man Kwan

A thesis submitted to the Department of Chemistry

In conformity with the requirements for

the degree of Doctor of Philosophy

Queen's University

Kingston, Ontario, Canada

(June, 2012)

Abstract

In this thesis, we document a comprehensive study of the cation-directed self-assembly of three guanosine derivatives: i) guanosine 5'-monophosphate (5'-GMP), ii) guanosine 5'-thiomonophosphate (5'-GSMP), and iii) 2',3',5'-*O*-triacetylguanosine (TAG). We discovered that, under the neutral pH condition, Na_2(5'-GMP) molecules self-assemble into a right-handed helix structure consisting of alternating all-C2'*endo* and all-C3'*endo* planar G-quartets stacking on top of each other with a 30° twist. This self-assembled supramolecular structure uses multiple non-covalent forces (e.g., hydrogen-bond, phosphate-hydroxyl, π-π (base-base) stacking, ion-carbonyl, and ion-phosphate) to align individual monomers in a way that resembles RNA and DNA sequences in which covalent bonds are used to link monomers. Na^+ ions are located in the channel and surface sites of the G-quadruplex. In contrast, under acidic pH conditions, Na_2(5'-GMP) molecules self-assemble into a continuous right-handed helix where guanine bases are hydrogen-bonded in a lock-washer fashion with only C3'-*endo* monomers. Na^+ ions are absent in the channel site due to smaller channel radius and lesser repulsions between phosphate groups (-1 vs. -2 charge under neutral pH) contribute to the stronger stacking mechanism. In Na_2(5'-GSMP), a longer phosphate bond compared with Na_2(5'-GMP) allows stronger $P\text{-}O^{-}\cdots Na^{+}\cdots{}^{-}O\text{-}P$ interactions to occur, thus enhancing self-assembly. Solid-state NMR, FT-IR, powder x-ray diffraction, model building, and calculation showed that Na_2(5'-GSMP) forms the same self-assembled structure as Na_2(5'-GMP) but with significantly greater tendency. This study proves that single-bond modification can enhance stacking in G self-assemblies, and shows direct evidence that Na^+ ions reside at

the surface (phosphate) sites. Lastly, using lipophilic TAG, we were able to show for the first time that trivalent lanthanide metal ions can facilitate G-quartet formation. A new mode of metal ion binding in G-quartet structures (i.e., a triple-decker G dodecamer containing a single metal ion in the central G-quartet) is reported. We also report the first ^{1}H and ^{43}Ca NMR characterization of Ca^{2+}-templated G-quartet formation in a $[TAG_8\text{-}Ca]^{2+}$ octamer.

Acknowledgements

First of all, I would like to sincerely thank my supervisor, Professor Dr. Gang Wu, for being such a great mentor throughout my graduate studies. I would like to thank him for all the opportunities, guidance, support, and patience he gave me during my studies, and all his help with the thesis. I would also like to knowledge him for all the solid-state NMR experiments performed for this thesis. I have learned very much from him in the past few years, and I shall forever be grateful for these valuable knowledge and experiences in the lab. Thank you again, Dr. Wu!! ☺

Secondly, I would like to thank my committee members Drs. Anne Petitjean and J. Hugh Horton for their advices over the years. My Wu group colleagues Jennifer Adams, Parisa Akhshi, Dr. Ramsey Ida, Dr. Xianqi Kong, Xin Mo, Dr. Alan Wong, and Dr. Jianfeng Zhu are acknowledged for their fruitful discussions, support, and friendships in and outside the lab. Alan is also thanked for helping us with the ^{43}Ca NMR experiments at University of Warwick. I would also like to thank Drs. Françoise Sauriol and Harmut Schmeider (High Performance Computing Virtual Laboratory) for their help with the NMR spectrometers and quantum chemical calculations, respectively. I thank Mr. Alan Grant (Geology) for x-ray powder diffraction analysis, and Dr. Yi-Min She for his assistance in ESI-MS experiments. I would also like to thank Drs. Zhimin Yan and Yining Huang of the University of Western Ontario for the REDOR experiment, and Drs. Eric Ye and Victor Terskikh for helping me with the 2D BABA, ^{31}P{^{1}H} HETCOR, and 1D ultra-fast MAS ^{1}H experiments at the 900 MHz NMR facility in Ottawa. Access to the 900 MHz NMR spectrometer was provided by the National Ultrahigh Field NMR

Facility for Solids (Ottawa, Canada), a national research facility funded by the Canada Foundation for Innovation, the Ontario Innovation Trust, Recherche Québec, the National Research Council Canada, and Bruker BioSpin and managed by the University of Ottawa. I would also like to thank Dr. Xiaohu Yan (Medicine) for the training in using a scanning electron microscope, and Dr. Suning Wang for the access of a fluorescence spectrometer. Dr. David Hodgson (Durham, UK) is acknowledged for providing us the 5'-GSMP sample.

I would also like to express gratitude to my parents Kwan Kin Ming and Mak Oi Kam, and siblings Shuk Man (Joyce) and Chun Kit (Peter) for their love, support, and encouragement throughout all these years. I am also grateful to all of my aunts, uncles, and cousins for the joyous times we shared. Jeffrey W. Walsh and his family are acknowledged for having been holding my hands during difficult times. Thank you for your continuous beliefs in me. I also want to express gratitude to all my friends around the world, for their friendships and encouraging words from time to time.

Lastly, I would like to dedicate this thesis to my late grandparents, especially my grandmother Pak Hang Fong. Thank you for your unconditional love and care when I was young and little. I hope you all rest in peace now, and continue to watch over us from above.

Statement of Originality

I hereby certify that all of the work described within this thesis is the original work of the author. Any published (or unpublished) ideas and/or techniques from the work of others are fully acknowledged in accordance with the standard referencing practices.

Irene Ching Man Kwan

June, 2012

Table of Contents

List of Figures

List of Tables

List of Abbreviations & Symbols

ν_{max}	Puckering amplitudes
σ_{ref}	Absolute shielding constant for reference sample
2D	2-dimensional
3'-GMP	Guanosine 3'-monophosphate
5'-GMP	Guanosine 5'-monophosphate
5'-GSMP	Guanosine 5'-thiomonophosphate
A	Adenine
ATP	Adenosine triphosphate
BABA DQ-MAS	Back-to-Back Double Quantum Magic-Angle-Spinning
C	Cytosine
CD	Circular Dichroism
COSY	Correlation Spectroscopy
cP	centi-Poise (unit)
dC	Deoxy-Cytosine
DFT	Density Functional Theory
dG	Deoxy-Guanosine
DLS	Dynamic Light Scattering
DNA	Deoxyribonucleic acid
DOSY	Diffusion-Ordered Spectroscopy
DOSY-NOESY	Diffusion-Ordered Nuclear Overhauser Spectroscopy
DQF-COSY	Double Quantum-Filter Correlation Spectroscopy
D_t	Translational diffusion rate
EFG	Electric Field Gradient
ESI-MS	Electrospray-Ionization Mass-Spectrometry
FT-IR	Fourier-Transform Infra-Red spectroscopy
G	Guanine
GIAO	Gauge Including Atomic Orbital
HETCOR	Heteronuclear Correlation Spectroscopy
HMBC	Heteronuclear Multiple-Bond Correlation spectroscopy

HSQC	Heteronuclear Single Quantum Coherence spectroscopy
I	Inosine
J	Indirect spin-spin coupling constant
K	Kelvin (unit)
Long-range COSY	Long-range Correlation Spectroscopy
LW	Linewidth
MAS	Magic-Angle-Spinning
N	C3'-*endo* puckering
NMR	Nuclear Magnetic Resonance
NOE	Nuclear Overhauser Effect
NOESY	Nuclear Overhauser Effect Spectroscopy
ORD	Optical Rotatory Dispersion
P	Pseudorotation phase angle
ppm	Parts per million (unit)
REDOR	Rotational-Echo Double-Resonance spectroscopy
Refocused HMBC	Refocused Heteronuclear Multiple-Bond Correlation spectroscopy
RNA	Ribonucleic acid
ROESY	Rotating frame Overhauser Effect Spectroscopy
S	C2'-*endo* puckering
T	Thymine or Tesla (unit)
TAG	Triacetylguanosine
TOCSY	Total Correlation Spectroscopy
U	Uracil
UV	Ultra-violet

Chapter 1
Introduction

1.1 Nucleic Acids and the double-helix model

Hereditary genetic material in organisms, also known as deoxyribose nucleic acid (DNA), was discovered by a Swiss biochemist, Friedrich Miescher, in 1869.[1] James Watson, Francis Crick, Rosalind Franklin, and Maurice Wilkins deciphered its structure in 1953 using x-ray diffraction data and molecular modeling.[2] Later on, multiple ribose nucleic acids (RNA) that play different roles in protein synthesis were also discovered.[3] Both DNA and RNA are composed of polynucleotide chains. The basic building block, mononucleotide, has three parts: 1) nucleobase, 2) ribose/deoxyribose sugar, and 3) phosphate. There are four basic nucleobases in DNA (adenine, cytosine, guanine, and thymine; abbreviated as A, C, G, and T, respectively) and four in RNA (A, C, G, and uracil (U)). Both A and G consist of purine rings and thus are referred to as the "purine-bases", while C, T, and U are referred to as the "pyrimidine-bases".[4] All purine and pyrimidine bases are planar because the ring systems are conjugated including exocyclic carbonyl and amino groups.[5] As shown in Figure 1-1, the ribose carbons are designated with primed numbers from 1' through 5', and the nucleobase atoms are labeled from 1 through 9.[4] When the ribose sugar is attached to the nucleobase at C1' position, the molecule is called a "nucleoside", and together with the phosphate group attached at the C5' position the molecule becomes a "nucleotide" (Figure 1-1).[4]

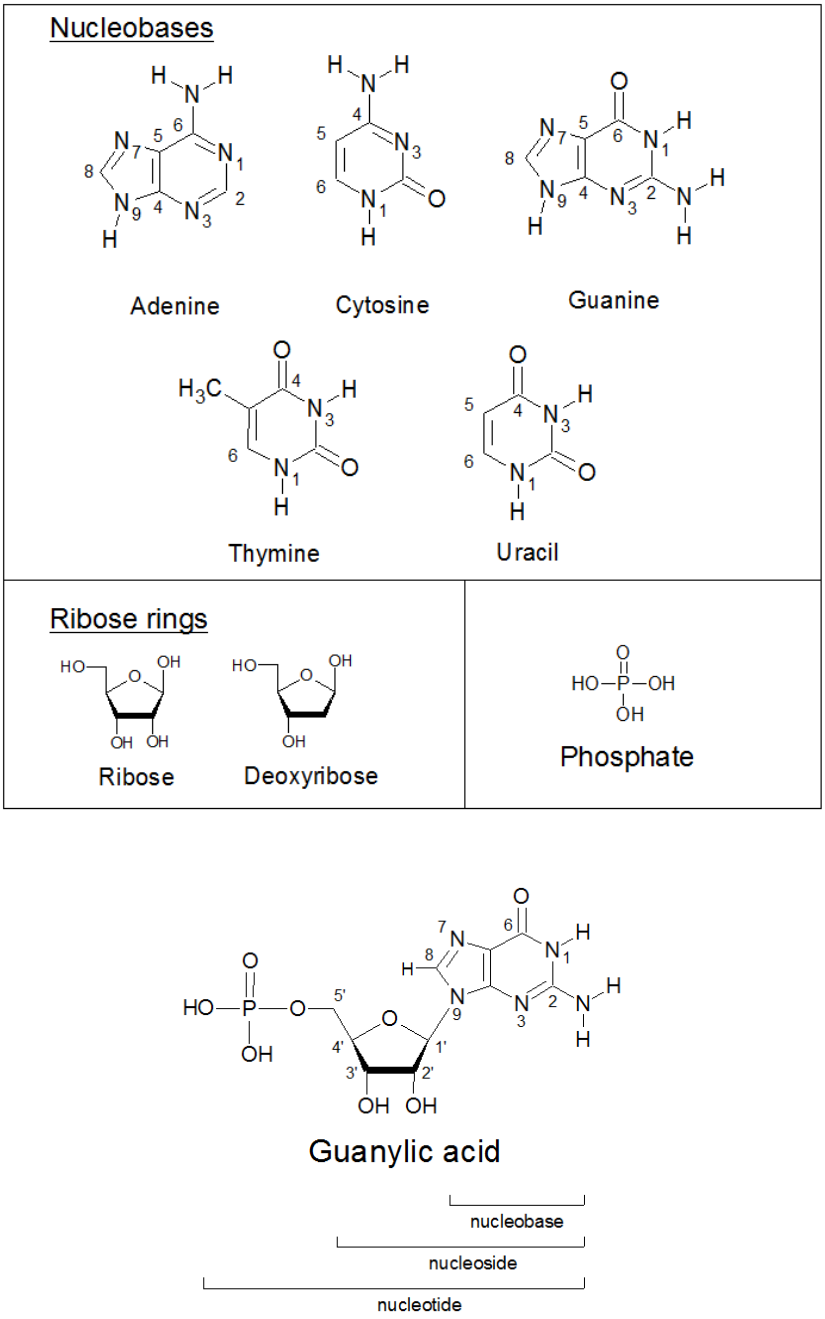

Figure 1-1. (Top) Basic components of DNA and RNA: nucleic acid bases, pentose sugar, and phosphate. (Bottom) An example of mononucleotide: guanylic acid (also known as guanosine 5'-monophosphate) with all atom labels.[4]

The ribose sugar moiety contains a hydroxyl (-OH) group at the C2' position in RNA, which is replaced by a hydrogen in DNA (hence the name "deoxyribose"). Unlike the planar nucleobases, the five-membered ribose ring can adapt several energetically stable conformations. An "*endo*" conformation is manifested by a carbon atom sitting above the ribose ring, as opposed to an "*exo*" conformation where a carbon is below the ring. The two most commonly observed conformations in DNA/RNA structures are the C2'-*endo* and C3'-*endo* conformations, denoted "^{2}E" (or "S") and "^{3}E" (or "N"), respectively (Figure 1-2).[4]

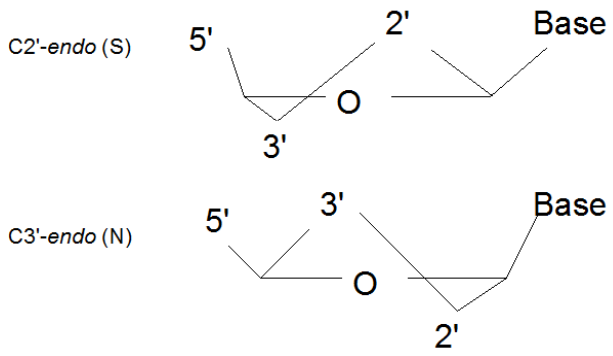

Figure 1-2. C2'-*endo* (S) and C3'-*endo* (N) puckering of the ribose ring.

Besides the planar nucleobases and a puckered ribose sugar, a nucleotide can have many conformations depending on how the three parts are related to each other spatially.[4] Table 1-1 lists the torsion angles that are used to describe different nucleic acid conformations. The torsion angles χ and γ decide the most notable structural features of a mononucleotide. With respect to the sugar ring, two main orientations about the glycosyl C1'-N9 bond, called *anti* and *syn*, is defined by the torsion angle χ (Figure 1-3). In the

anti conformation (180° ± 90°), the nucleobase is directed away from the sugar, while it is towards or above the sugar in a *syn* conformation (0° ± 90°).[4]

Table 1-1. Definitions of different torsion angles used to describe nucleic acid structures (n = a particular nucleotide in the polynucleotide chain).[4]

Torsion angles	Atoms involved (in a polynucleotide chain)
α	(n-1) O3'-P-O5'-C5'
β	P-O5'-C5'-C4'
γ	O5'-C5'-C4'-C3'
δ	C5'-C4'-C3'-O3'
ε	C4'-C3'-O3'-P
ξ	C3'-O3'-P-O5' (n+1)
χ	O4'-C1'-N9-C4 (purine)/C2 (pyrimidine)
ν_o	C4'-O4'-C1'-C2'
ν_1	O4'-C1'-C2'-C3'
ν_2	C1'-C2'-C3'-C4'
ν_3	C2'-C3'-C4'-O4'
ν_4	C3'-C4'-O4'-C1'

Another important torsion angle in nucleic acids is the exocyclic C4'-C5' angle γ, which describes how O5' and its substituents assume different positions relative to the sugar ring. The three main conformations with substituents in staggered positions are shown in Figure 1-4. The three conformations are *gauche-gauche* (*gg*), *gauche-trans* (*gt*), and *trans-gauche* (*tg*).[4] In general, the torsion angles of a nucleotide are determined by

the constraints imposed by the polynucleotide and double-helix structures as described below.

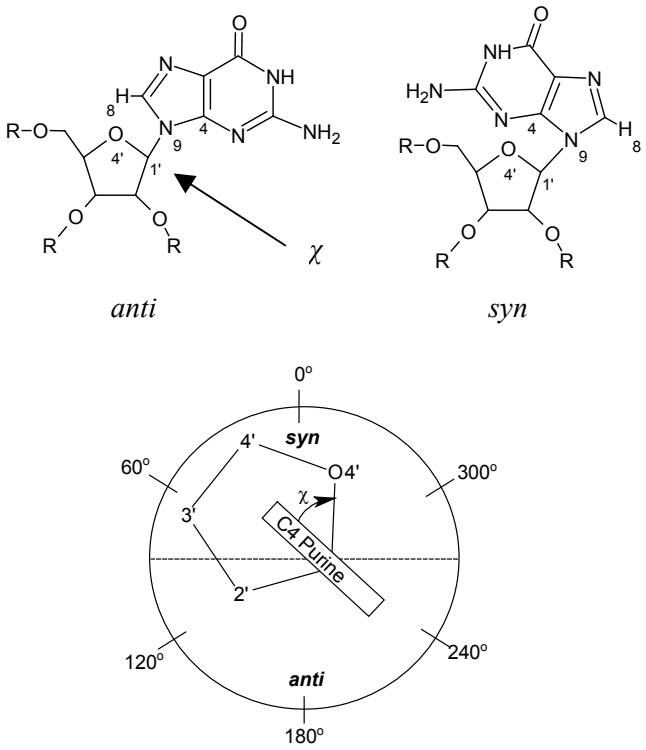

Figure 1-3. Definitions of *anti* and *syn* conformations in a guanylic acid molecule.

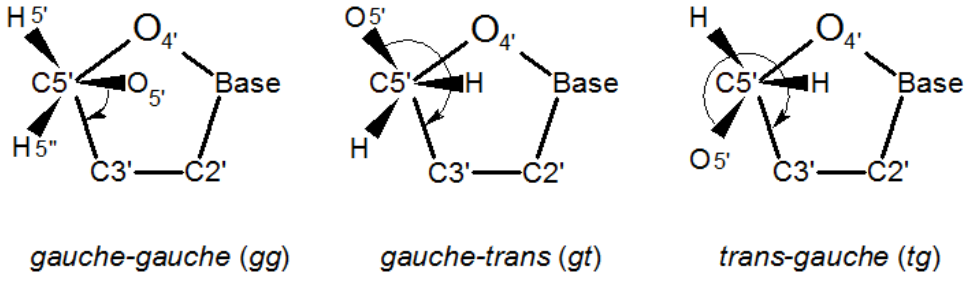

Figure 1-4. Definitions of the torsion angle γ along the C4'-C5' bond, looking in the direction of C5' to C4'.

Mononucleotides can be joined using enzymes (polymerases) that create phosphodiester bonds to form a polynucleotide chain. A covalent bond is formed between the 5'-phosphate (n) and the 3'-hydroxyl group of the next mononucleotide (n+1) through a condensation reaction. The free 5'-phosphate group is termed the "5'-end", while the free 3'-hydroxyl group is called the "3'-end" (Figure 1-5).[4] A polynucleotide chain is also negatively charged due to deprotonation of backbone phosphate groups at neutral pH.

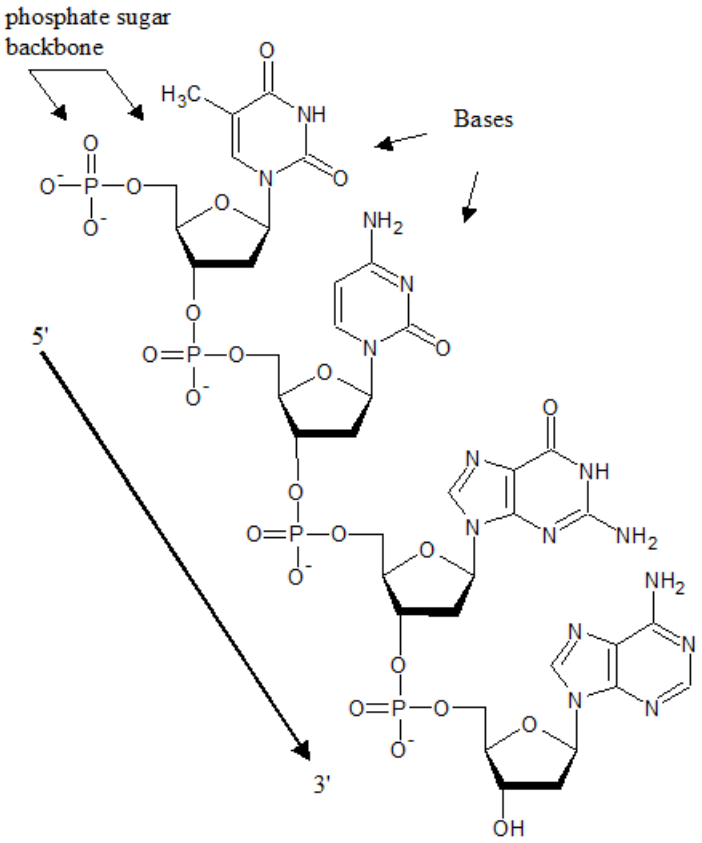

Figure 1-5. A DNA polynucleotide chain.

Besides elongation through phosphodiester bonds, mononucleotides can also bind to each other through hydrogen bonds. In terms of chemical structure, a nucleoside

has many hydrogen-bond donors and acceptors (Figure 1-1). The major hydrogen-bond donors include imino (-NH) and amino ($-NH_2$) groups for nucleobases, and the major acceptor groups are carbonyl C=O and -N= groups. Since these donors and acceptors are part of a π-conjugated system, π-bond polarization occurs during hydrogen-bond formation, and enhances the stability of the hydrogen bonds in nucleic acids.[5] In fact, the double helix structures of DNA and RNA are formed due to hydrogen bonding between two polynucleotide chains. The principle of "base pairing" unique to DNA/RNA is shown in Figure 1-6 where a purine forms either two or three hydrogen bonds with a pyrimidine. The allowed base pairings include A•T (or A•U in RNA) and G•C. These are collectively known as the "Watson-Crick base pairings" and other types of pairing are generally considered mismatches in DNA/RNA structures.

Using hydrogen bonds between bases and other weak forces, such as van der Waals base-stacking interactions, hydrophilic (backbone)/hydrophobic (bases) effects, and electrostatic repulsion or attractions between the negatively charged nucleotides and surrounding ions, two DNA polynucleotide chains form a double-helix with regular, repeating structure but random sequence of bases. The sugar-phosphate backbones are on the outside while the bases are in the inside and the entire double-helix is made without covalent bonds between the two strands. In terms of base pairing, small pyrimidine bases must only pair with large purines or else a bulge (from two purines) or a hole (from two pyrimidines) would form. The spacing between stacking base pairs is 3.4 Å, and the overall helix repeat distance is about 34 Å (~10 base pairs). The two polynucleotide strands are anti-parallel to each other, i.e., one has 5' → 3' polarity from the top to bottom, while the other has a 3' → 5' polarity from the same direction.[4]

There are three types of double-helices: A, B, or Z forms (Figure 1-7). The structure proposed by Watson and Crick in 1953 is the B-form DNA. It exists in high humidity (92%) while the A-form exists in a dryer condition (75% humidity).[4] Both A- and B-forms are right-handed helices composed of *anti* nucleotides. The A-form that is more common in RNA, has only C3'-*endo* puckering, while B-form in DNA contains only C2'-*endo* ribose. In the B-form DNA, all base pairs are horizontal while they are slightly tilted towards the helix axis in the A-form. Rich and colleagues discovered that Z-DNA with alternating purines and pyrimidines nucleotides (e.g., poly[G-C]•poly[C-G]) forms a Z-form DNA. The Z-form only exists occasionally in DNA with high salt concentrations.[6] Contrary to the A- and B-forms, Z-DNA has a left-handed helix with a dinucleotide repeating unit, with all cytosines being in *anti* with C2'-*endo* puckering, and all guanosines are in *syn* with C3'-*endo* puckering.[6]

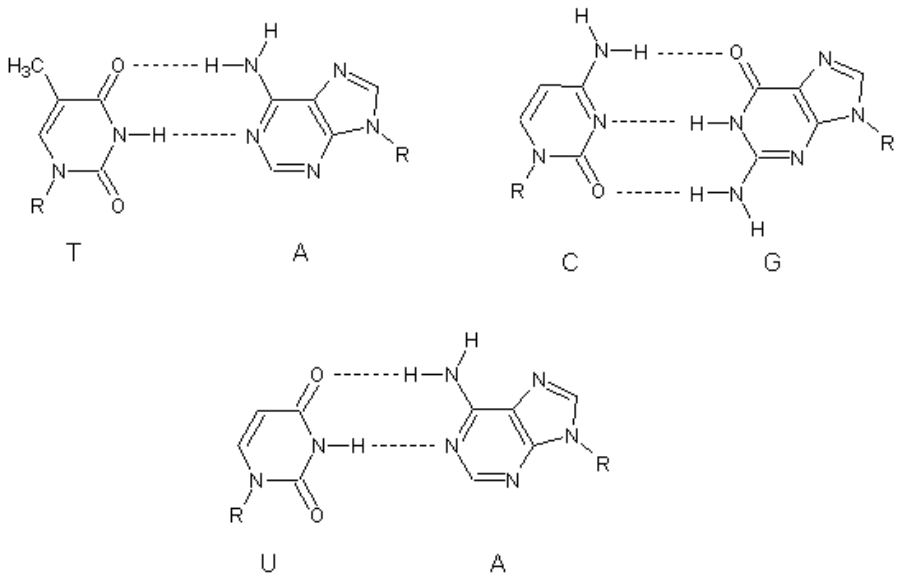

Figure 1-6. Watson-Crick base pairings in DNA and RNA. R = ribose and phosphate groups.[4]

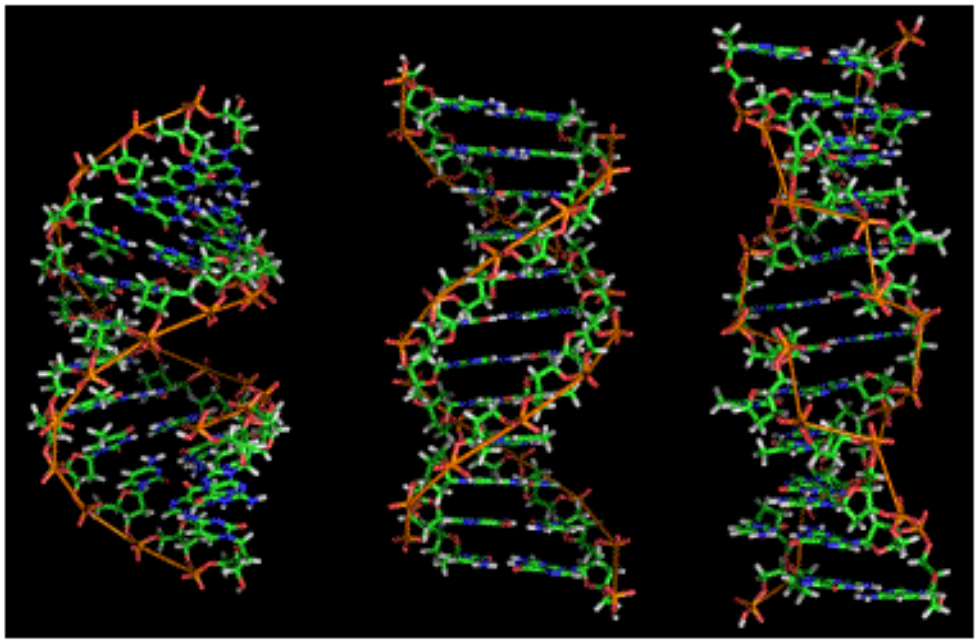

Figure 1-7. (From left to right) A, B, and Z-form of DNA.[7]

1.2 A special kind of nucleic acid structure: G-quadruplex

Besides the Watson-Crick type of base pairing found in a double-helix, other types of hydrogen bonds were also found naturally among the four bases. In 1966, Crick proposed the "Wobble base-pairing theory" that explains the recognition of certain mismatched RNA during protein translation.[8] Some of the Wobble-base pairs include A•A, A•C, A•G, C•C, G•G, G•U, G•T, U•C, and U•U. This theory explains the amount of transfer RNA (tRNA) present in nature being smaller than expected because the tRNA (anticodon) is relaxed in selectivity with respect to the receiver (codon) present in messenger RNA (mRNA), a phenomenon known as "codon degeneracy".[8] While the "Wobble base-pairing theory" being a biological phenomenon, another type of irregular

base pairing proposed by Hoogsteen in 1963, named "Hoogsteen base-pairing", needs to be discussed in further detail as it has huge biological and chemical implications.

Using x-ray crystallography, Hoogsteen observed a stable structure in which N3 of thymine could form a hydrogen bond with N7 of adenine, instead of N1 as in the Watson-Crick pairing model (Figure 1-8).[9] The Hoogsteen type of base pairing is then defined as any base pairing using hydrogen donors and/or acceptors different from those used in the Watson-Crick model. Hoogsteen base-pairing is very rarely observed in transcribing DNA (<1%) and its discovery revolutionized the traditional view on nucleic acid structure. Using the Hoogsteen type of base pairing, DNA and RNA molecules now become building blocks of a vast amount of possible, alternate structures including triplex or even quadruplex DNA helices.[10] One of the most important structures is the quadruplex of guanosine-rich DNA sequences, or "G-quadruplexes".

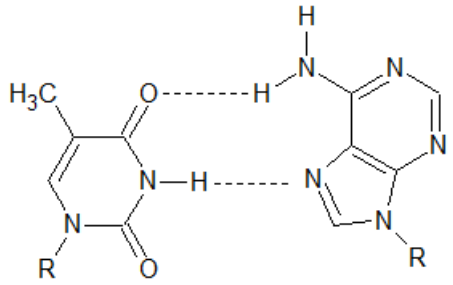

Figure 1-8. Hoogsteen type of base-pairing between A and T.

Guanine, being one of the DNA bases, is very unique because its hydrogen bond donors and acceptors are 90º to each other (Figure 1-9). Under slightly acidic conditions, guanosine 5'-monophosphate, or 5'-GMP, was observed to form a gel in aqueous environments.[11] X-ray fiber diffraction, UV, CD, and IR studies of this gel revealed a

structure where four 5'-GMP molecules self-assemble into a "G-quartet" using Hoogsteen-type of hydrogen bonds (Figure 1-10).[12,13,14]

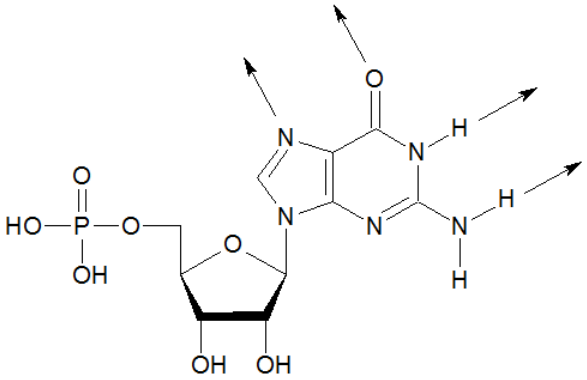

Figure 1-9. Hydrogen bond donors and acceptors of guanosine 5'-monophosphate which participate in G-quadruplex formation.

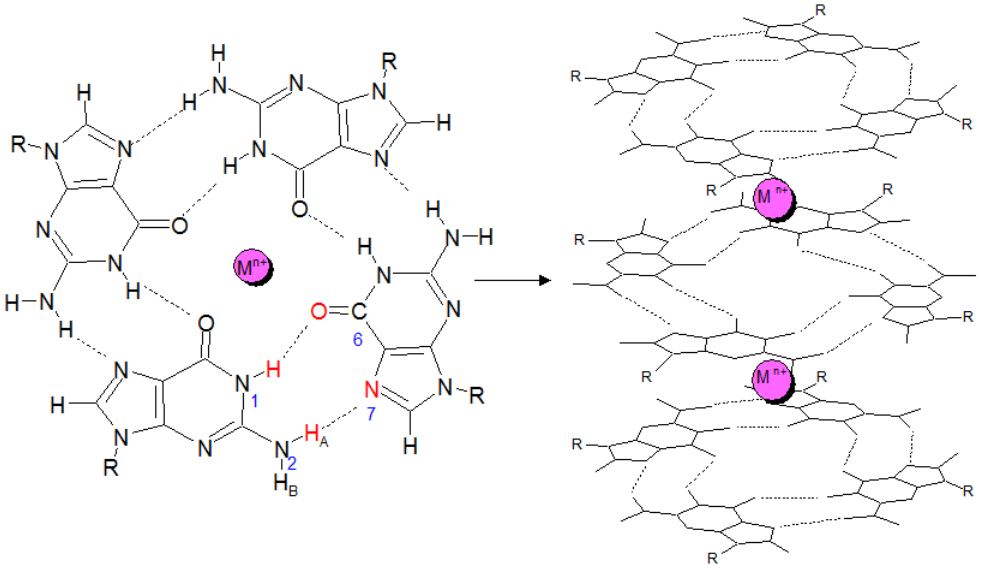

Figure 1-10. (Left) G-quartet with Hoogsteen hydrogen-bonding atoms labeled and (right) G-quadruplex formed with multiple layers of stacked G-quartets and metal cations. R = 5'-phosphate ribose.

Each G-quartet is formed via four pairs of Hoogsteen-type of hydrogen bonds between $N^1H\cdots O6$ and $N^2H_A\cdots N7$ (Figure 1-10). These G-quartets can stack on top of each other with a separation of ~3.4 Å and a twist of 30-45° to form a column-like G-quadruplex.[12] Metal cations are sandwiched between G-quartets and have ion-dipole interactions with the surrounding eight carbonyl-oxygens. Other non-covalent forces include π-π stacking between the nucleobases, ion-phosphate interactions, as well as electrostatic repulsion between cations. It is also important to know that only certain metal cations with an appropriate ionic radius, such as Na^+ or K^+, can fit into the channel of the G-quadruplex column.[15] More details about the G-quadruplex structure are discussed in the next session.

Before 1990, research on G-quartet or G-quadruplex structures was mostly in the hands of chemists and driven largely by curiosity. However, several discoveries made in the early 1990s suggested that G-quartets might be present *in vivo*. These important discoveries include the crystal structure of a four-stranded *Oxytricha* telomeric DNA,[16] and the first NMR structure of human telomere quadruplex in Na^+-containing solution.[17]

A telomere is a protein/DNA complex found at the very end of each chromosome and plays a critical role in cell senescence. Since G-quadruplexes could exist in telomere DNA, its potential of being a therapeutic target in cancer research has been heavily investigated.[18,19] The DNA sequence of human telomeres consists of repeats of a short sequence 5'-TTAGGG-3'. Every time DNA is replicated, some TTAGGG units are lost, eventually the telomere sequence is shortened below a critical length and the cell dies. However, cancer cells can prevent the telomere from being shortened by expressing

telomerase, a protein that facilitates telomere extension.[20] One of the approaches to inhibit telomerase activity is to block telomerase-substrate interactions. While the single-stranded G-rich telomere is a substrate of telomerase, the folded G-quadruplex is not. Therefore, formation of G-quadruplexes could prevent telomerase from binding to the DNA strand, and hopefully cancer cell formation can be prohibited through this mechanism.[21,22,23] For example, tumour oncogenes have been shown to be suppressed via stabilization of the G-quadruplex structure in the presence of sodium ions.[24] It is also known that several human genes associated with diseases such as Fragile X Syndrome contain G-quadruplexes in its sequences.[25] Therefore, it is not surprising that biological G-quartets have received numerous attention in the last two decades. Figure 1-11 shows a crystal structure of a human telomeric G-quadruplex formed in the presence of K^+ ions.[26]

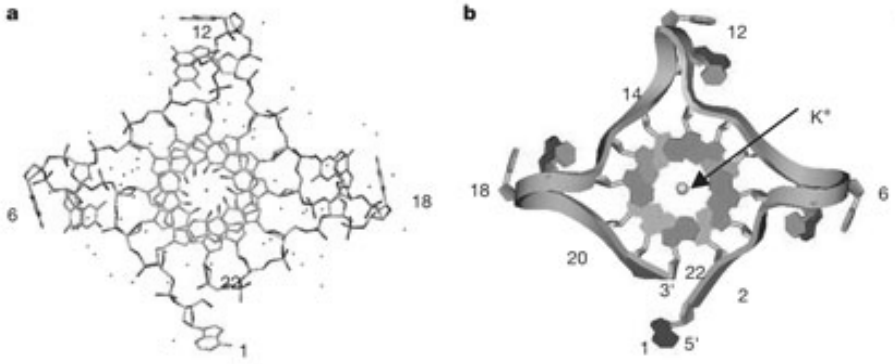

Figure 1-11. (a) Viewed on the 5' end, a stick representation of the G-quadruplex formed from a human telomere sequence, d[AGGG(TTAGGG)$_3$] (22-mer), in the presence of K^+ ions. (b) Same structure viewed from the 3' end of the G-quadruplex looking down the helical axis. Phosphate backbone (ribbon) shows 5'-to-3' directionality. (Picture adopted from Ref. 26.)

Another important biological implication of G-quadruplex is its resemblance to transmembrane ion channels. The environment around K^+ ions in the selectivity filter of K^+-channel proteins is very similar to that inside a G-quadruplex channel.[27,28] In both cases, the cation is surrounded by eight carbonyl groups in an antipyrimidal or cubic fashion.[27] Many attempts have been made to mimic ion channel proteins with G-quadruplex systems.[29,30,31]

Besides these two applications, both biological and synthetic G-quadruplex systems have been utilized as extractants of the radioactive ^{226}Ra or biosensors based on their affinity to different types of metal ions,[32,33,34] as well as DNA nanomachines[35], surface ligands[36], macroscopic membrane films[37], hydrogels that could serve as bioactive molecule carriers[38], and photo- or electro-active molecular electronic devices[39]. Numerous G derivatives and their abilities to form various supramolecular structures are thoroughly documented in the literature.[40,41,42,43,44,45]

1.3 The first biological G-quadruplex: 5'-GMP

Almost a century ago, Ivar Christian Bang (1869-1918) discovered that, under acidic conditions, 5'-GMP molecules form a white gel while they remain as a clear liquid at neutral pH (Figure 1-12).[11] In 1962, Davies and colleagues examined the x-ray fiber diffraction data for 5'-GMP and 3'-GMP gels and proposed that the structural basis of gel formation is a hydrogen-bonded guanine tetramer now termed as a G-quartet.[12,46,47]

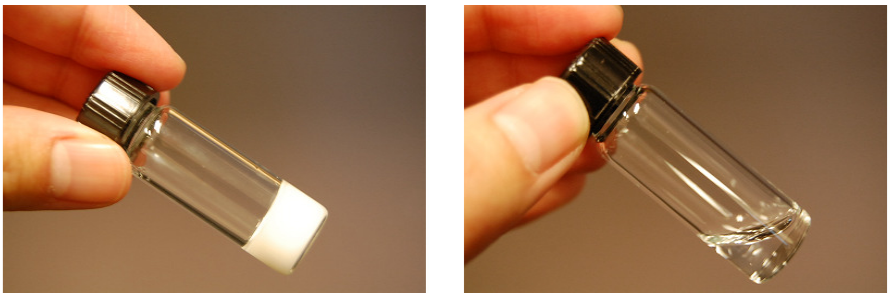

Figure 1-12. Disodium guanosine 5'-monophosphate aggregates formed under pH 5 (left) and pH 8 (right) conditions. The samples are of the same concentrations.

As mentioned earlier, each G-quartet consists of four pairs of Hoogsteen-type of hydrogen bonds between $N^1H\cdots O6$ and $N_2H^A\cdots N7$ atoms. The angles between the hydrogen-bond donors and acceptors make it possible to form a square-shaped, planar tetramer. Davies and colleagues further proposed that G-quartets could stack on top of one another using weak π-π interactions between guanine rings. At about the same time, Miles and Frazier used infrared (IR) spectroscopy to study 5'-GMP solution under a neutral pH.[13] They found evidence that 5'-GMP self-associates into an ordered structure in neutral solution.[4] The authors also found that the self-assembly of 5'-GMP is reversible as the aggregate dissociates into monomers with increasing temperature and forms an ordered structure again when the temperature is decreased. It appears that 5'-GMP gel formation only occurs when the phosphate group is singly protonated ($C\text{-}O\text{-}PO_3H^-$) at pH < 5. Under a neutral or slightly basic condition (pH 7-8), strong repulsion between doubly negatively charged phosphate groups ($C\text{-}O\text{-}PO_3^{2-}$) makes it more difficult to form extensive self-assemblies. Using circular dichroism (CD) spectroscopy, Chantot et al. also noticed that cations play an important role in 5'-GMP self-assembly.[14] The authors

claimed that aggregates of 5'-GMP are formed only under conditions of "high 5'-GMP concentration, low temperature, defined pH range, and high ionic strength".[14] In 1975, Pinnavaia and colleagues decided to use solution-state NMR to study 5'-GMP self-assembly in neutral solutions.[48] Their study was the first NMR study of 5'-GMP under high concentration, neutral pH, and low temperature conditions and provided a great deal of useful information on 5'-GMP self-assembly. First, ^{1}H NMR spectra provide direct evidence that the guanine imino ($N^{1}H$) and amino ($N^{2}H_{A}$) protons are involved in hydrogen bonds. Secondly, the authors reported the observation of four different ^{1}H NMR signals for each proton of 5'-GMP. Because the four distinct signals from proton H8 appear well separated from other signals, they were used to analyze the four different 5'-GMP species (denoted H8 α, β, γ, and δ) present concurrently in the sample (Figure 1-13). Neurohr and Mantsch also reported the ΔG° for 5'-GMP to form aggregates at pH 7.4 and 30°C in aqueous environment to be -0.6 kJ/mol.[49]

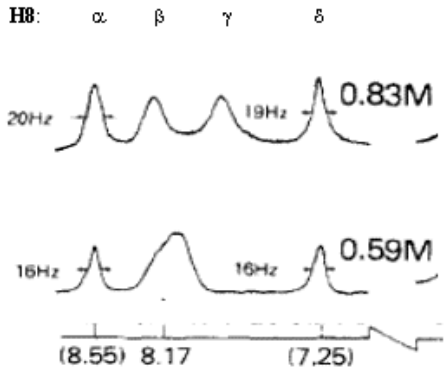

Figure 1-13. Partial ^{1}H NMR spectra of neutral disodium guanosine 5'-monophosphate solutions at different concentrations showing the four H8 signals (spectra adopted from Ref. 48; the bottom axis represents ^{1}H chemical shift in ppm).

Based on spin-lattice relaxation measurements, the authors suggested that both α and δ (1:1 ratio) were signals from a head-to-tail stacking octamer (C_4 symmetry), while β was another type of octamer, perhaps tail-to-tail or head-to-head stacking (D_4 symmetry) and γ was assigned the monomer or dimer 5'-GMP molecules. Over the next decade, Pinnavaia and colleagues studied the 5'-GMP system in neutral solution using other NMR techniques such as ^{13}C, ^{31}P, relaxation measurements, and nuclear Overhauser effect (NOE).[50,51,52] They also found that the G-quadruplex structure exhibits different affinity for different metal ions.[15] In a G-quadruplex, each cation is sandwiched between two G-quartets. It can be imagined that each cation is being encapsulated in a pseudo-cage where eight carbonyl oxygen atoms form the corners (Figure 1-10). Both ionic radius and charge of the cation are critical for the formation and stability of the G-quadruplex structure. Pinnavaia and colleagues discovered that neither too small nor too large cations such as Li^+ and Cs^+ (ionic radius 0.92 and 1.69 Å, respectively) promote G-quadruplex formation, whereas Na^+, K^+, and Rb^+ (ionic radius 1.18, 1.51, and 1.61 Å, respectively) are necessary for stable G-quadruplex structures.[15] Because small cations are too far from the corners of this pseudo-cage to balance the electronegative carbonyl oxygens, no G-quadruplex is formed. The opposite occurs for large cations, as the G-quadruplex will be forced to break apart when a large cation enters the cage. The averaged $O_6 \cdots M^+$ distance in a stable G-quadruplex is 2.2-2.3 Å, and among monovalent cations, K^+ has the highest affinity for G-quadruplex formation followed by Na^+ and Rb^+.[15]

Pinnavaia and colleagues also noted that two different cation-binding sites exist for the G-quadruplex formed by 5'-GMP in neutral solution.[51] The specific structure-

directing site, also known as the "channel" site, is where the cations reside inside the G-quadruplex. The other non-specific binding site, also known as the "surface" site, is the phosphate group (C-O-PO_3^{2-}) of the 5'-GMP molecules. Cations binding to the surface site can balance the electrostatic repulsion between neighboring phosphate groups, therefore they also play a role in G-quadruplex stability.[51] In the early 1980s, Detellier et al. used NMR to study binding affinity and found that, when Na^+ and K^+ are both present in 5'-GMP solution, the stoichiometry of the aggregate is approximately $4Na^+(G_4\text{-}K^+\text{-}G_4)$. In particular, K^+ ions have a higher binding affinity for the channel site while Na^+ ions are preferred at the surface sites.[53] Detellier et al. were also the first to use NMR for direct detection of alkali metal ions (e.g., $^{23}Na^+$, I = 3/2) in G-quadruplex systems. These authors confirmed the formation of octamers and/or hexadecamers in neutral 5'-GMP solutions.[54,55]

Several other research groups had also studied the neutral 5'-GMP system. In 1982, Peterson et al. reported the presence of two different types of dimers in Na_2(5'-GMP) solution using ^1H, ^{13}C, and ^{31}P NMR results.[56] The proposed asymmetric hydrogen-bonded dimer was essentially one half of a G-quartet, while the symmetric dimer model was a pure speculation at the time. Although the asymmetric dimer model has been largely discarded by other researchers in the field, the observed fast exchange between the H_8 β and γ signals is consistent with the possibility of β being the stacking symmetric dimers instead of the isomeric *D_4* octamers as suggested by Pinnavaia and colleagues.[48,57] Another single-crystal x-ray study by Lipanov et al. confirmed that monomers from a neutral 5'-GMP sample form G-quartets that are perpendicular to the helical axis.[58] The authors also reported the 5'-GMP G-quadruplex to be a right-handed

helix composed of twelve molecules (i.e., three G-quartets). Further studies using CD and NMR yielded contradicting results such as a left-handed helix composed of fourteen residues, etc.[59,60] It is clear that, despite considerable effort, the 5'-GMP self-assembly process has never been fully understood.

1.4 Motivation and organization of the thesis

Because of the aforementioned biological implications of G-quartet and G-quadruplex, a huge amount of effort has been devoted to this field since the 1990s largely led by biochemists and molecular biologists. However, it is rather remarkable that the exact structure of 5'-GMP helix, the first G-quartet system, is still unknown after nearly 50 years. In 2000, in a search for NMR signatures for channel and surface ions in G-quadruplex DNA, Wu and Wong revisited the neutral 5'-GMP system using solid-state NMR.[61,62] These authors examined the Na^+ ions using magic-angle spinning (MAS) ^{23}Na NMR and established the signature signal of Na^+ in G-quadruplex systems.[61] The authors also found the channel and surface ^{39}K signals using a very high magnetic field (900 MHz) and proved the capability of examining G-quadruplex structures using solid-state NMR on cation nuclei.[62] In addition, the same authors were able to quantitatively determine the free energy differences for ion competition among Na^+, K^+, NH_4^+, Rb^+, and Cs^+ in both channel and surface sites.[63]

Out of all the methods employed to study 5'-GMP G-quadruplex, none were able to reveal the true aggregate size until Jurga-Nowak et al. studied the system using dynamic light-scattering (DLS).[64] In this case, the hydrodynamic radius of the self-assembled structure as a function of temperature, ionic strength, and nucleotide

concentration were determined by measuring translational and rotational diffusion coefficients of the aggregates from which the size and shape of G-quadruplexes could be calculated. The authors reported that, in a highly concentrated 5'-GMP solution, there are at least 32 layers of G-quartets present in a single helix.[64] This provoking result prompted Spindler et al. to study a similar G-derivative (5'-dGMP) using ^{31}P NMR and DLS,[65] which ultimately led to a collaboration between Spindler and Wu in using both diffusion-ordered NMR spectroscopy (DOSY) and DLS to study Na_2(5'-GMP) under neutral conditions.[66] Similar to DLS, a DOSY experiment measures the translational diffusion rate (D_t) of a molecule, which is a function of molecular size, solvent viscosity, and temperature. In this study, the authors reported several significant results. First, at 18-34% w/w Na_2(5'-GMP) concentrations, two types of rod-like cylinders were observed: the stacking monomer cylinder and the G-quartet cylinder. Each G-quartet cylinder is about 8-30 nm long and corresponds to 24-87 stacking G-quartets.[66] Another finding was that the column length increases with the 5'-GMP concentration, but insensitive to the Na^+ concentration, which suggests that an equilibrium is established between the stacking monomers and G-quartets. Further introduction of Na^+ ions would not shift the system to form more G-quadruplexes. The authors also observed an increase of monomeric aggregate size when the temperature of solution decreases, while the size of G-quartet aggregates was found to remain unaffected by temperature. The authors proposed a common stacking mechanism between the monomer and G-quartet cylinders as a linear relationship was observed between cylinder sizes and Na_2(5'-GMP) concentration.[66]

The aforementioned new results regarding the size of 5'-GMP self-assembly have not only provided new insights into the 5'-GMP self-assembly process, but also

called for a new interpretation of the previously reported NMR data. This renewed interest in 5'-GMP self-assembly and its relevance to G-quadruplex nucleic acid structures led us to ask the unavoidable question: what is the exact helical structure of 5'-GMP in the neutral to slightly basic (referred to as "neutral" only in the text) solution? In Chapter 2, we present the structural determination of Na_2(5'-GMP) self-assembly in neutral solution. In Chapter 3, we investigate the structure of acidic Na_2(5'-GMP) gel and disapprove a long-believed model of this G-quadruplex helix. In Chapter 4, we investigate the self-assembly of disodium thioguanosine 5'-monophosphate (5'-GSMP). In Chapter 5, we report for the first time that a lipophilic guanosine derivative forms G-quadruplexes in the presence of trivalent metal cations (M^{3+}). Lastly, Chapter 6 provides concluding remarks for this thesis.

Chapter 2

Structure determination of disodium guanosine 5'-monophosphate G-quadruplex in neutral solution

2.1 Introduction

As mentioned in Chapter 1, the exact structure of Na_2(5'-GMP) helix formed under neutral conditions remains unknown. The current information reveals that, at high concentrations and in the presence of Na^+ ions, ordered G-quadruplexes are formed. The G-quadruplexes are large aggregations composed of stacking layers of G-quartets, whose size depends on concentration and temperature. Because single crystals are extremely difficult to obtain from concentrated neutral Na_2(5'-GMP) solutions, we decided to use NMR to determine the exact structure of Na_2(5'-GMP) G-quadruplex in aqueous solution.

2.2 Experimental Details

2.2.1 Sample preparation

The D_2O sample was prepared by dissolving 305 mg Na_2(5'-GMP)·$6H_2O$ (Sigma, Lot 035K1194, no further purification) twice in D_2O (0.6mL, 99.99%) to remove H_2O from the hydrous 5'-GMP. The sample is then degassed with N_2 for 20 min to remove any dissolved O_2. For the H_2O/D_2O sample, Na_2(5'-GMP) was dissolved in equal amounts of H_2O and D_2O without degassing the sample. Final concentration of both D_2O and H_2O/D_2O samples is 1.0 M (50% w/w). Acidity of these samples is pH 8.0 without introducing any acids or bases. All ^{31}P titration experiments were performed using a dilute Na_2(5'-GMP) sample (1.5×10^{-2} to 5.0×10^{-2} M in D_2O) and pH was adjusted using

concentrated $DCl_{(aq)}$. The final pH values were obtained using the formula: pH = pD + 0.4.[67]

2.2.2 NMR spectroscopy

All solution-state NMR spectra were recorded on a Bruker Avance 600 MHz spectrometer (14.1 T), including both 1D and 2D experiments. All chemical shifts were reported in parts per million (ppm). For ^{1}H experiments, the ^{1}H 90° and 180° pulse widths at a pulse power of 0.0 dB were 13.0 μs and 26.0 μs, respectively. For ^{13}C experiments, the ^{13}C 90° and 180° pulse widths at a pulse power of -1.5 dB were 25 μs and 50 μs, respectively. The ^{31}P 180° pulse was 50 μs at 0.0 dB, and 85% $H_3PO_{4(aq)}$ was used as an external reference. For solution-state ^{23}Na NMR, the Hahn-echo pulse sequence HE.GW.TXT without H-decoupling was used with a 180° pulse of 32 μs at 5 dB. Delay time 0.2 s was used, and a total of 1,024 transients with 2,024 scans were collected. An analogue filter was used with processing parameter lb=10Hz. Sample was referenced externally to 1.0 M $NaCl_{(aq)}$ at 0 ppm. All pulse sequences were available in the program Bruker Xwin NMR Version 3.5, and experimental temperatures were carefully controlled by a Bruker BT-3000 unit.

COSY. 2D homonuclear shift correlation (^{1}H-^{1}H COSY) spectra which detects ^{1}H-^{1}H through scalar coupling was carried out on the D_2O 5'-GMP sample at 278.0 K using the pulse program COSYGPQF (Bruker XWinNMR Version 3.5) on a Bruker Avance 600 MHz spectrometer. The data were collected using a 90° pulse of 10.0 μs at a power of 0 dB and a relaxation delay of 3.0 s. The spectral width was 4194.63 Hz on

either dimension. Two scans were collected. Final data matrix was 2048 (F2) x 1024 (F1).

^{1}H-^{31}P COSY. Proton-detected 2D heteronuclear shift correlation was performed on the D_2O sample at 298.0 K. The 90° and 180° pulse widths of ^{31}P at pulse power 0.0 dB were 22.0 μs and 44.0 μs, respectively. ^{31}P chemical shift was externally referenced to 85% $H_3PO_{4(aq)}$ at 298.0 K. The spectral widths were 2403.8 Hz (F2) and 971.8 Hz (F1). A total of 20 scans were collected with a relaxation delay of 10.0 s, and the final data matrix was 1024 (F2) x 256 (F1).

Long-range COSY. 2D long-rage homonuclear shift correlation spectra which detects ^{1}H-^{1}H of < 3 Hz scalar coupling was carried out on the D_2O 5'-GMP sample at 298.0 K using the pulse program COSYLGQF (Bruker XWinNMR Version 3.5) on a Bruker Avance 600 MHz spectrometer. The data were collected using a 90° pulse of 12.0 μs at pulse power 0 dB, and a relaxation delay of 2.0 s. The fixed delays for evolution of long-range coupling (d6) were varied between 0.01-0.1s. The spectral width was 4194.631 Hz on either dimension. Eight scans were collected. Final data matrix was 2048 (F2) x 512 (F1).

DOSY. ^{1}H diffusion experiment was carried out on the D_2O 5'GMP sample at 278.0 K. The pulse sequence of longitudinal eddy current delay with bipolar-gradient pulse (LEDBPGP2s) was employed. The pulse field gradient duration (δ) was 7.5 ms, and the variable gradient strength (G) was 5.645-5.750 G/mm. The diffusion period (Δ) was 75.0 ms, and a total of 4096 transient points with 16 scans were collected for each of the 32 increment steps with a recycle delay of 5.0 s. The eddy current delay (t_w)

employed was 5 ms, and the gradient recovery delay was set at 0.2 ms. Calibration of the field gradient strength was performed by measuring the value of translational diffusion coefficient (D_t) for the residual ^{1}H signal in D_2O (99.99% ^{2}H atom), where D_t = 1.90 x 10^{-9} m^2/s.[68] The spectral width was 4194.6 Hz and a line-broadening of 10 Hz was employed in data processing (F2).

DOSY-NOESY. A 2D experiment was created (by Dr. Gang Wu) by modifying the 3D DOSY-NOESY experiment (LEDBPGPNO3s3d) and was carried out on the D_2O sample at 298.0 K. The NMR experimental parameters were identical to the DOSY experiment, except the pulse field gradient duration (δ) was 1.0 ms, and the diffusion period (Δ) was 300.0 ms. A total of 8 scans were collected with a recycle delay of 3.0 s. The mixing time (τ_{mix}) for NOE was 100 ms, and the final data matrix was 2048 (F2) x 512 (F1).

DQF-COSY. 2D homonuclear shift correlation spectrum (COSY) with double quantum filter using gradient selection was recorded at 298.0 K on the D_2O sample from the pulse program COSYDFETGP. A total of 16 scans and a relaxation delay of 6.0 s were collected for a spectrum with 2403.8 Hz on either dimension. The final data matrix was 2048 (F2) x 512 (F1). Contrary to regular COSY experiment, the signals observed are all derived from double-quantum coherence present between the second and third 90° pulses. This allows all the lines in the spectrum having all double absorption mode lineshape (compare to COSY where cross and diagonal peaks have opposite lineshapes). However, because only the double-quantum part of the coherence is observed, signal intensity is less compared to COSY experiments.

HMBC. 2D spectrum of ^{1}H-^{13}C correlation through heteronuclear zero and double quantum coherence transfer was performed using the pulse program HMBCGPLPNDQF at 298.0 K on the H_2O/D_2O sample. A low-pass *J*-filter was employed to suppress one-bond correlations, and no ^{13}C decoupling was applied during acquisition. The long-range coupling delay was 62.5 ms (corresponds to a long-range coupling of 8 Hz) and the one-bond coupling delay was 3.45 ms (145 Hz). A total of 450 scans were collected with a relaxation delay of 1.0 s. The spectrum widths were 6009.6 Hz (F2) and 21,130.1 Hz (F1), and the final data matrix was 4096 (F2) x 256 (F1).

Refocused-HMBC. 2D ^{1}H-^{13}C correlation via heteronuclear zero and double quantum coherence was performed with the pulse program HMQCGPQF on a 90% H_2O/ 10% D_2O sample at 298.0 K. The long range coupling delay was 15 ms (corresponds to a *J*-coupling of 33.3 Hz). The ^{13}C decoupling sequence employed in the experiment was *garp*, and the 90° pulse for decoupling sequence was 85 μs at a power level of –1.5 dB. A total of 1000 scans were collected with a relaxation delay of 10.0 s. The spectral widths were 3591.9 Hz (F2) and 10,565.3 Hz (F1), and the final data matrix was 4096 (F2) x 32 (F1).

HSQC. (1) 2D ^{1}H-^{13}C heteronuclear one-bond correlation via double inept transfer was performed on the D_2O sample at 298.0 K using the pulse program HSQCETGP with decoupling (phase sensitive using echo/antiecho-TPPI gradient selection). (2) Another HSQC experiment was performed using the pulse program HSQCETGPSISPNP without decoupling. A trim pulse (1 ms, F1 dimension) was employed in both experiments in the inept transfer while shape pulses were employed on

the F2 dimension. The 180° shape pulses for inversion and refocusing at –1.3 dB on the F2 dimension were 500 μs and 2000 μs, respectively. A correlation delay of 1.25 ms, which corresponds to a $^{1}J_{HC}$-coupling of 200 Hz, was used to observe ^{1}H-^{13}C correlations. The spectrum widths were 6613.7 Hz (F1) and 21,129.4 Hz (F2). A total of 30 scans were collected with a relaxation delay of 1.0 s, and the final data matrix was 2048 (F2) x 1024 (F1).

NOESY. The 2D homonuclear correlation via dipolar coupling NOESY spectrum was performed at 278.0 K on the H_2O/D_2O sample using the pulse program NOESYGPPH with a mixing time (τ_{mix}) of 50 ms. The relaxation delay was 4.0 s, and a spectral width of 7183.9 Hz in each dimension was employed. A total of 16 scans were collected for each experiment, and the final data matrix was 2048 (F2) x 512 (F1).

ROESY. A 2D homonuclear NOE experiment measured under spin-locked condition was performed on the 1:1 H_2O/D_2O sample at 298.0 K using the pulse program ROESYETGP. A continuous wave spinlock was used for mixing with an echo/antiecho-TPPI gradient selection. A series of experiment with different spin-lock pulses (5 - 40 ms), which corresponds to the "mixing time" in ROESY, was employed at a power level of 24.61 dB. The spectral width was 4194.6 Hz on either dimension, and a total of 16 scans were collected with a relaxation delay of 3.0 s. The final data matrix was 2048 (F2) x 512 (F1).

TOCSY. 2D total-correlation COSY was performed on the H_2O/D_2O sample at 298.0 K using the pulse sequence DIPSI2ETGPSI with Hartmann-Hahn transfer using DIPSI2 sequence for mixing. A series of experiments with different TOCSY mixing time

(50 – 400 ms) was employed at a power level of 10 dB. The spectral width was 4194.6 Hz on either dimension, and a total of 8 scans were collected with a relaxation delay of 4.0 s. The final data matrix was 2048 (F2) x 512 (F1).

2.2.3 Quantum chemical calculations

Quantum chemical calculations of NMR parameters such as chemical shielding and indirect spin-spin coupling constants were performed on a Sun Fire cluster using the Gaussian 03 suite of programs. The Sun Fire cluster is comprised of seven Sun Fire 25000 servers. Each of the Sun Fire 25000 servers is equipped with 72 x (2 MB on-chip L2 cache and 32 MB L3 cache) dual-core (CPU) UltraSPARC-IV+ processors and 576 GB of RAM. The level of calculations was B3LYP/6-311++G(d,p).

2.3 Results and Discussion

2.3.1 Confirmation of G-quadruplex formation

Because both Na_2(5'-GMP) monomers and G-quadruplexes exist in concentrated samples, it is necessary to identify their respective ^{1}H chemical shifts. Figure 2-1 shows the ^{1}H NMR spectrum of a 0.1 M Na_2(5'-GMP) sample where only monomers exist. The chemical shift assignment of monomeric 5'-GMP is listed in Table 2-1.

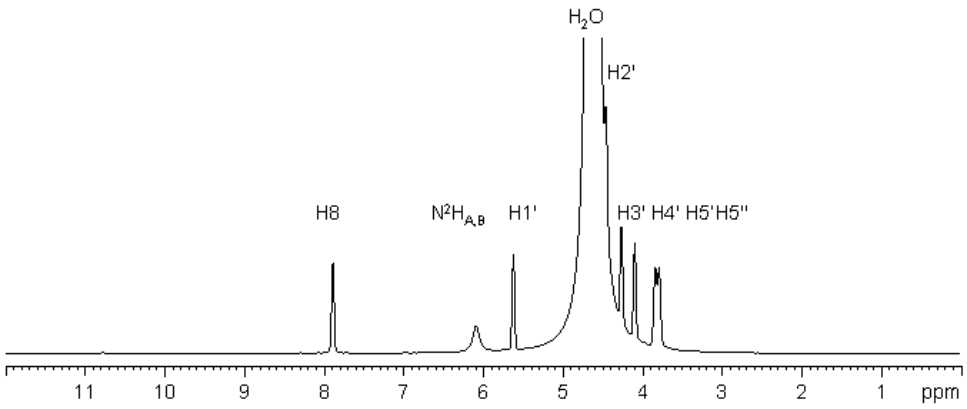

Figure 2-1. The ^{1}H NMR spectrum of a 0.1 M neutral Na_2(5'-GMP) in D_2O at 298 K.

Table 2-1. A list of proton chemical shifts of monomeric Na_2(5'-GMP) in water at 298 K in reference to TMS.

Protons	^{1}H chemical shift (ppm)
$N^2H_{A/B}$	6.1
H8	7.9
H1'	5.6
H2'	4.5
H3'	4.3
H4'	4.1
H5'/ H5''	3.8

According to Pinnavaia et al., a highly concentrated Na_2(5'-GMP) solution yields four sets of distinct proton signals in the ^{1}H NMR spectrum.[15] Figure 2-2 shows the ^{1}H NMR spectra of a concentrated 1.0 M Na_2(5'-GMP) sample in D_2O at various temperatures. It is clear from these ^{1}H NMR spectra that four sets of H8 resonances are observed at both 298 and 278 K. The ribose signals in the 3-6 ppm region are heavily overlapped and a reliable chemical shift assignment is not possible at the moment. Figure

2-3 displays the proton NMR spectra of the same 1.0 M Na_2(5'-GMP) sample in 1:1 ratio of H_2O and D_2O to illustrate exchangeable imino (N^1H) and amino ($N^2H_{A,B}$) protons.

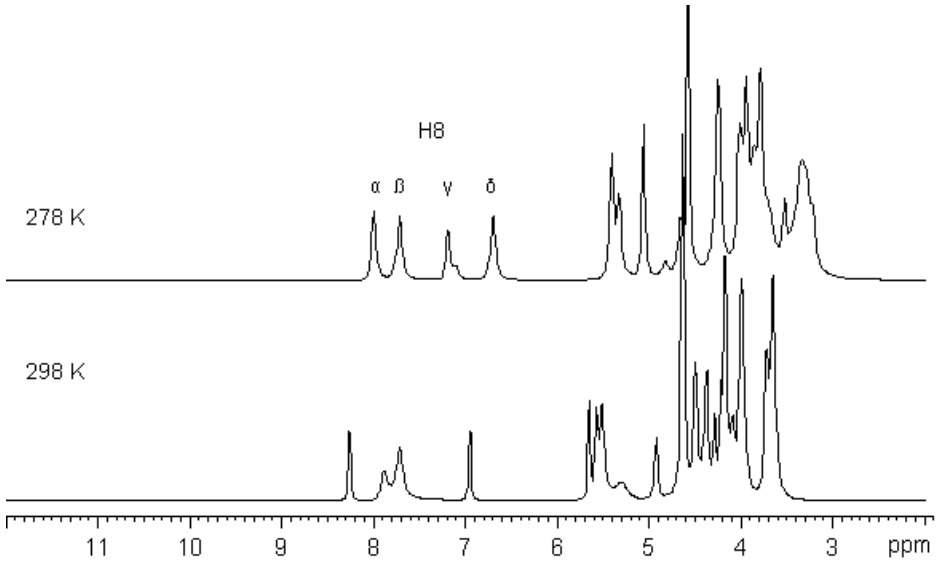

Figure 2-2. ^1H NMR spectra of a neutral 1.0 M Na_2(5'-GMP) solution in D_2O at various temperatures and 14.1 T and pH 8.

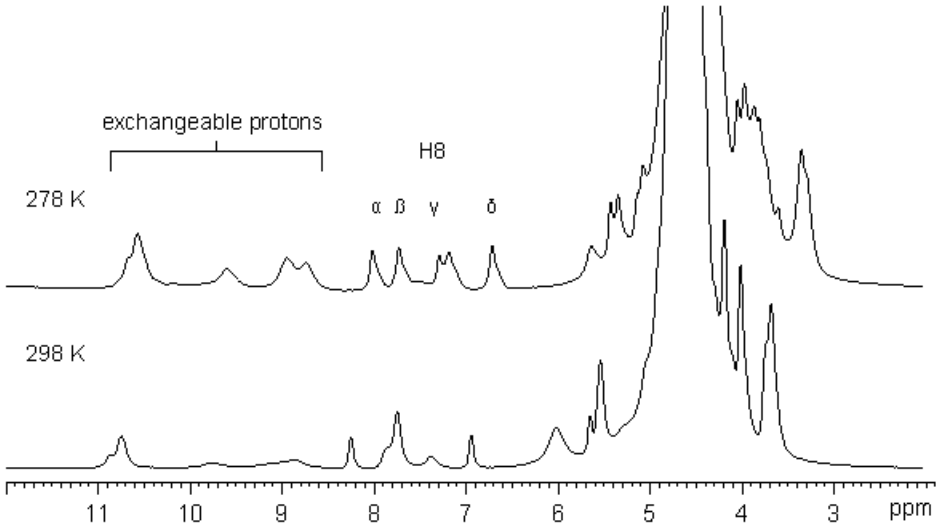

Figure 2-3. ^1H NMR spectra of a neutral 1.0 M Na_2(5'-GMP) solution in 1:1 H_2O/D_2O at various temperatures and 14.1 T and pH 8. The broad shoulder next to H8γ belongs to an unassigned hydrogen-bonded proton.

It can be seen in the ^{1}H-NMR spectra that hydrogen-bonded structures are formed when the chemical shifts of exchangeable protons are shifted towards high frequency from 6.1 ppm of the monomers to the 8.5-12.0 ppm region under high concentrations (Figure 2-3). It is also observed that signal intensities of H8α and H8δ (G-quadruplexes) increase at lower temperatures while the intensities of the other signals decrease. This observation confirms previous observation that H8β and H8γ are indeed monomeric and dimeric (non-G-quadruplex) aggregates because their signals "disappear" at lower temperatures when larger G-quadruplexes are formed. Moreover, although the signal intensities of H8β and H8γ vary at different temperatures, the ratio of H8α and H8δ signals always remains 1:1 (Figure 2-4). The ^{1}H chemical shifts of all four H8 signals are (in ppm): H8α = 8.26, 8.26; H8β = 7.87, 7.95; H8γ = 7.76, 7.57; and H8δ = 6.96, 6.96 at 298 K and 278 K, respectively. Using these distinct H8 signals, the approximate G-quadruplex concentration can be calculated using peak deconvolution of these four signals:

Equation 2-1

$$\frac{G-quadruplex_{(H8\alpha+H8\delta)}}{All\ aggregates_{(H8\alpha+H8\beta+H8\gamma+H8\delta)}}\times 100\%$$

The G-quadruplexes formed in the 1.0 M solution under different temperatures are shown in Figure 2-4 and their population percentages were calculated using Equation 2-1 and the results are shown in Table 2-2. Since there are other exchangeable proton(s) embedded within the H8 region, the population calculated using peak intensities is slightly smaller in the H_2O/D_2O sample.

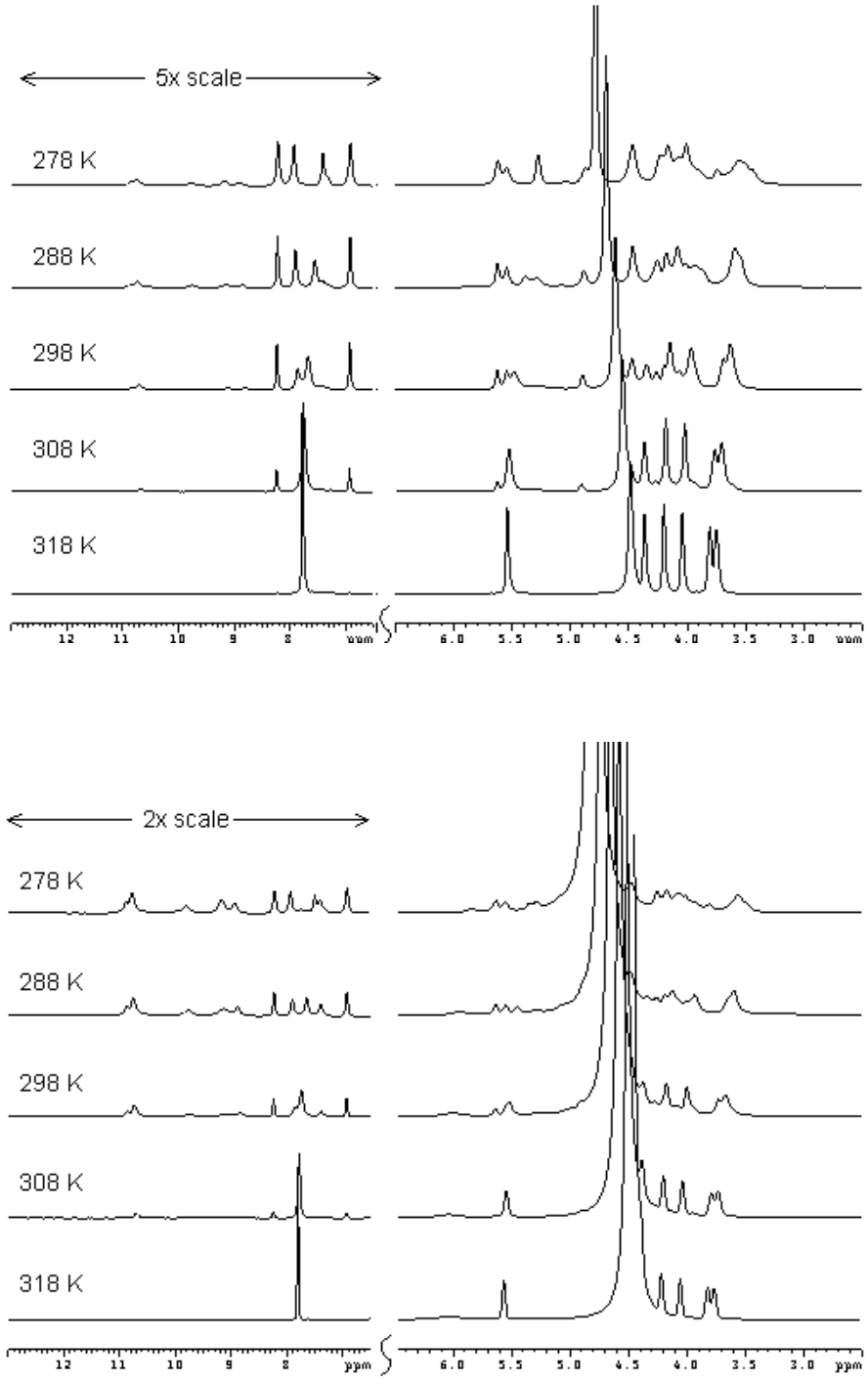

Figure 2-4. ^{1}H NMR spectra of a neutral 1.0 M Na_2(5'-GMP) solution in D_2O (top) and 1:1 H_2O/D_2O (bottom) at various temperatures and 14.1 T.

Table 2-2. Estimated percentages of G-quadruplex in a 1.0 M Na_2(5'-GMP) sample with different solvents at various temperatures calculated using Equation 2-1.

Temperature (K)	D_2O (%)	H_2O/D_2O (%)
278	49.3	41.1
288	45.3	35.1
298	37.7	28.6
308	20.0	10.4
318	1.2	0.0

Besides the high frequency shift of exchangeable protons and the appearance of four H8 signals, the third piece of evidence of G-quartet formation is provided by 2D NOESY spectrum that yields spatial relationships between protons within 5.0 Å through dipole-dipole interactions. The signature NOESY cross peaks of a G-quartet are formed between the imino (N^1H) and one of the amino protons (N^2H_A) with H8 from a neighbour molecule within the G-quartet, as illustrated in Figure 2-5.

In this case, because the signature NOE cross peaks involve exchangeable protons, an NOESY experiment was performed on the 1:1 H_2O/D_2O sample. Intra-molecular cross peak are expected to be more intense than the inter-molecular ones because of shorter distances between them (i.e., stronger dipole interaction). Figure 2-6 shows the NOESY spectrum of a 1.0 M Na_2(5'-GMP) solution at 278 K, and cross peaks

between the exchangeable protons (intra-molecular) and with the two H8 species (inter-molecular) confirmed G-quartet formation.

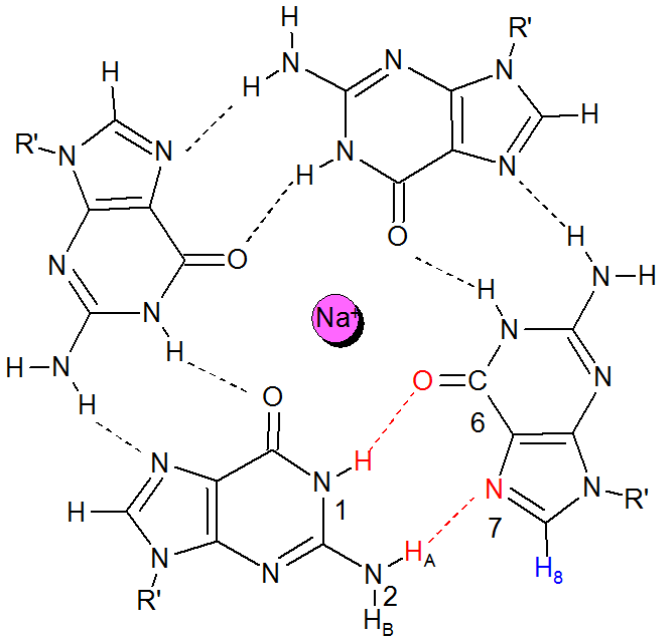

Figure 2-5. G-quartet with one pair of Hoogsteen-type of hydrogen-bonds highlighted in red. Nuclear Overhauser effect (NOE) is present between protons N^1H-N^2H_A (intra-molecular), and H8-N^1H, H8-N^2H_A (inter-molecular). R' = 5'-phosphate ribose.

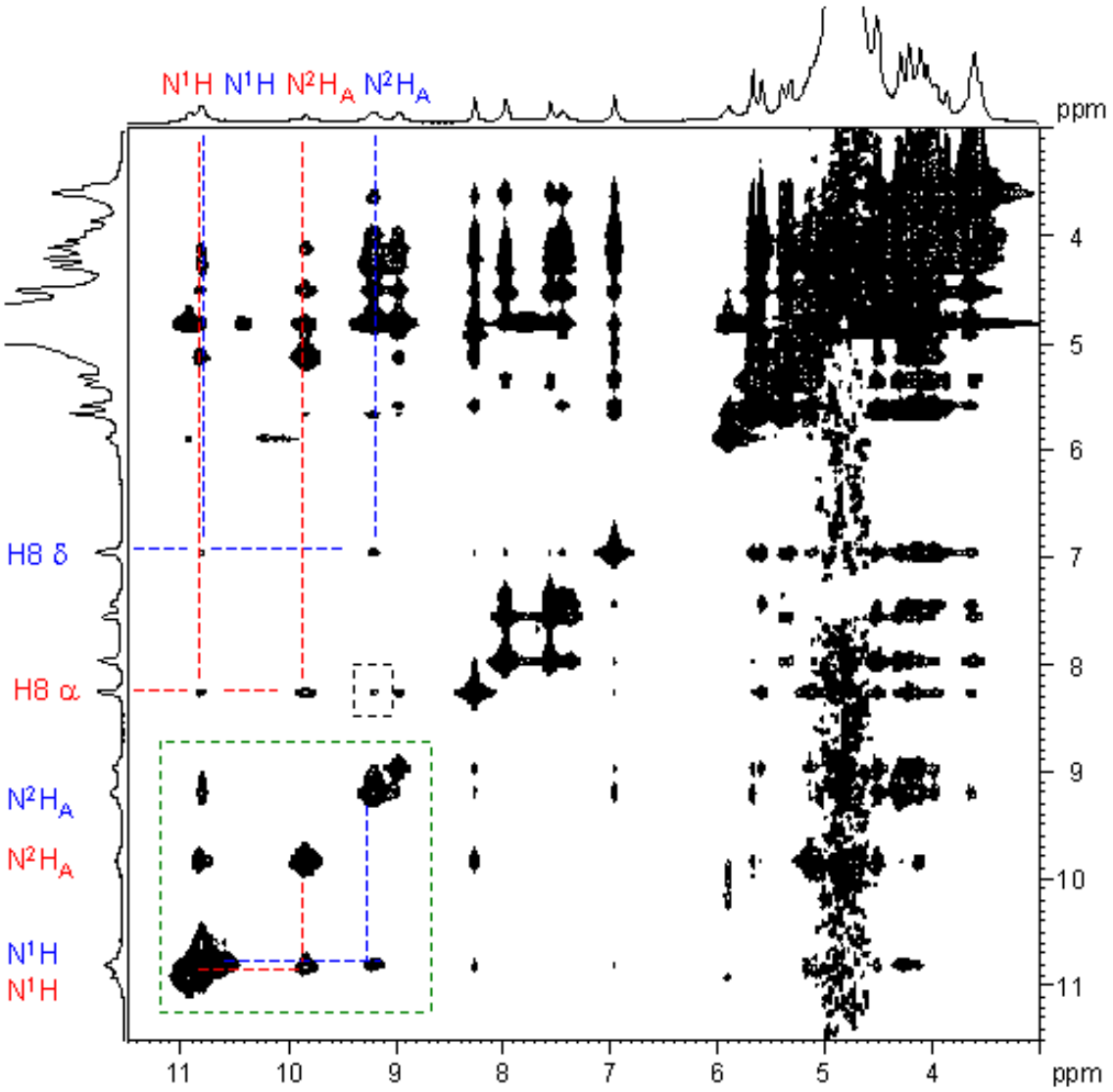

Figure 2-6. 2D NOESY spectrum of a neutral 1.0 M Na_2(5'-GMP) solution in 1:1 H_2O/D_2O at 278 K and 14.1 T with a mixing time of 50 ms showing the H8 and exchangeable protons regions. Intra-molecular NOE's between N^1H and N^2H_A are highlighted in the green box. H8(α)-N^2H_A(δ) cross peak is highlighted in the black box (see text for explanation). α and δ species are represented in red and blue, respectively.

Moreover, we also observed cross peak H8(α)-N^2H_A(δ) but not H8(δ)-N^2H_A(α) in the NOESY spectrum (Figure 2-6, black box). This inconsistency could arise from two situations. First, α and δ are signals of two distinct types of G-quadruplexes that are composed entirely of either α or δ monomers, and they have almost identical populations as shown in their 1:1 signal intensities in the ^{1}H NMR spectrum. The H8(α)-N^2H_A(δ) cross peaks arose from simply "inter-quadruplex" interactions. The second explanation is that there is only one type of G-quadruplex and it has two proton environments. For example, α and δ monomers are arranged alternatively or adjacent to each other in the same G-quartet. However, only one set of H8-N^2H_A combination is observed. In this case, the absence of such cross peaks suggests that this G-quadruplex is composed of alternating all-α and all-δ G-quartets. These two types of G-quartets within the same G-quadruplex give rise to the 1:1 H8 signal ratio (α or δ) in the proton spectrum, and the H8α-N^2H_Aδ cross peaks are "inter-quartet" signals. We think that the latter explanation is more reasonable as detection of NOE is more effective within a short distance, hence the H8(α)-N^2H_A(δ) cross peaks are likely to be inter-quartet rather than between quadruplexes.

2.3.2 Relative sizes of Na_2(5'-GMP) aggregates

After obtaining evidence of G-quartet formation, the next task is to study the sizes of the four species present in neutral Na_2(5'-GMP) solution. In this case, we employed diffusion-ordered spectroscopy (DOSY) NMR technique. DOSY is an NMR method that is used to measure the translational diffusion coefficient (D_t) of molecules

dissolved in solution, which in turn provides information about molecular size. DOSY NMR has been widely used to determine the size of molecular aggregates such as polymers or nanoparticles.[69,70] The diffusion coefficients being measured are affected by various parameters including temperature, concentration, solvent viscosity, the size and shape of the molecule of interest. According to the Stokes-Einstein equation,[71] a sphere's diffusion coefficient is inversely related to the hydrodynamic radius of the molecule and solvent viscosity:

Equation 2-2 $$D_t = \frac{kT}{6\pi\eta R}$$

where k = Boltzmann constant, T = temperature, R = hydrodynamic radius, and η = solvent viscosity. However, it has been known that G-quadruplexes are of rod-like cylinder shapes instead of behaving like a sphere. Therefore, another equation for hydrodynamic models using experimental D_t data is employed:

Equation 2-3 $$D_t = \frac{kT}{3\pi\eta L}(\ln p + \nu)$$

where kT is the Boltzmann constant, η is the solvent viscosity, L is the length of the symmetric cylinder, p is the axial ratio of the cylinder ($p = L / d$, where d = diameter of cylinder), and ν as the end-effect correction term. Tirado and Garcia de la Torre[72] calculated that when $2 \leq p \leq 30$, the end-effect correction is expressed as:

Equation 2-4 $$\nu = 0.312 + 0.565p^{-1} - 0.100p^{-2}.$$

In this case, the diameter (d) of the cylinder is 26 Å, and the viscosity of D_2O at 278 K and 298 K were 1.988 cP and 1.097 cP, respectively.[73] (Note: 1 cP = 0.001 kg/m·s).

Wong et al. reported that at a concentration of 24.6 % w/w (0.8 M) and 278 K, the estimated number of stacking G-quartets is 48 ± 3 with a D_t value of 2.5 x 10^{-11} m^2/s.[66] Translational diffusion rates of the four H8 signals from the DOSY experiment at 278 K are shown in Figure 2-7. Both α and δ signals were of the same size (both D_t = 8.8 x10^{-12} m^2/s), and they are larger aggregates compared to those reported in Wong et al. because of higher concentration.[66] Meanwhile β was assigned to a smaller aggregate (stacking dimers with D_t = 11.6 x10^{-12} m^2/s), and γ to a even smaller aggregate (stacking monomers, D_t = 17.2 x10^{-12} m^2/s, as previously suggested).[56,48] The fact that both α and δ species shared the same diffusion rate further suggests that these two H8 signals were from the same G-quadruplex that had two different H8 environments.

Because 5'-GMP solutions with similar concentration was reported to have a *p* value within the range set by Tirado and Garcia de la Torre,[72] Equation 2-3 and Equation 2-4 were employed to obtain the length of the G-quadruplex in our experiment. Since each stacking is separated by 3.4 Å, the number of stacking (*n*) would equal to (*L* + 0.34 nm)/0.34 nm. The calculated *p*, *L*, and *n* values using the above equations are listed in Table 2-3. The increased concentration of 5'-GMP in this work explained the smaller D_t value and larger aggregate size observed under the same temperature. Because the *p* value (i.e., 34.7) obtained at 278 K is not far from the application range of $2 \leq p \leq 30$ in Equation 2-4, it is employed in estimating the number of G-quartet stacking at this temperature. Note that the $\ln(I/I_o)$ plot where D_t values are derived is not shown. The D_t values are obtained directly from the SimFit function in the Bruker XWinNMR T1/T2 package.

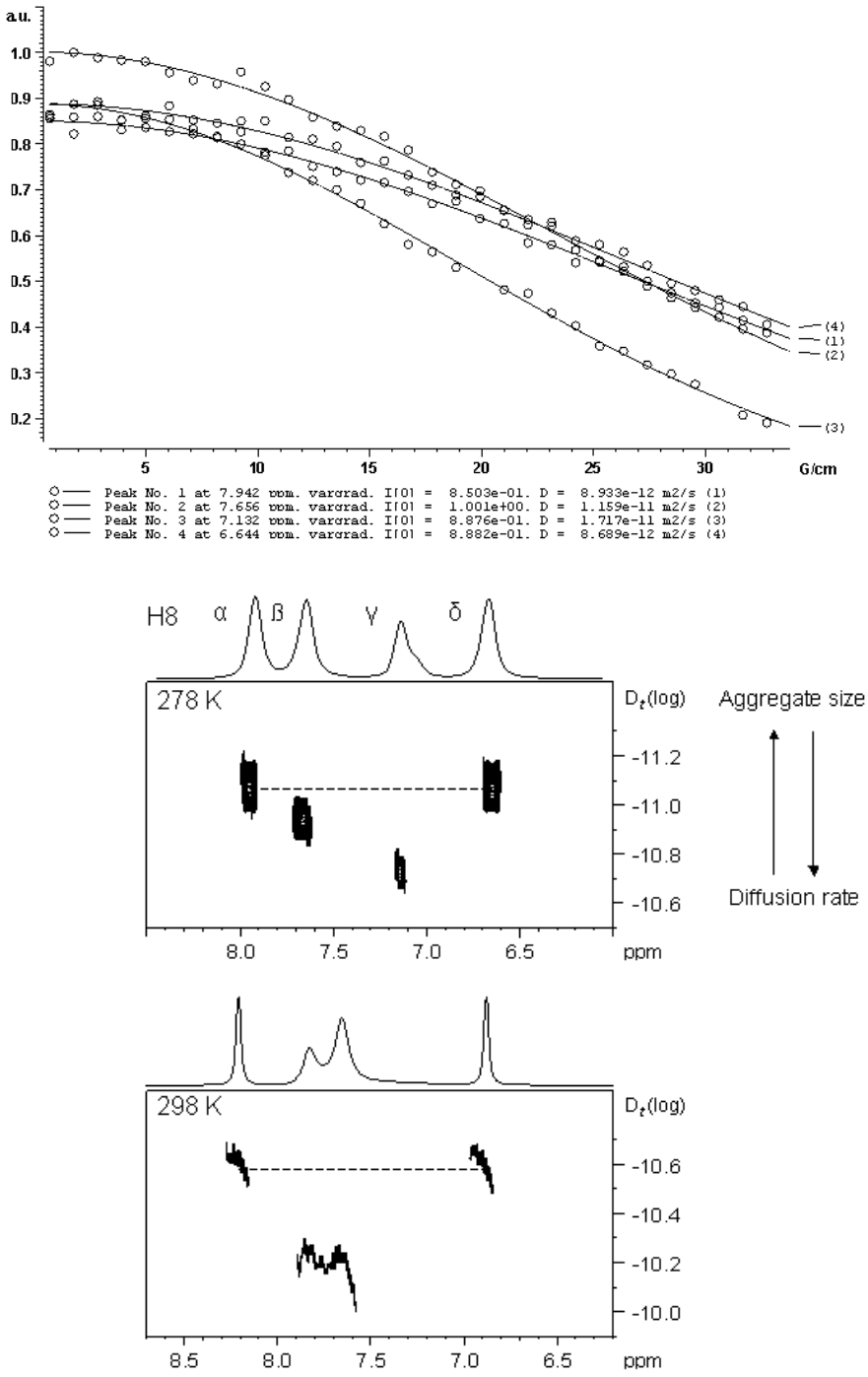

Figure 2-7. (Top) Diffusion ^{1}H NMR results of 1.0 M neutral Na_2(5'-GMP) in D_2O at 278.0 K and 14.1 T. The four curves represent proton signals H8α, β, γ, and δ. (Bottom) 2D DOSY spectra showing the relative log(D_t) values of the four H8 signals at 278 K and 298 K.

Table 2-3. Experimental NMR translational diffusion coefficients (D_t) for neural Na_2(5'-GMP) self-assemblies at various temperatures and number of stacking G-quartets (n).

Temperature (K)	D_t (m^2/s)[a]	p	L (nm)	n
298	2.70×10^{-11}	18.6	48.4	143 ± 15
278	0.88×10^{-11}	34.7	90.2	266 ± 27

[a] The uncertainty in D_t was estimated to be $\pm 0.3 \times 10^{-11}$ m^2/s (298 K) and $\pm 0.1 \times 10^{-11}$ m^2/s (278 K).

As a summary, four signals were identified in a concentrated, neutral Na_2(5'-GMP) solution using ^{1}H NMR and DOSY experiments. These four signals represent G-quadruplexes (α and δ), stacking dimers (β), and stacking monomers (γ) as previously suggested by Wong et al.[66] 2D NOESY data also suggest that these G-quadruplexes are composed of alternating all-α and all-δ G-quartets.

2.3.3 G-quadruplex building blocks: monomer structures

One of the major tasks of studying the neutral Na_2(5'-GMP) helix is to understand its individual monomers because they are the building blocks that self-assemble into an ordered G-quadruplex. Now that we have confirmed the origin of α and δ signals as G-quadruplex formation in the 1.0 M solution, we need to answer the question as to why two (α and δ), instead of one signal, are present for G-quadruplex. To this end, it is important to identify all the proton chemical shifts that belong to both α and δ species.

2.3.3.1 Proton resonance assignment

2D homonuclear COSY experiments were performed to identify the chemical shifts of the proton spins that are scalar coupled to each other. Figure 2-8 shows the COSY spectrum of a neutral Na_2(5'-GMP) sample in D_2O. From COSY, the spin-spin coupled (^3J) protons of the ribose sugar are identified and the assigned chemical shifts are listed in Table 2-4. Note that the assignment of H5' and H5" are arbitrary for now as the COSY spectrum does not provide any stereo information of these two protons relative to the ribose and phosphate groups.

The assigned chemical shifts were also confirmed using total correlation spectroscopy (TOCSY). TOCSY is similar to COSY, except cross peaks are shown for spins that are connected by an unbroken chain of couplings. If a single cross-section of a spin is taken at a certain chemical shift, all of the spins that are involved in the coupling network would show. For example, along the chemical shift of H1', the cross peaks chain H1'-H2'-H3'-H4'-H5'/H5" of ribose would all be shown. Figure 2-9 shows several TOCSY spectra obtained at various mixing times that allowed for correlation spin to develop, demonstrating the connections between the four sets of ribose signals. A complete chain of chemical shifts from H1' to H5'/H5" is clearly visible for both the α and δ signals in Figure 2-9(a) and (d). The TOCSY data complement the peak assignments from the ^{1}H-^{1}H COSY data. It is also interesting to note that the peak intensities for both α and δ signals are quite different with the former having higher peak intensities than the latter. This arises from different magnitudes of *J*-coupling constants between these two sets of signals. Since COSY experiment is suitable for detection of spin-spin couplings between 3-15 Hz, it is possible that anything smaller than 3 Hz is not

detected in the δ species which show weaker signals intensities. In order to eliminate this possibility, a long-range COSY (or selective COSY) is performed. The purpose of this experiment is to introduce a mandatory delay into the pulse sequence where the weakest spin-spin couplings are detected. In this case, no extra cross-peaks are observed in the long-range COSY spectrum (Figure 2-10), hence the COSY and TOCSY data sets showed all short and long-range coupling interactions.

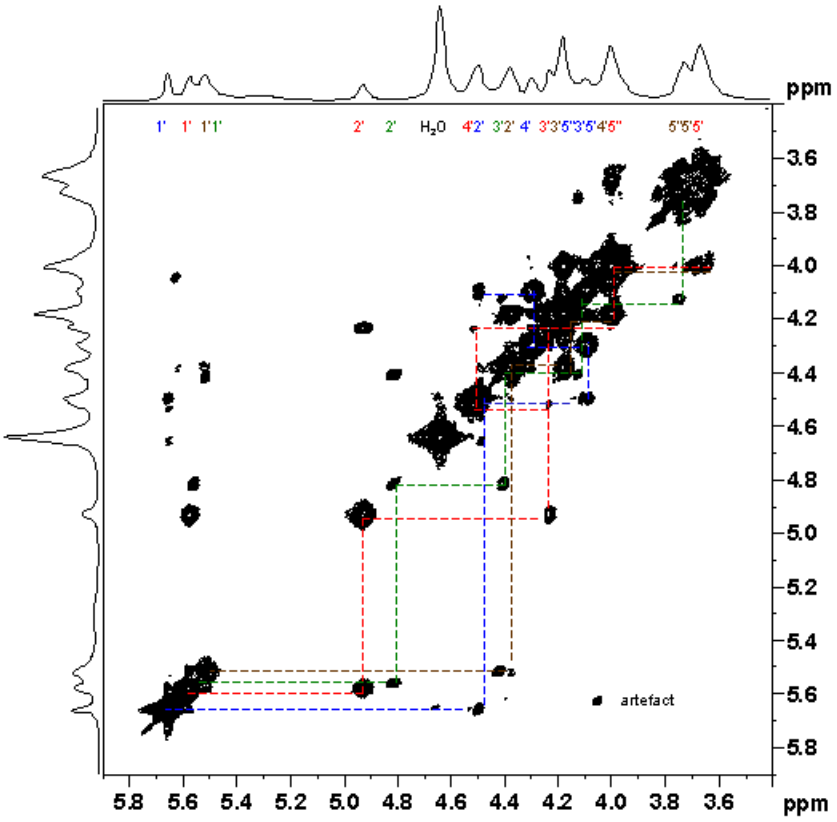

Figure 2-8. 2D ^{1}H-^{1}H COSY spectrum showing the ribose region of 1.0 M neutral Na_2(5'-GMP) in D_2O at 298 K and 14.1 T. Cross peaks with scalar couplings are connected with lines. Note that the stereospecific assignment of *pro*S and *pro*R protons (H5'/H5") are arbitrarily assigned. (Color code for the four species: red α, green β, brown γ, blue δ).

Table 2-4. ^{1}H NMR chemical shifts of the ribose protons in a neutral 1.0 M Na_2(5'-GMP) sample obtained from COSY experiment (Figure 2-8).

^{1}H chemical shift (ppm)	H1'	H2'	H3'	H4'	H5'/ H5" *
α	5.59	4.93	4.21	4.52	3.63 / 3.98
β	5.52	4.82	4.41	4.12	3.74 /3.83
γ	5.52	4.37	4.18	4.00	3.68 / 3.74
δ	5.67	4.50	4.10	4.29	3.99 / 4.15

*Stereospecific assignment of *pro*S and *pro*R protons was not available.

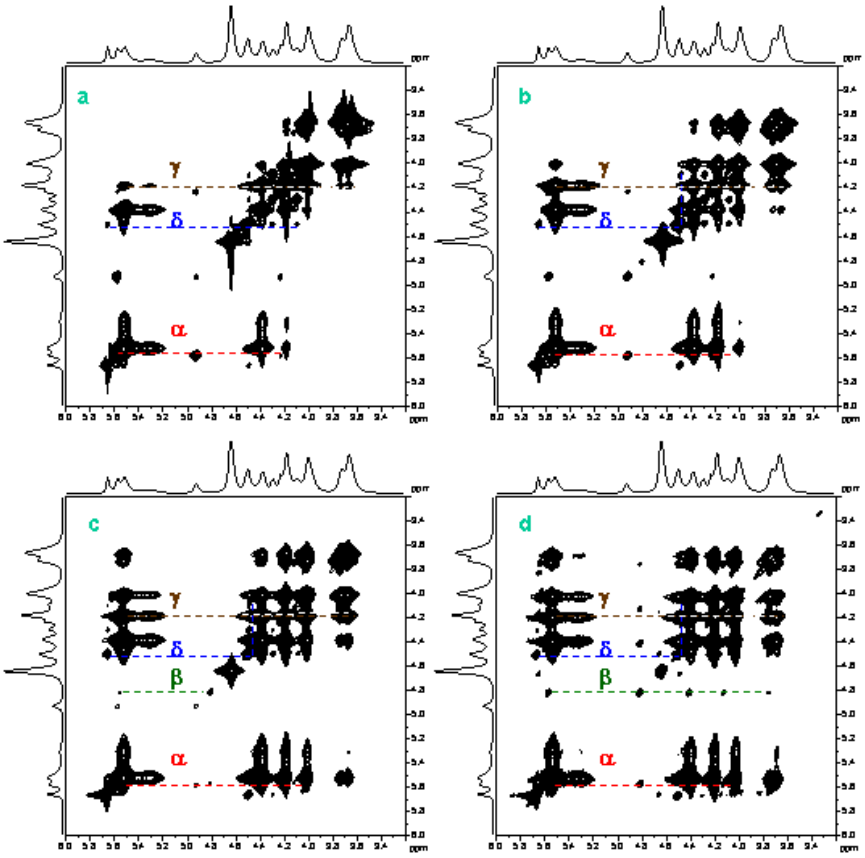

Figure 2-9. 2D TOCSY spectra of 1.0 M neutral Na_2(5'-GMP) in D_2O at 298 K and 14.1 T. Cross peaks of spins from an unbroken chain of scalar coupling are connected with dotted lines. Mixing times: a) 50 ms, b) 100 ms, c) 200 ms, and d) 400 ms.

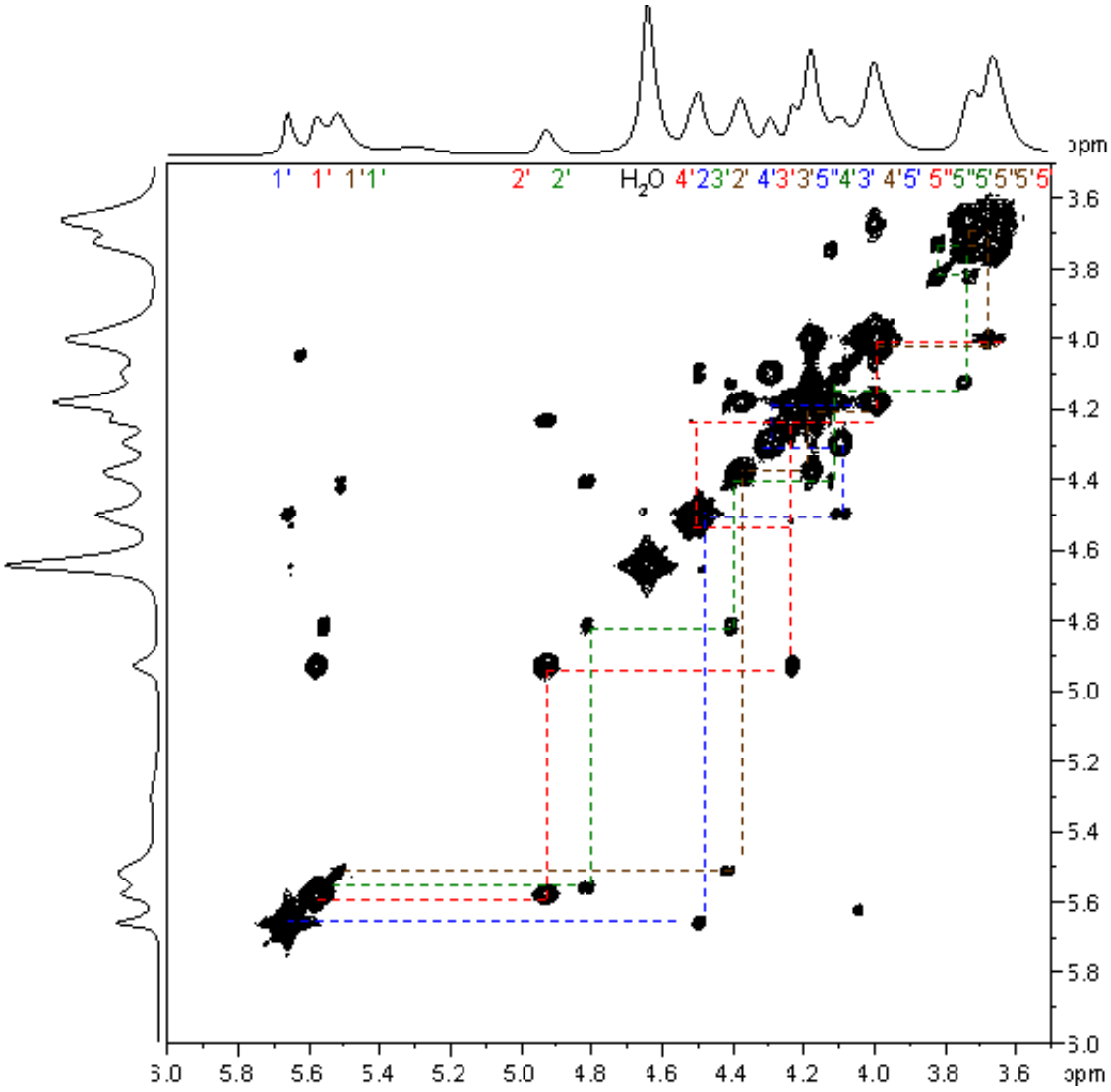

Figure 2-10. Long-range COSY spectrum showing the ribose region of 1.0 M neutral Na_2(5'-GMP) in D_2O at 298.0 K and 14.1 T. Cross peaks with scalar couplings are connected with lines. Note that the stereospecific assignment of *pro*S and *pro*R protons (H5'/H5") were arbitrarily assigned for all species. (Color code for the four species: red α, green β, brown γ, blue δ).

As a summary, the ^{1}H-^{1}H COSY, ^{1}H-^{1}H TOCSY, and long-range COSY spectra provided the chemical shift assignments of all the ribose protons for the four α, β, γ, δ species except the temporarily stereospecific assignments of protons (H5'/H5").

2.3.3.2 *Anti* vs. *syn*, C2'-*endo* vs. C3'-*endo* conformations, and $^3J_{HH}$ coupling constants

Since we are only interested in the α and δ G-quadruplexes signals, a new approach called DOSY-NOESY was introduced to "filter" out the β and γ cross peak signals in order to obtain a simplified spectrum. The diffusion rate was carefully selected so that only signals from large molecules were detected. This novel NMR approach allows us to connect H8 signals to the formerly crowded region of ribose sugars. From the DOSY-NOESY spectrum shown in Figure 2-11, H8(α) and H8(δ) signals have a strong NOE with the H2' and H3' protons, but a weak NOE with H1', H4', and H5'/H5" protons. This suggests that both α and δ molecules adopt an *anti* conformation instead of *syn*. Observations of nucleosides in the *syn* conformer are rare because the C1'-N9 glycosidic bond is flexible and *anti* is preferred due to the steric effect. The *syn* conformers have been observed mostly in purines with C8 substituents that form intra-molecular hydrogen bonding. The fact that both molecules are *anti* in this case explains the multiple stacking of G-quartets in forming large G-quadruplexes, as *syn* conformers would hinder such stacking due to repulsion between G-quartets. Moreover, the relative intensities between H8 and the ribose sugars (H1', H2', H3', H4', H5', and H5") in the DOSY-NOESY spectrum can pinpoint the glycosidic angle χ. For example, protons H1' and H4' are located at the bottom of the ribose ring and cross peak intensities with H8 would be weaker compared to H2' and H3' as H8 sits directly above the latter two protons in an *anti* conformation. In this case, the α molecule has strong H8-H2', medium H8-H3', and equally weak H8-H1' and H8-H4' dipole interactions. This would put the guanine ring in a certain position with respect to the ribose ring with the estimated χ angle to be -

60º (high-*anti*). Using the same analogy, the δ molecule would have an estimated χ angle of -130º (*anti*) because of strong H8-H3', medium H8-H2'/H4'/H5'/H5" and weak H8-H1' dipole interactions. On the other hand, we also observed that H8-H2' NOE has a stronger intensity for α, while δ has a strong NOE cross peak between H8 and H3'. This observation immediately suggests that α signals arise from a C2'-*endo* molecule, while δ represents a C3'-*endo* molecule. The proton chemical shifts of C2'-*endo* and C3'-*endo* H8 signals are measured to be 8.26 and 6.96 ppm, respectively. Since the presence of both types of puckering conformation (C2'-*endo* and C3'-*endo*) was such an important structural clue, we decided to further verify this structural feature using DQF-COSY where $^3J_{HH}$ are obtained and linked to nucleic acid dihedral angles using the Karplus relation.

As mentioned above, COSY is a useful 2D NMR experiment that allows us to trace out the proton *J*-coupling network in the molecule. Although it is not obvious in the spectrum shown in Figure 2-8, each COSY cross peak multiplet (from *J*-coupling) actually has a pattern called "anti-phase square array" as illustrated in Figure 2-12. The four peaks in the two-dimensional spectrum are constructed by multiplying the anti-phase doublets on both ω_1 and ω_2 dimensions. For example, the top left peak is positive as the peaks along ω_1 and ω_2 from which it is derived are both positive (Figure 2-12). This COSY cross peak is centered at ν_A on the ω_1 dimension, and ν_x on the ω_2 dimension, and is split by the coupling constant J_{AX} (in Hz) in each dimension. If the coupling $J_{AX} = 0$, there will be no cross peak multiplets.

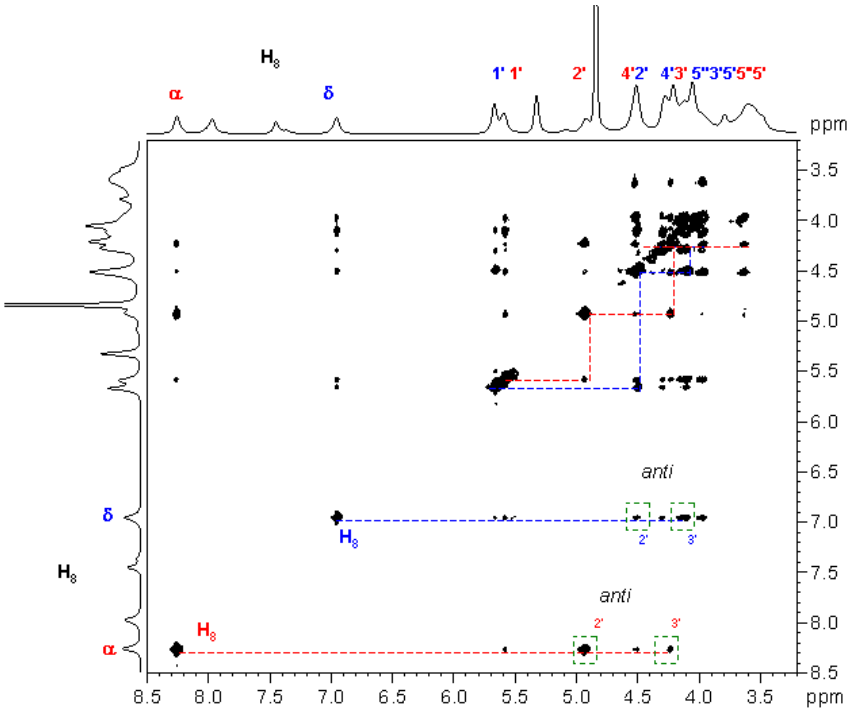

Figure 2-11. 2D DOSY-NOESY spectrum of 1.0 M neutral Na_2(5'-GMP) in H_2O/D_2O at 278 K and 14.1 T. Mixing time 50 ms. Cross peaks that give structural information are boxed in.

As the coupling constant becomes smaller, the two anti-phase lines begin to overlap. Since they are of opposite sign, they begin to cancel each other and the overall intensity of the cross peaks gets smaller, and eventually the anti-phase doublet is no longer visible. In addition to the magnitude of J_{AX}, the amount of cancellation also depends on the linewidth (LW, measured at half height) of the signal. If $J_{AX} >>$ LW, there will be no cancellation. If LW > J_{AX}, the amount of cancellation is very significant, as is explained in Figure 2-13. Moreover, as the diagonal peak multiplets in COSY are all in-phase, they reinforce one another and making it more difficult to locate weaker cross peaks close to the diagonal. This problem can be practically eliminated using double-

quantum filtered COSY (DQF-COSY) where both the diagonal and cross peak multiplets are in anti phase. By making the diagonal peaks less dominant in DQF-COSY, it will be easier to extract coupling constants from cross peaks.

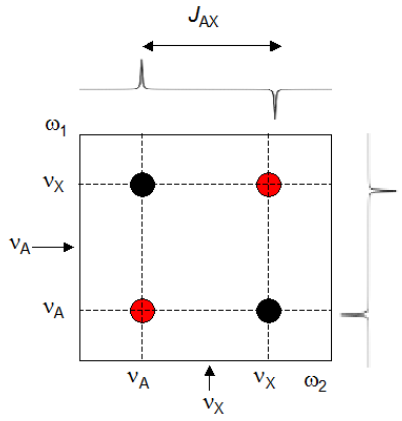

Figure 2-12. Contour plot of the cross peak expressed as an "anti-phase square array" of multiplets. Positive contours are colored black, and negative red. The anti-phase doublet is plotted for both axes.

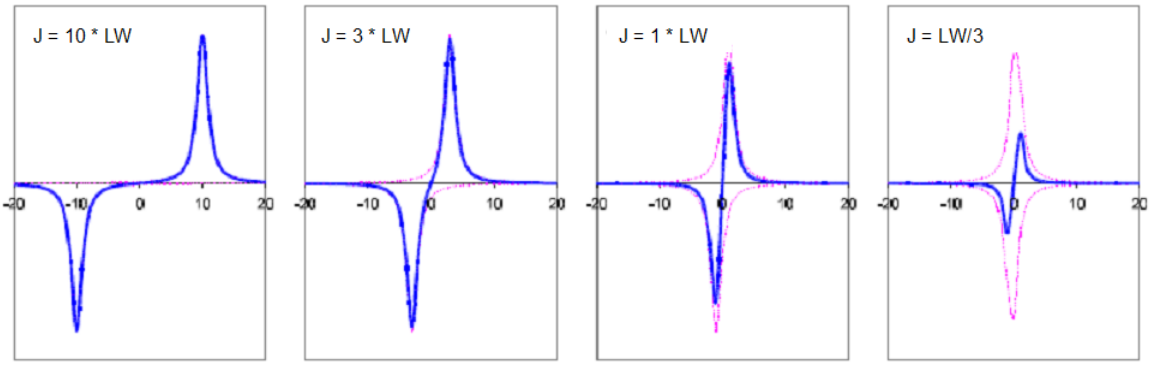

Figure 2-13. Relationship between *J* and linewidth (LW) in affecting the intensity of a 2D COSY cross peak signal.[74] (Figure adopted from Ref.72).

In DQF-COSY, all of the observed signals are generated from selecting double-quantum coherences with either phase cycling or pulse field gradients. This means that

uncoupled spins (such as solvent signals) will not be detected in the DQF-COSY spectrum, as they cannot pass the double-quantum filter. Both diagonal and cross peaks can be phased to have the same line shape and show anti-phase structure in both dimensions. However, the intensity of signals in DQF-COSY is reduced to one half when compared with the conventional COSY due to the double-quantum filtering.[75]

In a DQF-COSY spectrum, the intensity of cross peaks depends on the type (active and passive) and the magnitude of the *J*-coupling involved. Active-*J* refers to the coupling responsible for the cross peak, while passive-*J* is the coupling from another spin that involves one of the spins participating in the cross peak. For example, Figure 2-14 shows the expected DQF-COSY spectrum with correlation H1 → H2 → H3 → H4. In box a, the active-*J* would be J_{12} on ω_2, and there are no passive-*J*. The passive-*J* on ω_1 for the same cross peak would be J_{23}. In box b, J_{23} would be the active-*J* on ω_2 because it is responsible for the cross peak between H2 and H3, and J_{12} is the passive-*J* because H2 is also coupled to H1. On the other hand, J_{23} would be the active-*J* on ω_1 for the same cross peak and J_{34} would be the passive-*J*. Table 2-5 shows the expected in-phase and anti-phase multiplicities of different spin systems.

Another complication in analyzing anti-phase cross peak is that, as Wüthrich et al. documented, the apparent separation in an anti-phase doublet (i.e., apparent-*J*) is usually larger than the real *J*-coupling constant and that it is not possible to measure any *J* when the apparent-*J*/linewidth ratio is below 0.576.[76] Because of the complexity in reading these convoluted COSY cross peaks (especially in multi-spin systems), simulations are often used in order to find the real *J*-coupling constants. Table 2-6 shows

the equations used to generate the simulation plot of anti-phase systems shown in Figure 2-15.

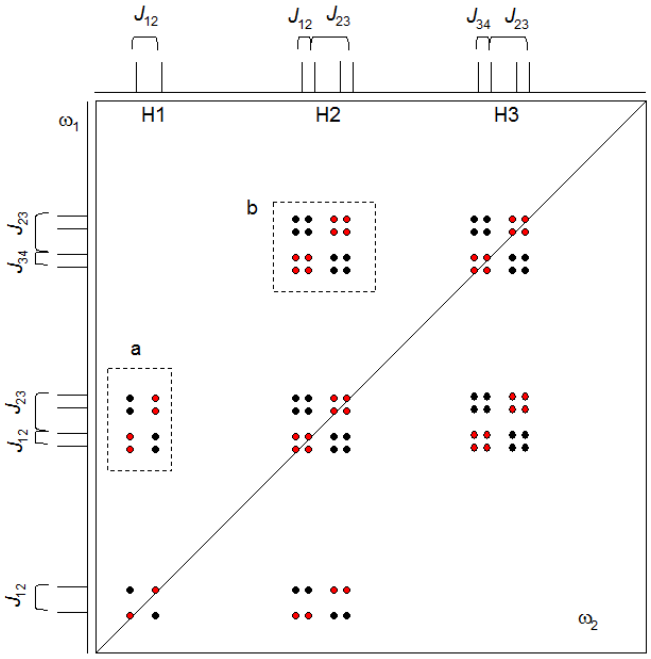

Figure 2-14. Partial plot of a theoretical DQF-COSY spectrum of a four-spin system.

Table 2-5. Cross peak multiplicities in DQF-COSY spectra assuming $J_{AX} > J_{AM}$.

Multiplicity	In-phase	Anti-phase
A	1	0
AX	1 1	1 -1
AX_2	1 2 1	1 0 -1
AXM	1 1 1 1	1 1 -1 -1
AMX	1 1 1 1	1 -1 1 -1

Using this simulation process, we obtained the $^3J_{HH}$ coupling constants of the 5'-GMP ribose protons from the DQF-COSY spectrum (Figure 2-16) and the results are shown in Table 2-7. The drastically different values of $^3J_{(H1',\ H2')}$ for the two sets of

signals, 9 and 2 ± 1 Hz, suggest that the H8(α) signal is related to 100% C2'-*endo* conformation, while the H8(δ) signal is due to 100% C3'-*endo* conformation.[77]

Table 2-6. Equations used to generate the Lorentzian plot in Figure 2-15.

Variable		Equation
ν1	=	ν-(active-*J*/2)-(passive-*J*/2)
ν2	=	ν-(active-*J*/2)+(passive-*J*/2)
ν3	=	ν+(active-*J*/2)-(passive-*J*/2)
ν4	=	ν+(active-*J*/2)+(passive-*J*/2)
I1	=	(LW*0.5)*(LW*LW*0.25 + ν1*ν1)
I2	=	(LW*0.5)*(LW*LW*0.25 + ν2*ν2)
I3	=	(LW*0.5)*(LW*LW*0.25 + ν3*ν3)
I4	=	(LW*0.5)*(LW*LW*0.25 + ν4*ν4)
in-phase	=	I1+I2+I3+I4
anti-phase (AXM)	=	I1+I2-I3-I4
anti-phase (AMX)	=	I1-I2+I3-I4

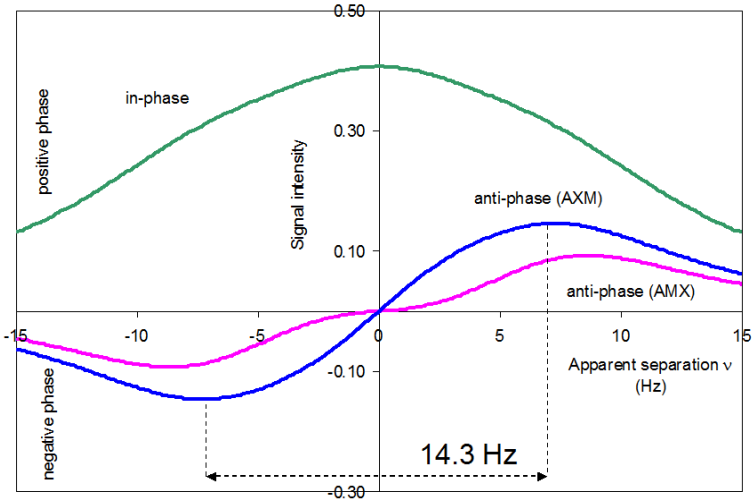

Figure 2-15. Simulated multiplicities of a three-spin system using equations listed in Table 2-6 with controllable parameters: active-*J* = 9 Hz, passive-*J* = 6 Hz, and LW = 14 Hz.

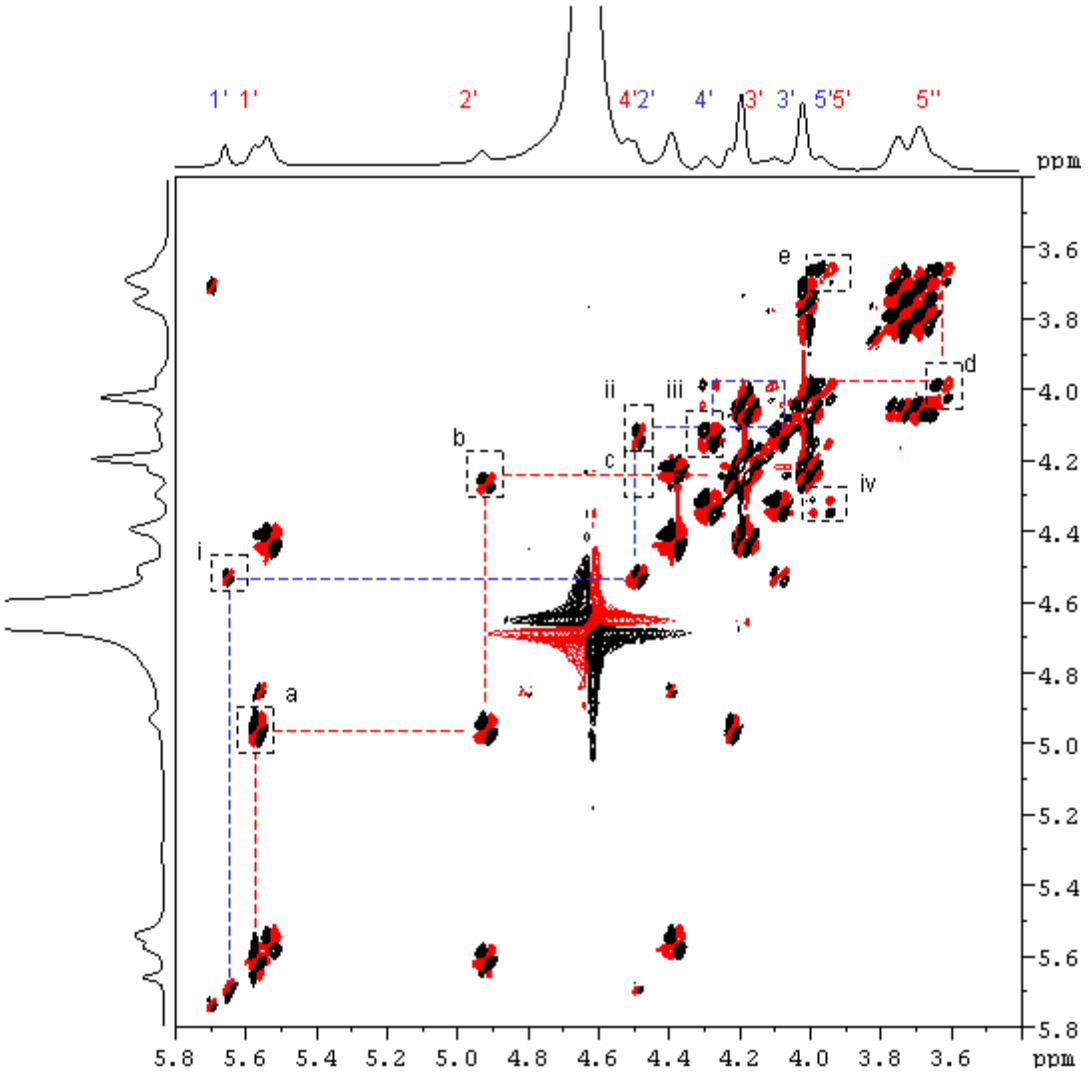

Figure 2-16. Phase sensitive DQF-COSY of 1.0 M neutral Na_2(5'-GMP) in D_2O at 298 K and 14.1 T. Positive contour is colored black, and negative red. Correlations ($^3J_{HH}$) of GMP ribose protons are linked using red and blue dotted line for C2'-*endo* and C3'-*endo* G-quadruplex, respectively. Coupling constants are extracted from cross peaks (labeled boxes with measured "apparent *J*-couplings") in next page.

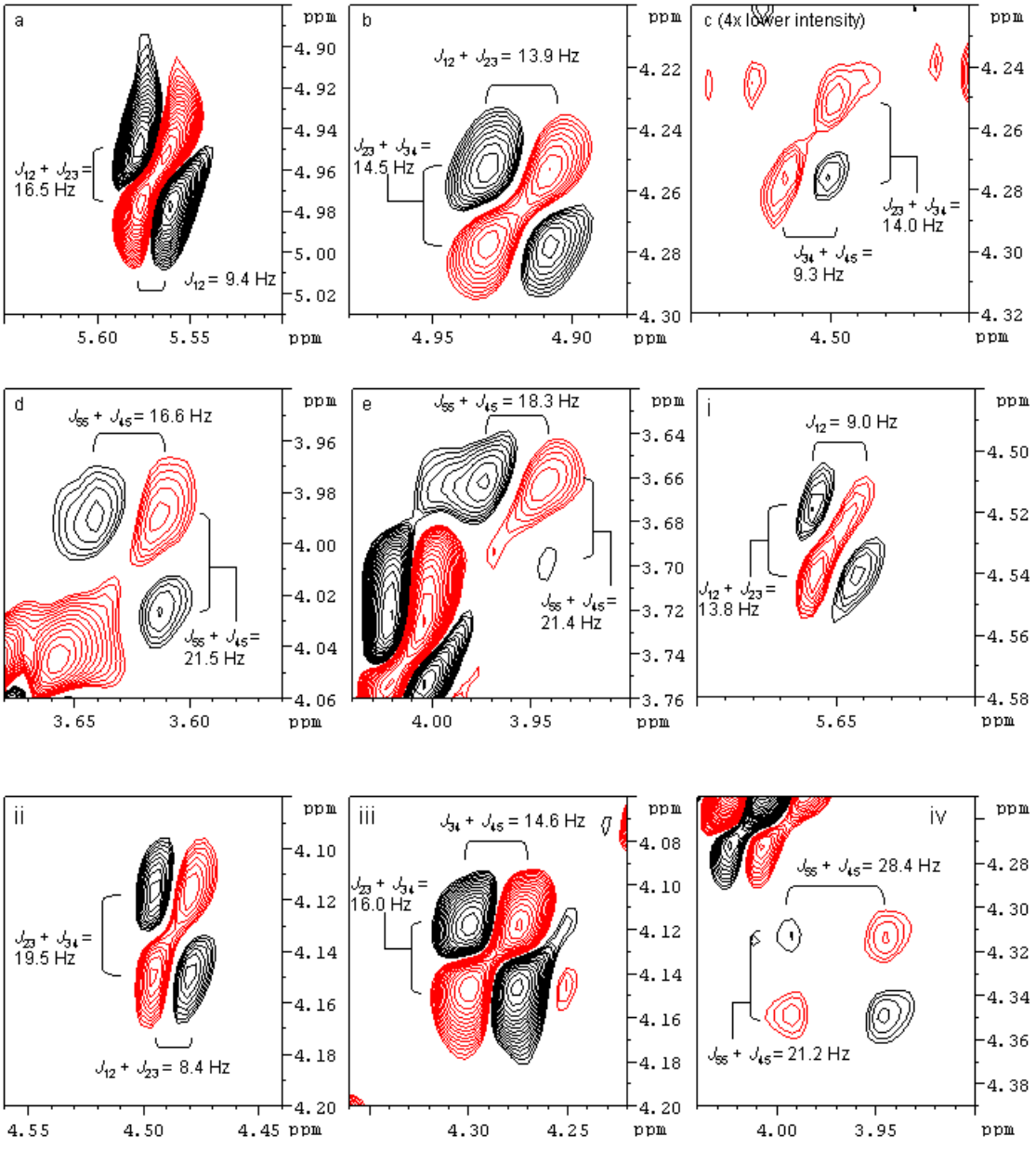

Figure 2-16. (continued)

Table 2-7. $^{3}J_{HH}$ coupling constants (in Hz) of the 5'-GMP ribose protons extracted from DQF-COSY experiment.

$^{3}J_{HH}$	C2'-*endo* (S)	C3'-*endo* (N)
H1'-H2'	9 ± 1	< 2
H2'-H3'	6 ± 1	7 ± 1
H3'-H4'	< 2	8 ± 1
H4'-H5'	2 ± 1	2 ± 1
H4'-H5"	3 ± 1	8 ± 1

2.3.3.3 Carbon-13 chemical shifts, $^{1}J_{CH}$ coupling constants, and assignment of H5' and H5"

The ^{13}C-^{1}H heteronuclear single quantum coherence (HSQC) spectrum of 1.0 M neutral Na_2(5'-GMP) solution is shown in Figure 2-17. The one-bond $^{1}J_{CH}$ is at least ten times larger than two-bond or three-bond couplings, and is used to establish direct correlation between ^{1}H and ^{13}C.[78] In this case, we performed an HSQC experiment without decoupling during acquisition where the $^{1}J_{CH}$ coupling constants can be measured (Figure 2-17). For clarity, the determination of $^{1}J_{CH}$ coupling constants is shown in the C8-H8 region only. We also performed a high resolution 1D ^{13}C NMR experiment for ^{13}C chemical shift assignment (Figure 2-18). Both experimental results are listed in Table 2-8.

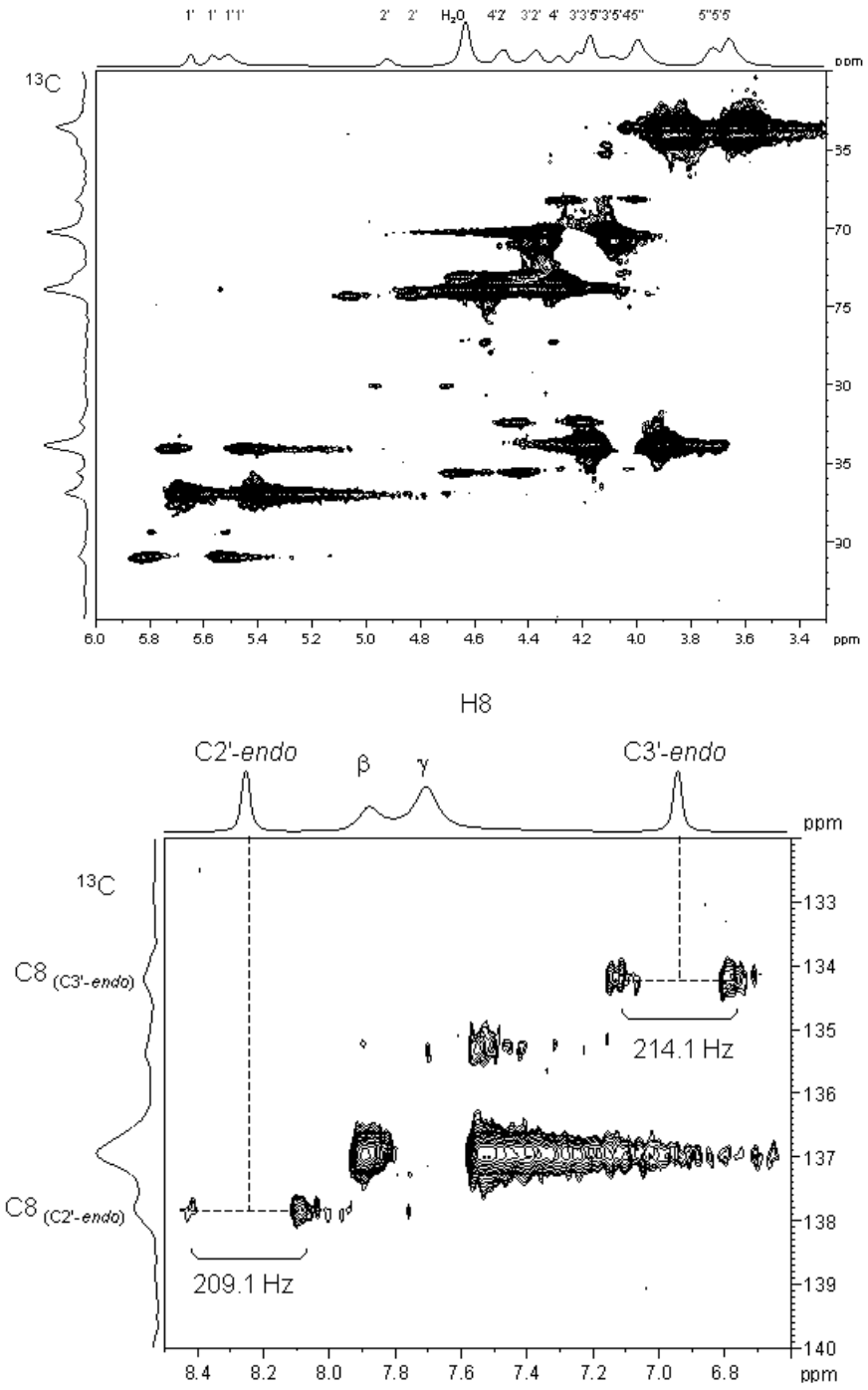

Figure 2-17. (Top) HSQC spectrum of neutral 1.0 M Na_2(5'-GMO) in D_2O at 298 K and 14.1 T showing the ribose region. (Bottom) The same HSQC spectrum showing the heteronuclei C8-H8 spin-spin correlations. $^1J_{CH}$ coupling constants are measured directly from the spectrum.

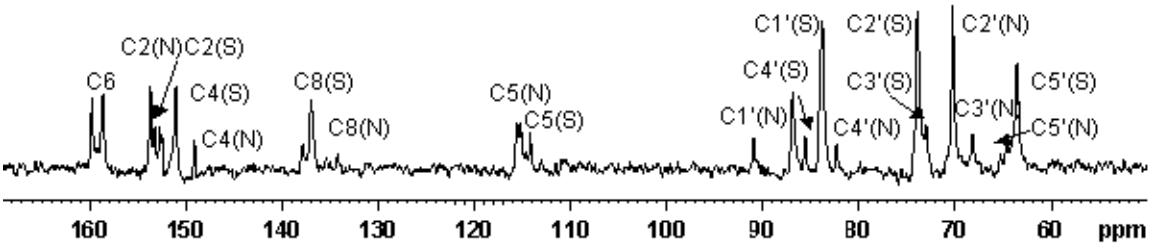

Figure 2-18. ^{13}C-NMR spectrum of neutral 1.0 M Na_2(5'-GMP) in D_2O at 298 K and 14.1 T.

Table 2-8. Carbon-13 resonances (in ppm) and $^1J_{CH}$ coupling constants (in Hz) for 1.0 M Na_2(5'-GMP) at 278 K.

	C2'-*endo* (S)		C3'-*endo* (N)	
	^{13}C chemical shift	$^1J_{CH}$	^{13}C chemical shift	$^1J_{CH}$
Ribose carbons				
C1'	83.8	162.5	90.7	172.6
C2'	74.1	144.2	72.8	153.8
C3'	73.5	154.2	67.9	144.2
C4'	85.3	151.3	82.1	150.4
C5'	64.5	155.4/150.4	65.0	150.6/144.6
Base carbons				
C2	152.7		153.2	
C4	152.5		148.9	
C5	114.0		115.0	
C6	159.7		159.7	
C8	137.6	209.1	133.9	214.1

It is also known that stereochemical assignment of the H5' and H5" signals can be achieved using the literature definition where the two observed $^1J_{(C5', H5)}$ couplings are

assigned to belong to H5' (with the larger ^1J value) and H5" (with the smaller ^1J value), respectively.[79] Using the results obtained from the above HSQC experiment, the final H5' and H5" chemical shifts are assigned to be 3.63/3.98 ppm (C2'-*endo*) and 3.99/4.15 ppm (C3'-*endo*), respectively. This result is consistent with the listing of stereo-specificity of H5' and H5" protons in Table 2-5 and Table 2-7.

2.3.3.4 Connectivity between H8 and H1' signals

As discussed in the previous section, H8 and ribose sugar signals in the DOSY-NOESY spectrum are used in determining both the χ angle and puckering. However, DOSY-NOESY data cannot be used to determine if these H8-ribose interactions are intra or inter-molecular. In order to connect the H8 signals to the ribose resonances of the same molecule, we need to perform experiments that utilize *J* couplings. This could be achieved using a COSY experiment except that the size of $^4J_{(H8,H1')}$ is too weak to be detected. Another approach would be heteronuclear multiple-bond correlation (HMBC) where long-range (2 to 4-bonds) ^{13}C-^{1}H couplings are measured. As shown in Figure 2-19, both H8 and H1' can be correlated through carbons C4 and C5 in the guanine ring by either ^3J or ^4J, and both H8-C1' and H1'-C8 couplings (^3J) are also useful in establishing this connectivity. A series of HMBC experiments were performed using different preset J_{CH} coupling constants in order to capture the above correlations that link H8 to H1'. Unfortunately the coupling constants between H8 and the carbons are very different from those between H1' and the same carbons. Direct observation of H8-H1' was not possible through HMBC. To solve this problem, Phan[80] suggested a combination of HMBC and HSQC experiments in order to establish the connectivity between H8 and H1' resonances.

Figure 2-20 displays the ^{13}C-decoupled HSQC and HMBC spectra side by side of each other. The H8-H1' connectivity within the same molecule is achieved via H8-C8 (HSQC) and C8-H1' (HMBC) correlations.

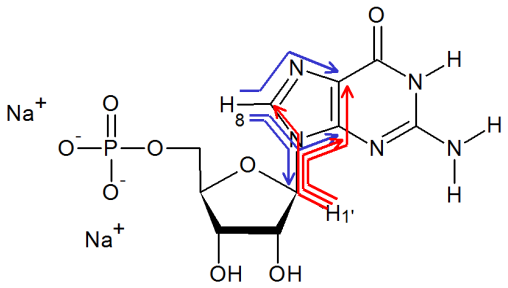

Figure 2-19. ^{13}C-^{1}H heteronuclear couplings (^{3}J or ^{4}J) for protons H8 (blue) and H1' (red) that connects them to each other in the Na_2(5'-GMP) molecule.

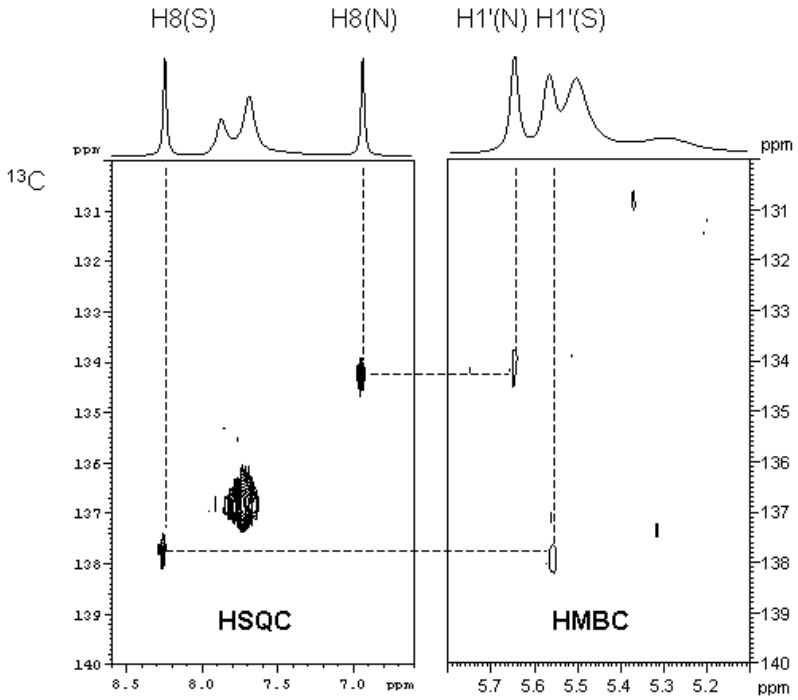

Figure 2-20. (Left) 2D ^{1}H-^{13}C HSQC and (right) gradient-enhanced HMBC spectra of 1.0 M Na_2(5'-GMP) in D_2O at 298 K and 14.1 T.

2.3.3.5 Connectivity between H8 and base exchangeable protons

Because H8 and the base exchangeable protons (N^1H, $N^2H_{A/B}$) from the same 5'-GMP molecule are too far apart to have NOE interactions, we cannot assign the latter protons to either set of signals (S or N). Here we used a refocused-HMBC approach to establish the connectivity between H8 and N^1H through a common carbon atom: H8 → C5 → N^1H (Figure 2-21). Then the imino and amino protons are connected to each other using NOESY as shown in Figure 2-6. The assigned imino and amino proton chemical shifts are listed in Table 2-9.

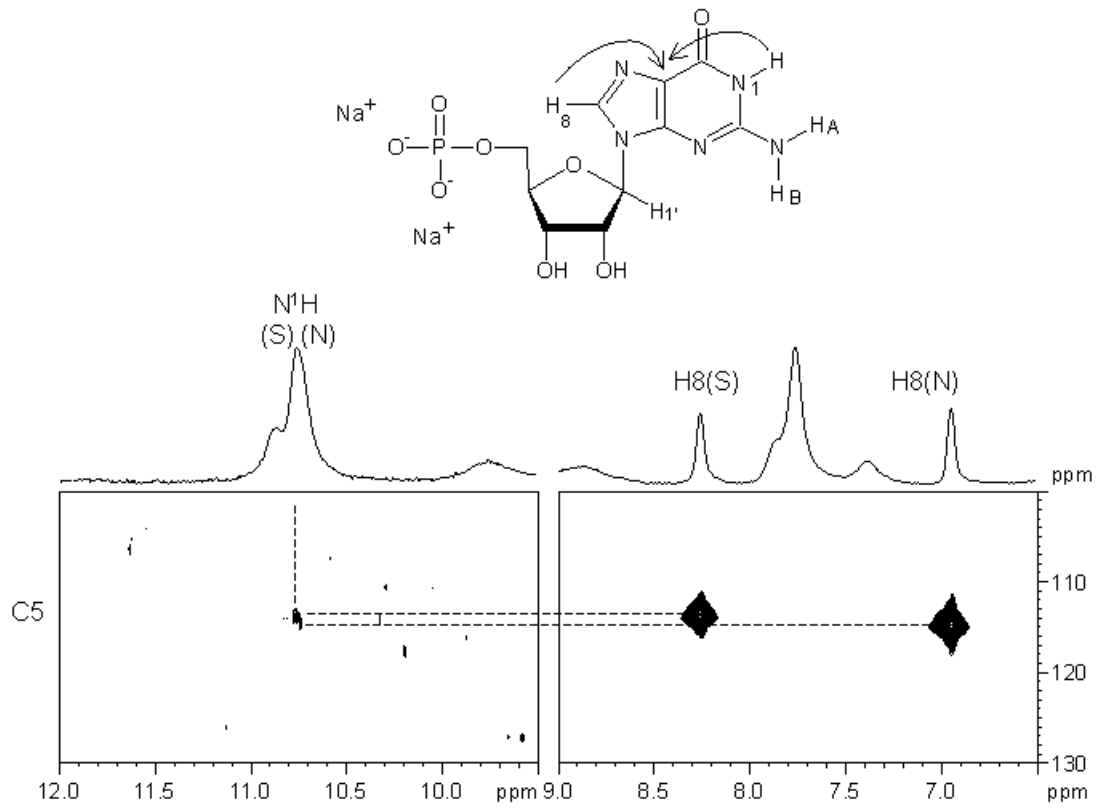

Figure 2-21. (Top) ^{13}C-^1H heteronuclear couplings that connects H8 and N^1H through C5 in Na_2(5'-GMP). (Bottom) 2D refocused-HMBC spectrum of 1.0 M Na_2(5'-GMP) in 90% H_2O/ 10% D_2O at 298 K and 14.1 T.

Table 2-9. Experimental chemical shifts (in ppm) of guanine exchangeable protons in 1.0 M Na_2(5'-GMP) at 298 K.

Proton	C2'-*endo* (S)	C3'-*endo* (N)
N^1H	10.83	10.78
N^2H_A	9.83	9.30
N^2H_B	5.12	4.29

2.3.3.6 Heteronuclear ^{1}H-^{31}P COSY and $^3J_{PH}$ coupling constants

Besides proton-proton coupling constants, the proton-phosphorous ($^3J_{HP}$) relationship is also studied using the heteronuclear 2D experiment ^{1}H-^{31}P COSY. In this case, the phosphorous-31 nucleus is *J*-coupled to neighboring protons, such as H5', H5", and sometimes H4' ($^4J_{HP}$). Figure 2-22 shows the ^{1}H-^{31}P COSY spectrum with the corresponding 1D ^{31}P and ^{1}H spectra shown on the F1 and F2 dimension, respectively. We observe that the ^{31}P signals from either C2'-*endo* or C3'-*endo* molecules have very different chemical shifts, possibly due to different orientations of the phosphate groups and the subsequent different magnetic environments in the two molecules (see next section). Moreover, we observe cross peaks between these two ^{31}P signals with protons from the ribose sugar. The measured $^3J_{HP}$ coupling constants of both C2'-*endo* or C3'-*endo* molecules, as well as the ^{31}P chemical shifts (in ppm) of these two types of molecules are listed in Table 2-10. The monomer has a ^{31}P chemical shift of 4.5 ppm.

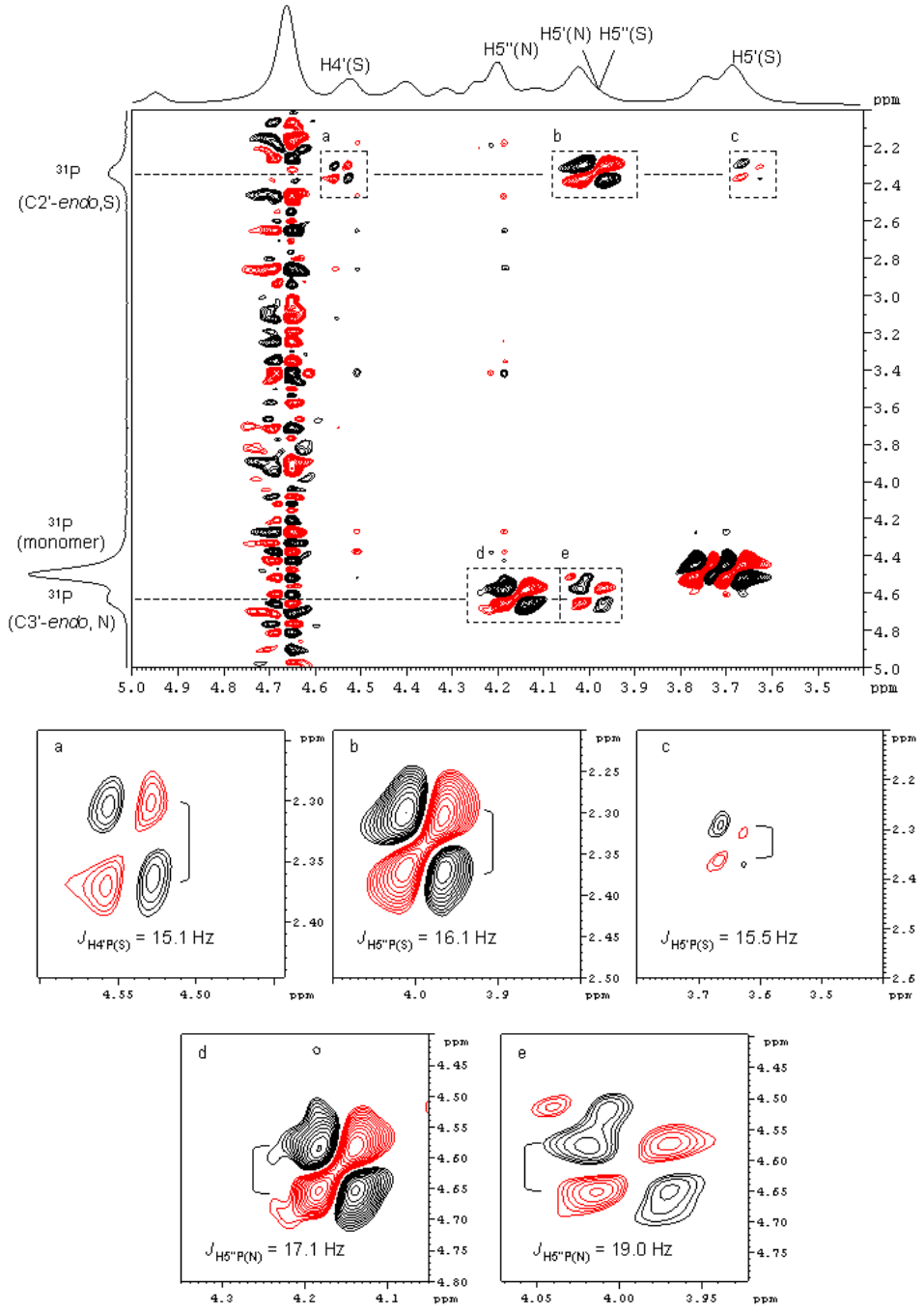

Figure 2-22. Phase sensitive, proton-detected ^{1}H-^{31}P COSY of 1.0 M neutral Na_2(5'-GMP) in D_2O at 298 K and 14.1 T. Positive contour is colored black, and negative red. Correlations ($^{3}J_{HP}$) are linked using dotted lines. Labeled boxes are expanded views of ^{1}H-^{31}P COSY cross peaks used to measure "apparent *J*-couplings".

Table 2-10. $^{3}J_{HP}$ coupling constants (in Hz) of 5'-GMP protons and phosphorous extracted from ^{1}H-^{31}P COSY experiment, and ^{31}P chemical shifts from ^{31}P NMR spectrum.

$^{3}J_{HP}$	C2'-*endo* (S)	C3'-*endo* (N)
^{31}P-H4'	2 ± 2	NA
^{31}P-H5'	< 2	9 ± 2
^{31}P-H5"	7 ± 2	9 ± 2
δ (^{31}P) (ppm)	2.3	4.6

2.3.3.7 Torsion angles β, γ, and δ in C2'-*endo* and C3'-*endo* monomers

The torsion angles β and γ of a guanosine molecule are defined in Chapter 1. The well-known Karplus equation (derived by Martin Karplus)[77,81] can be used to link dihedral angles to vicinal $^{3}J_{HH}$ coupling constants:

Equation 2-5 $$^{3}J_{HH} = A + B\cos\theta + C\cos2\theta,$$

where θ = dihedral angle, and A, B, and C are constants whose values depend on the atoms and substituents involved on the carbon atoms where these coupling-constants are measured.[81] The Karplus equation has been well established in carbohydrate, protein, and nucleic acid systems.[82,83,84] As shown in Figure 2-23, the γ angle can be estimated using the hill-and-valley expression of the Karplus equation specific for nucleic acids. In this case, the γ angle is determined using the coupling constants $J_{H4'H5'}$ and $J_{H4'H5''}$ and the final results are ca. 40-50º and 200-220º for C2'-*endo* and C3'-*endo* molecules, respectively. These angles represent a distinct C4'-C5' bond orientations for these two species: (+)

gauche for the C2'-*endo* sugar and *trans* for the C3'-*endo* sugar. By the same token, torsional angle β can also be deduced using the Karplus equation. As shown in Figure 2-24, the estimated β angles are ca. -150° and -130°, for C2'-*endo* and C3'-*endo* molecules, respectively.

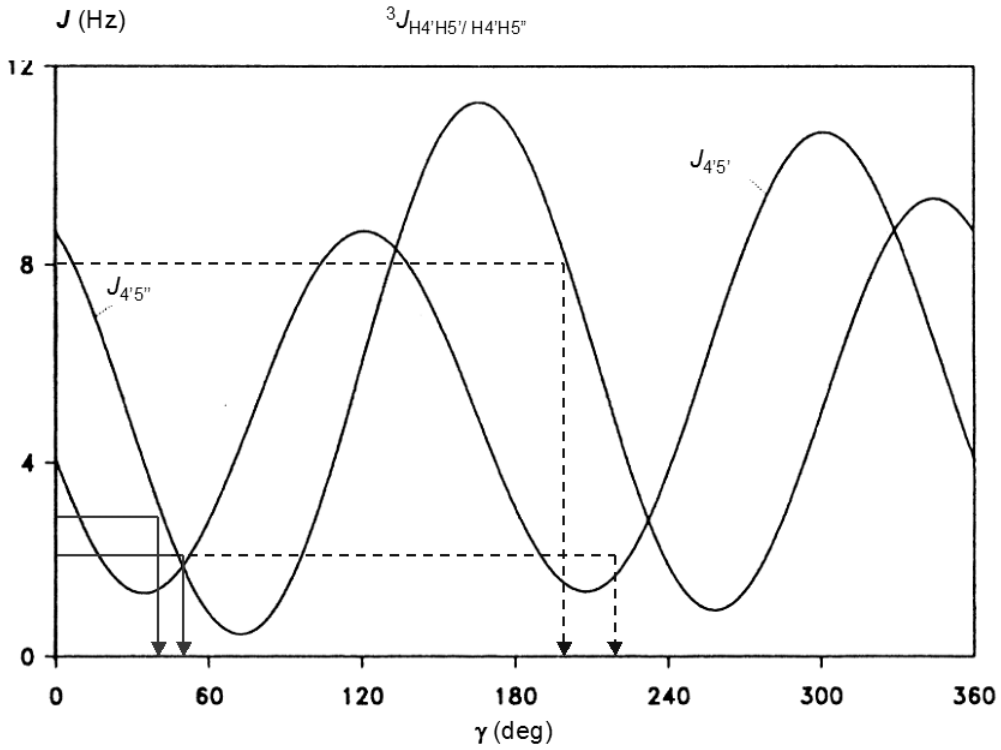

Figure 2-23. The $^3J_{H4'H5'}$ and $^3J_{H4'H5''}$ coupling constants calculated as a function of the torsion angle γ (O5'-C5'-C4'-C3') on the basis of their Karplus relations. Solid and dotted straight lines represent experimental coupling constants from C2'-*endo* and C3'-*endo* molecules, respectively.[77] (Plot adopted from Ref. 75).

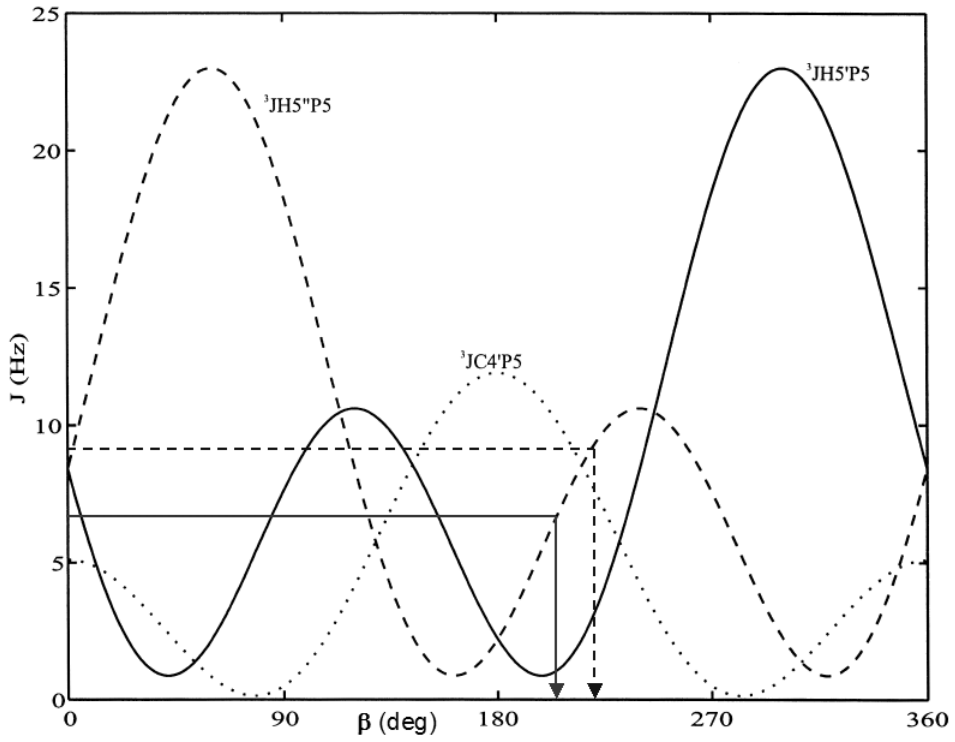

Figure 2-24. The $^{3}J_{H5'P5}$ and $^{3}J_{H5''P5}$ coupling constants calculated as a function of the torsion angle β (P5-O5'-C5'-C4') on the basis of their Karplus relations. Solid and dotted straight lines represent experimental coupling constants from C2'-*endo* and C3'-*endo* molecules, respectively.[77] (Plot adopted from Ref. 75).

2.3.3.8 Confirmation of monomer structures using quantum chemical calculations

Now that we know there are two types of monomers (C2'-*endo* and C3'-*endo*) as building blocks of the G-quadruplex, and their bulk structural features (χ, β and γ angles) are determined, we can verify and refine their structures using quantum chemical calculations. Because chemical shifts and coupling constants observed from NMR experiments are primarily determined by molecular geometry, individual C2'-*endo* and

C3'-*endo* monomers were chosen as the basic units of calculation instead of a tetramer (G-quartet).

First, models of both C2'-*endo* and C3'-*endo* monomers were built using known 5'-GMP crystal structures and were manually optimized to fit experimental data (e.g., DOSY-NOESY and NOESY).[47,48,58] Since it is difficult to obtain experimental ^{15}N and ^{17}O chemical shifts, as well as the infeasibility of comparing the overlapped ^{1}H chemical shifts to the calculated results, we decided to perform calculations on ^{13}C chemical shifts for the two conformers. The calculated ^{13}C chemical shifts were then compared to experimental results. The geometries of these models may be different from the real structures because a vast amount of adjustable parameters exist, including bond lengths, angles, and torsional angles. Therefore an extensive amount of calculations were performed in order to obtain the most representative structure of the models.

Each $[5'\text{-GMP}]^{2-}$ molecule contains 36 atoms and all quantum chemical calculations were performed at the density functional theory (DFT) level using the hybrid B3LYP exchange functional with the 6-311++G(d,p) basis set.[85,86] The gauge-including-atomic-orbital (GIAO) approach as implemented in Gaussian 03 was used in shielding and coupling constant calculations.[87] To make direct comparison between the calculated shielding and the observed chemical shift, the absolute ^{13}C shielding scale of $\sigma_{ref} = 185.4$ ppm was used.[88] As shown in Figure 2-25, the correlation (R value) for the two different sets of data was 0.984 and 0.992 for C2'-*endo* and C3'-*endo* monomers, respectively. This shows good agreements between experimental and calculated ^{13}C chemical shifts of the final models. However, the large intercept (approximately 9 ppm) for both sets of data

suggested that there were factors preventing the calculation from agreeing with the actual experimental results. These factors may include basis-set limitation where the current basis set does not have sufficient basis functions to fully represent the molecule. In addition, the experimental data were obtained at room temperature while the calculation was performed at absolute zero with no thermal correction. The gas phase molecule is also not representative of the solution-state 5'-GMP sample. Moreover, the lack of neighboring Na^+ atoms might have also contributed to the differences between the computation and experimental results.

Because of these various reasons that might have contributed to inconsistency, direct comparison between calculations and experimental ^{13}C chemical shifts may not be very useful. Therefore, we decided to evaluate the difference in ^{13}C chemical shifts between the two conformers instead. The difference in ^{13}C chemical shifts was defined as (in ppm): the ^{13}C chemical shift of a particular carbon of the C2'-*endo* monomer subtracts the ^{13}C chemical shift of the same carbon in the C3'-*endo* conformation. The final ^{13}C and ^{1}H chemical shift differences between these two molecules are compared with experimental values and are shown in Figure 2-26. The x-axis of this graph shows the various carbon atoms of the 5'-GMP molecules, while the y-axis shows the differences of the chemical shifts between the two puckering molecules of the same carbon atom. Proton chemical shifts are also used as complementary data. It should be noted that because ^{13}C has a larger chemical shift range compared with proton, a larger difference between experimental and calculation result is expected. Nonetheless, the calculations are in good agreement with experimental values, and two final puckering molecules served as the building blocks of the G-quadruplex are produced. Figure 2-27 shows the

structures of these two monomers, and their Cartesian coordinates in protein-data-bank (PDB) format are listed in Appendix I.

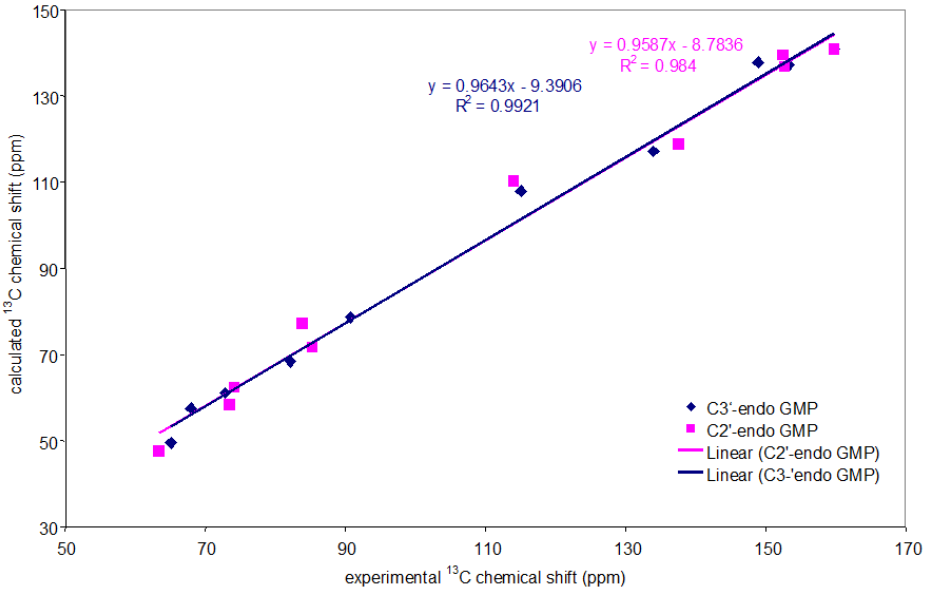

Figure 2-25. Experimental and calculated (B3LYP/6-311++G(d,p)) ^{13}C NMR chemical shifts of the C2'-*endo* and C3'-*endo* 5'-GMP monomers.

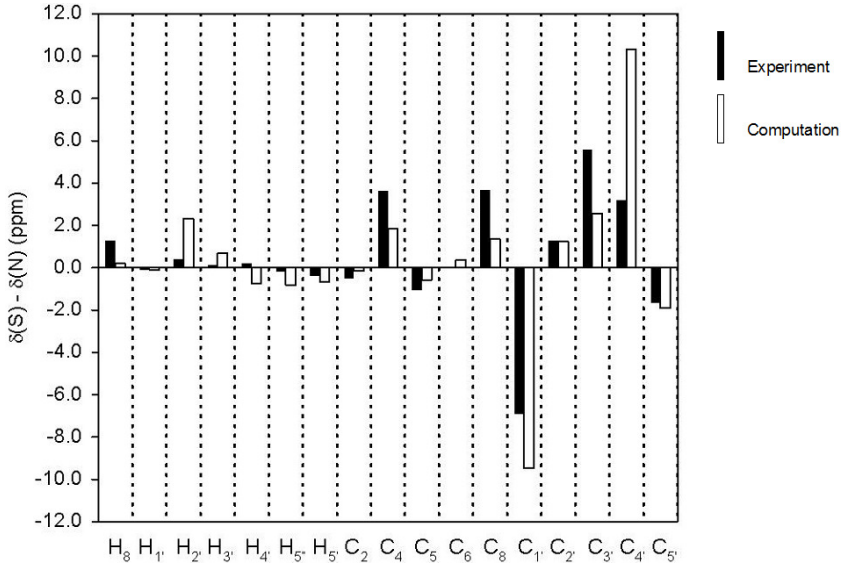

Figure 2-26. Differences in experimental and calculated ^{1}H and ^{13}C chemical shifts between the C2'-*endo* and C3'-*endo* conformers.

All computed ^{1}H and ^{13}C chemical shifts and coupling constants for these 5'-GMP molecules are listed in Table 2-11. The final pseudorotation phase angle (P), and puckering amplitudes (ν_{max}) of C2'-*endo* and C3'-*endo* molecules are also calculated using the following equations[89] and the results are summarized in Table 2-12. The definitions of $\nu_{0\text{-}4}$ are listed in Table 1-1, Chapter 1.

Equation 2-6

$$\tan P = \frac{(\nu_4 + \nu_1) - (\nu_3 + \nu_0)}{2\nu_2(\sin 36 + \sin 72)}$$

Equation 2-7

$$\nu_{max} = \frac{\nu_2}{\cos P}$$

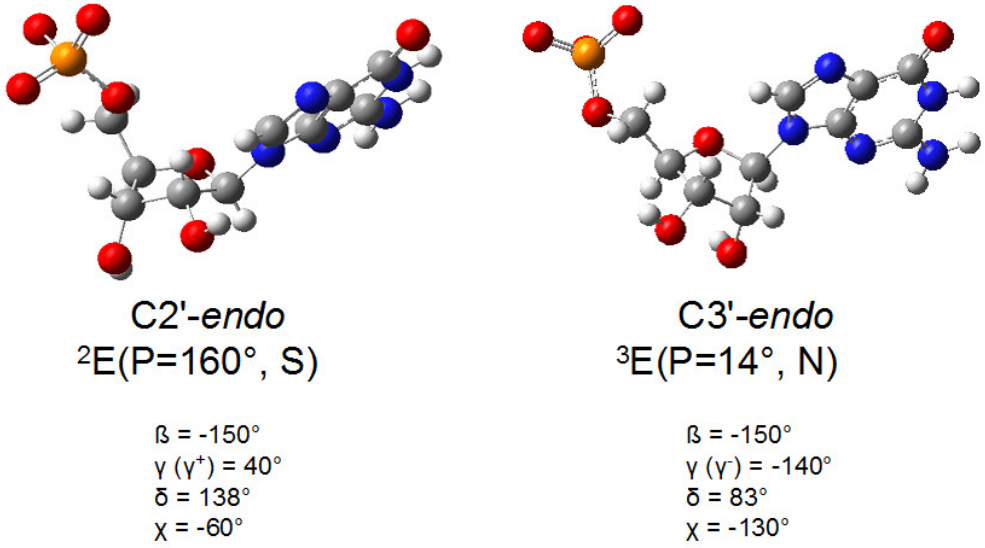

Figure 2-27. Final models of calculated 5'-GMP molecules using B3LYP/6-311++G(d,p).

Table 2-11. Computed ^{1}H and ^{13}C chemical shifts (in ppm) and $^{1}J_{CH}$ coupling constants (in Hz) for 5'-GMP molecules in C2'-*endo* and C3'-*endo* sugar pucker conformations. The level of calculation is B3LYP/6-311++G(d,p).[a]

	C2'-*endo* (S)	C3'-*endo* (N)	(^{13}C)/($^{1}J_{CH}$)	C2'-*endo* (S)	C3'-*endo* (N)
Non-exchangeable protons			Ribose carbons		
H8	8.26	8.06	C1'	87.9 (171.6)	97.4 (173.8)
H1'	5.44	5.55	C2'	78.5 (155.3)	77.2 (158.6)
H2'	5.40	3.06	C3'	75.5 (170.3)	72.9 (143.3)
H3'	4.63	3.94	C4'	93.7 (147.0)	83.3 (153.6)
H4'	3.33	4.08	C5'	58.9 (139.7/133.3)	60.9 (138.6/131.1)
H5'	2.62	3.27			
H5"	3.38	4.20	Base carbons		
			C2	157.6	157.7
			C4	159.9	158.0
			C5	126.0	126.6
			C6	162.0	161.6
			C8	141.4 (194.7)	140.0 (195.2)

[a] Chemical shifts (δ) are converted from the calculated shielding (σ) using $\delta = \sigma_{ref} - \sigma$, where $\sigma_{ref}(^{13}C) = 185.4$ ppm and $\sigma_{ref}(^{1}H) = 34.9$ ppm.

Table 2-12. Torsion angles, pseudorotation phase angle (P), and puckering amplitudes (ν) determined for the two 5'-GMP molecules. All quantities are in degrees.

Pucker	χ	β	δ	γ	ν_0	ν_1	ν_2	ν_3	ν_4	P	ν_m
C2'-*endo*	-60	-150	138	40	-18.8	30.2	-28.4	17.6	0.6	159.9	30.2
C3'-*endo*	-130	-150	83	-140	3.4	-25.7	37.3	-36.2	20.8	13.7	38.4

2.3.4 G-quartet arrangement

In Section 2.3.3.5, we have established the connection between H8 and N^1H of the same 5'-GMP molecule using ^1H-^{13}C refocused HMBC experiment, and concluded that the observed H8 with N^1H/N^2H_A cross peaks in NOESY were from the same quartet instead of inter-quartets. Moreover, the same NOESY spectrum does not show any cross peaks that would indicate a mixed C2'-*endo*/C3'-*endo* G-quartet formation, i.e., no H8(S)-N^1H/N^2H_A(N) or H8(N)-N^1H/N^2H_A(S) cross peaks are observed; see Figure 2-28. This concludes that the G-quartets are all-C2'-*endo* (all-S) and all-C3'-*endo* (all-N), instead of adjacent-C2'-*endo*/C3'-*endo* or alternate-C2'-*endo*/C3'-*endo*. This is consistent with the observation discussed in session 2.3.1 about all-α and all-γ G-quartets.

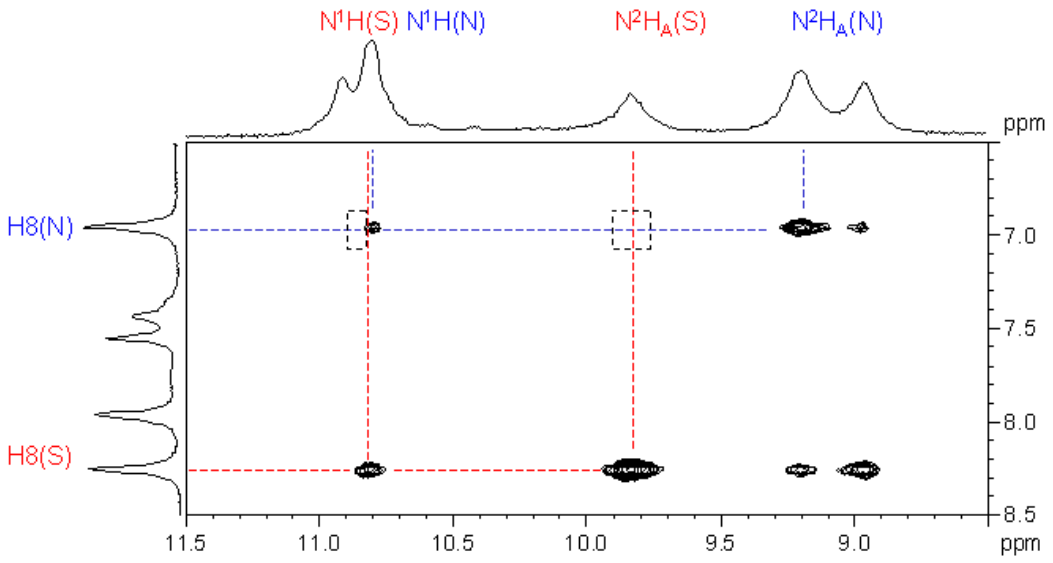

Figure 2-28. NOESY spectrum of a neutral 1.0 M Na_2(5'-GMP) solution in 1:1 H_2O/D_2O at 278 K and 14.1 T with a mixing time of 50 ms. Expected cross peak for adjacent-C2'-*endo*/C3'-*endo* or alternate-C2'-*endo*/C3'-*endo* G-quartet are enclosed in the boxes. (This spectrum is an enlarged portion of Figure 2-6).

2.3.5 G-quadruplex formation

Now that we have two types of G-quartets (all-S and all-N), we need to find the stacking pattern with which G-quartets form a G-quadruplex helix. In this regard, both NOESY and DOSY-NOESY can provide spatial arrangement information between stacking G-quartet layers. Eleven inter-quartet cross peaks including H1'(S)-H8/H4'/H5'/H5''(N), H2'(S)-H2'/2'OH(N), H8(S)-H1'/H2'/2'OH(N), and N^2H_B(S)-H2'/H3'(N) are highlighted in the NOESY spectrum (Figures 2-29 and 2-30). The H1'(S)-H8 cross peak gives an indication that the head face of the all-S quartet is opposed to the tail face of an all-N quartet, i.e., head-to-tail stacking. The "head" and "tail" faces of a G-quartet refer to the direction of the Hoogsteen hydrogen-bond from the donor to the acceptor (Figure 2-31). It is called a "head" face when the direction is clockwise, and it is called a "tail" face when the direction is counter-clockwise.

In this case, the head-to-tail stacking suggests alternate stacking of all-S and all-N quartets on each other to form a G-quadruplex. This is a reasonable stacking pattern as either head-to-head or tail-to-tail hinders formation of long columns due to repulsion. Using molecular models, the NOE cross peaks H8(S)-H2'(N) and H1'(S)-H5'/H5''(N) also suggest that the quartets are twisted 30° relative to each other in a right-handed fashion with a separation of 3.4 Å between G-quartets. This is in agreement with the G-quadruplex model suggested by Zimmerman using x-ray fiber diffraction.[47] From the same NOESY spectrum, the chemical shifts of the hydroxyl protons are also discovered (in ppm): 2'-OH = 5.09 (S), 7.44 (N), and 3'-OH = 9.30 (S), 9.20 (N). It is very interesting to note that, three of these four hydroxyl groups are located at high frequency, suggesting

their involvement in hydrogen-bonding. Using this information, a G-quadruplex model is built using the final C2'-*endo* and C3'-*endo* models from calculations (Figure 2-32).

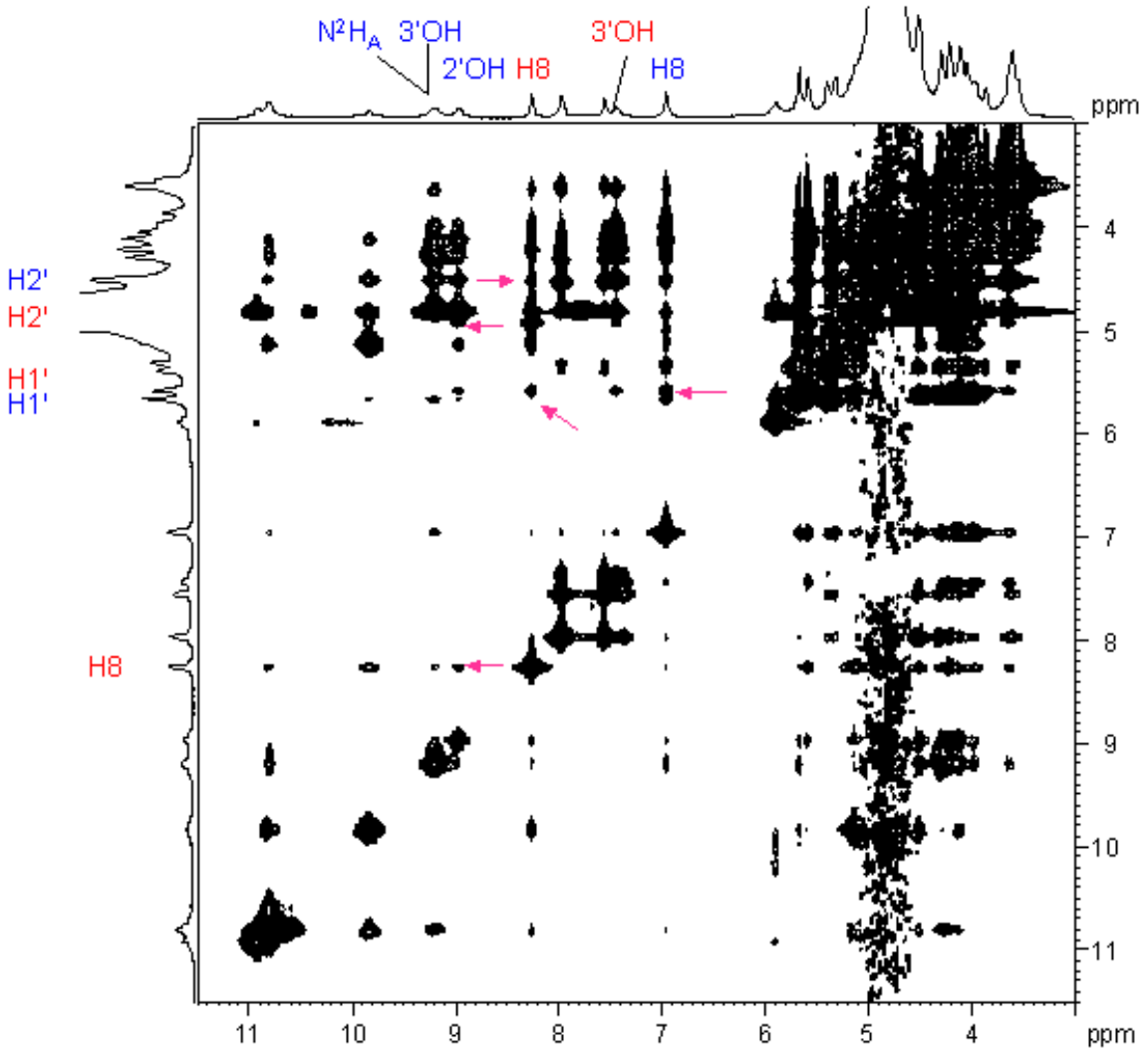

Figure 2-29. 2D NOESY spectrum of a neutral 1.0 M Na_2(5'-GMP) solution in 1:1 H_2O/D_2O at 278 K and 14.1 T with a mixing time of 50 ms. The inter-quartet cross peaks are highlighted using arrows. C2'-*endo* and C3'-*endo* signals are in red and blue, respectively.

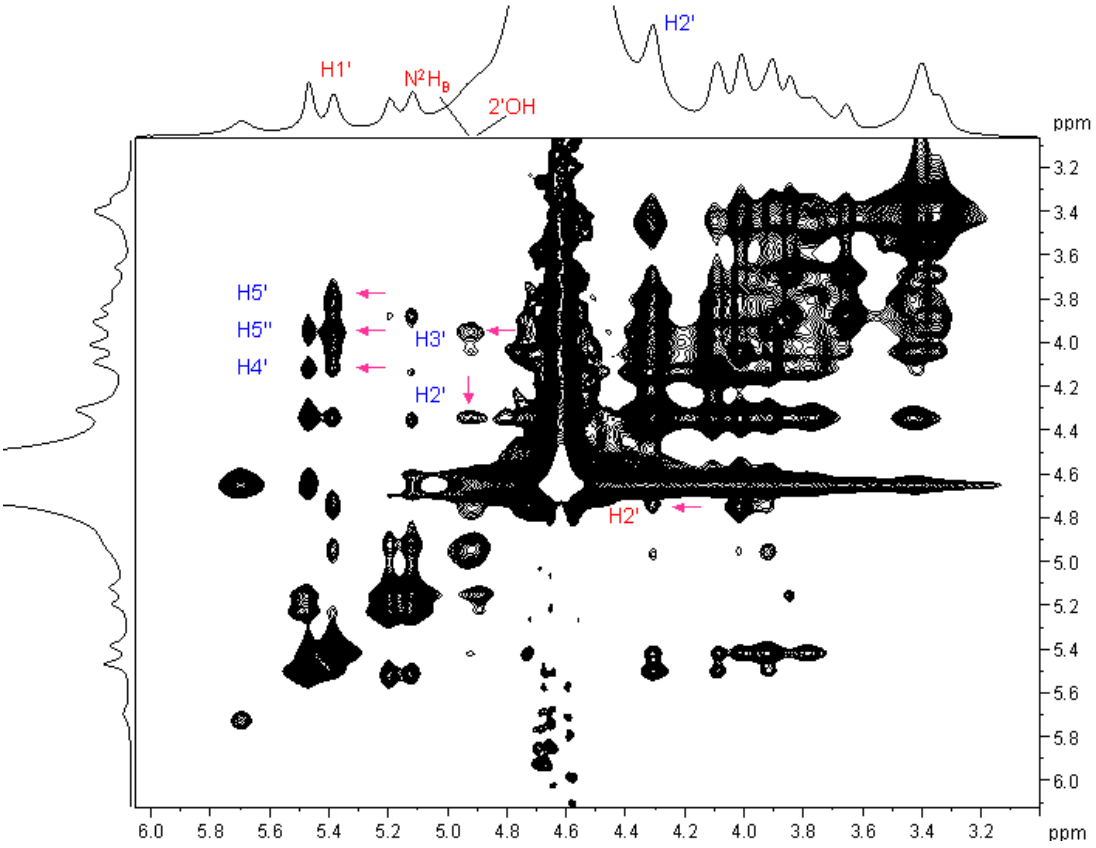

Figure 2-30. Enlarged 2D NOESY spectrum showing the ribose region of a neutral 1.0 M Na_2(5'-GMP) solution in 1:1 H_2O/D_2O at 278 K and 14.1 T with a mixing time of 50 ms. The inter-quartet cross peaks are highlighted using arrows. C2'-*endo* and C3'-*endo* signals are in red and blue, respectively.

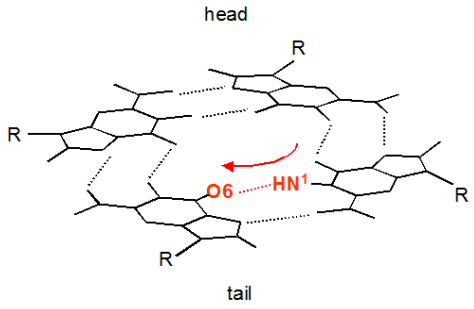

Figure 2-31. The two faces of a G-quartet. Hoogsteen hydrogen bond with a clockwise rotation from donor to acceptor is called the "head" face, and the "tail" face has a counter-clockwise rotation.

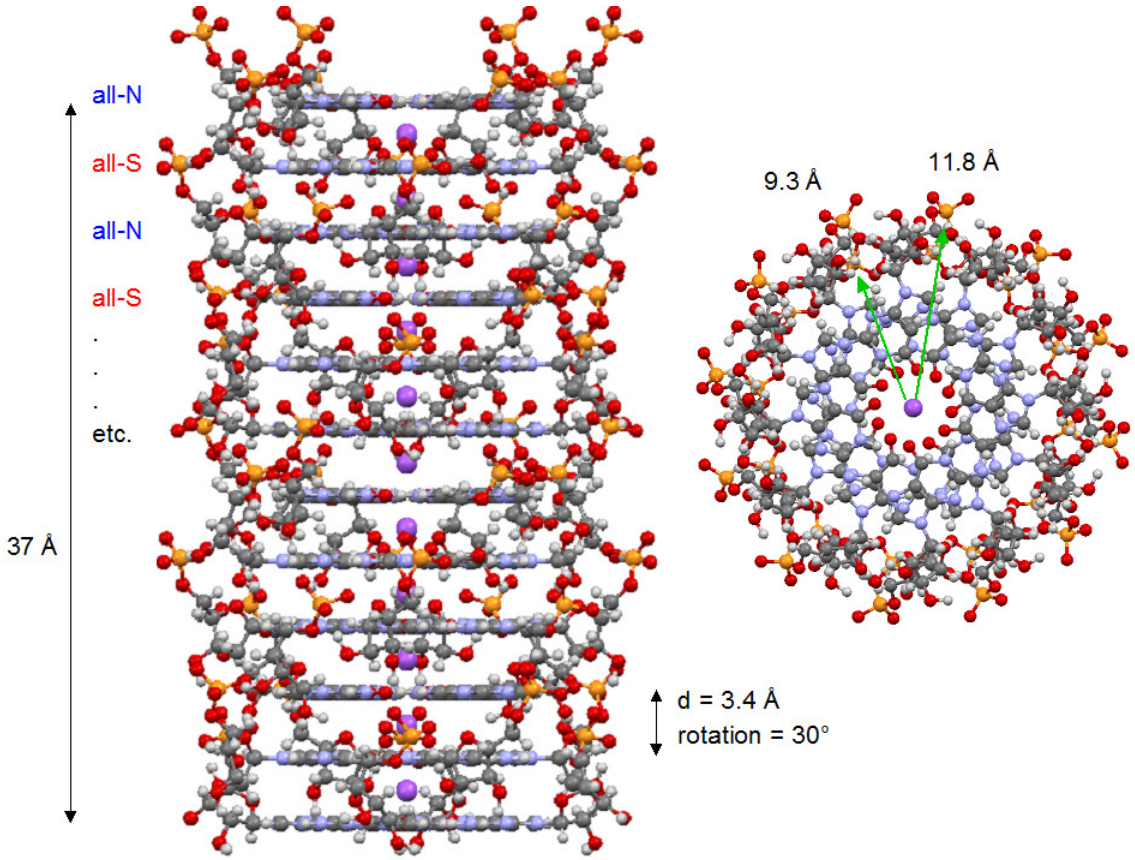

Figure 2-32. (Left) A full turn of the right-handed 5'-GMP G-quadruplex with Na^+ ions (purple balls) reside in the channel site. (Right) Top view of the G-quadruplex where Na^+-P distances are highlighted and labeled.

The final G-quadruplex model is composed of twelve layers of G-quartets in a full rotation of the helix (360º) with a total molecular weight of approximately 17 kDa (48 GMP molecules x 364 g/mol). It is of C_4 symmetry with alternate C2'-*endo* and C3'-*endo* quartets stacking onto each other in a head-to-tail fashion. The coordinates of the first two G-quartets (all-S and all-N) are provided in Appendix I. The following equations are used to generate the whole 5'-GMP G-quadruplex:

Equation 2-8 $x' = x(\cos\phi) - y(\sin\phi)$

Equation 2-9 $y' = y(\cos\phi) + x(\sin\phi)$

Equation 2-10 $z' = z + 6.8$

where x, y, and z are the original coordinates from the calculated models, and ϕ is the twist angle (90°, 180°, and 270°) used in making a single all-S or all-N G-quartet. When building the G-quadruplex, the next all-S layer is twisted 60° and 6.8 Å away from the previous all-S layer because of alternating all-S and all-N stacking. The same rules also apply to all-N quartets when stacking. The intra-molecular, intra-quartet, and inter-quartet distances of all protons in the 5'-GMP G-quadruplex are listed in Appendix I as well.

Upon examining this 12-layer 5'-GMP G-quadruplex model, several interesting observations are made. First, hydrogen bonds are observed to form between the phosphate group P(S)-O^- and the hydroxyl group H-O3'(N) three quartets away, as shown in Figure 2-33. This kind of inter-quartet hydrogen-bond formation along the helix has never been reported, and they certainly contribute further to the stability of the G-quadruplex structure. This reaffirms the pH dependence in G-quadruplex formation because phosphate group has two negatively charged oxygens for phosphate-hydroxyl bond only at neutral to slightly alkaline pH. Secondly, we observed that the arrangement of adjacent 5'-GMP molecules in the helix is almost identical to those in polynucleotides systems where they are linked by covalent phosphodiester bonds. This type of automatic self-alignment could perhaps shed a light on how mononucleotides might have arranged into oligomers under prebiotic conditions.

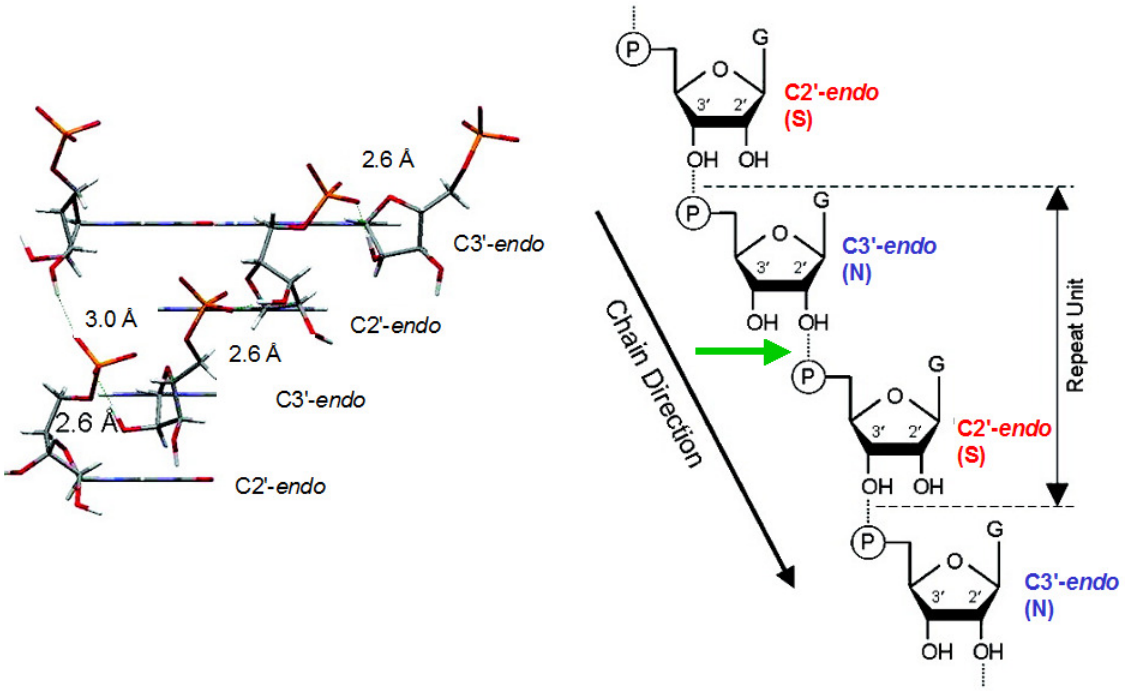

Figure 2-33. (Left) A partial structure of the 5'-GMP helix showing inter-quartet phosphate-hydroxyl hydrogen-bonds, where O···O distances are given. (Right) Schematic display of the hydrogen-bond linkage along the 5'-GMP helix.

As shown in Table 2-13, it is interesting to observe that only Z-DNA shares the property of having two types of sugar puckering in the same system with Na_2(5'-GMP), although Z-DNA has a left-handed helix and has both types of *anti* and *syn* glycosidic angles. Since the C2'-*endo* sugar pucker of 5'-GMP is in high-*anti* conformation (χ = -60°), rather than *syn*, this explains the right-handed helix formation in the 5'-GMP system. Moreover, Z-DNA is composed of both dG and dC polynucleotides while our 5'-GMP G-quadruplex is only comprised of G mononucleotides. We believe that the right-handed Na_2(5'-GMP) G-quadruplex formed under neutral condition represent a new class of nucleotide structure that has not been reported before.[90]

Table 2-13. Comparison of geometric parameters of common nucleic acid helices.

	B-DNA	A-DNA A-RNA	Z-DNA	PolyG[91]	Na_2(5'-GMP)[46] (solid-state)	Na_2(5'-GMP) (this work)
Helix sense	Right	Right	Left	Right	Right	Right
Base per turn	10	11	12	11.5	12	12
Rise per base (Å)	3.4	2.6	3.7	3.36	3.4	3.4
Rotation per base (º)	36.0	32.7	-60 (per dimer)	31.2	30	30
Glycosyl bond	*anti*	*anti*	dC: *anti* dG: *syn*	*anti*	*anti*	*anti*
Sugar pucker	C2'-*endo*	C3'-*endo*	dC: C2'-*endo* dG: C3'-*endo*	C3'-*endo*	C3'-*endo*	C2'-*endo* C3'-*endo*
Exocyclic C4'-C5' bond (º)	38	47	dC: 55 dG: -170	68	47	40 (C2'-*endo*) -140 (C3'-*endo*)
Distance of P from axis (Å)	9.0	8.7	d(CpG): 6.9 d(GpC): 8.0	10.0	9.6	9.3 (C2'-*endo*) 11.8 (C3'-*endo*)

2.3.6 Role of metal ions

As for metal ions, the ratio of Na^+ to 5'-GMP is 2:1 in our study of Na_2(5'-GMP). Some Na^+ ions are participating in G-quadruplex formation as they reside in the G-quadruplex channel (Figure 2-34), while the rest of the Na^+ ions are believed to be attached to the surface sites (PO_4^{2-}) of 5'-GMP as suggested by Detellier et al.[11] In this case, because the distance between P(S)/P(N) and P(N)/P(S) atoms in adjacent G-quartets were large (6.7 Å and 7.2 Å, respectively), it is possible for Na^+ to fit in between these phosphate groups and formed P-$O^{-}\cdots Na^{+}\cdots O^{-}$-P interactions. This could further stabilize the helix by balancing the negative charges between phosphate groups. This hypothesis will be tested further in Chapter 4, where a 5'-GMP derivative with a longer O5'-P5' bond

is examined. Such P-O^{-}···Na^{+}···O^{-}-P interactions seem important in G-quadruplex formation and stability, as replacement of Na^+ ions by K^+ or Rb^+ will lead to formation of different yet known ordered structures.[15]

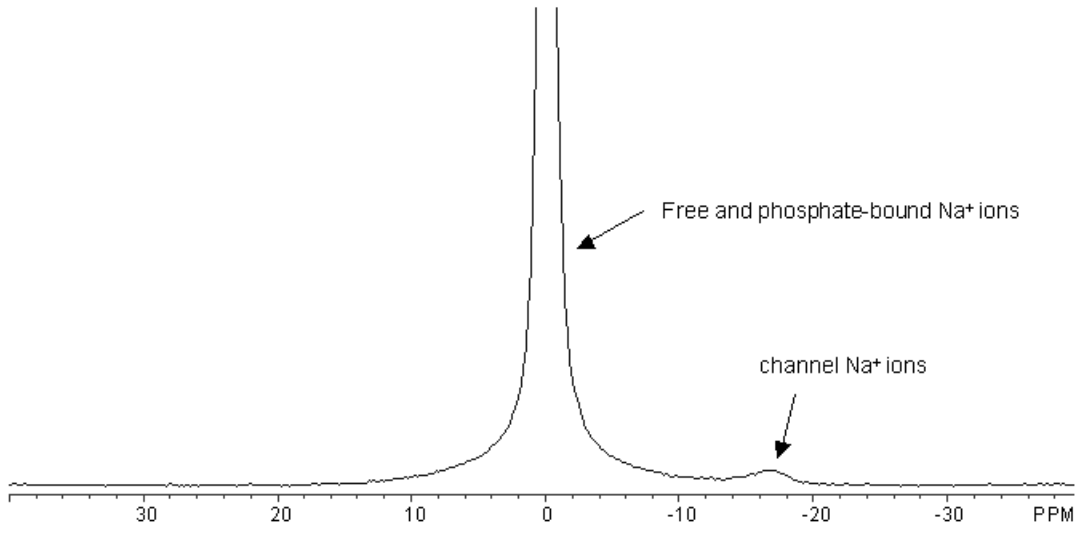

Figure 2-34. Solution-state ^{23}Na NMR of 1.0 M Na_2(5'-GMP) in D_2O at 298 K and 14.1 T. Peaks assignment for phosphate-bound and channel Na^+ ions are obtained using reference.[61]

2.3.7 Confirmation of stacking dimers

From the same NOESY spectrum mentioned in Section 2.3.1, we also observed a high frequency shift of N^1H of the β species due to hydrogen bonding. Interestingly, the NOESY spectrum did not show the signature cross peak between H8 and N^1H (Figure 2-35, box). This can be explained by the formation of a centrosymmetric dimer, where two 5'-GMP monomers were held together by two N^1H···O6=C hydrogen bonds (Figure 2-36). The absent of N^2H_2 (β) resonances in the same G-quartet signature region also supports this conclusion. This type of dimer arrangement is named $GG3^2$ in Jeffrey and

Saenger's notations.[92] Moreover, the assignment of β as stacking dimers is also supported by the ROESY experiment, where exchange activity is observed between dimer (β) and monomer (γ) species (Figure 2-37). ROESY is an experiment similar to NOESY, except it measures NOE in the rotating frame. ROESY cross peaks are basically due to cross-relaxation effect from spins close to each other in space, and chemical exchange. Because ROESY is carried out in the rotating frame, the NOE in the transverse plane (i.e., ROE) is always opposite phase from the diagonal. Hence, in a ROESY spectrum, when the diagonal has a positive phase, the ROE would have a negative phase, and the chemical exchange signals would have a positive phase. As shown in Figure 2-37, the same phase cross peaks (compared with the diagonal) between the H8 signals (β and γ) suggests that they are exchanging in the millisecond NMR time scale. However, exchange between these two species with either G-quadruplex signal (α and γ) are not observed (Figure 2-37). This is consistent with a previous ^{31}P magnetization-transfer NMR study of Na_2(5'-GMP).[57] The presence of dimers also support the results of Wong et al., where stacking dimers are observed in a concentrated solution of Na_2(5'-GMP) at neutral pH.[66] Proton and carbon-13 chemical shifts and coupling constants of both monomer and dimer signals are extracted from COSY, NOESY and HSQC experiments, and the values are shown in Table 2-14.

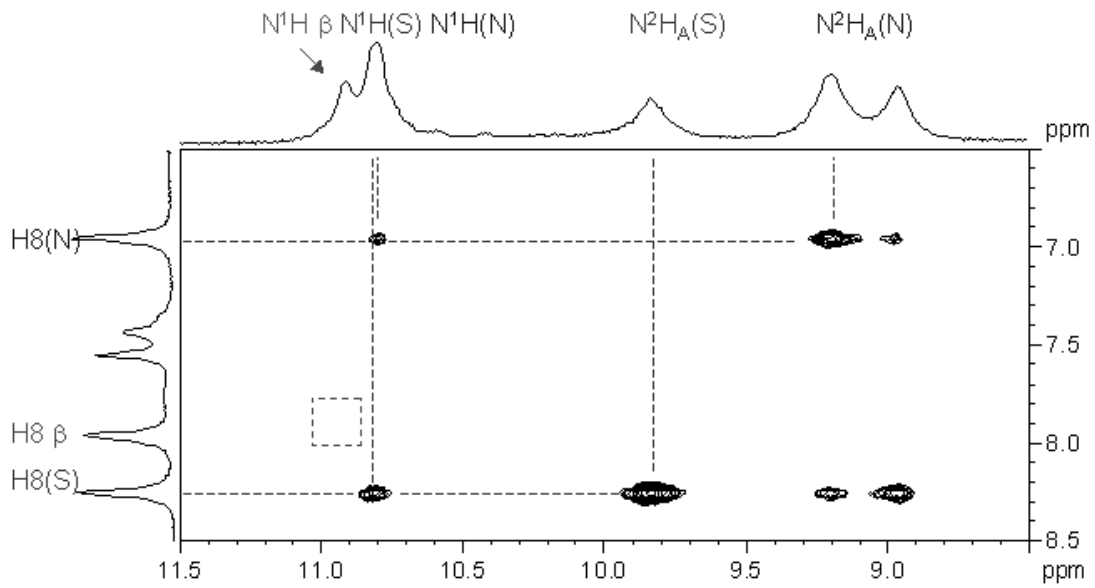

Figure 2-35. NOESY spectrum of a neutral 1.0 M Na_2(5'-GMP) solution in 1:1 H_2O/D_2O at 278 K and 14.1 T with a mixing time of 50 ms. Expected G-quartet cross peak between H8(β) and N^1H(β) is shown in the box. (This spectrum is an enlarged portion of Figure 2-6).

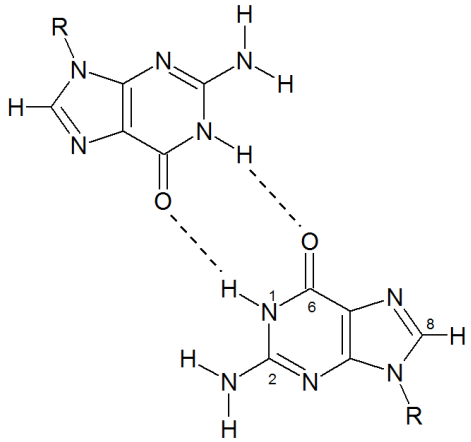

Figure 2-36. The structure of a $GG3^2$ dimer according to Jeffrey and Saenger's notations.[92] R = 5'-phosphate ribose.

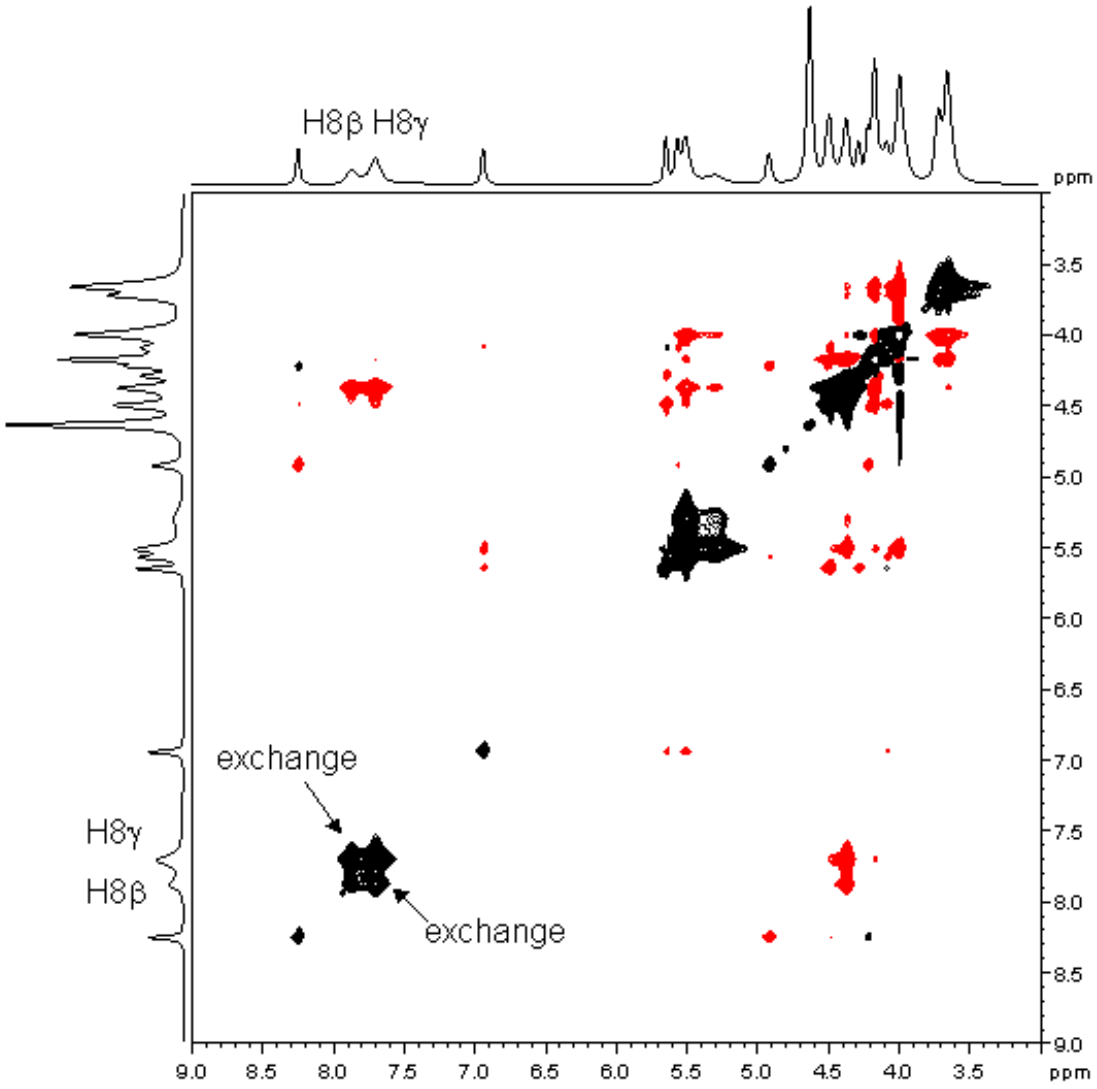

Figure 2-37. ROESY spectrum of a 1.0 M Na_2(5'-GMP) solution in H_2O/D_2O at 298 K and 14.1 T, with a mixing time of 100 ms. The cross peaks due to chemical exchange are labeled. Diagonal and exchange cross peaks are in the same phase (black), while NOE cross peaks are in opposite phase (red).

Table 2-14. Proton and carbon-13 resonances (in ppm) and indirect spin-spin coupling constants (in Hz) for monomer and dimer aggregates in 1.0 M Na_2(5'-GMP) at 278 K (m = monomer, d = dimer).

	^{1}H chemical shift		^{13}C chemical shift	$^1J_{CH}$
Non-exchangeable protons		Ribose carbons		
H8	7.95 (m) / 7.57 (d)	C1'	86.7	165
H1'	5.40 (m) / 5.33 (d)	C2'	73.6	153.6
H2'	NA	C3'	70	154.6
H3'	4.11	C4'	83.6	150.7
H4'	4.04	C5'	63.3	140.0/145.3
H5'	3.86	Base carbons		
H5"	3.59	C2	157.4	
		C4	121	
Exchangeable protons		C5	115.5	
N^1H	10.91 (d)	C6	168.8	
N^2H_2	5.81-6.01	C8	135.0 (m)	215.7
	(broad, m/d)		136.6 (d)	

2.4 Conclusion

In summary, we are able to determine successfully two self-assembled structures of Na_2(5'-GMP) under neutral conditions using both NMR and computation methods. A GG3[2] dimer and a right-handed G-quadruplex helix with head-to-tail all-S on all-N stacking form spontaneously under neutral pH using various weak, non-covalent forces. The G-quadruplex is formed using hydrogen-bonds (base-base and hydroxyl-phosphate), π-π stacking (base-base), ion-dipole interaction between the channel Na^+ ions and the surrounding carbonyl oxygens ($Na^{+\cdots}O6$), as well as ion-phosphate interactions

(P-$O^{-}\cdots Na^{+}\cdots O^{-}$-P) as previously suggested.[61] Since the G-quadruplex expressed less temperature dependence (from 278 to 298 K), we believe that the same structure exists in solid-state. It is also possible that similar structures exist in compounds form by guanosine derivative self-assembles, or in other nucleic acid systems.

Chapter 3

Structural determination of disodium guanosine 5'-monophosphate G-quadruplex under acidic conditions

3.1 Introduction

Gel formation of guanosine 5'-monophosphate (5′-GMP) under slightly acidic conditions (e.g., pH 5) was first discovered by Ivar Christian Bang in 1910 (Figure 1-1, Chapter 1).[11] However, it was not until 50 years later that the structural basis of such 5'-GMP gel was examined. In 1962, Gellert et al. used x-ray fiber diffraction data to show that different GMP isomers form different helical structures.[12] For 3'-GMP gel, the helical structure is formed by successive stacking of planar hydrogen-bonded guanine tetramers now known as G-quartets on top of each other.[12] For 5'-GMP gel formed at pH 5, in contrast, the planar (disc-like) G-quartet is broken at one side forming a continuous helix using hydrogen bonds between 5'-GMP bases in a lock-washer fashion (Figure 3-1).[12] The authors suggested that the helix formed by such linear aggregation using hydrogen-bonds and van der Waals attractions should form a cylinder (now known as G-quadruplex) where there is enough room in the channel for water molecules to reside. They also stated the specific types of inter-molecular hydrogen-bonds form between phosphate and i) amino (i.e., NH···O=P) from the layer above, ii) neighboring phosphates, and iii) a 2'-hydroxyl of a neighboring ribose. Together with electrostatic repulsions between phosphate groups, these forces contribute to the stability of the G-quadruplex. Based on their x-ray data and the subsequently built model, acidic Na_2(5'-GMP) gel adopts a left-handed helical structure.[12]

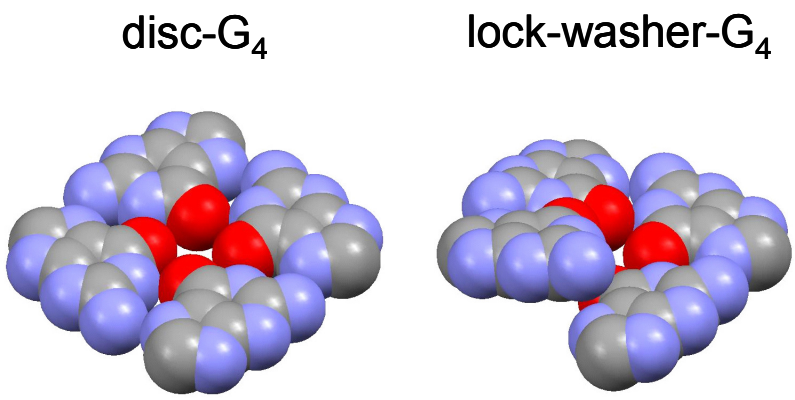

Figure 3-1. Illustration of planar G-quartet (left) as in neutral Na_2(5'-GMP) solution and acidic Na_2(3'-GMP) gel; (right) open-ended G-quartet as in acidic Na_2(5'-GMP) gel. Red = O, blue = N, and gray = C. Ribose rings and hydrogen atoms are omitted for clarity.

In 1964, Miles and Frazier studied 3'-GMP and 5'-GMP gels using solution-state IR, UV rotatory dispersion, and optical rotatory dispersion (ORD).[13] Although the Cotton effect from UV cannot distinguish the handedness of helical structures, they found that Na_2(5'-GMP) gel has a similar ORD profile as poly-inosine (poly-I) fibers, that were known to have right-handed helix conformation.[93] The possibility of acidic Na_2(5'-GMP) gel having a right-handed helical conformation was later supported by Homer and Mason (1966) when they observed a positive, parallel-polarized CD band at 244 nm for acidic 5'-GMP gel.[94]

Within the next ten years, Chantot et al. (1971) found that a large negative Cotton effect at around 260 nm is associated with an *anti* conformation of G residues.[14] They documented that Na_2(5'-GMP) forms gel between pH 2.2 and 5.8 only, and the atoms N7, O6, N1, and one hydrogen of the amino group are essential in forming a gel.

In 1972, Chantot took a different approach and quantified the thermodynamics properties of the self-associating 5'-GMP gel system, for which he found that 20.9 kJ/mol (5 kcal/mol) is involved in hydrogen-bonded base-base interactions, and 14.6-16.7 kJ/mol (3.5-4 kcal/mol) for stacking interactions. These results support the importance of the "vertical" hydrogen-bonds between G-quartets and other van der Waals interactions in forming a stable G-quadruplex structure.[95] In 1975, Sasisekharan and colleagues proposed a continuous, left-handed 15/4 helix (i.e., 15 monomers in 4 turns) for acidic Na_2(5'-GMP) gels using x-ray fiber diffraction.[46] Since then, it is commonly believed that this helix is left-handed and is composed of 5'-GMP monomers all in the C2'-*endo* sugar pucker conformation.[46] However, in their original paper, although the authors were quite certain with the continuous helix model, they were not sure about the sugar puckering and helical handedness.[46] Because the 5'-GMP helix is not constrained by covalent phosphodiester bonds, it is possible to have either right or left-handed helices. In this case, the helix was "arbitrarily assigned" as left-handed, assuming that monomers are of C2'-*endo* puckering. According to the same authors, it is also possible to have a right-handed helix if the sugar pucker conformation is C3'-*endo*. It is also clear from the study of Sasisekharan et al. that whether the acidic 5'-GMP helix is left-handed or right-handed depends critically on the sugar pucker conformation. Clearly the x-ray fiber diffraction data cannot provide enough information to distinguish between these two models. Furthermore, the authors noticed that the quality of the x-ray diffraction data "dramatically" improved after the salt concentration was reduced in the sample. This seems to suggest that this continuous helix is quite different from the G-quadruplex helix where salt ions were required.[46]

Since there is no one consistent and absolute structure proposed for acidic Na_2(5'-GMP) gel, we decided to further investigate this system using the knowledge gained from our studies of neutral 5'-GMP as described in Chapter 2. It is important to note that, 5'-GMP (pK_{a2} = 7.5) is doubly charged under neutral to slightly alkaline condition such as pH 8 while it is singly charged under acidic conditions (i.e., pH 5). The difference in the phosphate charge and the potential state for ion coordination are drastically different between neutral and acidic Na_2(5'-GMP) systems as evidenced by their physical states (see Figure 1-12, Chapter 1). In this chapter, we use solid-state ^{13}C NMR and FT-IR results to deduce the true helical structure of acidic Na_2(5'-GMP) gel.

3.2 Experimental

3.2.1 Sample preparation

The Na_2(5'-GMP) gel sample was prepared by acidifying 0.5 M Na_2(5'-GMP) aqueous solution to pH 5 using concentrated $HCl_{(aq)}$ or acetic acid. The pH is measured at room temperature using a calibrated Fisher Scientific Accumet Basic pH probe.

3.2.2 Solid-state 1D NMR

Solid-state ^{13}C NMR experiments were performed by Dr. Gang Wu on a Bruker Avance-600 spectrometer operating at 159.91 MHz for ^{13}C with the following parameters: sample spinning frequency, 11 kHz; cross polarization mixing time, 2 ms; ^{1}H decoupling, 80 kHz, recycle time, 10 s; 4866 transients. All ^{13}C chemical shifts were referenced to that of TMS. Solid-state ^{23}Na NMR experiments were performed on a Bruker Avance-500 spectrometer operating at 132.72 MHz for ^{23}Na nuclei with the

following parameters: sample spinning, 10 kHz, ^{1}H decoupling, 65 kHz; recycle time, 10 s; 64 transients. All ^{23}Na chemical shifts were referenced to that of 1.0 M $NaCl_{(aq)}$.

3.2.3 Solid-state 2D NMR

^{23}Na{^{31}P} rotational-echo double-resonance spectroscopy (REDOR) experiments were performed by Dr. Zhimin Yan and Dr. Yining Huang of the University of Western Ontario (London, ON). Using the original version of the pulse sequence,[96] this 2D solid-state experiment was performed on a Varian/Chemagnetics Infinity-plus 400 WB spectrometer operating at a magnetic field strength of 9.4 T. The ^{31}P and ^{23}Na resonance frequencies at this field strength are 161.72 and 105.67 MHz, respectively. All MAS spectra were acquired using a Varian/Chemagnetics T3 4-mm triple-tuned MAS probe. Typical RF power levels corresponded to 180° pulse lengths of 7.0 and 7.8 μs for ^{23}Na and ^{31}P nuclei, respectively. A total of 512 transients were accumulated for each REDOR measurement. The sample spinning rate was kept constant at 10,000 ± 2 Hz. The recycle delay was 0.2 s. The curve fitting was performed using the *Simulation Package for Solid-state NMR Spectroscopy* (SIMPSON, version 1.1.0) program.[97]

2D back-to-back double-quantum magic-angle-spinning experiments (BABA DQ-MAS) were performed by Dr. Eric Ye (National Ultrahigh Field NMR Facility for Solids, Ottawa, ON) on the Na_2(5'-GMP)/acetic acid gel at 21.1 T. The MAS experiment was performed using a 1.3 mm rotor spinning at an ultra-fast spinning rate (62.5 kHz) and the pulse program ggba.st2d. The ^{1}H NMR data were collected using a pulse of 1.5 μs (13.0 dB) and a relaxation delay of 8 s with 48 scans collected. The spectral width is

63,000 Hz on F1 dimension (DQ), and 50,000 Hz on F2 dimension (SQ). The final data matrix is 1024 (F2) vs. 160 (F1).

$^{31}P\{^{1}H\}$ heteronuclear correlation spectroscopy (HETCOR) experiments were also performed by Dr. Eric Ye at the 900 MHz solid-state facility in Ottawa. The sample Na_2(5'-GMP)/acetic acid gel was spinning at a rate of 33 kHz in a 2.5 mm rotor. The pulse program used is ggcphet.ye.2d, and the operating frequencies of ^{31}P and ^{1}H are 900.1 MHz and 364.4 MHz, respectively. The 180º pulses for ^{31}P are 2 μs (8.5 dB) and 2.5 μs (12 dB) for ^{1}H. A total of 128 scans were collected with a relaxation delay of 5 s. The spectrum dimension is 2048 (F2, ^{31}P) x 90 (F1, ^{1}H).

3.2.4 FT-IR

All FT-IR spectra were obtained from a Scimitar 1000 FT-IR (Varian) as KBr pellets with a resolution of 4 cm^{-1} from wavenumber 500 to 3000 cm^{-1}. A total of 10 scans were accumulated for each spectrum with a sensitivity of 1 cm^{-1}.

3.3 Results and Discussion

3.3.1 Determination of helix-orientation using ^{13}C NMR and FT-IR

Since fiber x-ray crystallographic data did not yield the information about the helical orientation of acidic Na_2(5'-GMP) gel, we decided to use solid-state ^{13}C NMR. From solid-state ^{13}C NMR spectra, it is relatively easy to obtain ^{13}C chemical shifts for the sugar carbons. As shown in Figure 3-2, the solid-state ^{13}C NMR spectrum is very simple, suggesting that the gel system is well ordered. The observed ^{13}C chemical shifts

for sugar carbons C1', C2', C3', C4', and C5' are 87.9, 76.3, 69.3, 82.2, and 62.8 ppm, respectively. These chemical shifts are similar to those obtained for the neutral Na_2(5'-GMP) sample. Harbison and coworkers recently established a general procedure in linking ^{13}C chemical shifts to sugar pucker conformation.[98] In particular, they studied solid-state ^{13}C NMR spectra of 25 nucleotides and nucleosides with known crystal structures from x-ray crystallography. The authors paired up the chemical shifts of the sugar carbons and noticed the distribution of two distinct groups when the ^{13}C chemical shifts were plotted against each other. They observed that these two groups correspond to either N or S puckering conformation. Furthermore, a plot of C1' versus C5' chemical shifts separates the N group into two clusters corresponding to the *gg* and *gt* configurations. To verify that the distribution of these distinct clusters was not due to chance, the researchers performed some canonical discrimination calculations, using linear combinations of variables that maximize the statistical discrimination between two populations (e.g., N or S, *gg* or *gt*). In this case, the authors found out that it is possible to use canonical calculations to verify chemical shift-structure relationship in terms of puckering and exocyclic angle γ, but not the glycosidic angle χ. This method was further verified by Ohlenschlager and colleagues who performed the same canonical discrimination calculations on approximately 400 RNA residues with complete sugar and backbone carbon data.[99] Two values were calculated using empirically derived constants and chemical shifts of the sugar carbon atoms (Equations 3-1, 3-2), and they were plotted against each other. The location of the residue's coordinate in this plot along with a preset limit for these values from experimental data allowed the prediction of sugar puckering

and exocyclic torsion angle to be obtained with 93-94% accuracy.[99] The authors also pointed out that different limits must be used for on purine and pyrimidine residues.

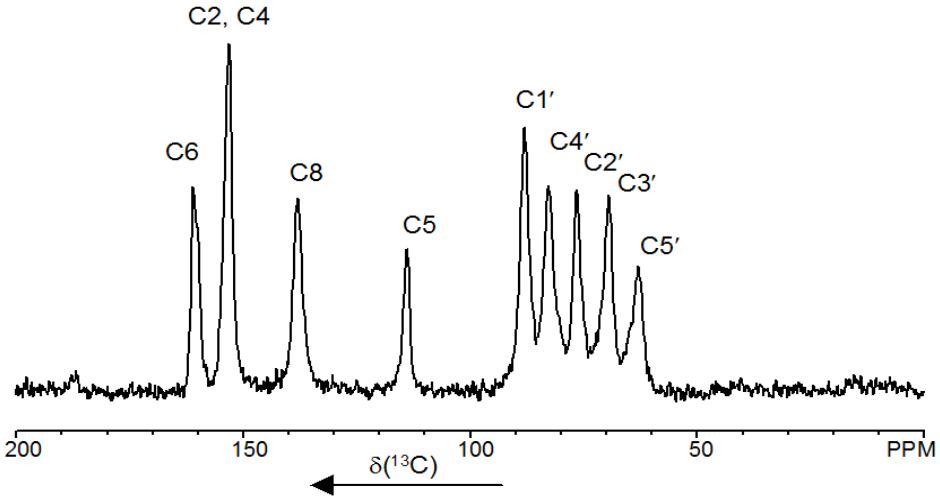

Figure 3-2. Solid-state ^{13}C CP-MAS spectrum of acidic Na_2(5'-GMP)/HCl gel at 14.1 T and spinning at 11 kHz.

Equation 3-1 $$can1 = 0.179\delta_{C1'} - 0.225\delta_{C4'} - 0.0585\delta_{C5'}$$

Equation 3-2 $$can2 = -0.0605\delta_{(C2'+C3')} - 0.0556\delta_{C4'} - 0.0524\delta_{C5'}$$

To test the validity of this approach for 5'-GMP compounds, we first examine Na_2(5'-GMP) heptahydrate, for which the sugar is known to adopt only C2'-*endo* conformation[100], and the Na_2(5'-GMP) sample at neutral pH for which both C2'-*endo* and C3'-*endo* conformations are present. The final *can*1 and *can*2 values for Na_2(5'-GMP)·$7H_2O$ are –7.7 and –17.5, respectively. As seen in Figure 3-3, these values clearly reside in the C2'-*endo* region. The *can*1 and *can*2 values for neutral Na_2(5'-GMP) are –

8.0 and –17.1 (C2'-*endo*) and –6.0 and –16.5 (C3'-*endo*), respectively. They also correspond to the correct puckering regions in the same plot. In general, we conclude that ^{13}C chemical shifts allow a reliable determination of the sugar puckering in RNA systems. Using the same equations, the *can*1 and *can*2 values for acidic Na_2(5'-GMP) gel are –6.6 and –16.8, respectively, and this reveals that Na_2(5'-GMP) at low pH indeed has a C3'-*endo* puckering instead of C2'-*endo* which was suggested by Sasisekharan et al.[46] Moreover, the fact that can1 > –6.77 and can2 > –16.82 for acidic Na_2(5'-GMP) gel strongly suggests that the sugar pucker conformation is C3'-*endo* with the exocyclic γ-torsion angle being in *gg* conformation.[99]

Another piece of evidence comes from the FT-IR spectrum. Tajmir-Riahi[101] established that the IR signature bands for C3'-*endo* and C2'-*endo* sugars appear at ranges 800-806 and 817-824 cm^{-1}, respectively. As shown in Figure 3-4, the FT-IR spectrum of acidic Na_2(5'-GMP) gel contains a signature band at 800 cm^{-1}. Therefore, contrary to the long-believed model, this finding leads to the conclusion that the continuous helix of acidic Na_2(5'-GMP) gel is composed entirely of C3'-*endo* monomers and is indeed right-handed instead of left-handed. Combining this new structural feature with the helical parameters of Sasisekharan et al.,[46] we were able to build a right-handed 15/4 helix model as illustrated in Figure 3-5. (Atomic coordinates are listed in Appendix II).

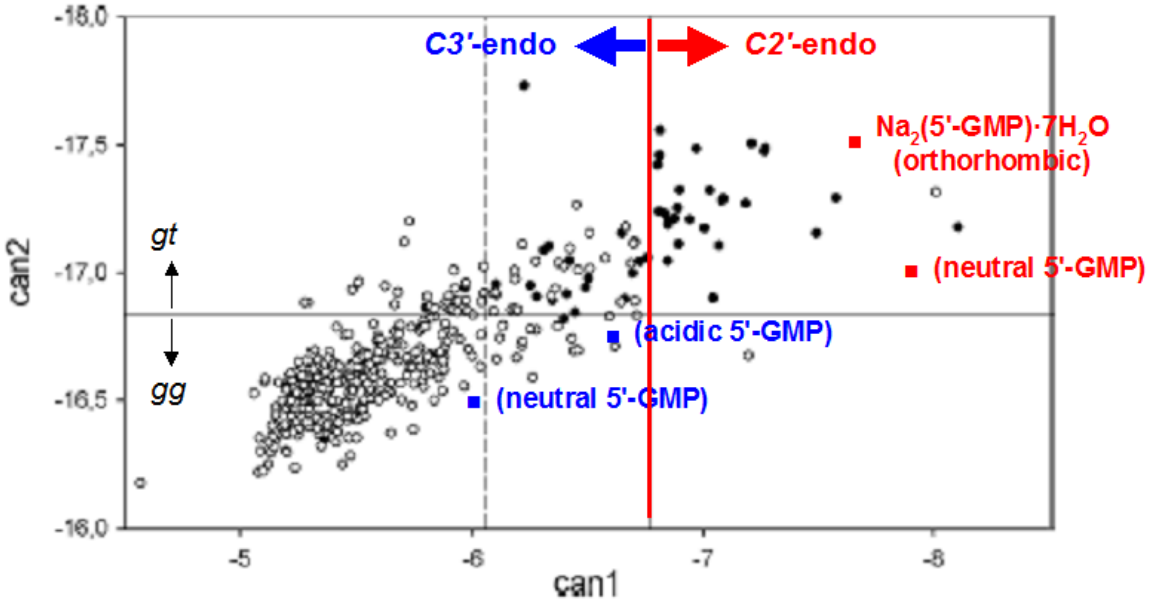

Figure 3-3. Canonical coordinate prediction plot for RNA ribose C2'/C3'-*endo* puckering adopted from Olenschlager et al.[99] The white and black dots represent RNA residues with known C3'-*endo* and C2'-*endo* structures, respectively. The dashed vertical line is the threshold proposed for pyrimidine, and the solid line for purines. The horizontal line separates the *gg* and *gt* conformations. (Plot adopted from Ref. 97).

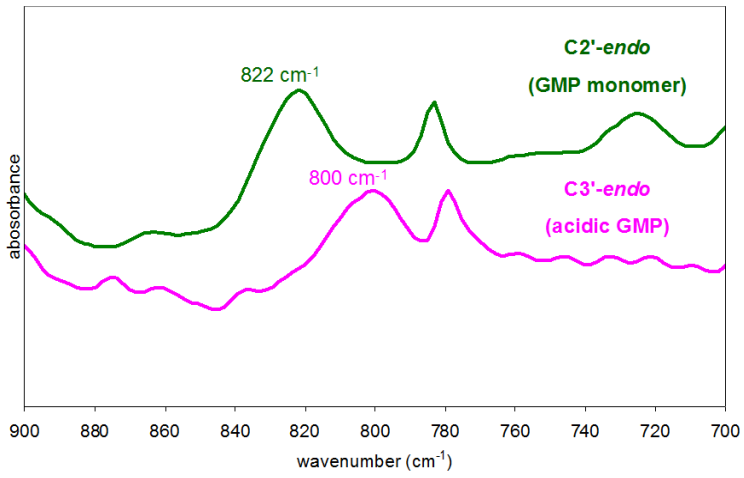

Figure 3-4. FT-IR spectra of Na_2(5'-GMP) monomers and dried Na_2(5'-GMP)/HCl acidic gel using KBr disc.

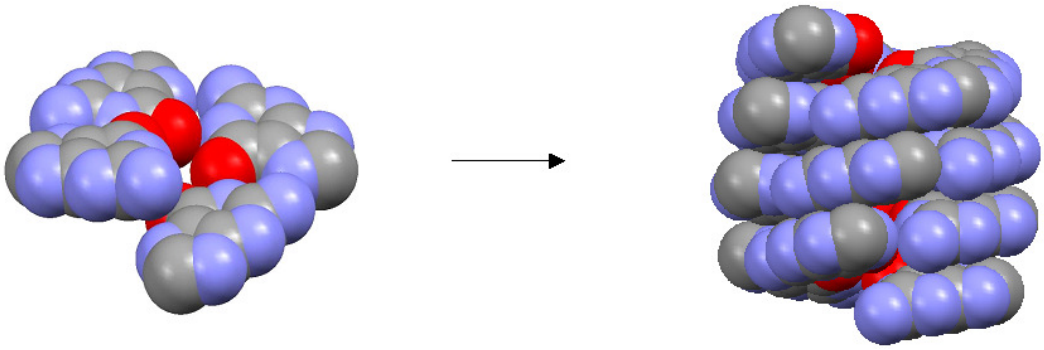

Figure 3-5. Continuous right-handed helix model of acidic Na_2(5'-GMP) G-quadruplex constructed using x-ray fiber diffraction data.[46] Red = O, blue = N, gray = C. Ribose rings and hydrogen atoms are omitted for clarity.

3.3.2 A unique G-quadruplex feature: absence of channel ions

Once the helix orientation is determined, the next step is to examine the weak forces that drive 5'-GMP self-aggregation. Being the most crucial component in G-quadruplex formation, ion-carbonyl interaction at the channel site and ion-phosphate binding at the surface site might behave differently in acidic Na_2(5'-GMP) gels compared to those observed in neutral Na_2(5'-GMP) solution. To further investigate how Na^+ ions are bound in the acidic 5'-GMP structure, we recorded solid-state ^{23}Na NMR spectra for the acidic Na_2(5'-GMP) gel. As seen from Figure 3-6, only two ^{23}Na NMR signals are observed for acidic Na_2(5'-GMP) gel. The sharp signal at 7.2 ppm is due to excessive NaCl in the sample. The other signal is centered at –5.0 ppm, typical of phosphate-bound Na^+ ions.[61] Indeed, this signal is very similar to that of the phosphate-bound Na^+ ions observed for a solid 5'-GMP sample prepared from neutral solution as described in Chapter 2.

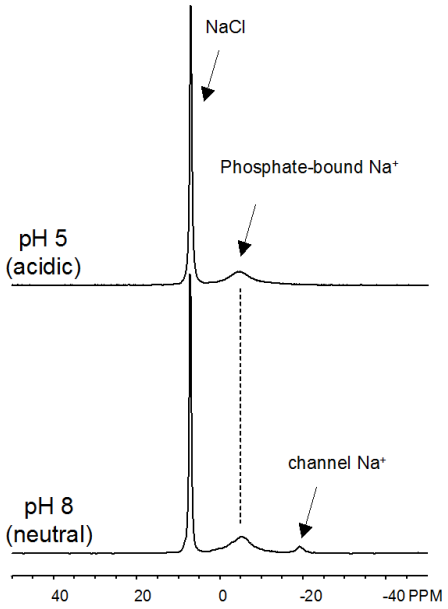

Figure 3-6. Solid-state ^{23}Na NMR spectra of (top) acidic and (bottom) neutral Na_2(5'-GMP).

According to the x-ray model, where phosphate groups are 5.2 Å apart (P-P distance),[46] it is possible that a Na^+ ion bridges the phosphate groups to reduce repulsion. To determine if the solid-state ^{23}Na signal at –5 ppm in acidic GMP is due to phosphate-bound Na^+ ions, a ^{23}Na{^{31}P} rotational-echo double resonance (REDOR) experiment was performed. REDOR, first introduced by Gullion and Schaefer on nuclei ^{1}H and ^{31}C,[102] is a high resolution solid-state NMR experiment for measurement of inter-nuclear distances between heteronuclei (i.e., ^{23}Na and ^{31}P in this case). Typically, a normalized REDOR difference signal is plotted versus the rotor periods or dephasing time. Then the inter-atomic distance is extracted from the slope using a theoretical curve. A steep slope indicates a short distance between the two heteronuclei. Figure 3-7 shows the ^{23}Na{^{31}P}REDOR plot obtained for both neutral and acidic dried Na_2(5'-GMP) systems, as well as a reference sample, the A-form DNA from calf thymus. In A-form DNA, the

only possible binding site for Na^+ is on the singly charged phosphate group. As shown in Figure 3-7, the slopes at the small dephasing times are similar among the three systems. Assuming that the ^{23}Na and ^{31}P nuclei can be treated as an isolated two-spin system, the calculated inter-nuclear distance obtained from REDOR for dried acidic Na_2(5'-GMP) gel is 3.5 Å. This short ^{23}Na-^{31}P distance indicates that they are in the first-coordination shell of each other, hence confirming the direct binding of ^{23}Na ions at –5 ppm to the phosphate sites in acidic Na_2(5'-GMP). The binding of ^{23}Na to ^{31}P is only observable in the solid phase in this case because Na^+ ions undergo rapid exchange in solution, hence it is not possible to detect the direct binding of ^{23}Na to ^{31}P in liquid phase.

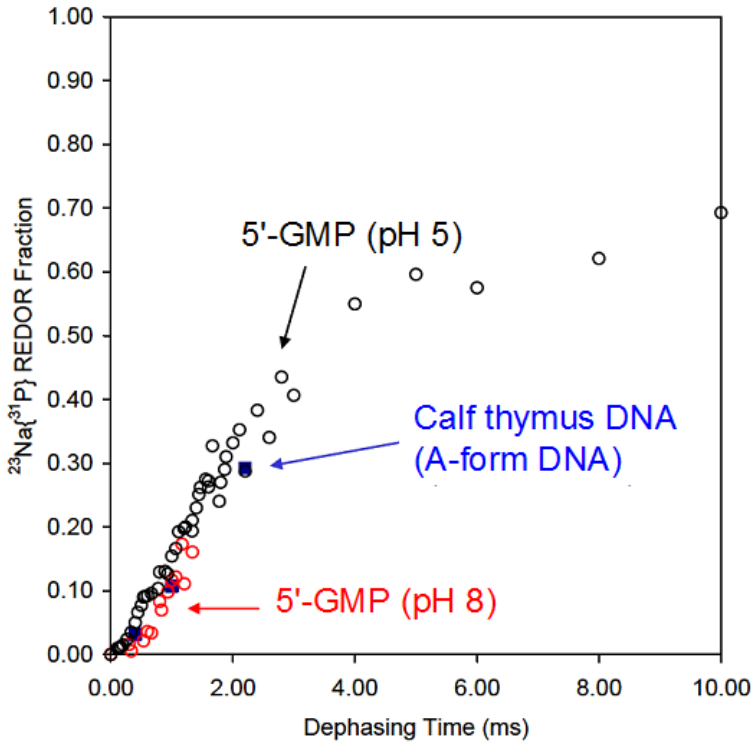

Figure 3-7. $^{23}Na\{^{31}P\}$ REDOR results of the reference (A-form DNA) and the two types of Na_2(5'-GMP) aggregates at various pH conditions.

The ^{23}Na NMR spectrum of acidic Na_2(5'-GMP) gel shown in Figure 3-6 also reveals that the established spectral signature for Na^+ ions residing inside a G-quadruplex channel at −18 ppm is missing.[61,103] This observation immediately suggests that there are no Na^+ ions inside the central channel of the continuous helix formed by 5'-GMP under slightly acidic conditions. This aspect of the helix is totally unexpected, because there are very few G-quadruplex systems without a channel cation. However we can try to understand it using a structural model. As shown in Figure 3-8, when a disc-like G_4 is twisted into a washer-like G_4, the size of the central cavity surrounded by carbonyl oxygen atoms is significantly reduced. As a result, a Na^+ ion can no longer fit into this cavity.

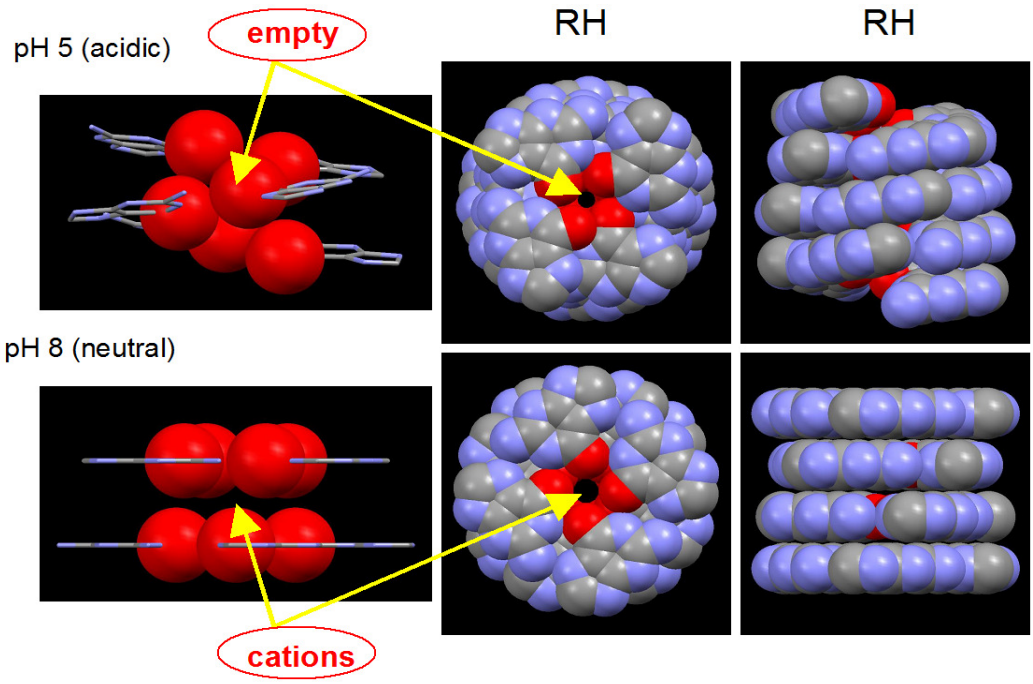

Figure 3-8. Na_2(5'-GMP) G-quadruplexes formed under different pH conditions. A planar, tetrameric stacking under neutral pH (bottom), and a continuous, lock-washer-like helix under acidic pH (top). Helix senses are both right-handed (RH).

3.3.3 Phosphate-amino hydrogen-bonds

At this point, it is worth comparing the acidic 5'-GMP helix with that determined for 5'-GMP under neutral or slightly basic conditions (Chapter 2).[90] Since the phosphate group of 5'-GMP has a pK_{a2} of 7.5, it is doubly charged at pH 8 but only singly charged at pH 5. As we mentioned in Chapter 2, phosphate groups in the 5'-GMP helix formed at pH 8 are possibly bridged by Na^+ ions. For the 5'-GMP helix formed at pH 5, singly charged phosphate groups form a continuous hydrogen-bonded chain along the helical "strand" (i.e., $\cdots$HO–P–$O^-\cdots$HO–P–$O^-\cdots$). Because the repulsion between singly charged phosphate groups is much weaker than that between doubly charged phosphates, the P$\cdots$P distance is significantly shorter in the acidic 5'-GMP helix (5.2 Å) than in the neutral 5'-GMP helix (6.7 and 7.2 Å).

Another unique feature in the acidic 5'-GMP helix is the formation of a phosphate-base hydrogen bond. In particular, as Sasisekharan et al.[46] also noted, the i^{th} phosphate group can be hydrogen-boned to the exocyclic amino group of the $(i+3)^{th}$ guanine base (i.e., N–H$\cdots$O=P, Figure 3-9). In our model, the N$\cdots$O distance is ca. 2.82 Å. We postulate that the weaker repulsing forces between singly charged phosphate groups and the formation of this hydrogen bond are largely responsible for the helical formation of 5′-GMP at pH 5. To verify if these hydrogen-bonds are consistent with a right-handed helix model, we performed 2D solid-state back-to-back double-quantum magic-angle-spinning (BABA DQ-MAS) ^{1}H NMR and ^{31}P{^{1}H} HETCOR NMR experiments.

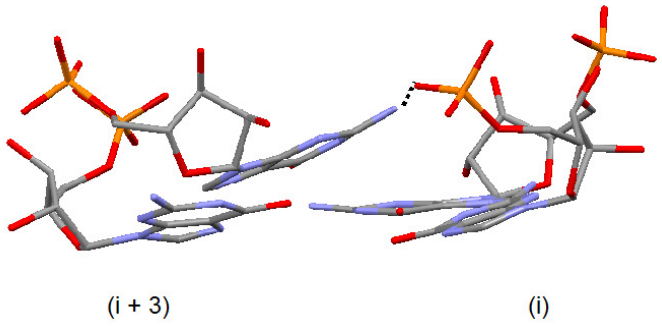

Figure 3-9. Scheme of the phosphate-base hydrogen bond between phosphate (i) and N^2H_B (i+3) three monomers away in the right-handed, continuous helix model of acidic Na_2(5'-GMP).

The 2D BABA DQ-MAS experiment is often used in determining hydrogen bonding networks, such as self-assembling C^G rosette nanotubes.[104] The experiment utilizes the creation of the ^{1}H-^{1}H double quantum coherence via the homonuclear dipole-dipole couplings. As a result, DQ signals can be used directly to infer spatial distances between two protons. Like spins (AA) give rise to the so-called "diagonal" spins located at [ν_A, (ν_A + ν_A)], while unlike spins (AX) have "cross peaks" at both [ν_A, (ν_A + ν_X)] and [ν_X, (ν_A + ν_X)] locations. The unique feature of BABA DQ spectra is that the resonance frequency on the DQ dimension is the sum of two single-quantum frequencies of the two spins involved, as illustrated in Figure 3-10. Hence, a 2D BABA spectrum can be read as a regular NOESY spectrum except the appearance of "cross peaks" is slightly different.

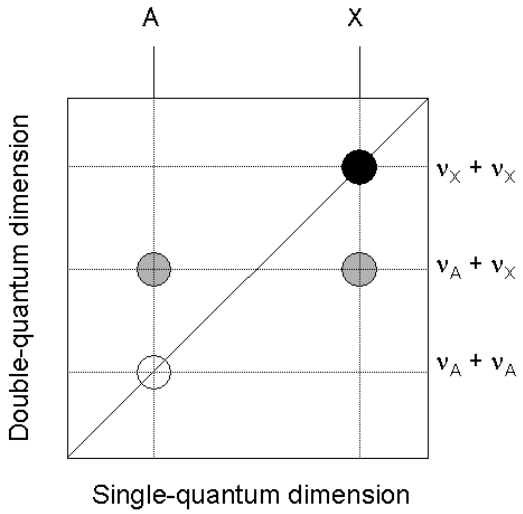

Figure 3-10. A 2D double-quantum spectrum. Protons A and X have different frequency values and the identity peaks are located at ($\nu_A + \nu_A$) and ($\nu_X + \nu_X$), respectively. Cross peaks between them are located at ($\nu_A + \nu_X$).

The 1D proton MAS spectrum of Na_2(5'-GMP)/acetic acid gel spinning at 62.5 kHz and 21.14 T is shown in Figure 3-11. The 1D ^{1}H spectrum exhibits reasonably high resolution to allow detection of several key proton signals. From the 2D BABA experiment, also shown in Figure 3-11, several ^{1}H-^{1}H dipolar interactions can be deduced. First, intra-molecular interactions N^2H_A-N^1H and H8-ribose are observed (blue bars). The high frequency locations of both N^2H_A and N^1H suggest their involvement in hydrogen-bonding. The H8-ribose cross peak also indicates that the 5'-GMP molecules are in *anti* conformation because H8 would not have any strong dipole interactions with the ribose protons if the sugars were in a *syn* conformation. Secondly, the signature inter-molecular cross peak between N^2H_A and H8 (red bar) confirms the G-quartet formation (Figure 3-11, inset).

As mentioned earlier, N^2H_A and N^2H_B from the same amino group have very strong dipole interaction, and thus a very intense cross peak is observed in the BABA spectrum. Using this relationship, N^2H_B is assigned at 8.3 ppm on the single-quantum axis, and it has a larger chemical shift than expected. For example, in Chapter 2 we learned that the non-hydrogen bonded N^2H_B signal appears near the region of 4-5 ppm. The unusual high frequency shift of the N^2H_B signal indicates that it is now involved in a hydrogen bond environment, possibly in the N–H···O=P hydrogen bond as first proposed by Sasisekharan et al.[46] Unfortunately, the resolution of the 2D BABA spectrum is not high enough to allow a direct observation of the hydrogen bonds between the phosphate group and the same amino proton (N^2-H_B···O=P-OH) three monomers away in the helix. The dipole interaction between these two protons could be too small for detection since the distance between them is 4.2 Å, while the distances between the above proton pairs that give strong cross peaks range from 1.6 to 3.8 Å. In this case, we turn to another experiment, $^{31}P\{^1H\}$ HETCOR, where we can observe the direct dipolar coupling of proton and phosphorous nuclei in the phosphate group.

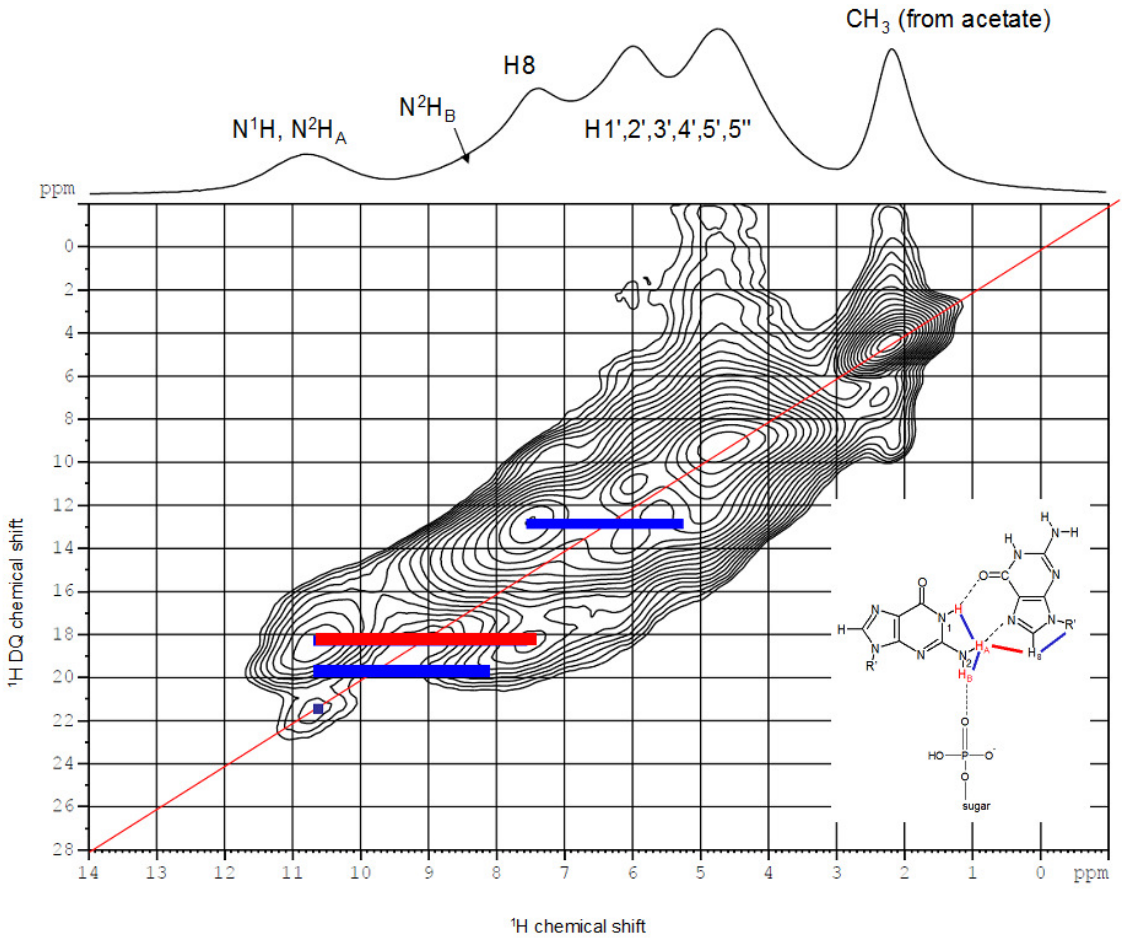

Figure 3-11. 2D BABA DQ-MAS spectrum of dried acidic Na_2(5'-GMP)/acetic acid gel 21.1 T and very fast spinning (62.5 kHz) at room temperature. The blue bars represent intra-molecular dipole interactions, and the red bar represents inter-molecular dipolar interactions. The scheme of these dipolar couplings between two 5'-GMP molecules in a G-quartet is shown in the insert.

$^{31}P\{^{1}H\}$ HETCOR is a 2D heteronuclear NMR experiment similar to HMQC where direct interaction via dipolar-coupling are detected. However, unlike HMQC, direct detection is used in HETCOR since ^{31}P has a natural abundance of 100%. As shown in Figure 3-12, the relatively sharp signal at 2 ppm on the F2 dimension (^{31}P)

represents the single ^{31}P environment from the phosphate group. In the F1 dimension (^{1}H), we observe cross peaks forming at 4.7, 8.3, and 10.5 ppm, and their assignments are shown in Table 3-1.

Similar to other experiments that detect dipolar coupling, the time allowed for the two nuclei to "communicate" is crucial for observation of such relationship. In this case, a contact time of 2 ms used in the HETCOR experiment allowed us to observe several intra and inter-molecular ^{31}P-^{1}H bonds. First of all, the strong cross peak at 4.7 ppm (F2 dimension) represent the intra-molecular P/H5' and P/H5" bonds. The next intramolecular interaction would be at 10.5 ppm on the F1 dimension where ^{31}P of the phosphate is binding to its own proton. Most importantly, the cross peak at 8.3 ppm ($N^{2}H_{B}$) confirmed the $N–H_{(i+3)}\cdots O=P_{(i)}$ bonding suggested by Sasisekharan[46] but was not observed directly before (Figure 3-9).

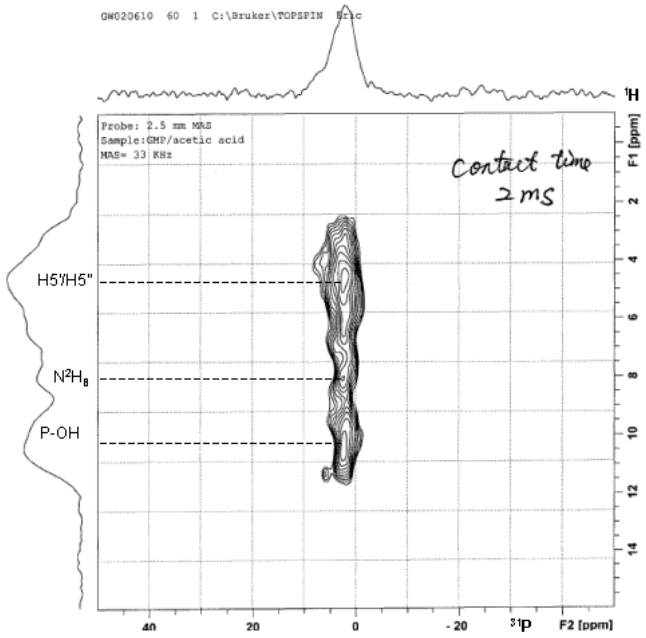

Figure 3-12. 2D $^{31}P\{^{1}H\}$ HETCOR spectrum of dried Na_2(5'-GMP)/acetic acid gel in a 2.5 mm MAS probe, and spinning at 33 kHz and a contact time of 2 ms.

Table 3-1. $^{31}P\{^{1}H\}$ HETCOR spectrum analysis. The ^{31}P-^{1}H distances are obtained from the right-handed model built using x-ray data from Sasisekharan et al.[46]

Cross peak on ^{1}H dimension (ppm)	Proton assignment	^{31}P-^{1}H distance (Å)	Intra/Inter-molecule
10.5	P-OH	2.00	intra
4.7	H5' *	2.75	intra
4.7	H5" *	2.71	intra
8.3	$N^2H_{B(i+3)}$	3.16	inter

* stereospecific assignment of *pro*S, *pro*R protons is not performed.

3.4 Conclusion

We have used modern 1D/2D solid-state NMR experiments, as well as FT-IR, and canonical calculations to prove that the acidic Na_2(5'-GMP) gel forms a right-handed helical structure composed of only C3'-*endo* monomers. This is in contrast to the long-believed C2'-*endo*/left-handed model in the literature. We also observed the absence of Na^+ ions inside the channel site due to a smaller cavity in the lock-washer-like helix as opposed to the planar, stacking tetramer model. The major forces that contribute to the acidic Na_2(5'-GMP) self-assembly include base-base hydrogen-bonds, Na^+-phosphate binding, and hydrogen-bonds between amino and phosphate groups among layers of tilted G-quartets. The gel formation of Na_2(5'-GMP) under the acidic condition can be attributed to these forces accentuated four times around the helix, as well as smaller repulsion forces between phosphate groups. This part of the Na_2(5'-GMP) study provides information on nucleic acid self-assembly under acidic pH and low salt conditions, which could be useful in designing other supramolecular structures under similar conditions.

Chapter 4

Self-assembled G-quadruplex structures of disodium guanosine 5'-thiomonophosphate: the role of cation bridging

4.1 Introduction

Guanosine 5'-thiomonophosphate, or 5'-GSMP, differs from 5'-GMP by substituting the oxygen atom at the 5' position with a sulfur atom (Figure 4-1). This molecule has a longer O-P-S5'-C5' bond compared to the O-P-O5'-C5' bond in 5'-GMP (Figure 4-1), and this causes the phosphate group to extend away from the nucleoside. Because there are no other structural differences at the guanine base and ribose ring, 5'-GSMP is expected to form G-quadruplexes in the presence of Na^+ ions, in a similar fashion as 5'-GMP.[105] If this is true, the elongated $^-$O-P-S5'-C5' bond will allow additional flexibility that will enable them to optimize their relative locations as the doubly charged phosphate groups exhibit strong repulsion to each other. (Figure 4-2). This repulsion force can often be offset by a positively charged cation, such as Na^+. This kind of cation-bridging system between two phosphate groups and a cation is identical to that discussed in the 5'-GMP G-quadruplex system (Chapter 2). It was documented in Chapter 3 that cations binding to the phosphate groups are discovered using both solution and solid-state ^{23}Na-NMR in G-quadruplexes systems.[53,55,61,63,103,105,106,107] There is also evidence that different ions can compete for the phosphate-binding site (Figure 4-2). However, there are no direct studies on the phosphate groups regarding cation-bridging from 5'-GMP's point of view. Fortunately, the molecule 5'-GSMP provides the opportunity to study this site directly. In this chapter, we investigate the self-assembly of

5'-GSMP using both solution- and solid-state NMR experiments, quantum calculations, and other methods.

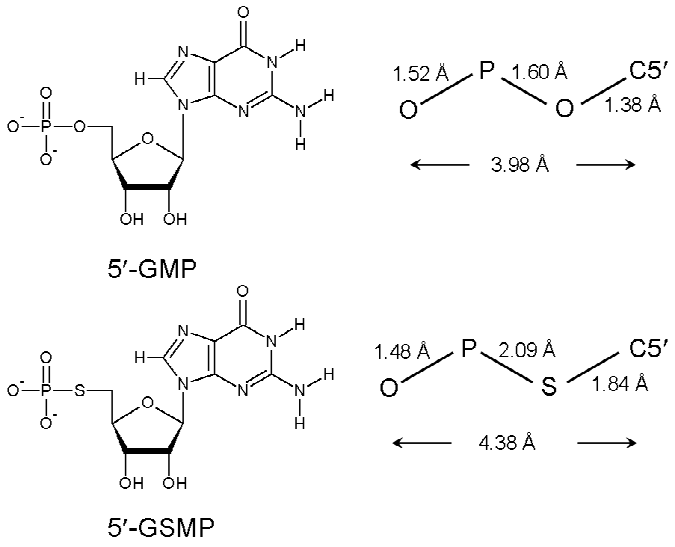

Figure 4-1. Structures of (left) 5'-GMP and 5'-GSMP molecules, and (right) the different bond lengths shown in detail.

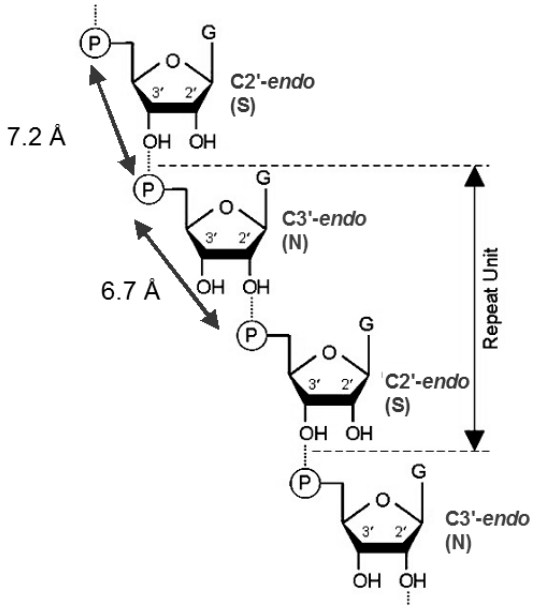

Figure 4-2. Illustration of short distances between phosphate groups in 5'-GMP G-quadruplex.

4.2 Experimental

4.2.1 Synthesis and solution sample preparation

Disodium 5'-deoxy-5'-thioguanosine 5'-monophosphate, Na_2(5'-GSMP), $C_{10}N_5O_7SPNa_2H_{12}$ (molecular weight 423.247 g/mol) was a gift from Dr. David Hodgson (Durham University, United Kingdom) and was synthesized using a modified method from the literature procedure.[108] To prepare a 0.17 M Na_2(5'-GSMP) solution for NMR experiments, 70.6 mg was dissolved in 1.0 mL D_2O. Because a small amount of NaOH was used in the synthesis of 5'-GSMP, the pH of the solution was initially ~10.5. The solution was brought to neutral pH 8.0 using a minute amount of concentrated $HCl_{(aq)}$. A clear viscous solution was observed, which turns to a gel upon standing at room temperature for several hours. Solution-state ^{1}H NMR experiments were performed at various temperatures on these wet gel samples. The pK_a value of the thiophosphoryl group was determined using solution-state ^{31}P NMR. A series of diluted solutions were also prepared including 10 mM, 25 mM, 50 mM, and 100 mM for aggregation process studies.

4.2.2 Solution-state NMR

All solution-state NMR spectra were recorded on a Bruker Avance 600 MHz spectrometer (14.1 T), including both 1D and 2D experiments. All chemical shifts were reported in parts per million (ppm). For ^{1}H experiments, the ^{1}H 90° and 180° pulse widths at a pulse power of 0.0 dB were 13.0 and 26.0 μs, respectively. The ^{31}P 180° pulse was 50 μs at 0.0 dB, and 85% $H_3PO_{4(aq)}$ was used as an external ^{31}P chemical shift

reference. All pulse sequences were available in the program Bruker Xwin NMR Version 3.5. Experimental temperatures were carefully controlled with a Bruker BT-3000 unit. Diffusion NMR experiments were carried out for 50 mM Na_2(5'-GSMP) in D_2O at 298 K. The pulse sequence of longitudinal eddy current delay with bipolar-gradient pulse (LEDBPGP2s) was employed. The pulse field gradient duration (δ) was 1.5 ms, and the variable gradient strength (G) was 5.655 mT/m. The diffusion period (Δ) was 75 ms, and a total of 8192 experiments with 8 scans were collected for each of the 16 increment steps with a recycle delay of 5.0 s. The eddy current delay (t_w) employed was 5 ms, and the gradient recovery delay was set at 9.2 ms. Calibration of the field gradient strength was performed by measuring the value of translational diffusion coefficient (D_t) for the residual ^{1}H signal in D_2O (99.99% 2H atom), where D_t = 1.90 x 10^{-9} m^2/s.[68] The total spectral width was 6009.6 Hz and a line-broadening of 2 Hz was employed in data processing.

4.2.3 Solid-state NMR

The same 0.17 M gel was dried under $N_{2(g)}$ environment for solid-state ^{13}C , ^{23}Na, ^{31}P NMR experiments, as well as FT-IR and powder x-ray analyses. Solid-state NMR experiments were performed by Dr. Gang Wu on Bruker Avance-500 and Avance-600 NMR spectrometers. Chemical shifts for ^{13}C, ^{23}Na, ^{31}P were referenced to the signals of TMS, 1.0 M $Na^+_{(aq)}$, and 85% $H_3PO_{4(aq)}$, respectively. The detail sample spinning rates in Magic Angle Spinning (MAS) experiments are listed in figure captions.

4.2.4 FT-IR and powder x-ray diffraction

All FT-IR spectra were obtained from a Scimitar 1000 FT-IR (Varian) as KBr pellets with a resolution of 4 cm^{-1} from wavenumber 500 to 3000 cm^{-1}. A total of 10 scans were accumulated for each spectrum with a sensitivity (digital resolution) of 1 cm^{-1}. All XRD spectra were obtained on a Philips X'Pert Pro Multi Purpose Diffractometer (2002) using Ni-filtered Cu K_α 1,2 radiation (λ_1 = 1.5406 Å, λ_2 = 1.5444 Å), a fixed divergence slit width of 0.5°, 0.02 Radian soller slit, 15 mm mask, 2 s revolution and 40 s count time. Samples were prepared on flat borosilicate glass discs and the diffraction data were collected from 10° to 70° using an X'pert X'celerator high speed detector for a total scan time per sample of approximately 20 min. Data were processed on a Pentium PC using PanAlytical X'pert HighScore for Windows XP.

4.2.5 Quantum chemical calculations

Quantum chemical calculations were performed using Gaussian 03 suite of programs[87] on a SunFire 6800 symmetric multiprocessor system. Each of the four nodes is equipped with 24 × 1.05 GHz (8 MB E-Cache) UltraSPARC-III processor and 96 GB of RAM. Shielding calculations were performed using the GIAO method as implemented in Gaussian 03. Basis sets of cc-pVTZ and 6-31G(d) were used for Na and other atoms, respectively. The computed absolute shielding constant (σ) was converted to the chemical shift scale (δ) using $\delta = \sigma_{ref} - \sigma$, where σ_{ref} is the absolute shielding constant for the reference sample. In this study, $\sigma_{ref}(^{13}C)$ = 185.4 ppm, $\sigma_{ref}(^{23}Na)$ = 574.6 ppm and $\sigma_{ref}(^{31}P)$ = 317.0 ppm were used.

4.2.6 Scanning Electron Microscopy (SEM)

A GSMP sample with a concentration of 10 $mM_{(aq)}$ was freshly prepared and transported to an aluminum stud using a Pasteur pipette and the droplet of solution was left to dry in a closed environment for one day prior to experimentation. The aluminum stud was then placed in a vacuum environment (purged twice with Ar) at 25 mTorr, and was plated with gold at 10 mAmp for 6 min using a Technics Hummer V voltage generator. The sample was then analyzed immediately with a Hitachi S-2300 SEM unit at 20 kV and images were captured using the computer program URSA200.

4.3 Results and Discussion

4.3.1 Solution-state experiments

First a very diluted Na_2(5'-GSMP) sample was prepared and studied using solution-state ^{1}H NMR. Figure 4-3 shows a 25 mM Na_2(5'-GSMP) solution at pH 10.5 where only monomeric 5'-GSMP molecules are present (the pK_{a1} of guanine at N^{1}H is ~9.0,[109] and N^{1}H is required in Hoogsteen hydrogen-bonding of a G-quartet, hence G-quartets do not form at pH > 9.0). The proton NMR signal assignments for 5'-GSMP monomers are shown in Figure 4-3, and the small amount of impurities (below 3 ppm) are thiol groups from decomposition. Next, the pH of the 5'-GMSP sample was brought down from 10.5 to a slightly basic 8.0 using a minute amount of hydrochloric acid, and the titration process was monitored using ^{31}P NMR. Since phosphorus-31 has a natural abundance of 100% and receptivity is ~38 times more sensitive compared to ^{13}C-NMR, ^{31}P-NMR is a good candidate in directly measuring the phosphate group compared to C5'. As shown in Figure 4-4, the ^{31}P chemical shifts are plotted against the acidity of the 25

mM 5'-GSMP solution from pH 10.5 to 2.0. These ^{31}P chemical shift data points were then fitted using a sigmoid curve with the following equation:

Equation 4-1 $$X = [X_b + X_a(10^{n(pK_a-pH)})]/[1 + 10^{n(pK_a-pH)}]$$

where X = observed chemical shift, X_b = chemical shift of base, X_a = chemical shift of acid, n = 1, pK_a = fitting parameter, and pH = range of pH observed. The midpoint between the protonation states, i.e., pH 5.1 ± 0.2, is determined to be the pK_{a2} of 5'-GSMP. Therefore, 5'-GSMP carries a doubly negative charge between pH 5.1 and 9.0, and any pH within this range would give 5'-GSMP the same protonation state on the phosphate group as 5'-GMP at pH 8 when the latter forms G-quadruplex.

Figure 4-5 shows a comparison of the proton NMR spectra of Na_2(5'-GMP) and Na_2(5'-GSMP), both at 0.1 M concentration and pH 8.0. It is clear that 5'-GSMP monomers have smaller intensities compared with 5'-GMP monomer signals due to aggregate formation. Therefore, we know that 5'-GSMP molecules are forming large aggregates that give broad signals beyond detection due to slow tumbling even at such a low concentration.

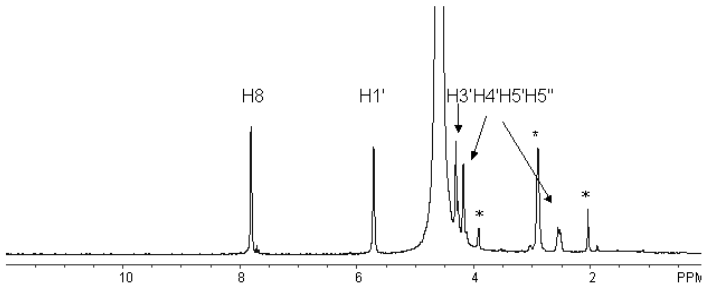

Figure 4-3. Proton NMR of 25 mM Na_2(5'-GSMP) in D_2O at pH 10.5 and 298 K. The impurities are marked with asterisks.

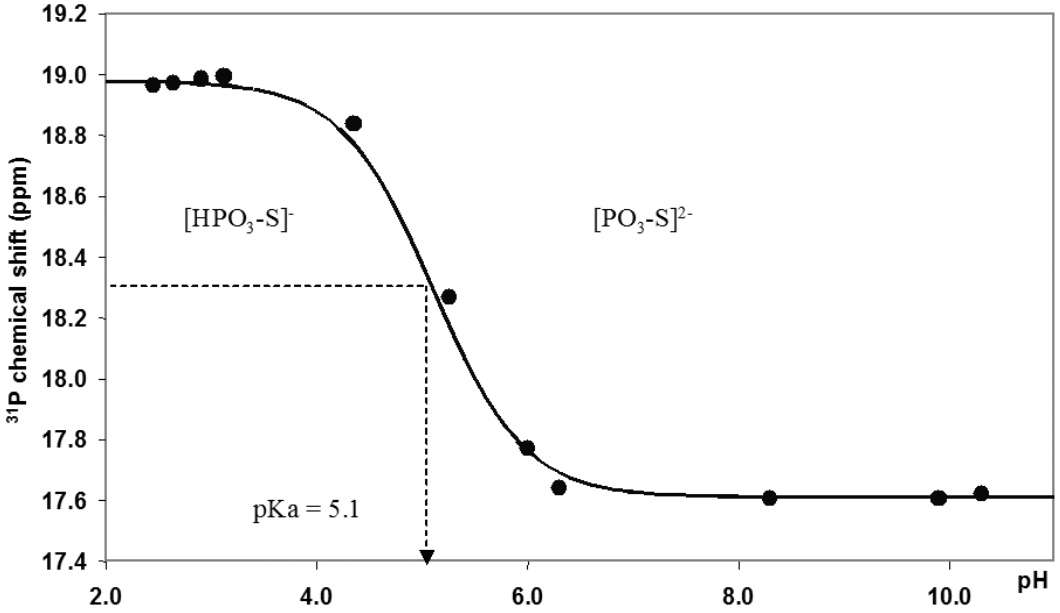

Figure 4-4. ^{31}P NMR titration curve of a diluted Na_2(5'-GSMP) solution at 298 K.

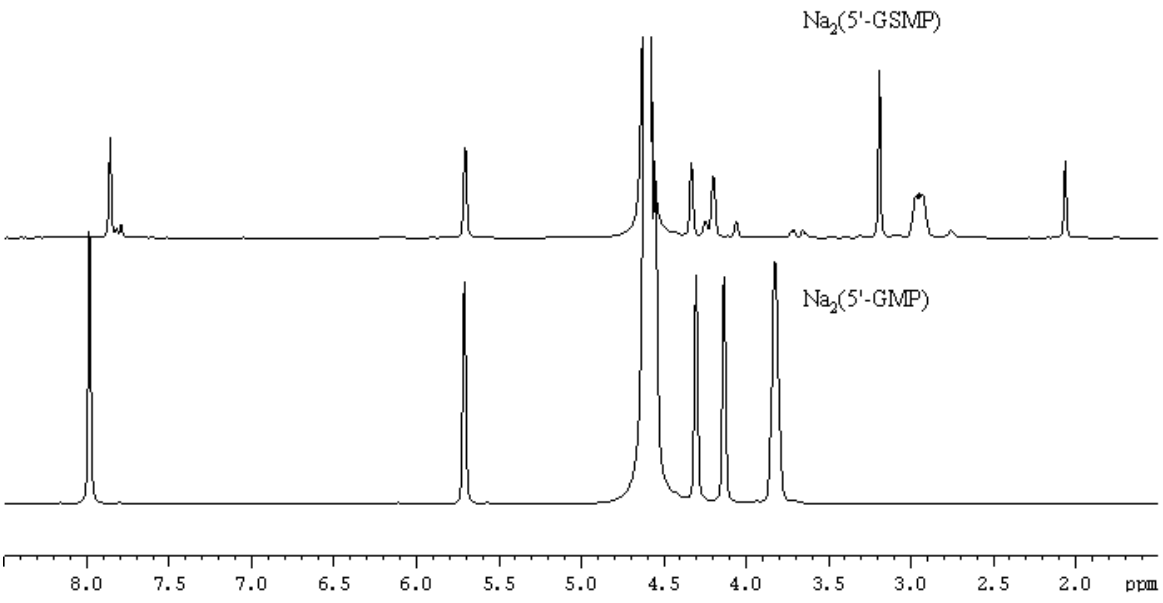

Figure 4-5. Proton NMR spectra of Na_2(5'-GMP) and Na_2(5'-GSMP) at pH 8.0 and 298 K in D_2O. Both solutions have a concentration of 0.1 M. Monomer signals are shown while aggregate signals are too broad to be detected.

With this information in hand, we decided to study neutral 5'-GSMP at a lower concentration (below 0.1 M) using ^{1}H-NMR, hoping that we can catch a glimpse of the aggregate formation, such as the four H8 signals unique to the 5'-GMP G-quadruplex. In this case, we have samples of 25, 50 mM at various temperatures, and 100 mM is used as a reference of aggregate formation. As shown in Figure 4-6, there are no G-quartet H8 signals observed in the ^{1}H NMR spectrum, but only the monomer signals at various concentrations and temperatures. Signal intensities increase as concentration increases, and the monomer signal intensities decrease as the temperature decreases. This can be attributed to the formation of large-size aggregates at lower temperatures. However, it is interesting to note that at 278 K, proton signals from various concentrations share the same intensity. This suggests that there is an equilibrium between monomers and aggregates at this temperature. Interestingly, there is a small signal to the right of H8 (~8 ppm) that could represent a different set of monomer or dimer signals. To understand this small signal, a 2D DOSY experiment was performed on the 50 mM sample at 298 K, and the result indicates that this small peak next to H8 has a similar size as the monomer stacks (Figure 4-7). The two signals have a D_t value of ~3.98 x 10^{-10} m^2/s. At this point, we can only conclude that solution-state NMR provided clues that aggregation, possibly G-quadruplexes, occurs in solution.

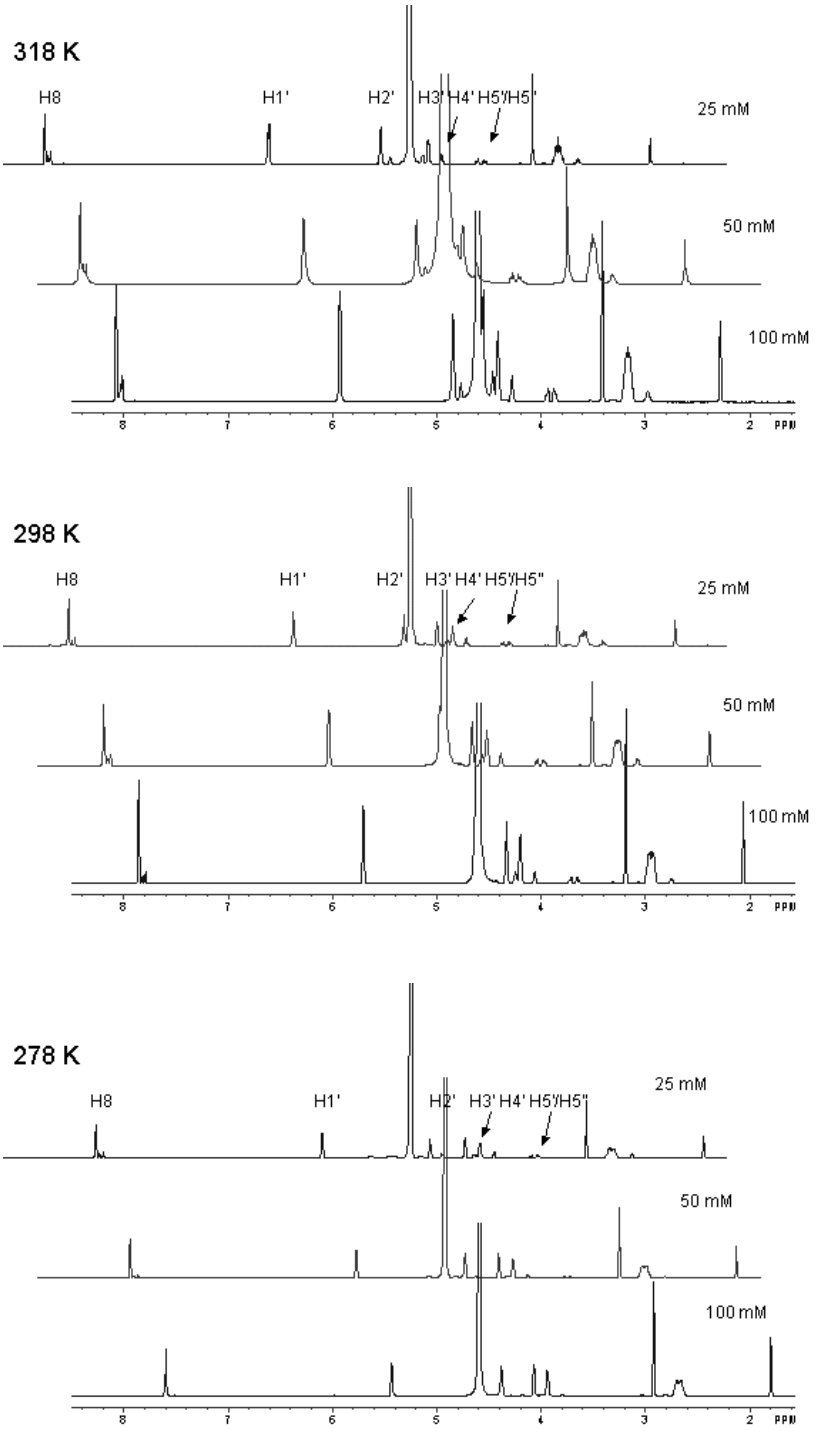

Figure 4-6. Proton NMR spectra of various concentrations of Na_2(5'-GSMP) at different temperatures and pH 8.0. Concentrations of samples are labeled in the spectra.

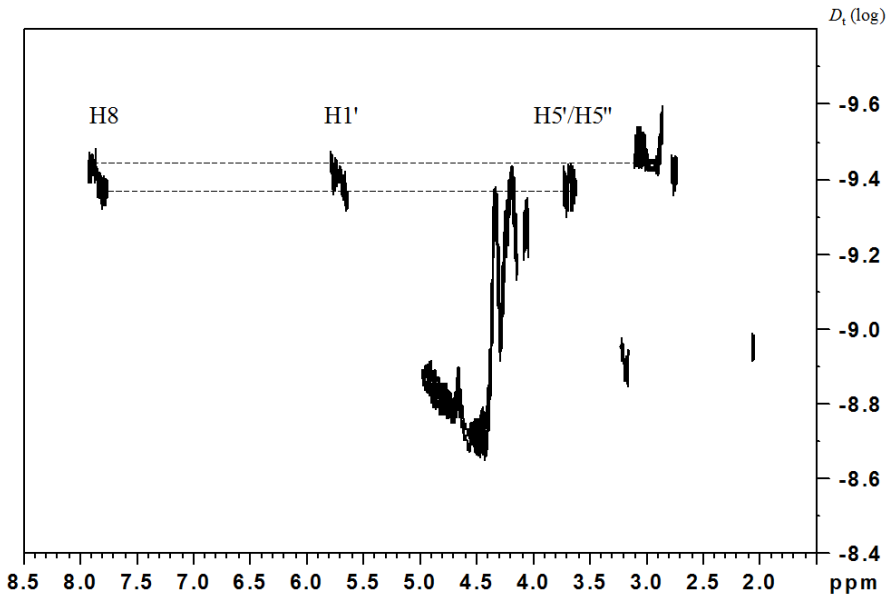

Figure 4-7. Diffusion ^{1}H NMR of 50 mM 5'-GSMP at pH 8, 14.1 T, in D_2O and 298 K.

4.3.2 Solid-state experiments

Figure 4-8 shows that upon sitting on the bench for several hours, Na_2(5'-GSMP) at pH 8 forms a clear and transparent gel at a concentration of 0.17 M. We also noted that concentrations > 0.17 M caused precipitation. The gelation gives strong evidence that G-quadruplex formation occurs in Na_2(5'-GSMP) similar to acidic Na_2(5'-GMP). This conclusion is supported by the powder x-ray diffraction study of dried Na_2(5'-GSMP) gel, which gives the characteristic signal that corresponds to a separation of 3.25 Å between stacking G-quartets (Figure 4-9). Moreover, the ability of 5'-GSMP to form a gel at a concentration of 0.17 M is remarkable, because 5'-GMP does not form any aggregates at such a low concentration at all (Chapter 2). This observation shows that G-quadruplex is formed with greater tendency in Na_2(5'-GSMP) compared to Na_2(5'-GMP).

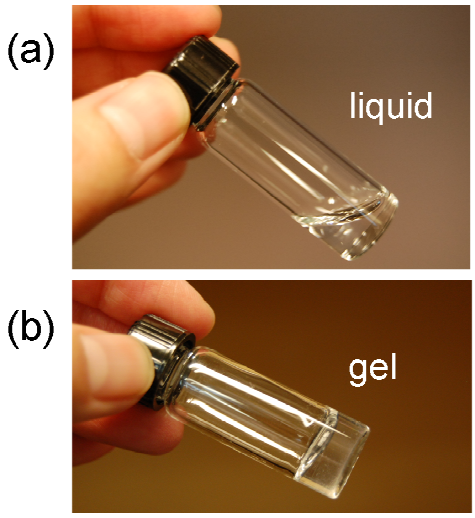

Figure 4-8. Physical states of (a) 1.7 M Na_2(5'-GMP) and (b) 0.17 M Na_2(5'-GSMP). Both are aqueous solutions at pH 8.0.

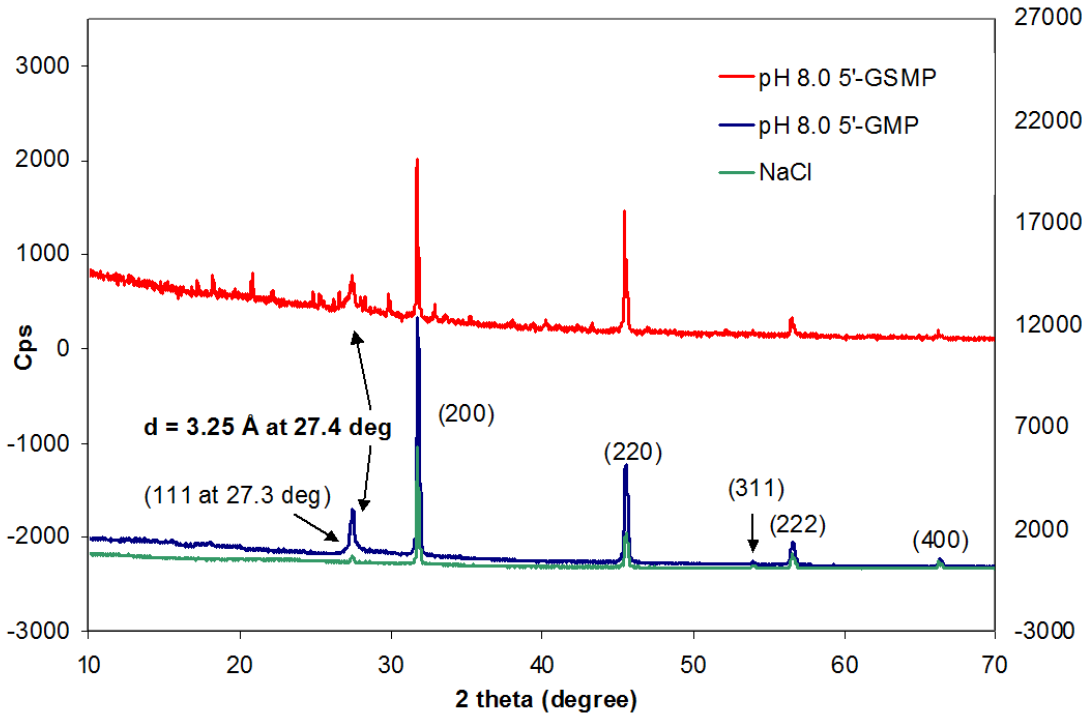

Figure 4-9. Powder x-ray diffraction patterns for Na_2(5'-GSMP), Na_2(5'-GMP), and NaCl.

To learn more about the molecular structure of the Na_2(5'-GSMP) gel, we recorded ^{13}C solid-state NMR spectra of a dried gel sample. Figure 4-10 shows that the ^{13}C CP-MAS NMR spectrum of GSMP is very similar to that of GMP except carbon C5', as it is now shifted to low frequency due to shielding from the presence of a sulfur atom. This experiment confirms that the Na_2(5'-GSMP) gel contains a G-quadruplex structure similar to that in dried Na_2(5'-GMP). Moreover, FT-IR experiment of the dried Na_2(5'-GSMP) gel shows that both C2'-*endo* and C3'-*endo* conformations identical to the signals observed in Na_2(5'-GMP) G-quadruplex are present (Figure 4-11). Since the presence of both ribose puckering is a unique feature of the Na_2(5'-GMP) G-quadruplex system, it further confirms the formation of G-quadruplex in Na_2(5'-GSMP).

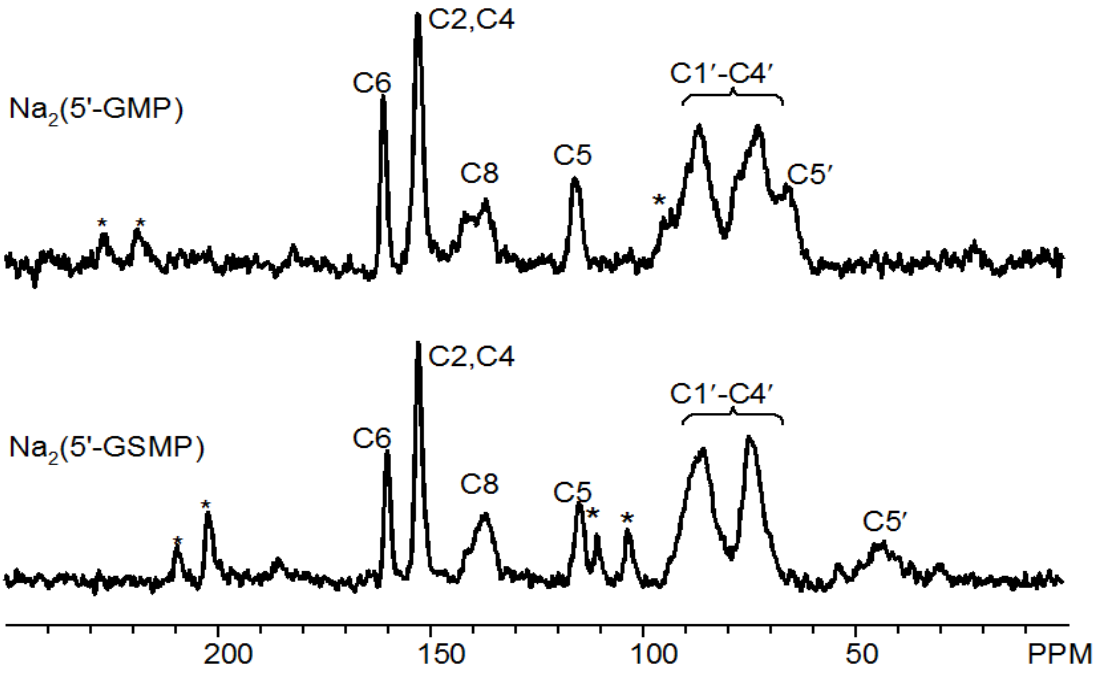

Figure 4-10. Solid-state ^{13}C CP-MAS spectra of dried Na_2(5'-GMP) and Na_2(5'-GSMP). All spinning sidebands are marked with an asterisk. The spinning rate for Na_2(5'-GSMP) is 10 kHz.

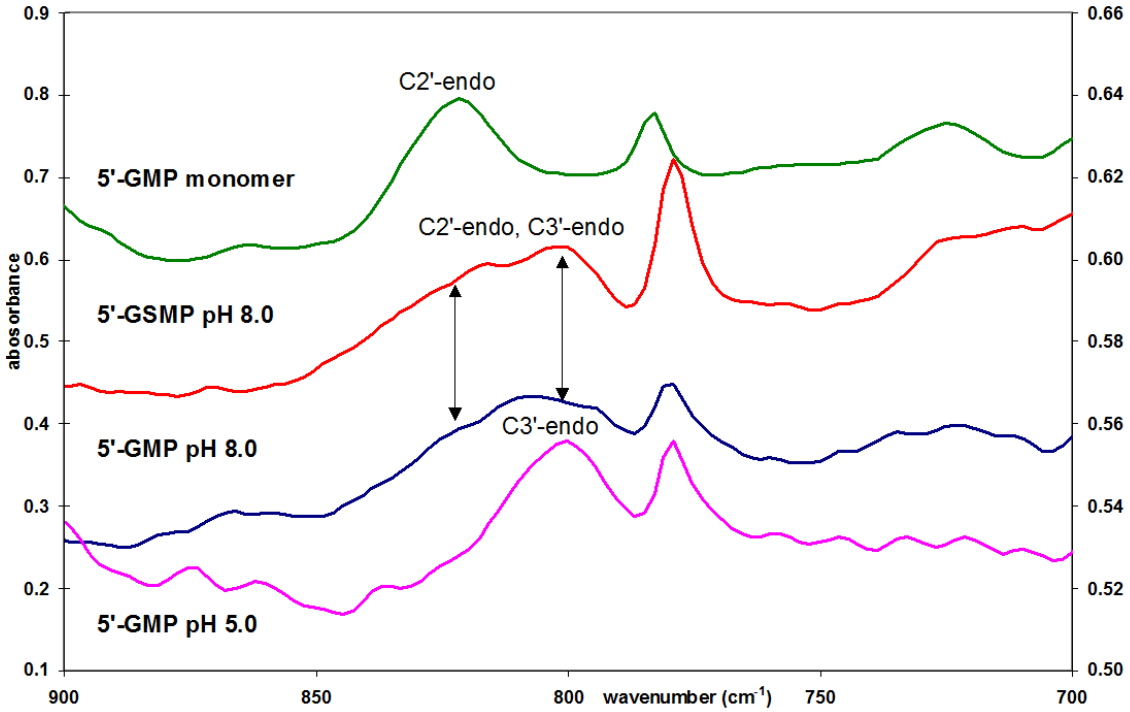

Figure 4-11. Solid-state FT-IR spectra of Na_2(5'-GMP) and Na_2(5'-GSMP) samples using KBr discs.

The next piece of evidence that confirms G-quadruplex formation for Na_2(5'-GSMP) comes from the solid-state ^{23}Na MAS experiments. As shown in Figure 4-12, there are three ^{23}Na signals observed for the dried Na_2(5'-GSMP) gel. The largest ^{23}Na signal arises from free NaCl and the ^{23}Na signal at -18 ppm is due to "channel" Na^+ ions. Interestingly, the phosphate-bound Na^+ ions in Na_2(5'-GSMP) has a slightly larger chemical shift (*ca.* +5 ppm) than that observed in Na_2(5'-GMP) G-quadruplex. This observation suggests that the surface Na^+ ions are now in a more deshielded environment (i.e., more electronegativity in the environment), possibly arising from a closer contact between negatively charged phosphate oxygens and Na^+ ion. A similar phenomenon was

also observed in the solid-state ^{31}P CP-MAS spectrum of dried Na_2(5'-GSMP) gel. As seen from Figure 4-13, the ^{31}P chemical shift of the phosphate group is now at 19.3 ppm compared to 17.6 ppm in monomers (Figure 4-4). This deshielding effect may come from the same source as observed for ^{23}Na chemical shifts. In order to learn if smaller P-O$^-$ $\cdots Na^+ \cdots ^-$O-P distances in 5'-GSMP G-quadruplex contribute to the observed changes in chemical shifts, we performed quantum chemical calculations.

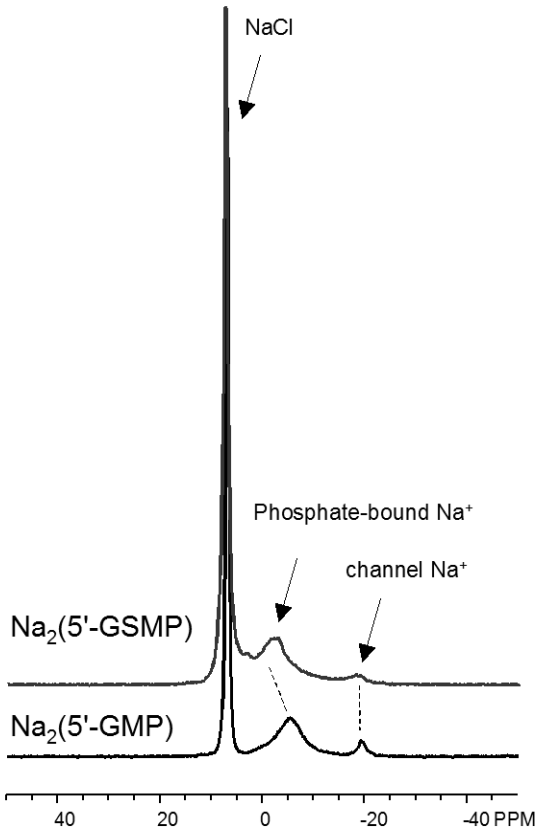

Figure 4-12. Solid-state ^{23}Na MAS NMR spectra obtained at 14.1 T. The sample's spinning rate was 10 kHz. High power ^{1}H decoupling is applied and 64 transients were collected with a recycle delay of 5 s.

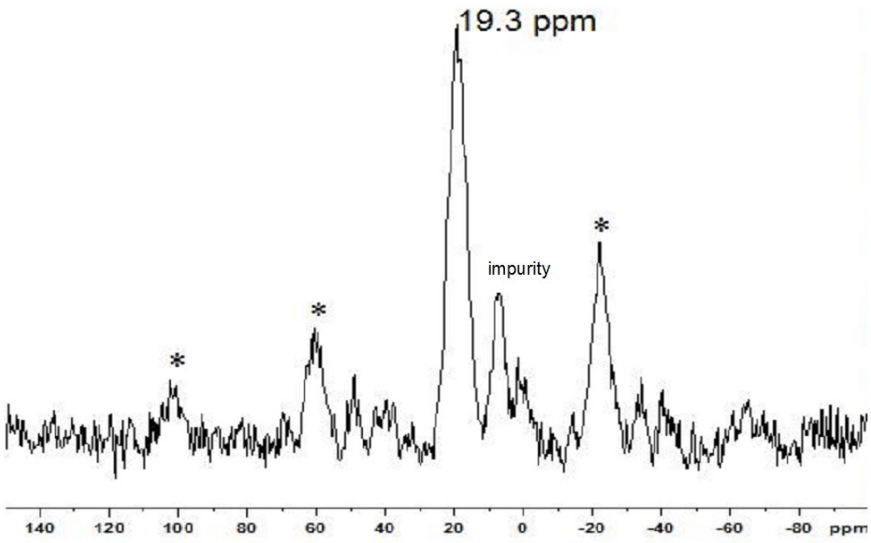

Figure 4-13. Solid-state ^{31}P CP-MAS spectrum of dried 0.17 M Na_2(5'-GSMP) gel at 14.1 T. The sample's spinning rate was 10 kHz.

For calculations, first a $[PO_3\text{-}S\text{-}CH_3]^{2-}$ model was generated and optimized at the B3LYP/6-31G(d) level. Then a Na^+ ion was placed between two of these optimized phosphate molecules, along with four waters surrounding the Na^+ atom to form an octahedral coordination shell (Figure 4-14). Table 4-1 shows the details of geometry of the final cluster: $[CH_3\text{-}S\text{-}PO_3\cdots Na(H_2O)_4\cdots O_3P\text{-}S\text{-}CH_3]^{3-}$. In this case, the variable is the distance between Na^+ and the closest oxygen from the phosphate group (i.e., Na-O) and calculations are performed on these models.

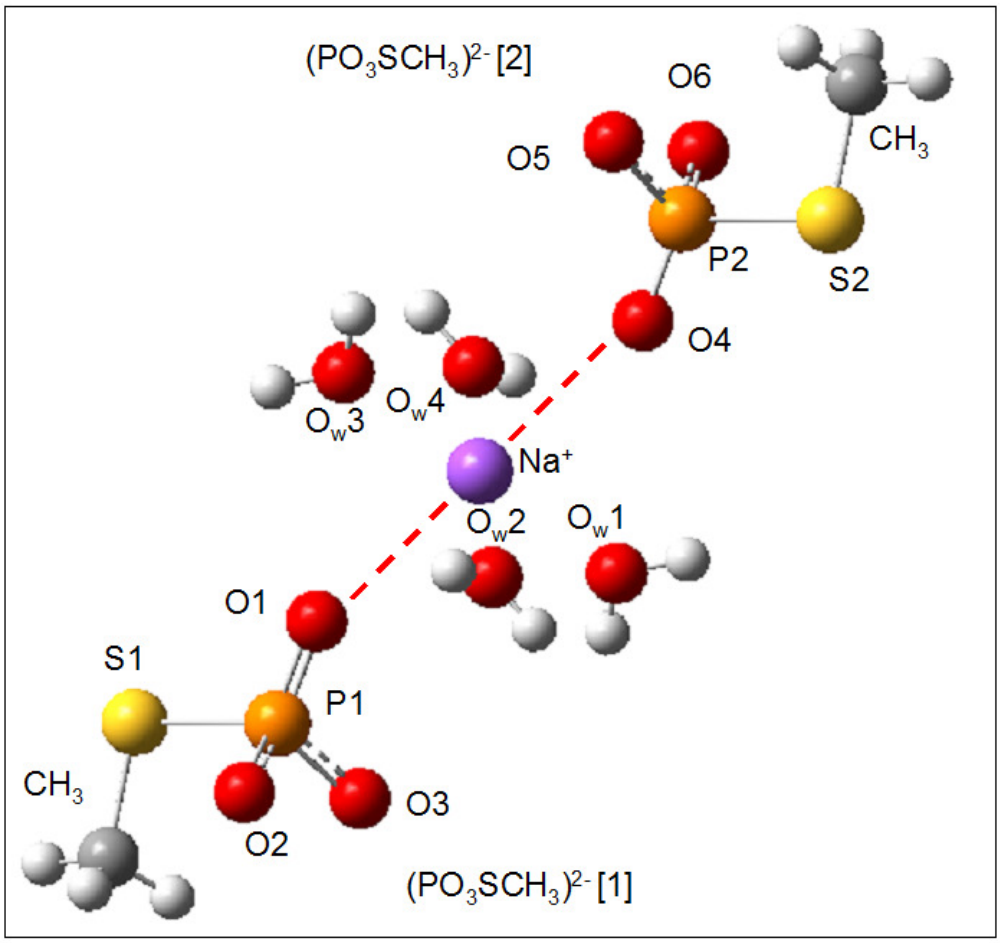

Figure 4-14. The cluster model $[CH_3\text{-}S\text{-}PO_3\cdots Na(H_2O)_4\cdots O_3P\text{-}S\text{-}CH_3]^{3-}$ used in *ab initio* calculations. The dotted lines indicate the variable (Na-O distance) in the calculations.

Table 4-1. Structural details of the cluster model used in quantum chemical calculations (using a Na-O distance of 3.2 Å).

Bond distances (Å)		Bond angles (º)	
Na-O1	3.20	Na-P1-S1	132
Na-O2	4.22	P1-S1-CH3	101
Na-O3	4.08	O1-P1-O2	119
Na-Ow_{1-4}	2.48	O1-P1-O3	114
		O2-P1-O3	100
P1-O1	1.48	O1-P1-S1	113
P1-O2	1.61	P1-Na-Ow_{1-4}	84-97
P1-O3	1.63		
P1-S1	2.10		
S1-C	1.84		
Ow_1-Ow_2	3.45		
Ow_1-Ow_3	4.96		
Ow_1-Ow_4	3.51		

CH_3-S-PO_3^{2-} [1] and CH_3-S-PO_3^{2-} [2] are related by an inversion center.

The plane of symmetry contains Na^+ and the four waters (square planar).

The two CH_3-S-PO_3^{2-} molecules and Na^+ are related by the following parameters:

Bond distances (Å)	Na-P2	same as Na-P1
	Na-O4	same as Na-O1
Bond angles (º)	P1-Na-P2	180
	P1-Na-S2	164
Dihedral angle (º)	P1-O1-O4-P2	180

The computational results are summarized in Figure 4-15, from which several observations were made. First, the ^{23}Na chemical shift appears to be more sensitive to the changing Na-O distance than does the ^{31}P chemical shift. Second, the calculated ^{23}Na chemical shifts are insensitive to the nature of the phosphate groups, as $[CH_3\text{-}S\text{-}PO_3\cdots Na(H_2O)_4\cdots O_3P\text{-}S\text{-}CH_3]^{3-}$ and $[CH_3\text{-}O\text{-}PO_3\cdots Na(H_2O)_4\cdots O_3P\text{-}O\text{-}CH_3]^{3-}$ systems give virtually identical results. Therefore, it is the Na-O distance rather than the presence of O5' or S5' atom that determines the ^{23}Na chemical shifts. Since the cluster model shown in Figure 4-14 may not represent the exact Na_2(5'-GSMP) G-quadruplex environment, only the trends instead of the absolute values are considered. In this regard, the calculations suggest that, as the Na-O distance decreases, both ^{23}Na and ^{31}P chemical shifts should increase.

As seen from Figure 4-15, an increase of 5 ppm in the ^{23}Na signal between 5'-GSMP and 5'-GMP corresponds to a shortening of the Na-O distance by about 0.1 Å. The same amount of distance reduction would yield an increase of the ^{31}P chemical shift by ca. 1 ppm, which is in accordance with the observed ^{31}P chemical shift increase of 1.7 ppm between monomers and G-quadruplex. Therefore, the calculations strongly support the hypothesis that enhanced cation bridging between phosphate groups in Na_2(5'-GSMP) is responsible for its gelation at only 0.17 M.

Figure 4-16 illustrates the arrangement of cation-bridging where it occurs along the helical axis of the G-quadruplex. The Na^+ ions are positioned between the phosphate groups linking to a C2'-*endo*$_{(i)}$ molecule and a C3'-*endo*$_{(i+1)}$ molecule.[110] As discussed in Chapter 2, the P-P distance between these two G-quartets is smaller in 5'-GMP (6.7 Å)

than that between C3'-*endo*$_{(i+1)}$ and C2'-*endo*$_{(i+2)}$ G-quartets (7.2 Å). Hence a Na^+ ion would most likely fit in and bridge the two phosphate groups in a fashion shown in Figure 4-16. It should also be noted that the enhanced cation-bridging in 5'-GSMP has a fourfold amplification around the helix. Moreover, the gelation observed in 5'-GSMP has a similar self-assembling mechanism compared with acidic GMP, where the longer $^-$O-P-S-C5' bond lengths compensate for the shorter P-P distance caused by smaller repulsion in the singly-charged phosphate groups in acidic 5'-GMP. As mentioned in Chapter 3, cation-bridging may play an important role in different G-quadruplex systems. For example, K^+, Rb^+, and NH_4^+ have been known to facilitate different, yet known 5'-GMP G-quadruplexes.[15,60,111]

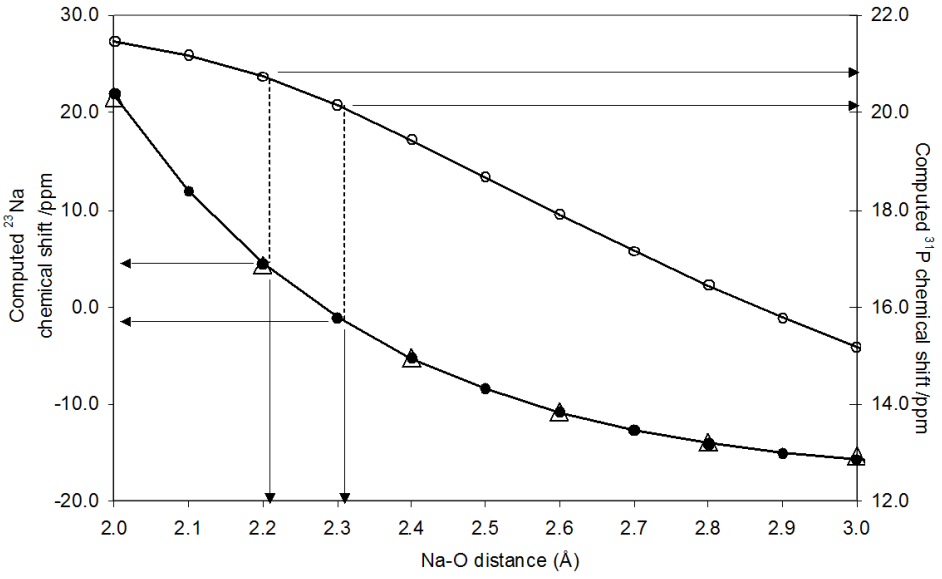

Figure 4-15. Computed results of ^{23}Na (closed circles) and ^{31}P (open circles) chemical shifts for the $[CH_3\text{-}S\text{-}PO_3^{\cdots}Na(H_2O)_4^{\cdots}O_3P\text{-}S\text{-}CH_3]^{3-}$ cluster model with various Na-O distances at B3LYP/6-31G(d)/cc-pVTZ(Na^+) level. The calculations of ^{23}Na chemical shifts using the $[CH_3\text{-}O\text{-}PO_3^{\cdots}Na(H_2O)_4^{\cdots}O_3P\text{-}O\text{-}CH_3]^{3-}$ cluster model are shown in triangles.

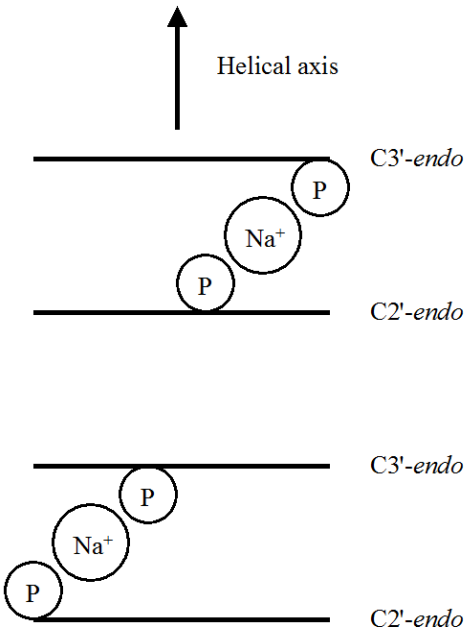

Figure 4-16. Scheme of cation-bridging between phosphate groups along the self-assembled 5'-GMP and 5'-GSMP G-quadruplex helices. The horizontal bar represents a G-quartet made of either C2'-*endo* or C3'-*endo* monomers, and only one of four phosphate groups is shown on each G-quartet.

Lastly, it is also interesting to observe physical evidence of right-handed Na_2(5'-GSMP) helices in SEM images (Figure 4-17). These short, rod-like structures measure 500-800 nm long with 200-500 nm diameters are clusters of G-quadruplexes. Striation is clearly observed on the sides of the rods and suggests that many parallel G-quadruplex systems combine to form one single column as documented in a SEM study of 5'-GMP.[111] A different view of these rods shows hair-like structures on the ends and suggests direction of growth of 5'-GSMP G-quadruplexes.

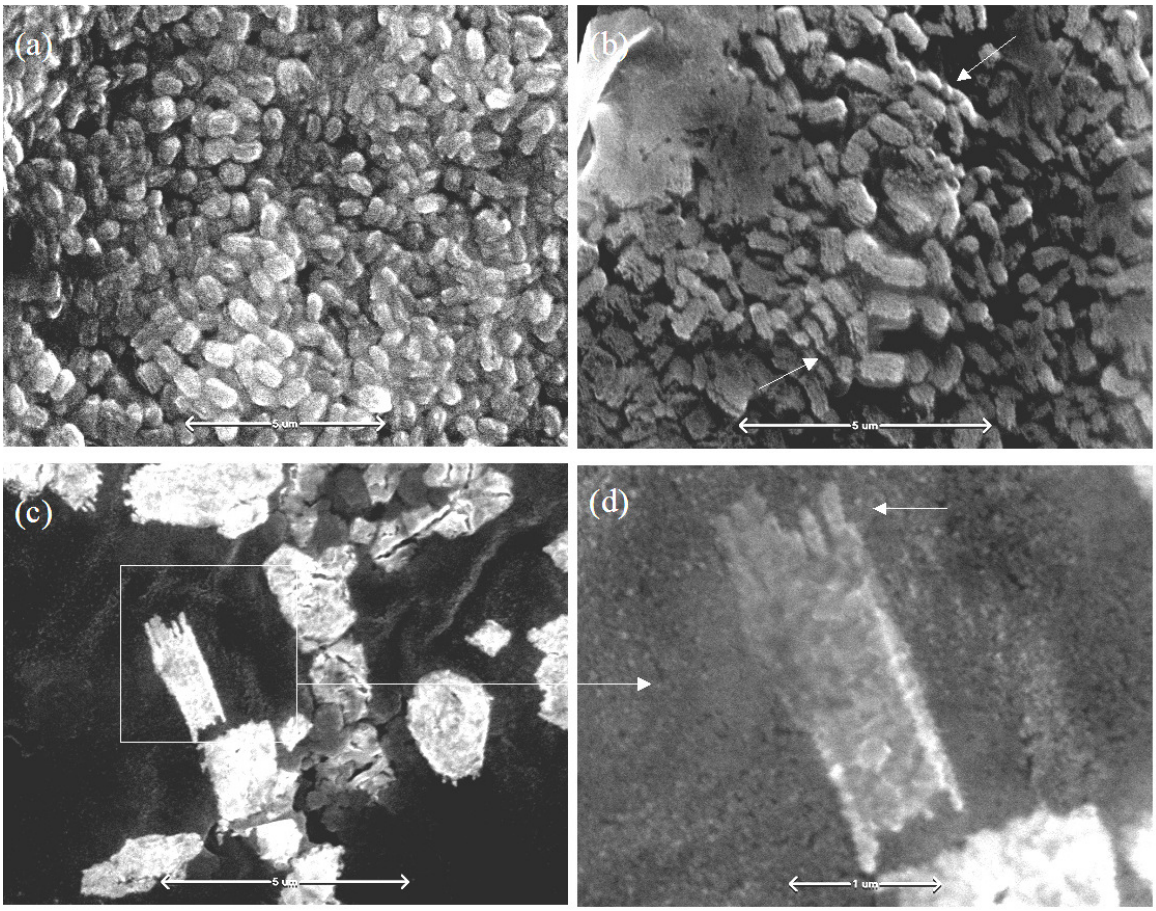

Figure 4-17. SEM images of dried, neutral pH, 50 mM Na_2(5'-GSMP). (a) Columns of Na_2(5'-GSMP) G-quadruplexes with obvious striations, (b) right-handed helices are highlighted with arrows, (c) hair-like extensions on the edge, and (d) increased magnification of a section in part c.

4.4 Conclusions

We have demonstrated that Na_2(5'-GSMP) forms a G-quadruplex similar to that of Na_2(5'-GMP). However, the longer phosphate bond in 5'-GSMP allows the neighboring phosphate groups to become closer, thus enhancing P-$O^{-}\cdots Na^{+}\cdots{}^{-}$O-P interactions. This enhanced cation bridging capability of Na_2(5'-GSMP) is responsible for

its ability to form gels at low concentrations under neutral conditions. Under the same conditions, Na_2(5'-GMP) remains to be a liquid even at high concentrations. This study represents an example that a single atom modification can lead to quite different self-assembly properties.

Chapter 5

G-quartet formation of 2', 3', 5'-*O*-triacetylguanosine promoted by divalent and trivalent cations

5.1 Introduction

In the past decade, G-quartet has attracted considerable attention in various areas of research ranging from molecular biology to nanotechnology.[41,112] Most previous studies on G self-assembly were carried out in water.[41] This is because many G derivatives are insoluble in organic solvents. In addition, base-stacking is weakened in organic solvents. However, Davis and Gottarelli et al. discovered that a lipophilic G nucleoside, 3',5'-didecanoyl-2'-dG, can form G-octamers in the presence of K^+ in $CDCl_3$.[113] Moreover, Spada et al. reported a series of deoxyguanosine derivatives that can extract alkali metal salts into organic solvents.[114] These studies show that formation of lipophilic G-quartets is clearly achievable in organic solvents. Lipophilic G derivatives can also form high-ordered aggregates that resemble transmembrane ion channels. The environment around K^+ ions in the selectivity filter of K^+-channel proteins is very similar to that inside of a G-quadruplex channel.[27] In both cases, each cation is surrounded by eight carbonyl groups in an antipyrimidal or cubic fashion.[27] Therefore, many lipophilic G-quadruplexes were made to mimic protein ion channels as artificial ion channels.[41] With only a few exceptions,[115,116,117] G-quartet formation generally requires the presence of metal ions. To date, only monovalent (Na^+, K^+, Rb^+, NH_4^+, Tl^+) and divalent (Sr^{2+}, Ba^{2+}, Pb^{2+}) cations have been found to assist G-quartet formation.[118] To our knowledge, trivalent cations have not been shown to induce G-quartet formation. In this chapter, we

report the first example of G-quartet formation of a simple lipophilic guanosine derivative (2',3',5'-*O*-triacetylguanosine, TAG; Figure 5-1) promoted by trivalent lanthanide metal ions (La^{3+}, Eu^{3+}, Tb^{3+}, Dy^{3+}, Tm^{3+}).[119]

The second part of this chapter describes our attempt to form G-quadruplex using TAG and Ca^{2+} cations. Being one of the most abundant elements in human bodies, Ca^{2+} also plays a huge role in signal transduction as a second messenger in biological systems. Studies in G-quadruplex formation between DNA sequences and Ca^{2+} cations,[120,121] including a recently revealed crystallographic structure of $[d(TG_4T)]_4$-G-quadruplex in the presence of Ca^{2+} cations,[122] show the potential of incorporating Ca^{2+} ions into G-quadruplex systems. We believe that our TAG/Ca^{2+} self-assembly can help in understanding the calcium binding site, as well as synthetic calcium channel studies. Lipophilic G derivative was previously observed to form a G-quadruplex ionophore with Ca^{2+} ions,[123] and our group was able to prepare discrete octamers using TAG and other divalent cations (i.e., Sr^{2+}, Ba^{2+}) in organic solvent.[124] We used NMR and ESI-MS methods to study [TAG]Ca^{2+} complexes, and ^{43}Ca NMR and quantum chemical calculation are also used to study the Ca^{2+} binding site within the G-quadruplex.[125]

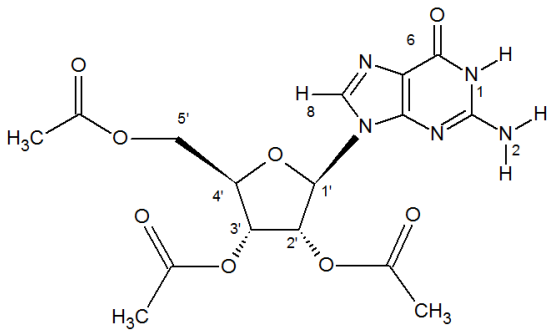

Figure 5-1. Scheme of 2',3',5'-*O*-triacetylguanosine (TAG).

5.2 Experimental

5.2.1 Sample preparation

[TAG]M^{3+} complexes. 2',3',5'-*O*-Triacetylguanosine (98% purity) was purchased from Sigma-Aldrich and used without further purification. [TAG]M^{3+} complexes were prepared using a solid-liquid extraction method in $CHCl_3$. Metal chlorides were used as the source of metal ions. After 24 hours of extraction, the organic phase became clear and was collected and subsequently dried under vacuum. The extraction ratio TAG:M^{3+} for extraction is 1:1 unless otherwise stated.

Picrate salts. Picrate salt (i.e., Ca-picrate$_2$) was synthesized by neutralizing picric acid (Aldrich, 99+%; WARNING: Explosive) with calcium hydroxide, $Ca(OH)_2$, in aqueous environment. Picrate salts were collected after crystallization.

[TAG]Ca^{2+} complexes. [TAG]Ca^{2+} complexes were prepared using a solvent-solvent extraction method: to one mole of TAG suspended in $CHCl_3$, one mole of picrate salt (Ca-picrate$_2$) dissolved in H_2O was added drop-wise to the stirring solution. The two-phase solution was stirred until the organic phase became visually clear. The aqueous phase was then removed, and solid TAG-Ca^{2+} complexes were obtained after the organic phase was dried in air.

5.2.2 Solution-state NMR

All solution-state NMR spectra were recorded on a Bruker Avance 600 MHz spectrometer and in $CDCl_3$ at 268.2 K and 298.2 K. For ^{1}H NMR experiments, a pi-pulse

of 20 μs at a power level of 0 dB was used. Temperatures were achieved and maintained carefully by a Bruker BT-3000 unit.

DOSY. ^{1}H diffusion experiments were carried out using the pulse sequence of longitudinal eddy current delay with bipolar-gradient pulses: LEDBPGP2s (Bruker XWinNMR Version 3.5) on 1.0 mM samples in $CDCl_3$. The pulse field gradient duration (δ) ranged from 1.0 to 2.0 ms, and the variable gradient strength (G) was changed from 5.75 to 5.8 mT/m. The diffusion period (Δ) was 50 ms. A total of 16 scans were collected for each of the 16 increment steps with a recycle delay of 5 s. The eddy current delay (t_e) was 5 ms, and the gradient recovery delay was 0.2 ms. All diffusion experiments were performed at 298.2 K. Calibration of the field gradient strength was performed by measuring the value of translational diffusion coefficient (D_t) for the residual ^{1}H signal in D_2O (99.99% ^{2}H atom), where D_t = 1.90 x 10^{-9} m^2/s.[68] All diffusion coefficients were acquired using integration of the proton peaks to a single exponential decay, using the Simfit software (Bruker XWinNMR Version 3.5).

NOESY. NOESY spectra for [TAG]M^{3+} were recorded using the pulse program NOESYGPPH (Bruker XWinNMR Version 3.5) with a mixing time (τ_{mix}) of 400 ms on a 1:2 (M^{3+}:TAG) mixing ratio at 268K $CDCl_3$. The experiments were performed using the phase-sensitive TPPI mode. The data were collected using a 90° pulse of 10.0 μs at 0 dB, and a relaxation delay of 2.0 s. Spectral width of 13,227 Hz in each dimension was employed. A total of 2 scans were collected for each time increment. Final data matrix was 2048 (F2) x 1024 (F1). The 2D NOESY spectrum for [TAG]Ca^{2+} was performed with a mixing time (τ_{mix}) of 400 ms and the phase-sensitive TPPI mode. The data were

collected using a 90° pulse of 10.0 μs and a relaxation delay of 3.0 s. A total of 8 scans were collected for each time increment. Final data matrix was 2048 (F2) x 1024 (F1).

^{43}Ca NMR. All solution ^{43}Ca NMR experiments were performed by Dr. Alan Wong on a Chemagnetics-Varian Infinity 600 (14.1 T) spectrometer operating at 40.386 MHz for ^{43}Ca nuclei at the University of Warwick, UK. A Varian T3 rotor (9.5 mm diameter) was used to increase the NMR sensitivity. The strength of the radio-frequency field was approximately 14 kHz. A spectral window of 50 kHz was used. All ^{43}Ca chemical shifts are referenced to the signal from 1.0 M $CaCl_{2(aq)}$, $\delta(^{43}Ca) = 0$ ppm.

5.2.3 Mass Spectrometry

ESI-MS spectra were recorded with an Applied Biosystems QSTAR XL quadrupole time-of-flight (QqTOF) mass spectrometer in positive mode. ESI-MS data were acquired using Analyst QS 1.1 software. Samples were dissolved in anhydrous nitromethane (CH_3NO_2) and injected with a syringe pump at a flow rate of 5.0 μL min^{-1}. The mass range of single MS measurements was set at *m/z* 300 to 6000. To observe $[TAG_n + M]^{3+}$ complexes, the declustering potential (DP) was set to 20 V during the MS experiment. Subsequent tandem mass spectrometry (MS/MS) measurements were performed using nitrogen as the collision gas. A collision induced dissociation (CID) energy of 35 eV was applied to break down the TAG dodecamers and TAG octamers. The mass range of MS/MS measurements was set at *m/z* 100 to 4000. For spectral assignment, theoretical MS peaks were generated using Data Explorer v. 4.0.0.0 (Applied Biosystems, 1997– 2000).

5.2.4 Fluorescence

Excitation and emission spectra were recorded on a Photon Technology International (PTI) QuantaMaster model C-60 spectrometer at room temperature using the software FeliX (v. 1.4, 1999) supplied by PTI.

5.2.5 Quantum chemical calculations

Quantum chemical calculations were performed using the Gaussian 03 suite of programs[87] on a SunFire 6800 symmetric multiprocessor system. Each of the four nodes is equipped with a 2461.05 GHz (8MB E-Cache) UltraSPARC-III processor and 96 GB of RAM. For the central Ca atom, we chose three different all-electron basis sets: 6-311++G(d,p), cc-pVTZ and Sadlej pVTZ.[126] A 6-31G(d) basis set was used for all other non-metal atoms. Each octamer model consists of 129 atoms. Chemical shielding calculations were performed at both Hartree–Fock (HF) and density-functional theory (DFT) levels using the GIAO method as implemented in Gaussian 03. The computed absolute shielding constant was converted to the chemical shift scale (δ) using $\delta = \sigma_{ref} - \sigma$, where σ_{ref} is the absolute shielding constant for the reference sample, a fully hydrated cluster, $[Ca(H_2O)_8]^{2+}$ (MP2/6-311++G(d,p) fully optimized geometry: Ca–O: 2.480 Å).

5.3 Results and discussion

5.3.1 [TAG]M^{3+} G-quadruplexes

5.3.1.1 Mixture of large G-quadruplexes

Figure 5-2 shows the ^{1}H NMR spectrum of TAG in DMSO where TAG remains monomeric. When preparing the TAG/M^{3+} complex in chloroform, a clear organic phase is used as an indication of successful M^{3+} extraction since TAG is not soluble in the weakly polar solvent by itself. Upon formation of G-quadruplexes, the hydrogen-bond donors and acceptors on the guanine bases of TAG are no longer available (due to Hoogsteen hydrogen-bonds in G-quartets), hence the polarity of the aggregates will decrease in general and allows them to be soluble in chloroform.

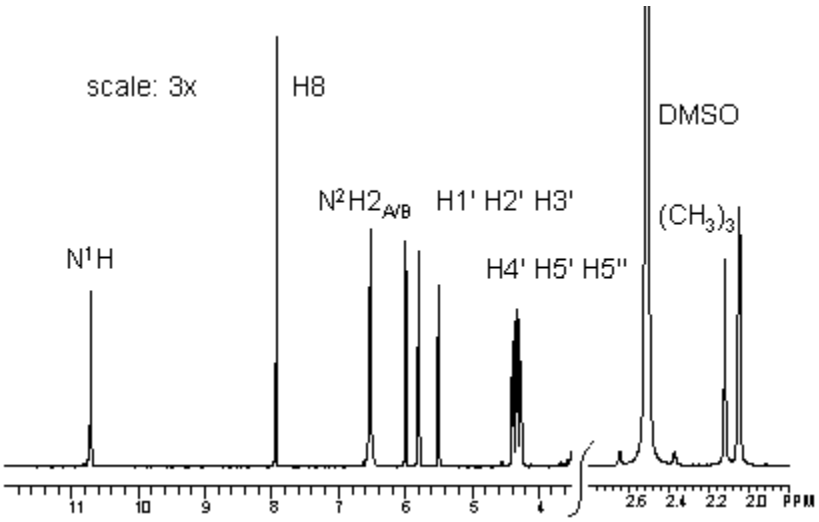

Figure 5-2. Proton-NMR spectrum of TAG in DMSO at 298.2 K.

It can be seen that upon adding metal cations, the ^{1}H NMR spectra exhibit very different features compared with the monomers (Figure 5-3). The heavily overlapped

signals are similar to those observed in $[TAG]M^{+}$,[127] which suggests formation of different types of aggregates with various sizes. It is also observed that the chemical shift range is very large (e.g., ~50 ppm in $[TAG]Tb^{3+}$) due to the paramagnetic nature of the lanthanide cations. Although the resolution of the spectra are relatively low, the approximate regions containing resonances of H8 and N^1H/N^2H_A can still be observed at the low frequency region.

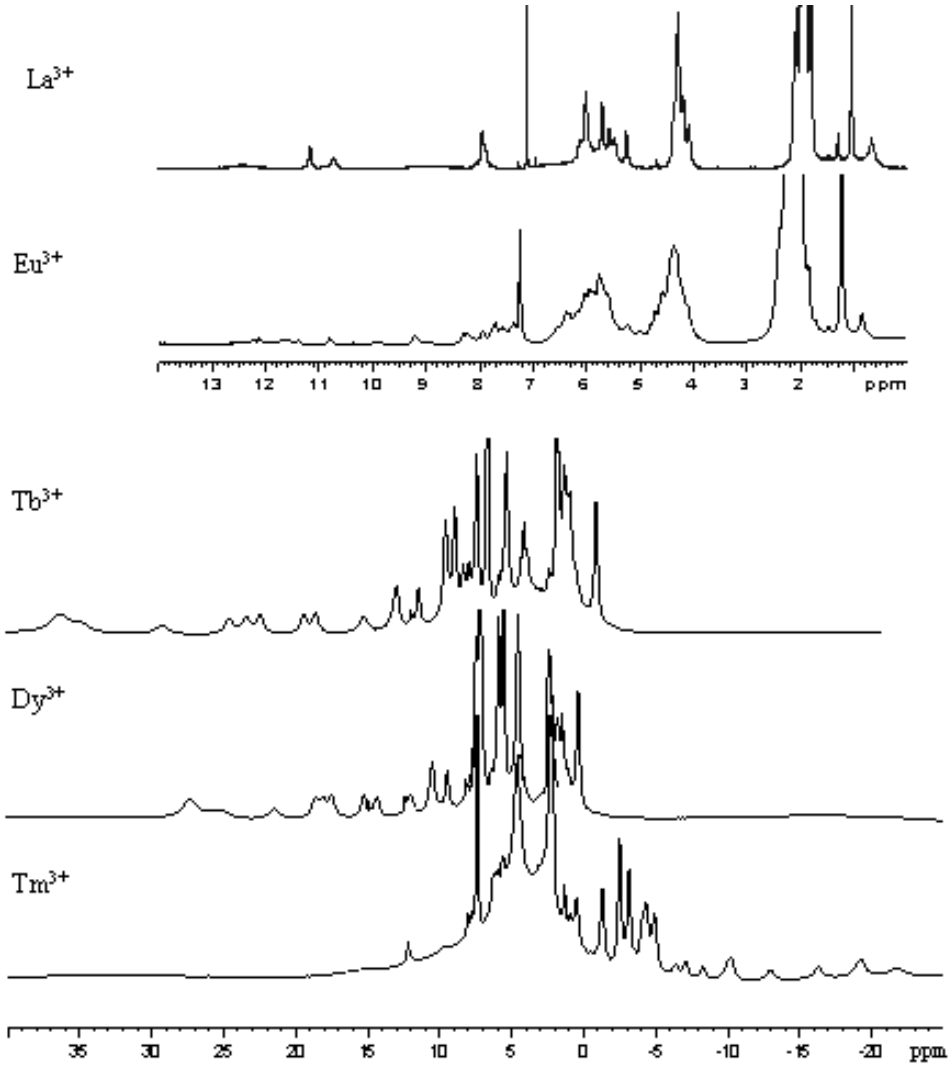

Figure 5-3. ^1H NMR spectra of $[TAG]M^{3+}$ species in $CDCl_3$ at 14.1 T and 298 K.

Moreover, Figure 5-4 shows the NOESY spectra of both [TAG]La^{3+} and [TAG]Eu^{3+} complexes with signature G-quartet cross peaks and confirmed the presence of G-quadruplex in [TAG]M^{3+} systems. Broad ^1H signals are observed in [TAG]Eu^{3+} due to the paramagnetic nature of the lanthanide ion. The G-quartet signature NOE peaks were not identified for Tb^{3+}, Dy^{3+}, and Tm^{3+} systems due to the lack of proper H8 and N^1H/N^2H_A signals assignment in the 1D proton spectra. Nonetheless, the TAG solutions were also clear upon extraction of these metal cations and suggested the possibility of G-quartet formation.

Another proof of aggregate formation was provided by the DOSY diffusion experiment. As shown in Table 5-1, the average translational diffusion coefficient (D_t) value of [TAG]M^{3+} species is the smallest compared to those of both monovalent and divalent cation complexes. Since D_t is inversely proportional to aggregate size, the DOSY data suggest that [TAG]M^{3+} aggregates are larger than those formed in the presence of M^+ and M^{2+} ions. It is previously known that M^{2+} promotes only octamers formation, and M^+ can assist the formation of octamers, dodecamers, and hexadecamers.[124,127] Because D_t is an averaged value in solution state, it is believed that the small D_t of [TAG]M^{3+} complexes could indicate that very large aggregates are present (i.e., larger than hexadecamer), or the majority of the aggregates present are large aggregates (i.e., dodecamer, hexadecamer). This is supported by the complex ^1H NMR spectra similar to that observed in [TAG]M^+ complexes where a mixture of aggregates are present.[127]

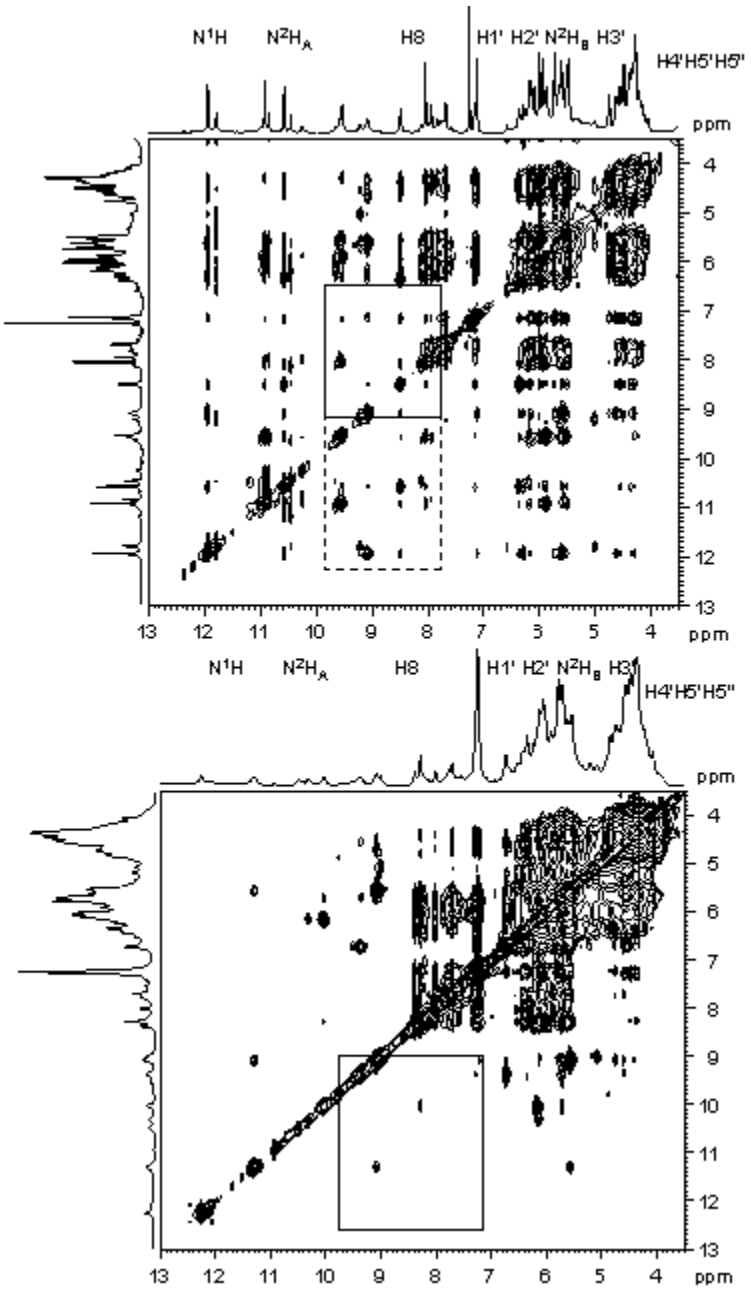

Figure 5-4. A portion of the 2D NOESY spectrum of the [TAG]La^{3+} (top) and [TAG]Eu^{3+} (bottom) complexes at 268 K. G-quartet signature cross peaks formed between N^2H_A and H8 were highlighted in the solid box while those formed between N^1H and H8 were enclosed in the dashed box. Estimated cross peaks formed between N^1H/N^2H_A and H8 were highlighted in the solid box for the [TAG]Eu^{3+} complex.

Table 5-1. Summary of experimental diffusion coefficients (D_t) of various TAG-cation complexes determined at different 1D proton chemical shifts at 298.2 K and 1.0 mM.[124,127]

Species	Average D_t (x 10^{-10} m^2/s)	No. of data points	Aggregate size
$[TAG]M^+$ $M^+ = Na^+, K^+, Rb^+$	4.35 ± 0.69	85	Hexadecamers, dodecamers, and octamers
$[TAG]M^{2+}$ $M^{2+} = Sr^{2+}, Ba^{2+}$	4.96 ± 0.36	41	Octamers
$[TAG]M^{3+}$ $M^{3+} = La^{3+}, Eu^{3+}$	3.35 ± 0.21	31	Mixed large aggregates

5.3.1.2 Ion-size dependent $[TAG]M^{3+}$ aggregate formation

Since $[TAG]M^{3+}$ could contain very large G-quadruplexes not previously observed, we decided to use mass-spectrometry to further examine $[TAG]M^{3+}$ aggregations. Figure 5-5 shows the high-resolution electrospray ionization mass-spectrometry (ESI-MS) spectra of various $[TAG]M^{3+}$ species ($M^{3+} = La^{3+}$, Eu^{3+}, Tb^{3+}, Dy^{3+}, and Tm^{3+}) obtained at the positive mode. All spectra were obtained under the same condition. For the La^{3+} and Eu^{3+} complexes, the predominant species is a TAG dodecamer containing only one metal ion, $[TAG_{12} + M]^{3+}$, whereas for the Tb^{3+}, Dy^{3+} and Tm^{3+} complexes, both dodecamer and octamer formations have large relative abundances. In each case, clusters corresponding to $[TAG_n + M]^{3+}$ (n = 9, 10, 11, 13, 14) are also present, but mostly with much weaker abundances (< 10%). There is also no

observation of any aggregates smaller than octamers, which suggests that the $[TAG_8 + M]^{3+}$ complexes are very stable. We also noted that some peaks arose from aggregates formed with a trace amount of Na^+ and K^+ present in the solvent (Table 5-2). For example, in the ESI-MS spectrum of the Eu^{3+} complex, an additional peak was observed between the signals for $[TAG_{11} + Eu]^{3+}$ (*m/z* 1551.418) and $[TAG_{12} + Eu]^{3+}$ (*m/z* 1686.809). This peak (*m/z* 1656.995) was assigned to $[TAG_8 + K + H]^{2+}$. However, these monovalent species do not constitute a significant portion of the aggregate population. The signal assignments and relative intensities of each $[TAG_n + M]^{3+}$ species after fragmentation are also shown in Table 5-2.

To further investigate whether the observed $[TAG_8 + M]^{3+}$ and $[TAG_{12} + M]^{3+}$ clusters were indeed related to G-quartet formation, we subsequently performed tandem ESI-MS/MS experiments. Figure 5-6 shows the ESI-MS/MS spectra of $[TAG_{12} + Tb]^{3+}$ (*m/z* 1689.476) and $[TAG_8 + Tb]^{3+}$ (*m/z* 1143.964) as two examples. Collision-induced dissociation of the TAG dodecamer at a low energy led to fragments of 11-mer, 10-mer, 9-mer and 8-mer, whereas a further breakdown of the TAG octamer gave rise to 7-mer, 6-mer, 5-mer and 4-mer (i.e., G-quartet). These observations are consistent with the expectation that a G-quartet is the basic unit of these clusters. The ESI-MS/MS spectra of the other complexes and their relative abundances are shown in Appendices III.

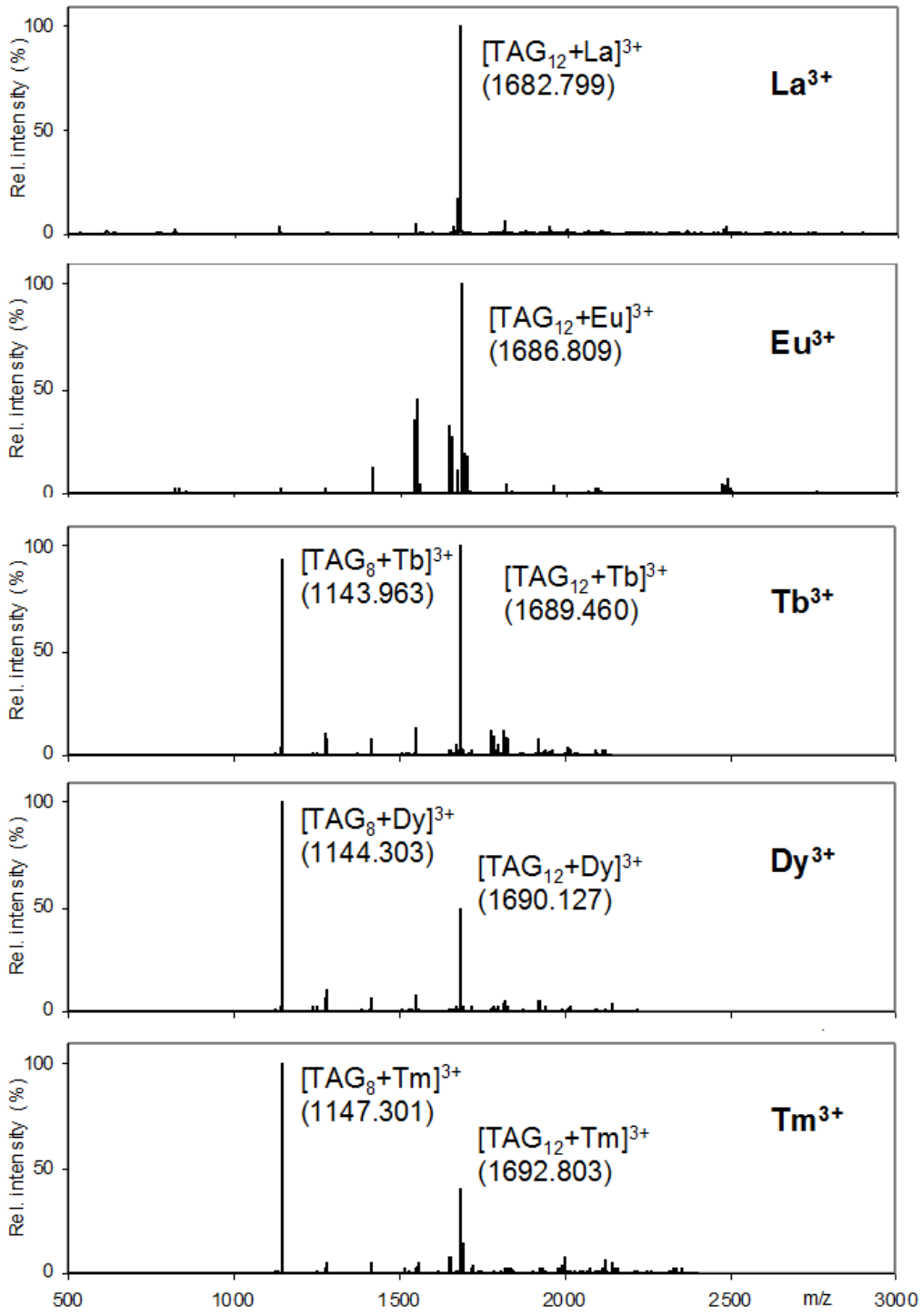

Figure 5-5. High-resolution ESI-MS(+) spectra of various $[TAG]M^{3+}$ complexes.

Table 5-2. Different species of $[TAG]_n(MCl_3)n$ analyzed from ESI-MS(+) spectra. M = monomeric TAG with 409.36 a.m.u.

$[TAG]_nLa^{3+}{}_n$	*m/z*	Rel. intensity	$[TAG]_nDy^{3+}{}_n$	*m/z*	Rel. intensity
$[M2]^+$	819.3	2.9	$[M8+Dy]^{3+}$	1145.6	100.0
$[M8+La]^{3+}$	1137.9	3.5	$[M9+Dy]^{3+}$	1282.4	9.7
$[M11+La]^{3+}$	1547.1	5.1	$[M10+Dy]^{3+}$	1419	4.9
$[M12+La]^{3+}$	1683.1	100.0	$[M11+Dy]^{3+}$	1555.1	5.7
$[M13+La]^{3+}$	1820.5	6.0	$[M12+Dy]^{3+}$	1691.5	49.8
$[M14+La]^{3+}$	1956..8	3.5	$[M8-H+Dy]^{2+}$	1717.9	2.0
$[M12+Na+K]^{3+}$	2485.3	3.1	$[M9-H+Dy]^{2+}$	1922.5	5.1
			$[M10-3H+K+Dy]^{2+}$	2146.1	3.0
			$[M12+2K]^{2+}$	2494.3	3.1

$[TAG]_nEu^{3+}{}_n$	*m/z*	Rel. intensity	$[TAG]_nTm^{3+}n$	*m/z*	Rel. intensity
$[M2]^+$	819.3	2.4	$[M8+Tm]^{3+}$	1147.6	100.0
$[M8+Eu]^{3+}$	1142.3	3.0	$[M9+Tm]^{3+}$	1284.3	5.6
$[M9+Eu]^{3+}$	1278.7	3.0	$[M10+Tm]^{3+}$	1420.7	3.8
$[M10+Eu]^{3+}$	1415.1	12.6	$[M11+Tm]^{3+}$	1557.1	4.5
$[M11+Eu]^{3+}$	1551.4	45.3	$[M12+Tm]^{3+}$	1693.5	39.8
$[M12+Eu]^{3+}$	1687.8	100.0	$[M8+K+H]^{2+}$	1656.9	7.9
$[M13+Eu]^{3+}$	1824.4	5.4	$[M10-H+Tm+HCl]^{2+}$	2148.6	5.4
$[M14+Eu]^{3+}$	1961.2	4.2	$[M11-H+Tm+HCl]^{2+}$	2353.6	3.0
$[M15+Eu]^{3+}$	2098.2	2.4	$[M12+K+Na]^{2+}$	2486.7	5.6
$[M8+K]^{2+}$	1656.9	33.0	$[M14-H+La+Na+K+CH_3NO_2H]^{3+}$	1997.2	7.8
$[M12+K+Na]^{2+}$	2486.7	7.8	$[M15+La+Na+CH_3NO_2H_2]^{3+}$	2121.6	6.3

$[TAG]_nTb^{3+}{}_n$	*m/z*	Rel. intensity
$[M8+Tb]^{3+}$	1144.3	94.6
$[M9+Tb]^{3+}$	1280.7	10.6
$[M10+Tb]^{3+}$	1417.4	7.2
$[M11+Tb]^{3+}$	1553.7	12.8
$[M12+Tb]^{3+}$	1689.8	100.0
$[M13+Tb]^{3+}$	1826.5	7.6
$[M12+Eu]^{3+}$	1687.8	12.2
$[M13+La]^{3+}$	1820.2	10.9
$[M9-H+Tb]^{2+}$	1920.9	6.4
$[M12+K+Na]^{2+}$	2487.1	3.6

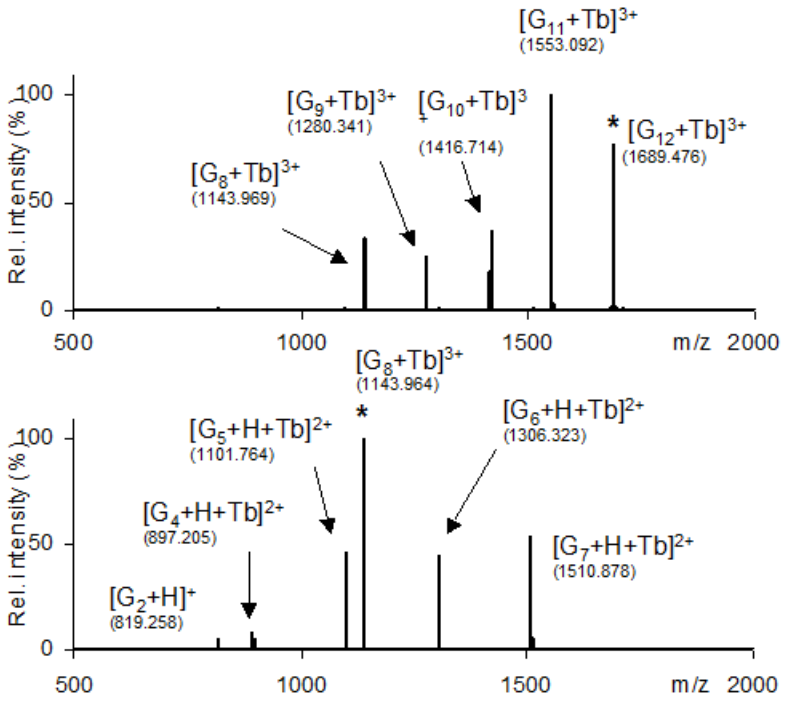

Figure 5-6. ESI-MS/MS(+) spectra of two Tb^{3+} complexes: $[TAG_{12} + Tb]^{3+}$ (top) and $[TAG_8 + Tb]^{3+}$ (bottom). The parent ion is marked by an asterisk (*).

After G-quartet formation was confirmed using NMR and ESI-MS techniques, it was interesting to us to understand the structure of the $[TAG]M^{3+}$ complex structure as the 12:1 ratio of ligand to metal ion has never been observed before (i.e., dodecamer with one M^{3+}). It has been known that monovalent and divalent cations in G-quadruplexes are sandwiched between G-quartets at the channel sites, and sodium ion is the only metal cation reported to be able to bind in the "in-plane" fashion.[128,129,130] Our ESI-MS data not only provide evidence that lanthanide metal cations facilitate formation of G-quadruplexes, but also suggest a new mode of ion-binding in G-quartet structures which is the triple-decker (dodecamer) model, as illustrated in Figure 5-7. We believe this

triple-decker model represents the most stable form of a dodecamer due to very strong ion dipole interactions between trivalent cations and all the O6 carbonyl oxygens atoms from the guanine bases. It is also possible that the G-quartets in an octamer and a dodecamer containing trivalent cations are more closely stacked than those in the octamers containing monovalent and divalent cations. This would further enhance the stability of the stacking G-quartets in the former complexes due to slightly stronger π-π interactions between stacking guanine bases.

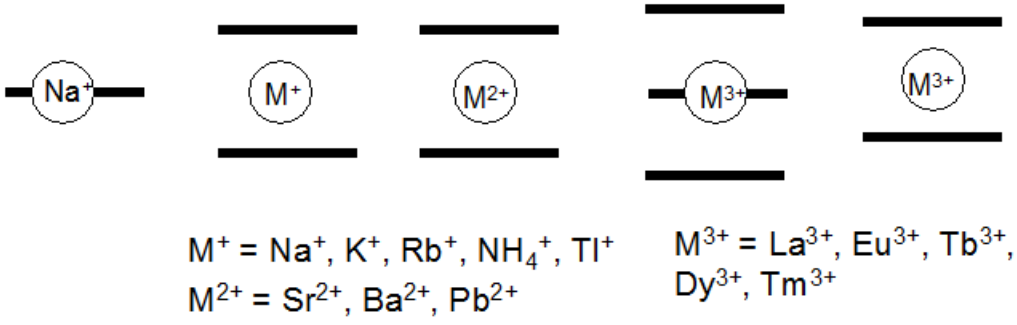

Figure 5-7. Illustrations of the various ion-binding modes in G-quartet systems. The bar represents a G-quartet plane.

We also observed that there is a correlation between the relative abundance of dodecamers and octamers, and the ionic radius of the metal ion. Figure 5-8 shows the relative abundance of dodecamers and octamers of different $[TAG]M^{3+}$ species and the respective ionic radius of the trivalent cations. The abundance of dodecamer decreases as the ionic radius of the metal ion decreases from La^{3+} to Tm^{3+}. This suggests that compared with other lanthanide ions, La^{3+} has an optimal size to fit into the G-quartet

plane to form a very stable ion-filled G-quartet. This is not surprising because with an ionic radius of 1.16 Å (for a coordination number of 8), La^{3+} has an almost identical ionic radius as Na^{+} ions (1.18 Å).[131] Hence La^{3+} can also adopt the in-plane position and form a stable dodecamer. Since Na^{+} has a smaller charge than La^{3+}, the weaker ion-carbonyl interaction explains why a G dodecamer containing a single Na^{+} ion has never been observed.

Since all ESI-MS spectra were obtained under the same condition, we may also use the fragmentation pattern as an indicator of TAG-quadruplex stability. For example, in the MS spectrum of the La^{3+} complex, only G dodecamer signal is observed, which indicates very little fragmentation and the structure of the dodecamer is very stable. However, in the MS spectrum of the Tb^{3+} complex, the signals from the dodecamers and octamers have almost equal intensities, suggesting that the TAG dodecamer containing a Tb^{3+} ion is not as stable as its La^{3+} analog. Using the relative intensities of each aggregate, the stability of TAG dodecamer formation is in the following order: La^{3+} > Eu^{3+} > Tb^{3+} > Dy^{3+} > Tm^{3+}, and that the stability of octamer formation is in the reverse order (Figure 5-8). This observation correlates with the ionic radii of the lanthanide ions and the stability of the octamer or dodecamer formed using these ions.

5.3.1.3 Fluorescence properties of [TAG]M^{3+} G-quadruplexes

Figure 5-9 displays the sensitized luminescence excitation spectrum of Tb^{3+} complex in $CHCl_3$, which exhibits characteristic peaks at 492 ($^5D_4 \rightarrow {}^7F_6$), 545 ($^5D_4 \rightarrow {}^7F_5$) and 584 ($^5D_4 \rightarrow {}^7F_4$) nm, giving rise to a green hue under the UV light. Both TAG monomers and $TbCl_3$ in $CHCl_3$ do not enhance Tb^{3+} fluorescence.[132] Thus formation of a

complex between TAG and Tb^{3+} leads to TAG → Tb^{3+} energy transfer. This indirect transfer of energy from the ligand to Tb^{3+} confirmed the formation of a [TAG]Tb^{3+} complex.

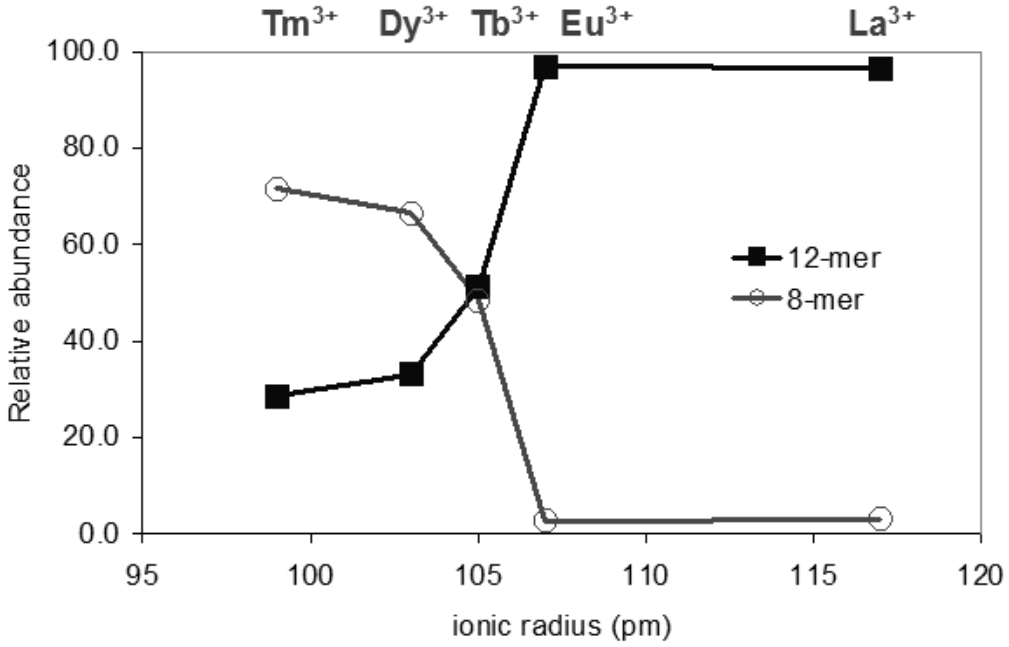

Figure 5-8. Relationship between the relative abundance of TAG dodecamers and TAG octamers observed in ESI-MS(+) spectra, and the ionic radius of the metal ion. All ionic radii correspond to a coordination number of 8.[131]

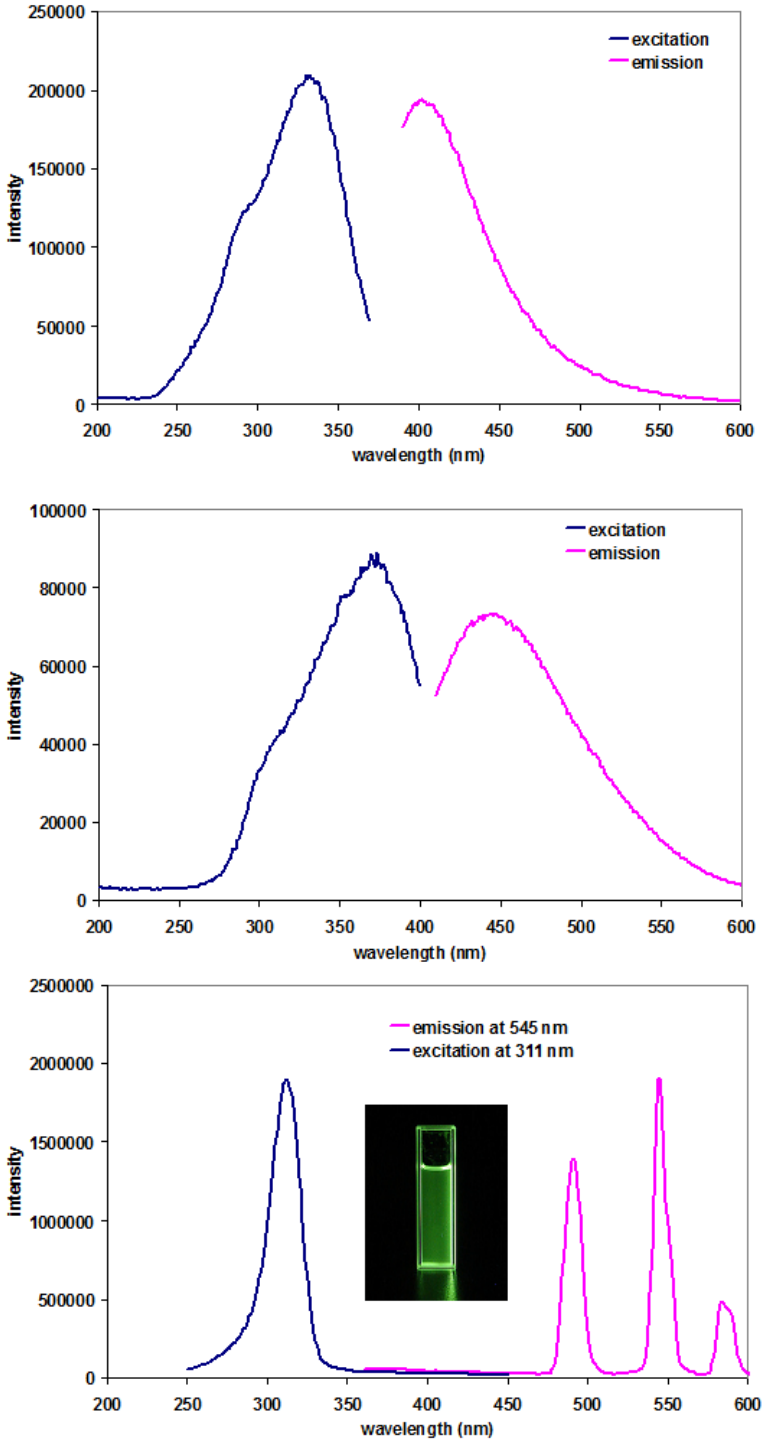

Figure 5-9. Excitation and emission spectra of the sparingly soluble $TbCl_3$ (top), TAG (middle) and the clear TAG-Tb solution (bottom) in $CHCl_3$ at room temperature.

5.3.2 [TAG]Ca^{2+} G-quadruplex

5.3.2.1 Formation of discrete octamers

Figure 5-10 shows the ^1H NMR spectra of monomeric TAG in DMSO and [TAG]Ca^{2+} complex in $CDCl_3$ at different temperatures. Compared to [TAG]M^{3+} complexes discussed earlier, [TAG]Ca^{2+} exhibits a much simpler proton NMR spectrum in which two sets of peaks in 1:1 ratio are observed. This kind of spectral appearance is likely due to the presence of both *syn* and *anti* TAG monomers in equal amounts based on examples reported in the literature.[113] As seem from Figure 5-10, the imino proton N^1H and one of the amino protons N^2H_A are deshielded (9.5-11.5 ppm), suggesting their participation in hydrogen-bonding. All of these observations suggest G-quartet formation. Moreover, according to the 4:1 signal integrations between TAG and the counter-ion picrate (with two protons), we conclude that an octamer is formed with eight TAG monomers and one Ca^{2+} ion. The formation of TAG octamers with M^{2+} cations such as Sr^{2+} and Ba^{2+} was previously observed,[124] and the 8:1 ratio is independent of the picrate concentration in the aqueous phase during the extraction process. This suggests that the [TAG_8]Ca^{2+} octamer is a very stable aggregate in organic phase. Signature intra-quartet cross-peaks (N^2H_A/H8 and N^1H/H8) are observed in the NOESY spectrum of [TAG_8]Ca^{2+}, as shown in Figure 5-11. The size of the octamer species is also confirmed using DOSY experiment, where the average D_t value is of the same magnitude as other octameric species including [TAG_8]Sr^{2+}, [TAG_8]Ba^{2+}, and another similar G derivative reported by Davis (Table 5-3).[133]

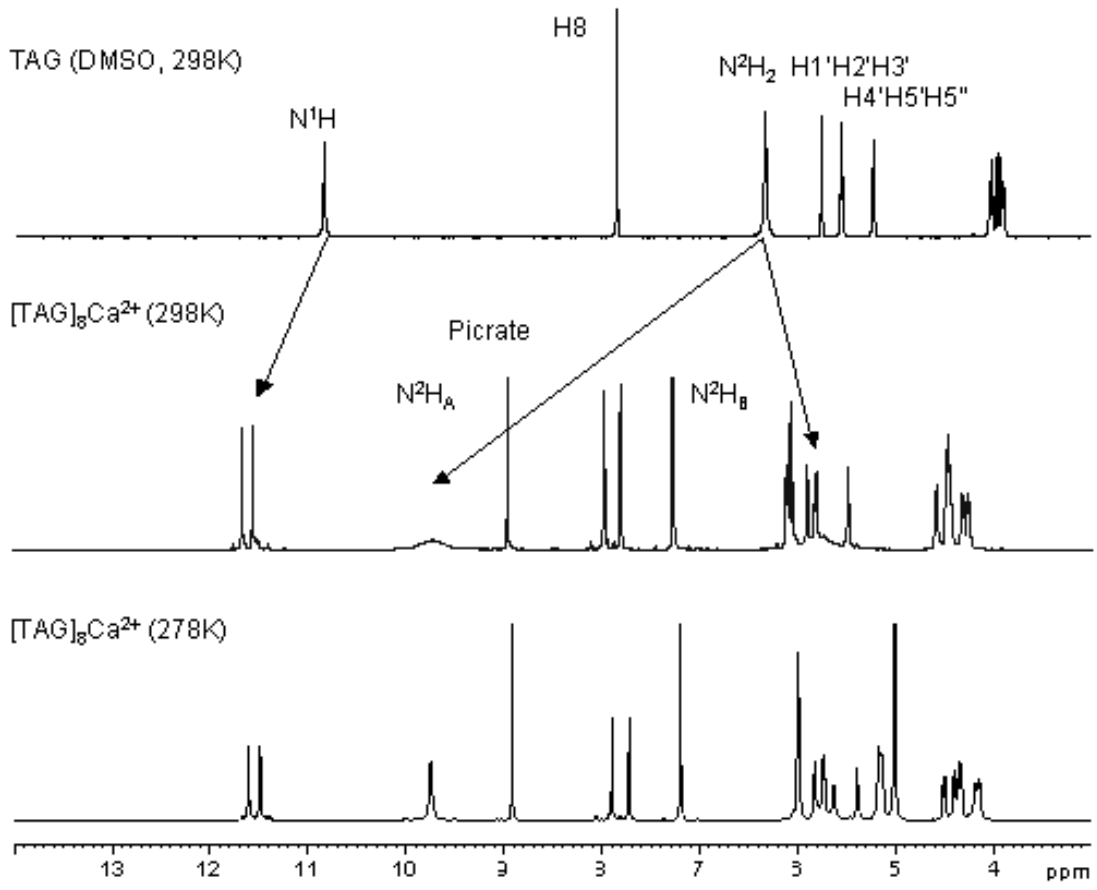

Figure 5-10. ^{1}H NMR spectra of TAG in DMSO and TAG-Ca^{2+} in chloroform.

Moreover, ESI-MS and tandem-MS/MS experiments were performed for the TAG-Ca^{2+} complex (see Appendix IV for detail analysis). As seen from Figure 5-12 and Table 5-4, the octamer peak (m/z 1656.424) is predominant. This also provides evidence that the octamer is composed of two G-quartets and one Ca^{2+}. Because the ionic radius of Ca^{2+} (1.12 Å for a coordination number of 8) is similar to those of Na^{+} (1.18 Å), K^{+} (1.33 Å) and Sr^{2+} (1.26 Å),[131] it is not surprising that a Ca^{2+} ion can fit into the central cavity between two G-quartets.

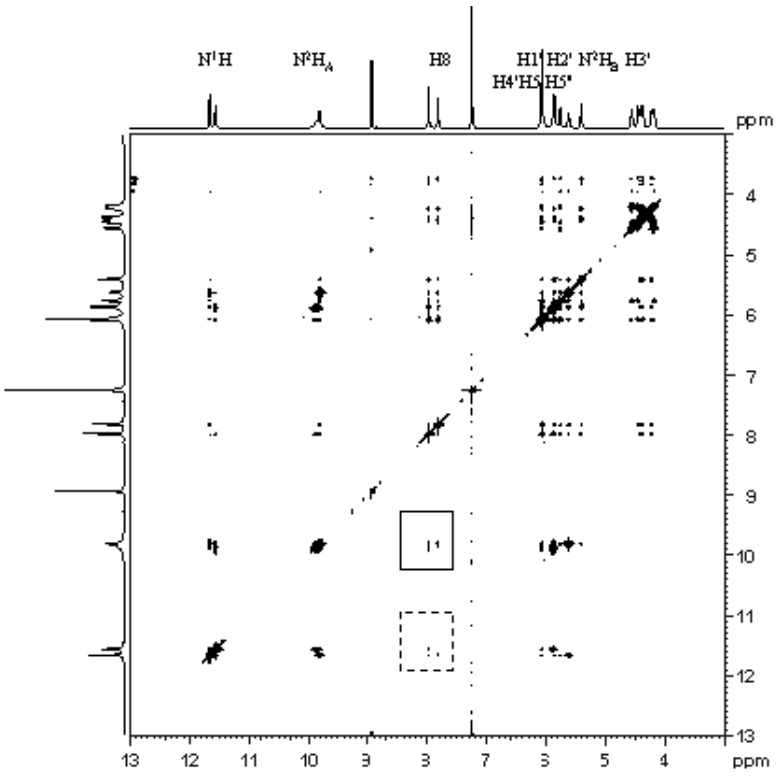

Figure 5-11. NOESY spectrum of the [TAG]Ca-pic$_2$ complex in CDCl3 at 268 K. Cross peaks formed between N^2H_A and H8 were highlighted in the solid box while those formed between N^1H and H8 were enclosed in the dashed box.

Table 5-3. Translational diffusion coefficients of various G octamers in the presence of metal cations.

Octamers (solvent: $CDCl_3$)	Concentration (mM)	Temp. (K)	Average D_t ($x10^{-10}$ m^2/s)	Ref.
$[TAG_8]Sr^{2+}$	1.875	298.2	4.02	124
$[TAG_8]Ba^{2+}$	1.875	298.2	3.68	124
$[TAG_8]Ca^{2+}$	1.875	298.2	3.47	this work
[(5′-O-acetyl-2′,3′-O-isopropylidene)$_8$]2Na·2Pic	1.713	294.2	4.06 ± 0.10	133

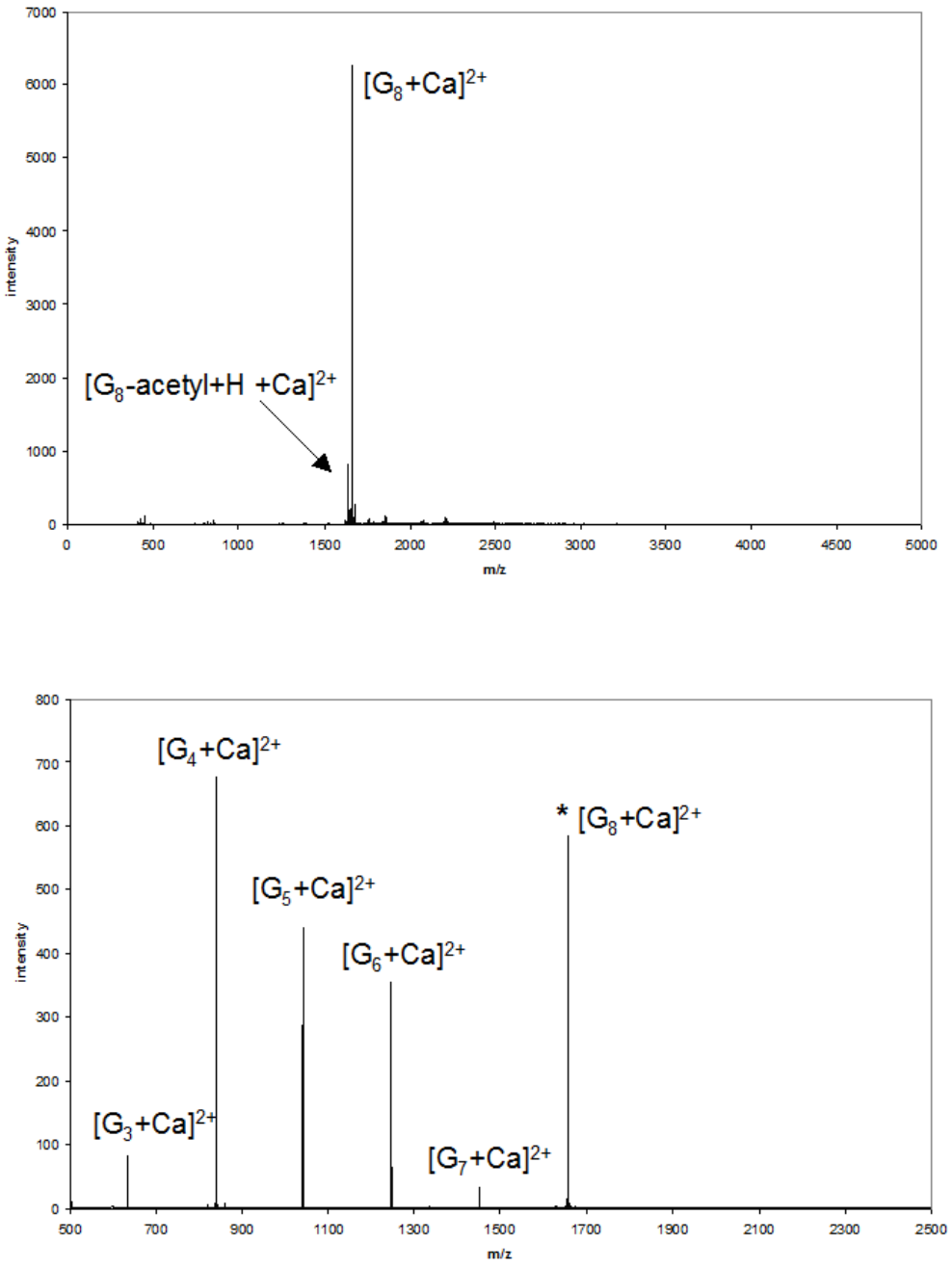

Figure 5-12. Positive mode of high resolution ESI-MS spectra of the $[TAG]Ca^{2+}$ complex (top) and the tandem-MS/MS spectrum of $[TAG_8]Ca^{2+}$ octamer at 1656.424 m/z (bottom). The parent ion is marked by an *. G = monomeric TAG with 409.360 a.m.u.

Table 5-4. Relative intensity of the tandem-MS/MS fragments of $[TAG_8]Ca^{2+}$ at 1656.424 m/z.

$[TAG]_nCa^{2+}{}_n$	*m/z*	Rel. intensity
$[G3+Ca]^{2+}$	633.673	10.6
$[G4+Ca]^{2+}$	838.242	100.0
$[G5+Ca]^{2+}$	1042.804	73.4
$[G6+Ca]^{2+}$	1247.362	58.0
$[G7+Ca]^{2+}$	1451.940	3.5
$[G8+Ca]^{2+}$	1656.504	53.1

5.3.2.2 Direct detection of Ca^{2+} by calcium-43 NMR

After confirming the G-quartet formation, we studied the calcium cation inside the octamer using ^{43}Ca NMR. ^{43}Ca is one of the low-γ quadrupole nuclei (spin = 7/2, natural abundance 0.145 %, Q = -40.8 x 10^{-31} m^2, υ_0 = 40.4 MHz at 14.1 T) that are difficult to study by NMR spectroscopy.[134] Bryant reported the first ^{43}Ca NMR study in 1969 on measuring the relaxation time of Ca-ATP.[135] Many ^{43}Ca NMR studies were performed in the last 40 years on compounds such as organic molecules[136], biological molecules[137], metalloproteins[138], salts[139], cement[140], glass[141], superconductors[142], (hydroxyl)apatite[143], nucleic acids[124,144], and inorganics[145]. Several reviews are excellent sources of information on ^{43}Ca NMR techniques mainly in biological applications.[146] Sugimoto et al. have discovered that calcium concentration lead to polymorphism in G-quadruplex formed by DNA $d(G_4T_4G_4)$.[121a-c] This study would be useful in examining the different Ca^{2+} ion sites between the polymorphs. However, for large G-quadruplexes, ^{43}Ca enrichment of the sample is almost necessary in order to increase NMR sensitivity.

A new approach using magic-angle coil spinning (MACS) detector could also be employed as a low-cost strategy for future ^{43}Ca solid-state NMR spectroscopy.[147] Recently, Bryce presented a comprehensive review with a focus on solid-state ^{43}Ca NMR in both organic and inorganic systems.[148] Figure 5-13 shows the natural abundance ^{43}Ca NMR signals obtained for $CaCl_{2(aq)}$, $CaPic_{2(aq)}$, and TAG-Ca^{2+} in $CDCl_3$ at 14.1 T. The $[TAG_8]Ca^{2+}$ octamer has a distinctive ^{43}Ca signal at -43 ppm.

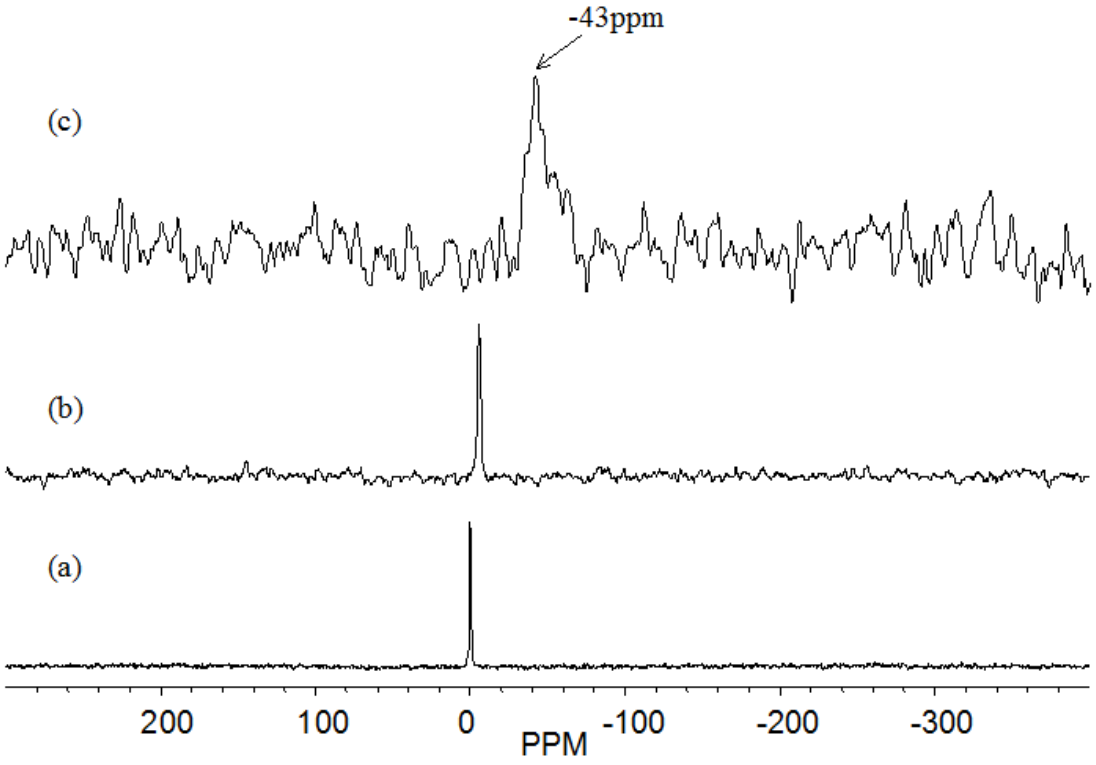

Figure 5-13. Natural abundance ^{43}Ca NMR spectra of (a) $CaCl_{2(aq)}$ (400 transients, 0.25 s recycle delay), (b) $CaPic_{2(aq)}$ (3757 transients, 0.25 s recycle delay), and (c) TAG-Ca^{2+} complex in $CDCl_3$ (approximately 60 mM, 544,890 transients, 0.25 s recycle delay) at 14.1 T. All ^{43}Ca chemical shifts are referenced to $CaCl_{2(aq)}$ at $\delta = 0$ ppm.

5.3.2.3 Quantum chemical calculations

To determine the relationship between the observed ^{43}Ca chemical shift and ion coordination geometry, quantum chemical calculations were performed using four different types of octamer models. The first model (Model I) is based on the crystal structure of 5′-silyl-2′,3′-O-isopropylidene guanosine with one Sr^{2+} ion, except the Sr^{2+} ion is now replaced by a Ca^{2+} ion.[149] Model II is the truncated ^{43}Ca site (Ca55) in Neidle's new crystal structure of a G-quadruplex formed from the DNA strand, $d(TG_4T)$.[122] Model III is the crystal structure of 5′-silyl-2′,3′-O-isopropylidene guanosine with one Na^+ ion, except Na^+ is replaced by a Ca^{2+} in the model. The last model (Model IV) is an octamer composed of geometrically optimized G-quartets (optimization performed at B3LYP/6-311G(d,p)) that are 3.32 Å apart with a Ca^{2+} ion located at the central channel site. All of these four models have one Ca^{2+} ion coordinating to eight guanine O6 atoms in a bipyramidal antiprism fashion as illustrated in Figure 5-14. From the perspective of the Ca^{2+} cation, the main difference between these models is the Ca^{2+}-O6 distance. Table 5-5 shows the calculated ^{43}Ca chemical shifts from these models.

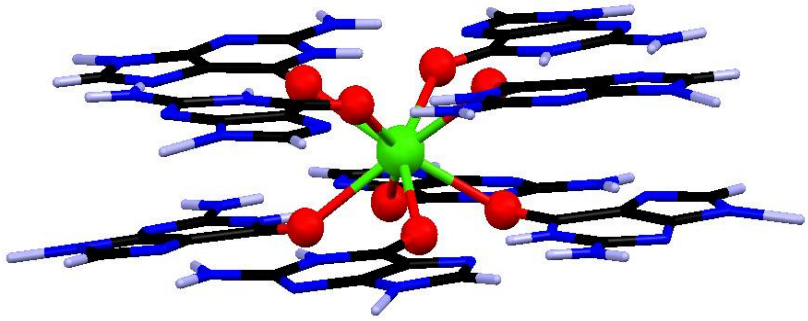

Figure 5-14. $[TAG_8]Ca^{2+}$ octamers model used in quantum chemical calculations. Color scheme: green = Ca^{2+}, red = O6, black = C, blue = N, and gray = H.

Figure 5-15 shows that a correlation exists between the calculated chemical shift and the average Ca-O6 distances. In fact, this strong correlation can be used to determine Ca-O6 distances as demonstrated by previous researchers in organic and inorganic systems.[136d,137a,145b/c/h] As seen from Figure 5-15, the calculated ^{43}Ca chemical shifts from all method and basis set combinations of each model lie within a range of 10 ppm. This is much smaller than the entire ^{43}Ca chemical shift range, i.e., 200 ppm.[134] Therefore the calculated chemical shifts can yield reliable and accurate results. The estimated Ca-O6 distance of the TAG-Ca^{2+} complex is 2.70 ± 0.05 Å. The estimation is reasonable compared to the Ca55 site in d(TG_4T) with a Ca-O6 distance of 2.76 Å.[122]

Table 5-5. Calculated and experimental ^{43}Ca chemical shifts (in ppm) for four models, each contains two G-quartets and a central Ca^{2+} ion. Atoms besides Ca^{2+} are calculated using the same method and basis set 6-31G(d).

Method/basis set (^{43}Ca)	Model I	Model II	Model III	Model IV
HF/6-311++G(d,p)	-38.1	-62.8	-75.0	-63.9
HF/cc-pVTZ	-28.8	-50.8	-63.8	-53.4
HF/Sadlej pVTZ	-34.5	-55.6	-66.8	-57.4
B3LYP/6-311++G(d,p)	-37.2	-63.0	-74.1	-62.9
B3LYP/cc-pVTZ	-26.4	-50.2	-63.5	-52.2
B3LYP/Sadlej pVTZ	-37.9	-61.3	-73.5	-63.4
Experimental	-43 ± 2			

Besides chemical shifts, electric field gradient (EFG) of all Ca^{2+} sites in the four models were also calculated. The calculated EFG's of ^{43}Ca sites are also consistent with

the small magnitude of the ^{43}Ca nuclear quadrupole coupling constants (C_Q). Because C_Q is proportional to line width, it explains the narrow line width (ca. 600 Hz or 15 ppm) observed in the ^{43}Ca spectrum of $[TAG_8]Ca^{2+}$.

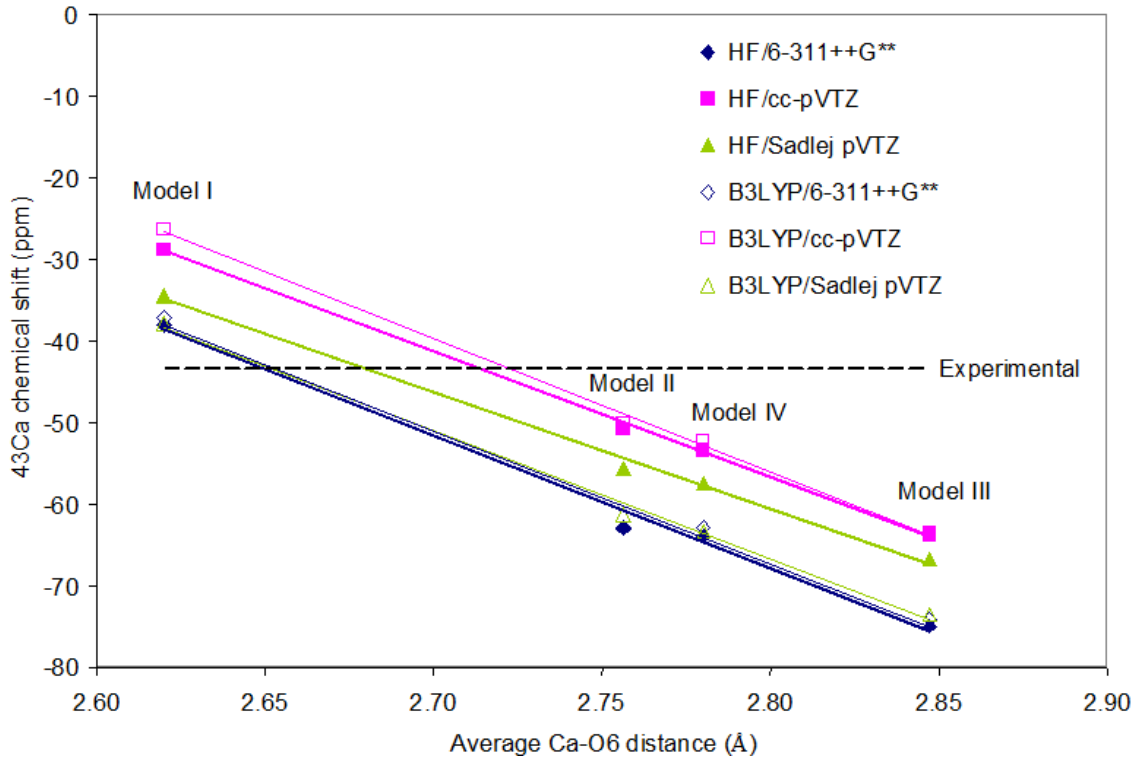

Figure 5-15. Relationship between computed ^{43}Ca chemical shifts and average Ca-O6 distances of four octamers models (see text for model descriptions).

5.4 Conclusion

In this chapter, we have studied a lipophilic G derivative, TAG, and discovered for the first time that trivalent lanthanide metal ions can facilitate G-quartet formation. A new mode of metal ion binding in G-quartet structures, i.e., a triple-decker G dodecamer containing a single metal ion in the central G-quartet is reported. Our findings open up

new possibilities in regard to designing the electronic, magnetic and photonic properties of guanosine-based materials for nanotechnology. Moreover, we report the first ^{1}H and ^{43}Ca NMR characterization of Ca^{2+}-templated G-quartet formation. The ^{43}Ca NMR signature observed for Ca^{2+} ions residing in the channel site provides a benchmark for future studies of Ca^{2+} ion binding in DNA G-quadruplex systems. Because calcium is ubiquitous in biological systems, its role in DNA G-quadruplexes or protein sites should be further investigated.

Chapter 6
Concluding remarks

This thesis documents the study of several G derivatives in forming self-assemblies called G-quadruplexes under various conditions (e.g., pH, cation, concentration, aqueous and lipophilic, etc). We have employed a wide range of spectroscopic techniques such as NMR, ESI-MS, FT-IR, as well as quantum chemical calculations to obtain structural information at the atomic level for these G-quadruplexes when x-ray crystallography is not applicable to our samples. The combination of the above methods enhances the accuracy of structural elucidation compared with previous studies of similar systems for which only bulk structural features were obtained.

As there are not many studies reported in the literature that examine G-quadruplexes formed from mononucleotides such as those discussed in this thesis, our research has produced a significant amount of new information. It is important to note that the greater degree of flexibility of mononucleotides (e.g., sugar pucker, glycosidic bond, exocyclic torsion angle, and the charge of the phosphate group, etc) provides an extra layer of complexity in studying the monomers and the subsequently formed G-quadruplexes compared to polynucleotides with rigid backbones. Moreover, G-quadruplexes with different sizes can also coexist. The presence of four sets of proton signals in neutral Na_2(5'-GMP) and the various distribution of octamers and dodecamers in [TAG]M^{3+} are excellent examples. These conformational changes and wide distribution of sizes often lead to multiple signals that are often too complicated to study. To resolve this problem, we have used a 2D NMR approach called DOSY-NOESY, to

selectively detect signals arising only from G-quadruplex molecules. This method allows us to study coexisting species separately provided that their transitional diffusion rates are considerably different.

We are especially delighted to have solved the structure of Na_2(5'-GMP) G-quadruplex formed under neutral conditions as this structure has been puzzling the scientific world for over 60 years. We also report for the first time the observation of a $GG3^2$ dimer. Our data confirms the alternate structure of a long-believed model of the acidic Na_2(5'-GMP) G-quadruplex, which also has a hollow channel site. This made acidic Na_2(5'-GMP) one of the few examples where channel cations are not required to form a G-quadruplex. The study of Na_2(5'-GSMP) allows us to recognize the power of self-assembly when modifying one single atom could lead to dramatic aggregation abilities between molecules. The introduction of trivalent and Ca^{2+} cations to TAG in organic solvent opens up doors for nanotechnology and ion-channel studies in biological systems, respectively, where these metal cations are often employed. We also discovered a new binding mode for trivalent cations where La^{3+}, with a suitable ionic radius, can sit in-plane in a $[TAG_{12}]La^{3+}$ dodecamer molecule.

In the future, several experiments can be performed to complement our G-quadruplex study. First, we can solve the puckering of 5'-GMP molecules present in dimer and its stacking helix. The chemical shift of the H8β signal sits between the 100% C2'-*endo* (H8α) and 100% C3'-*endo* (H8δ) resonances. It would be interesting to know if dimers undergo conformational change between these two forms or a new type of puckering is present. Secondly, a ^{15}N-labeled guanosine sample can be used in the

$^{15}N\{^{1}H\}$ HETCOR experiment where hydrogen bonding between the phosphate group and N^2H_B can be confirmed in the acidic Na(5'-GMP) sample. Second, our group has published the results in studying the movement of ions (Na^+, K^+, and NH_4^+) in G-quadruplexes DNA channels using computational methods.[150] We can also perform similar calculations on the release rate of channel Na^+ ions when changing the pH of Na_2(5'-GMP) from neutral to acidic condition, where the channel Na^+ ion is no longer present. The stability and population of the Na_2(5'-GMP) G-quadruplexes can also be enhanced by introducing stabilizing agents. The amine groups ($-NH_3^+$) on the ends of the polyamine can bind to surface sites ($-PO_4^{2-}$) of the G-quadruplex, while the long carbon chain can stabilize the structure similar to a "clamp". An ideal size of polyamine is yet to be determined because the amine groups must bind onto phosphate groups of the G-quadruplex that are separated with a specific distance. Moreover, we can also introduce other types of cation to 5'-GMP, such as M^{2+} or M^{3+}, with appropriate ionic radii that can fit into the channel site. G-quadruplex formation can be observed using techniques described in this thesis, and exotic nuclei NMR experiments of these ions can add onto our knowledge of ion channels formed using G-quadruplexes.

References

[1] Miescher, F. "Ueber die chemische Zusammensetzung der Eiterzeller". Medicinisch-chemische Untersuchungen. 1871, 4, 441-460.

[2] Watson, J.D.; Crick, F.H.C. "Molecular structure of nucleic acids: a structure for deoxyribose nucleic acid". *Nature*. **1953**, *171*, 737-738. Wilkins, M.H.F.; Stokes, A.R.; Wilson, H.R. "Molecular structure of nucleic acids: molecular structure of deoxypentose nucleic acids". *Nature*. **1953**, *171*, 738-740. Franklin, R.E.; Gosling, R.G. "Molecular configuration in sodium thymonucleate". *Nature*. **1953**, *171*, 740-741.

[3] Rich, A. "The era of RNA awakening: structural biology of RNA in the early years". *Q. Rev. Biophys.* **2009**, *42(2)*, 117-137.

[4] Saenger, W. *Principles of Nucleic Acid Structure*; Springer-Verlag New York Inc: New York, 1984.

[5] Jeffery, G.A. and Saenger, W. *Hydrogen Bonding in Biological Structures*; Springer-Verlag, Berlin Heidelberg: Germany, 1991.

[6] Wang, A.H.-J.; Quigley, G.J.; Kolpak, F.J.; Crawford, J.L.; Van Boom, J.H.; Van der Marel, G.; Rich, A. "Molecular structure of a left-handed double helical DNA fragment at atomic resolution". *Nature*. **1979**, *282*, 680-686.

[7] Picture credit: Wikipedia (original uploader Richard Wheeler) http://en.wikipedia.org/wiki/File:A-DNA,_B-DNA_and_Z-DNA.png (accessed Sept 17, 2011).

[8] Crick, F.H.C. "Codon-anticodon pairing: the wobble hypothesis". *J. Mol. Biol.*, **1966**, *19*, 548-555.

[9] Hoogsteen, K. "The crystal and molecular structure of a hydrogen-bonded complex between 1-methylthymine and 9-methyladenine". *Acta Cryst*. **1963**, *16*, 907-916.

[10] Nikolova, E.N.; Euane, K.; Wise, A.A.; O'Brien, P.J.; Andricioaei, I.; Al-Hashimi, H.M. "Transient Hoogsteen base pairs in canonical duplex DNA". *Nature.* **2011**, *470*, 498-502.

[11] Bang, I.C. “Untersuchungen über Guanylsäure”. *Biochemische Zeitschrift*, **1910**, *26*, 293-311.

[12] Gellert, M. ; Lipsett, M.N. ; Davies, D.R. “Helix formation by guanylic acid”. *Proc. Natl. Acad. Sci. U.S.A.* **1962**, *48*, 2013-2018.

[13] Miles, H.T.; Frazier, J. “Infrared spectra in D_2O solution of guanylic acid helices and of poly-G”. *Biochim. Biophys. Acta.* **1964**, *79*, 216-220.

[14] Chantot, J.-F.; Sarocchi, M.T.; Guschlbauer, W. “Physiochemical properties of nucleotides 4. Gel formation by guanosine and its analogs”. *Biochemie*. **1971**, *53(3)*, 347-354.

[15] Pinnavaia, T.J.; Marshall, C.L.; Mettler, C.M.; Fisk, C.L.; Miles, H.T.; Becker, E.D. “Alkali metal ion specificity in the solution ordering of a nucleotide, 5'-guanosine monophosphate”. *J. Am. Chem. Soc*. **1978**, *100(11)*, 3625-3627.

[16] Kang, C.; Zhang, X.; Ratliff, R.; Moyzis, R.; Rich, A. “Crystal structure of four-stranded *Oxytricha* telomeric DNA”. *Nature*. **1992**, *356*, 126-131.

[17] Wang, Y.; Patel, D.J. “Solution structure of the human telomeric repeat $d[AG_3(T_2AG_3)_3]$G-tetraplex”. *Structure (Cambridge, MA, United States).* **1993**, *1(4)*, 263-282.

[18] Zahler, A.M.; Williamson, J.R.; Cech, T.R.; Prescott, D.M. “Inhibition of telomerase by G-quartet DNA structures”. *Nature*. **1991**, *350(6320)*, 718-720.

[19] Guschlbauer, W.; Chantot, J.F.; Thiele, D. “Four-stranded nucleic acid structures 25 years later: from guanosine gels to telomere DNA”. *J. Biomol. Struct. Dyn*. **1990**, *8(3)*, 491-511.

[20] Blackburn, E.H. “Structure and function of telomeres”. *Nature*. **1991**, *350(6319)*: 569-573.

[21] Hahn, W.C.; Stewart, S.A.; Brooks, M.W.; York, S.G.; Eaton, E.; Kurachi, A.; Beijersbergen, R.L.; Knoll, J.H.M.; Meyerson, M.; Weinberg, R.A. “Inhibition of telomerase limits the growth of human cancer cells”. *Nat. Med.* **1999**, *5(10)*, 1164-1170.

[22] Han, H.; Hurley, L.H. "G-quadruplex DNA: a potential target for anti-cancer drug design", *Trends Pharmacol. Sci.* **2000**, *21*, 136-142.

[23] Neidle, S.; Parkinson, G. "Telomere maintenance as a target for anticancer drug discovery". *Nat. Rev. Drug Discovery*. **2002**, *1(5)*, 383-393.

[24] Ou, T.-M.; Lu, Y.J.; Zhang, C.; Huang, Z.S.; Wang, X.D.; Tan, J.H.; Chen, Y.; Ma, D.L.; Wong, K.Y.; Tang, J. C.O.; Chan, A.S.C.; Gu, L.Q. "Stabilization of G-quadruplex DNA and down-regulation of oncogene *c-myc* by quindoine derivatives". *J. Med. Chem*. **2007**, *50(7)*, 1465-1474.

[25] Wu, Y.; Brosh, Jr., Y.M. "G-quadruplex nucleic acids and human diseases". *FEBS J.* **2010**, *277(17)*, 3470-3488.

[26] Parkinson, G.N.; Lee, M.P.H.; Neidle, S. "Crystal structure of parallel quadruplexes from human telomeric DNA". *Nature*, **2002**, *417*, 876-880.

[27] Zhou, Y. ; Morais-Cabral, J.H.; Kaufman, A.; MacKinnon, R. "Chemistry of ion coordination and hydration revealed by a K^+ channel–Fab complex at 2.0 Å resolution". *Nature*. **2001**, *414*, 43-48.

[28] MacKinnon, R. "Ion channels: potassium channels and the atomic basis of selective ion condition" (Nobel lecture). *Angew. Chem. Int. Ed.* **2004**, *43*, 4265-4277.

[29] Daivs, J.T.; Tirumala, S.; Jenssen, J.R.; Radler, E. "Self-assembled ionophores from isoguanosine". *J. Org. Chem.***1995**, *60*, 4167-4176.

[30] Forman, S,L.; Fettinger, J.C.; Pieraccini, S.; Gottarelli, G.; Davis, J.T. "Towards artificial ion channels: a lipophilic G-quadruplex". *J. Am. Chem. Soc.* **2000***, 122,* 4060-4067.

[31] Kaucher, M.S.; Harrell, W.A.; Davis, J.T. "A unimolecular G-quadruplex that functions as a transmembrane Na^+ transporter". *J. Am. Chem. Soc.* **2006,** *128(1)*, 38-39.

[32] Van Leeuwen, F.W.B.; Miermans, C.J.H.; Beijleveld, H.; Tomasberger, T.; Davis, J.T.; Verboon, W.; Reinhoudr, D.N. "Selective removal of $^{226}Ra^{2+}$ from gas-field-produced waters". *Environ. Sci. Technol*. **2005**, *39(14),* 5455-5459.

[33] Shi, X.; Mullaugh, K.M.; Fettinger, J.C.; Jiang, Y.; Hofstadler, S.A.; Davis, J.T. "Lipophilic G-quadruplexes are self-assembled ion pair receptors, and the bound anion modulates the kinetic stability of these complexes". *J. Am. Chem. Soc.* **2003**, *125*, 10830-10841.

[34] Ma, L.; Iezzi, M.; Kaucher, M.S.; Lam, Y.-F.; Davis, J.T. "Cation exchange in lipophilic G-quadruplexes: not all binding sites are equal". *J. Am. Chem. Soc.* **2006**, *128(47)*, 15269-15277.

[35] Alberti, P.; Bourdoncle, A.; Saccà, B.; Lacroix, L.; Mergny, J.-L. "DNA nanomachines and nanostructures involving quadruplexes". *Org. Biomol. Chem.* **2006**, *4*, 3389-3391.

[36] Kunstelj, K.; Spindler, L.; Federiconi, F.; Bonn, M.; Drevenšek-Olenik, I.; Čopič, M. "Self-organization of guanosine 5'-monophosphate on mica". *Colloids Surf., B*. **2007**, *59*, 120-127.

[37] Arnal-Herault, C.; Pase, A.; Michau, M.; Cot, D.; Petit, E.; Barboiu, M. "Functional G-quartet macroscopic membrane films". *Angew. Chem. Int. Ed.* **2007**, *46(44)*, 8409-8413.

[38] Sreenivasacchary, N.; Lehn, J.-M. "Structural selection in G-quartet-based hydrogels and controlled release of bioactive molecules". *Chem. Asian J*. **2008**, *3(1)*, 134-139.

[39] Lena, S.; Neviani, P.; Masiero, S.; Pieraccini, S.; Spada, G.P. "Triggering of guanosine self-assembly by light". *Angew. Chem. Int. Ed.* **2010**, *49(21)*, 3657-3660.

[40] Gottarelli, G.; Sapada, G.P. "The stepwise supramolecular organization of guanosine derivatives". *Chem. Rec.* **2004**, *4(1)*, 39-49.

[41] Davis, J.T. "G-quartets 40 years later: from 5'-GMP to molecular biology and supramolecular chemistry". *Angew. Chem. Int. Ed*. **2004**, *43*, 668-698.

[42] Kaucher, M.S.; Harrell Jr., W.A.; Davis, J.T. "The G-quartets in supramolecular chemistry and nanoscience" in *Quadruplex Nucleic Acid*; Neidle, S.; Balasubramanian, S. Ed.; RSC Publishing: Cambridge, **2006**; p 253-296.

[43] Davis, J.T.; Spada, G.P. "Surpamolecular architectures generated by self-assembly of guanosine derivatives". *Chem. Soc. Rev*. **2007**, *36(2)*, 296-313.

[44] Lena, S.; Masiero, S.; Pieraccini, S.; Spada, G.P. "The supramolecular organization of guanosine derivatives". *Mini-reviews in organic chemistry*. **2008**, *5*, 262-273.
[45] Lena, S.; Masiero, S.; Pieraccini, S.; Spada, G.P. "Guanosine hydrogen-bonded scaffolds: a new way to control the bottom-up realization of well-defined nanoarchitectures". *Chem. Eur. J.* **2009**, *15*, 7792-7806.
[46] Sasisekharan, V.; Zimmerman, S.B.; Davies, D.R. "The structure of helical 5'-guanosine monophosphate". *J. Mol. Biol*. **1975**, *92*, 171-179.
[47] Zimmerman, S.B. "X-ray study by fiber diffraction methods of a self-aggregate of guanosine-5'-monophosphate with the same helical parameters as poly(rG)". *J. Mol. Biol.* **1976**, *106*, 663-672.
[48] Pinnavaia, T.J.; Miles, H.T.; Becker, E.D. "Self-assembly of 5'-GMP – NMR evidence for a regular, ordered structure and slow chemical exchange". *J. Am. Chem. Soc.* **1975**, *97(24)*, 7198-7200.

[49] Neurohr, K.L.; Mantsch, H.H. "The self-association of naturally occurring purine nucleoside 5'-monophosphates in aqueous solution". *Can. J. Chem.* **1979**, *57(15)*, 1986-1994.
[50] Fisk, C.L.; Becker, E.D.; Miles, H.T.; Pinnavaia, T.J. "Self-structured guanosine 5'-phosphate heptahydrate". *J. Am. Chem. Soc.* **1982**, *104*, 3307-3314.
[51] Bouhoutsos-Brown, E.; Marshal, C.L.; Pinnavaia, T.J. "Structure-directing properties of Na^+ in the solution ordering of guanosine 5'-monophosphate. Stoichiometry of aggregation, binding to ethdium, and modes of Na^+ complexation". *J. Am. Chem. Soc.* **1982**, *104*, 6576-6584.
[52] Walmsley, J.A.; Barr, R.G.; Bouhoutsos-Brown, E.; Pinnavaia, T.J. "Ordered forms of dianionic guanosine 5'-monophosphate with Na^+ as the structure director. ^1H and ^{31}P NMR studies of hydrogen bonding and comparisons of stacked tetramers and stacked dimmer models". *J. Phys. Chem*. **1984**, *88*, 2599-2605.

[53] Detellier, C.; Laszlo, P. "Role of alkali metal and ammonium cations in the self-assembly of the 5'-gunaosine monophosphate dianion". *J. Am. Chem. Soc.* **1980**, *102(3)*, 1135-1141.

[54] Detellier, C.; Laszlo, P. "Influence of amino acids, ammonium and potassium cations on the self-assembly of 5'-GMP". *Helvetica Chimica Acta*, **1979**, *62(5)*, 1559-1565.

[55] Borzo, M.; Detellier, C.; Laszlo, P.; Paris, A. "^{1}H, ^{23}Na, and ^{31}P NMR studies of the self-assembly of the 5'-guanosine monophosphate dianion in neutral aqueous solution in the presence of sodium cations". *J. Am. Chem. Soc.* **1980**, *102(3)*, 1124-1134.

[56] Peterson, S.B.; Led, J.J.; Johnston, E.R.; Grant, D.M.; Detellier, C.; Laszlo, P. "NMR studies of self-association of disodium guanosine 5'-monophosphate". *J. Am. Chem. Soc.* **1982**, *104(19)*, 5007-5015.

[57] Led, J.J.; Gesmar, H. "^{31}P magnetization-transfer NMR studies of the interchange between structures of self-assembled disodium guanosine 5'-monophosphate in solution". *J. Phys. Chem.* **1985**, *89*, 583-588.

[58] Lipanov, A.A.; Quintana, J.; Dickerson, R.E. "Disordered single crystal evidence for a quadruplex helix formed by guanosine 5'-monophosphate". *J. Biomol. Struct. Dyn.* **1990**, *8(3)*, 483-489.

[59] Gottarelli, G.; Proni, G.; Spada, G.P. "The self-assembly and lyotropic mesomorphism of riboguanylic acids (GMP)". *Liquid Crystals*, **1997**, *22(5)*, 563-566.

[60] Walmsley, J.A.; Burnett, J.F. "A new model for the K^{+}-induced macromolecular structure of guanosine 5'-monophosphate in solution". *Biochemistry*, **1999**, *38*, 14063-14068.

[61] Wu, G.; Wong, A. "Direct detection of the bound sodium ions in self-assembled 5'-GMP gels: a solid-state ^{23}Na NMR approach". *Chem. Commun.* **2001**, 2658-2659.

[62] Wu, G.; Wong, A.; Gan, A.; Davis, J.T. "Direct detection of potassium cations bound to G-quadruplex structures by solid-state ^{39}K NMR at 19.6 T". *J. Am. Chem. Soc.* **2003**, *125*, 7182-7183.

[63] Wong, A.; Wu, G. "Selective binding of monovalent cations to the stacking G-quartet structure formed by guanosine 5'-monophosphate: a solid-state NMR study". *J. Am. Chem. Soc.* **2003**, *125*, 13895-13905.

[64] Jurga-Nowak, H.; Banachowicz, E.; Dobek, A.; Patkowski, A. "Supramolecular guanosine 5'-monophosphate structures in solution. Light scattering study." *J. Phys. Chem. B*. **2004**, *108*, 2744-2750.

[65] Spindler, L.; Drevenšek-Olenik, I.; Čopič, M.; Cerar, J.; Skerjanc, J.; Pariani, P. "Dynamic light scattering and ^{31}P NMR study of the self-assembly of deoxyguanosine 5'-monophosphate: the effect of added salt". *Eur. Phys. J. E*. **2004**, *13*, 27-33.

[66] Wong, A.; Ida, R.; Spindler, L.; Wu, G. "Disodium guanosine 5'-monophosphate self-associates into nanoscale cylinders at pH 8: a combined diffusion NMR spectroscopy and dynamic light scattering study". *J. Am. Chem. Soc*. **2005**, *127*, 6990-6998.

[67] (a) Mikkelsen, K.; Nielsen, S.O. "Acidity measurement with the glass electrode in H_2O-D_2O mixtures". *J. Phys. Chem.* **1960**, *64*, 632–637. (b) Glasoe, P.K.; Long, F.A. "Use if glass electrodes to measure acidities in deuterium oxide". *J. Phys. Chem.* 1960, *64,* 188–190.

[68] Van Geet, A.L."Calibration of methanol nuclear magnetic resonance thermometer at low temperature". *Anal. Chem.* **1970**, *42(6)*, 679-680.

[69] Ten Cate, A.T.; Dankers, P.Y.W.; Kooijman, H.; Spek, A.L.; Sijbesma, R.P.; Meijer, E.W. "Enantioselective cyclization of racemic supramolecular polymers", *J. Am. Chem. Soc.* **2003**, *125*, 6860-6861.

[70] Kohlmann, O.; Steinmetz, W.E.; Mao, X.A.; Wuelfing, W.P.; Templeton, A.C.; Murray, R.W.; Johnson, C.S. "NMR diffusion, relaxation, and spectroscopic studies of water soluble, monolayer-protected gold nanoclusters", *J. Phys. Chem. B,* **2001**, *105*, 8801-8809.

[71] a) Einstein. A. "Über die von der molekularkinetischen Theorie der Wärme geforderte Bewegung von in ruhenden Flüssigkeiten suspendierten Teilchen", *Ann. Physik*, **1905**,

322(8), 549-560. b) Stokes, G.G. "On the steady motion of incompressible fluids". *Transactions of the Cambridge Philosophical Society*, **1842**, *7*, 439–453.

[72] (a) Tirado, M.M.; Garcia de la Torre, J. "Translational friction coefficients of rigid, symmetric top macromolecules. Application to circular cylinders". *J. Chem. Phys.* **1979**, *71*, 2581-2587. (b) Tirado, M.M.; Garcia de la Torre, J. "Rotational dynamics of rigid, symmetric top macromolecules. Application to circular cylinders". *J. Chem. Phys.* **1980**, *73*, 1986-1993. Tirado, M.M.; Lopez Martinez, C.; Garcia de la Torre, J. "Comparison of theories for the translational and rotational diffusion coefficients of rod-like molecules. Application to short DNA fragments". *J. Chem. Phys.* **1984**, *81*, 2047-2052.

[73] Cho, C.H.; Urquidi, J.; Singh, S.; Wilse Robinson, G. "Thermal offset viscosities of liquid H_2O, D_2O, and T_2O". *J. Phys. Chem. B.* **1999**, *103*, 1991-1994

[74] Figure adopted from www.intermnet.ua.es/inteRMNet/doc/chem843-4.PDF, copyright by Gerd Gemmecker, 1999 (accessed October 1, 2011).

[75] Keeler, J. *Understanding NMR Spectrscopy*; John Wiley & Sons Ltd: West Sussex, UK, 2005.

[76] Neuhaus, D.; Wagner, G.; Vašák, M.; Kägi, J.H.R.; Wüthrich, K. "Systematic application of high-resolution, phase-sensitive two-dimensional ^{1}H-NMR techniques for the identification of the amino-acid-proton spin systems in proteins Rabbit metallothionein-2". *Eur. J. Biochem.* **1985**, *151*, 257-273.

[77] Wijmenga, S.S.; Van Buuren, B.N.M. "The use of NMR methods for conformational studies of nucleic acids". *Prog. Nucl. Magn. Reson. Spectrosc.* **1998**, *32*, 287-387.

[78] Pavia, D.L., Lapman, G.M., Kirz, G.S., and Vyvyan, J.A. *Introduction to Spectroscopy*, Brooks/Cole, Cengage Learning: Belmont, USA, 2001.

[79] Ippel, J.H.; Wijmenga, S.S.; de Jong, R.; Heus, H.A.; Hilbers, C.W.; de Vroom, E.; Van der Marel, G.A.; Van Boom, J.H. *Magn. Reson. Chem*. **1996**, *34*, S156-S176. "Heteronuclear scalar couplings in the bases and sugar rings of nucleic acids: their determination and application in assignment and conformational analysis"

[80] Phan, A.T. "Through-bond correlation of sugar and base protons in unlabeled nucleic acids*". J. Magn. Reson.* **2001**, *153*, 223-226.

[81] (a) Karplus, M. "Contact electron-spin coupling of nuclear magnetic moments". *J. Chem. Phys*. 1959, *30,* 11-15. (b) Karplus, M. "Vicinal proton coupling in nuclear magnetic resonance". *J. Am. Chem. Soc*. **1963**, *85*, 2870-2871.

[82] Lerner, L.E. "Chapter 7: Carbohydrate structures and dynamics from NMR". In *NMR Spectroscopy and Its Application to Biomedical Research*; Sarkar, S.K., Ed.; Elsevier B.V., 1996; pg. 313-344.

[83] Weber, P.L. "Chapter 4: Protein structure determination from NMR data". In *NMR Spectroscopy and Its Application to Biomedical Research*; Sarkar, S.K., Ed.; Elsevier B.V., 1996; pg. 187-239.

[84] Wemmer, D.E. "Chapter 6: Nucleic acid structure and dynamics from NMR". In *NMR Spectroscopy and Its Application to Biomedical Research*; Sarkar, S.K., Ed.; Elsevier B.V., 1996; pg. 281-312.

[85] (a) Becke, A.D. "Density-functional thermochemistry. III. The role of exact exchange*". J. Chem. Phys.* **1993**, *98*, 5648. (b) Lee, C.; Yang, W.; Parr, R.G. "Development of the Colle-Salvetti correlation-energy formula into a functional of the electron density". *Phys. Rev. B*, **1988**, *37*, 785.

[86] 6-311++G(d,p) basis set reference: H, Li-Ne: Krishnan, R.; Binkley, J.S.; Seeger, R.; Pople, J.A. *J. Chem. Phys.* **1980**, *72*, 650; Na-Ar: McLean, A.D., Chandler , G.S. *J. Chem. Phys.* 1980, *72*, 5639; K-Ca: Blaudeau, J-P., McGrath, M. P., Curtiss, L.A., Radom, L. *J. Chem. Phys.* 1997, *107*, 5016; Ga-Kr: Curtiss, L. A., McGrath, M. P., Blandeau, J-P., Davis, N. E., Binning, R. C., Radom, Jr. L. *J. Chem. Phys.* **1995**, *103*, 6104; Glukhovstev, M.N., Pross, A., McGrath, M.P., Radom, L. *J. Chem. Phys.***1995**, *103*, 1878.

[87] Frisch, M.J.; Trucks, G.W.; Schlegel, H.B.; Scuseria, G.E.; Robb, M.A.; Cheeseman, J. R.; Montgomery Jr., J. A.; Vreven, T.; Kudin, K.N.; Burant, J.C.; Millam, J.M.; Iyengar, S.S.; Tomasi, J.; Barone, V.; Mennucci, B.; Cossi, M.; Scalmani, G *Inorg. Chim. Acta*.;

Rega, N.; Petersson, G.A.; Nakatsuji, H.; Hada, M.; Ehara, M.; Toyota, K.; Fukuda, R.; Hasegawa, J.; Ishida, M.; Nakajima, T.; Honda, Y.; Kitao, O.; Nakai, H.; Klene, M.; Li, X.; Knox, J.E.; Hratchian, H.P.; Cross, J.B.; Bakken, V.; Adamo, C.; Jaramillo, J.; Gomperts, R.; Stratmann, R.E.; Yazyev, O.; Austin, A.J.; Cammi, R.; Pomelli, C.; Ochterski, J.; Ayala, P.Y.; Morokuma, K.; Voth, G.A.; Salvador, P.; Dannenberg, J. J.; Zakrzewski, V.G.; Dapprich, S.; Daniels, A.D.; Strain, M.C.; Farkas, O.; Malick, D.K.; Rabuck, A.D.; Raghavachari, K.; Foresman, J.B.; Ortiz, J.V.; Cui, Q.; Baboul, A. G.; Clifford, S.; Cioslowski, J.; Stefanov, B.B.; Liu, G.; Liashenko, A.; Piskorz, P.; Komaromi, I.; Martin, R.L.; Fox, D.J.; Keith, T.; Al-Laham, M.A.; Peng, C.Y.; Nanayakkara, A.; Challacombe, M.; Gill, P.M.W.; Johnson, B.G.; Chen, W.; Wong, M.W.; Gonzalez, C.; Pople, J.A. GAUSSIAN 03 (Revision C.02), Gaussian, Inc., Wallingford, CT, 2004.

[88] Morin, F.G.; Solum, M.S.; Withers, J.D.; Grant, D.M.; Dalling, D.K." The temperature dependence of the magnetic susceptibility and proton and carbon-13 chemical shifts of tetramethylsilane". *J. Magn. Reson.* **1982**, *48*, 138-142.

[89] Altona, C.; Sundaralingan, M. "Conformational analysis of the sugar ring in nucleosides and nucleotides. A new description using the concept of pseudorotation." *J. Am. Chem. Soc.* **1972**, *94*, 8205-8212.

[90] Wu, G.; Kwan, I.C.M. "Helical structure of disodium 5'-guanosine monophosphate self-assembly in neutral solution". *J. Am. Chem. Soc.* **2009**, *131*, 3180-3182.

[91] Zimmerman, S.B.; Gerson, H.C.; Davies, D.R. "X-ray fiber diffraction and model-building study of polyguanylic acid and polyinosinic acid". *J. Mol. Biol.* **1975**, *92*, 181-192.

[92] Jeffrey, G.A.; Saenger, W. *Hydrogen Bonding in Biological Structures*. Springer-Verlag, Berlin, 1991.

[93] Rich, A. "Molecular structure of polyinosinic acid". *Biochim. Biophys. Acta*, **1958**, *29*, 502-509.

[94] Homer, R.B.; Mason, S.F. "Helix formation by guanosine 5'-phosphate". *Chem. Commun*. **1966**, *11*, 332-333.

[95] Chantot, J. F. "Nucleoside conformation. IX. A calorimetric study of gel formation by guanylic acids". *Arch. Biochem. Biophys*. **1972**, *153*, 347-356.

[96] Gullion, T.; Vega, A. J. "Measuring heteronuclear dipolar couplings for I = 1/2, S > 1/2 spin pairs by REDOR and REAPDOR NMR". *Prog. Nucl. Magn. Reson. Spectrosc.* **2005**, *47*, 123-136.

[97] Bak, M.; Rasmussen, J.T.; Nielsen, N.C. "SIMPSON: a general simulation program for solid-state NMR spectroscopy". *J. Magn. Reson.* **2000**, *147*, 296-330.

[98] Rossi, P.; Harbison, G. S. "Calculation of ^{13}C chemical shifts in RNA nucleosides: structure-^{13}C chemical shift relationships". *J. Magn. Reson.* **2001**, *151*, 1–8.

[99] Ohlenschläger, O.; Haumann, S.; Ramachandran, R.; Görlach, M. "Conformational signatures of ^{13}C chemical shifts in RNA ribose". *J. Biomol. NMR.* **2008**, *42*, 139–142.

[100] Katti, S. K.; Seshadri, T. P.; Viswamitra, M. A. "Structure of disodium guanosine 5'-phosphate heptahydrate". *Acta Crystallogr., Sect. B: Struct. Sci.* **1981**, *B37(10)*, 1825-31.

[101] Tajmir-Riahi, H.-A. "A comparative study of adenylic, guanylic and deoxyguanylic acids and their sodium salts as solid and in solution: structural information and conformational features". *Biochim. Biophys. Acta.* **1989**, *1009*, 168-176.

[102] Gullion, T.; Schaefer, J. "Rotational-echo double-resonance NMR". *J. Magn. Reson.* **1989**, *81*, 196-200.

[103] Wong, A.; Fettinger, J. C.; Forman, S. L.; Davis, J. T.; Wu, G. "The sodium ions inside a G-quadruplex channel as probed by solid-state ^{23}Na NMR". *J. Am. Chem. Soc.* **2002**, *124*, 742–743.

[104] Tikhomirov, G.; Brouwer, D.H.; Myles, A.J.; Bouatra, S.; Fenniri, H. "Elucidation of hydrogen bonding network of rosette nanotubes by solid-state NMR". (Manuscript in preparation, as shown in the 2007-2008 Annual Report of the National Ultrahigh-Field NMR Facility for solids).

[105] Delville, A.; Detellier, C.; Laszlo, P. "Determination of the correlation time for a slowly reorienting spine-3/2 nucleus: binding of Na^+ with the 5'-GMP supramolecular assembly". *J. Magn. Reson.* **1979**, *34*, 301-315.

[106] Wong, A.; Ida, R.; Wu, G. "Direct NMR detection of "invisible" alkali metal cations tightly bound to G-quadruplex structures". *Biochem. Biophys. Res. Commun.* **2005**, *337*, 363-366.

[107] Ida, R.; Wu, G. "Direct NMR detection of alkali metal ions bound to G-quadruplex DNA". *J. Am. Chem. Soc.* **2008***, 130*, 3590-3602.

[108] Zhang, B.; Cui, Z.; Sun, L. "Synthesis of 5'-Deoxy-5'-thioguanosine-5'-monophosphorothioate and its incorporation into RNA 5'-termini". *Org. Lett*. **2001**, *3*, 275-278.

[109] Jang, Y.H.; Goddard III, W.A.; Noyes, K.T.; Sowers, L.C.; Hwang, S.; Chung, D.S. "pK_a values of guanine in water: density functional theory calculations combined with Poisson-Boltzmann Continuum-Solvation model". *J. Phys. Chem. B.* **2003**, *107*, 344-357.

[110] Kwan, I.C.M.; Delley, R.J.; Hodgson, D.R.W.; Wu, G. "Single atom modification leads to enhanced nucleotide self-assembly: the role of cation bridging". *Chem. Commun.* **2011**, *47*, 3882-3884.

[111] Hightower, J.B.; Olmos, D.R.; Walmsley, J.A. "Supramolecular structure and polymorphism of alkali metal salts of guanosine 5'-monophosphate: SEM and NMR study". *J. Phys. Chem. B.* **2009**, *113(36)*, 12214-12219.

[112] Neidle, S.; Balasubramanian, S. Ed. *Quadruplex Nucleic Acids*; Royal Society of Chemistry, Cambridge: UK, 2006.

[113] Marlow, A.L.; Mezzina, E.; Spada, G.P.; Masiero, S.; Davis, J.T.; Gottarelli, G. "Cation-templated self-assembly of a lipophilic deoxyguanosine: solution structure of a K^+-dG8 octamer". *J. Org. Chem.* **1999**, *64*, 5116-5123.

[114] Gottarelli, G.; Masiero, S.; Spada, G. P. "Self-assembly in organic solvents of a deoxyguanosine derivative induced by alkali metal picrates". *Chem. Commun.* **1995**, *24*, 2555-2557.

[115] Sessler, J. L.; Sathiosatham, M.; Doerr, K.; Lynch, V.; Abboud, K.A. "A G-quartet formed in the absence of a templating metal cation: A New 8-(N,Ndimethylaniline) guanosine derivative". *Angew. Chem., Int. Ed*.. **2000**, *39*, 1300–1303.

[116] Kotch, F.W.; Sidorov, V.; Kayser, K.; Lam, Y. F.; Kaucher, M.S.; Li, H.; Davis, J.T. "Water-mediated association provides an ion pair receptor". *J. Am. Chem. Soc*. **2003**, *125*, 15140– 15150.

[117] Otero, R.; Schock, M.; Molina, L.M.; Laegsgaard, E.; Strensgaard, I.; Hammer, B.; Besenbacher, F. "Guanine quartet networks stabilized by cooperative hydrogen bonds". *Angew. Chem., Int. Ed*.. **2005**, *44*, 2270–2275.

[118] Hud, N.V. Ed. *Nucleic Acid-Metal Ion Interactions*; Royal Society of Chemistry, Cambridge: UK, 2009.

[119] Kwan, I.C.M.; She, Y.-M.; Wu, G. "Trivalent lanthanide metal ions promote formation of stacking G-quartets". *Chem. Commun*. **2007**, 4286.

[120] Toehl, J.; Eimer, W. "Interaction of a G-DNA quadruplex with mono- and divalent cations. A force field calculation". *Biophys. Chem.* **1997**, *67(1-3)*, 177-186.

[121] (a) Miyoshi, D.; Nakao, A.; Toda, T.; Sugimoto, N. "Effect of divalent cations on antiparallel G-quartet structure of d(G4T4G4)". *FEBS Lett.* **2001**, *496(2,3)*, 128-133. (b) Miyoshi, D.; Nakao, A.; Sugimoto, N. "Structural transition from antiparallel to parallel G-quadruplex of d(G4T4G4) induced by Ca^{2+} ". *Nucleic Acids Res.* **2003**, *31(4)*, 1156-1163. (c) Miyoshi, D.; Matsumura, S.; Li, W.; Sugimoto, N. "Structural polymorphism of telomeric DNA regulated by pH and divalent cation". *Nucleosides Nucleotide Nucleic Acid.* **2003**, *22(2)*, 203-221.

[122] Lee, M.P.H.; Parkinson, G.N.; Hazel, P.; Neidle, S. "Observation of the coexistence of sodium and calcium ions in a DNA G-quadruplex ion channel*". J. Am. Chem. Soc.* **2007**, *129*, 10106-10107.

[123] Van Leeuwen, F.W.B.; Davis, J.T.; Verboom, W.; Reinhoudt, D.N. "Non-covalent (iso)guanosine-based ionophores for alkali(ne earth) cations". *Inorg. Chim. Acta*, **2006**, *359(6)*, 1779-1785.

[124] Kwan, I.C.M.; She, Y.-M.; Wu, G. "Nuclear magnetic resonance and mass spectrometry studies of 2',3',5'-O-triacetylguanosine self-assembly in the presence of alkaline earth metal ions (Ca^{2+}, Sr^{2+}, Ba^{2+}). *Can. J. Chem.* **2011**, *89*, 835-844.

[125] Kwan, I.C.M.; Wong, A.; She, Y.-M.; Smith, M. E.; Wu, G. "Direct NMR evidence for Ca^{2+} ion binding to G-quartets". *Chem. Commun,* **2008**, 682.

[126] Sadlej, A.J. "Medium-size polarized basis sets for high-level-correlated calculations of molecular electric properties. IV. Third-row atoms: Ge through Br". *Theor. Chim. Acta*, **1992**, *81*, 45–63.

[127] Kwan, I.C.M. "Nuclear magnetic resonance and computational studies of cation-directed self-assembly of guanosine derivatives". M.Sc. thesis, Queen's University, Kingston, ON, Canada. **2007**.

[128] Fukushima, K.; Iwahashi, H. "Complex of guanine quartet with alkali metal cations detected by electrospray ionization mass spectrometry". *Chem. Commun.* **2000**, 895–896.

[129] (a) Laughlan, G.; Murchie, A.I.H.; Norman, D.G.; Moore, M.H.; Moody, P.C.E.; Lilley, D.M.J.; Luisi, B. "The high-resolution crystal structure of a parallel-stranded guanine tetraplex". *Science.* **1994**, *265,* 520–524. (b) Phillips, K.; Dauter, Z.; Murchie, A.I.H.; Lilley, D.M.J.; Luisi, B. "The crystal structure of a parallel-stranded guanine tetraplex at 0.95 Å resolution". *J. Mol. Biol.* **1997**, *273*, 171–182.

[130] Horvath, M.P.; Schultz, S.C. "DNA G-quartets in a 1.86 Å resolution structure of an oxytricha nova telomeric protein-DNA complex". *J. Mol. Biol.* **2001**, *310*, 367–377.

[131] Shannon, R.D. "Revised effective ionic radii and systematic studies of interatomic distances in halides and chalcogenides". *Acta Crystallogr., Sect. A: Cryst. Phys., Diffr., Theor. Gen. Cryst.,* **1976**, *32*, 751–767.

[132] Kato, D.; Shimoda, K. "Fluorescence spectrum of Tb^{3+} in the $POCl_3{\cdot}SnCl_4$ liquid", *Japan J. Appl. Phys.* **1970**, *9*, 581-582.

[133] Kaucher, M.S.; Lam, Y.-F.; Pieraccini, S.; Gottarelli, G.; Davis, J.T. "Using diffusion NMR to characterize guanosine self-association: insights into structure and mechanism". *Chem. Eur. J.* **2005**, *11*, 164-173.

[134] Smith, M.E. "Recent progress in solid-state NMR of low-γ nuclei". *Annu. Rep. NMR Spectrosc*. **2001**, *43*, 121–175.

[135] Bryant, R.G. "Nuclear magnetic resonance study of calcium-43". *J. Am. Chem. Soc*. **1969**, *91(7)*, 1870-1871.

[136] *Organic*: (a) Drakenberg, T. "Calcium-43 NMR relaxation times and quadrupole coupling constants for some small calcium complexes". *Acta Chem. Scand. Ser. A*. **1982**, *A36(1)*, 79-92. (b) Bryant, R.G.; Ganapathy, S.; Kennedy, S.D. "High-resolution calcium-43 NMR in solids". *J. Magn. Reson.* **1987**, *72(2)*, 376-378. (c) Bouhoutsos-Brown, E.; Murk Rose, D.; Bryant, R.G. "High resolution alkaline earth NMR". *J. Inorg. Nucl. Chem.* **1981**, *43(10)*, 2247-2248. (d) Wong, A.; Laurencin, D.; Wu, G.; Dupree, R.; Smith, M.E. "An Ab Initio Quantum Chemical Investigation of ^{43}Ca NMR Interaction Parameters for the Ca^{2+} Sites in Organic Complexes and in Metalloproteins". *J. Phys. Chem. A*. **2008**, *112(40)*, 9807-9813. (e) Laurencin, D.; Gervais, C.; Wong, A.; Coelho, C.; Mauri, F.; Massiot, D.; Smith, M.E.; Bonhomme, C. "Implementation of high resolution ^{43}Ca solid state NMR spectroscopy: toward the elucidation of calcium sites in biological materials". *J. Am. Chem. Soc.* **2009**, *131(37)*, 13430. (f) Pallagi, A.; Sebok, P.; Forgo, P.; Jakusch, T.; Palinko, I.; Sipos, P. "Multinuclear NMR and molecular modelling investigations on the structure and equilibria of complexes that form in aqueous solutions of Ca^{2+} and gluconate". *Carbohy. Res.* **2010**, *345(13)*, 1856-1864. (g) Pallagi, A.; Dudas, C.; Csendes, Z.; Forgo, P.; Palinko, I.; Sipos, P. "Structure and equilibria of Ca2+-complexes of glucose and sorbitol from multinuclear (^{1}H, ^{13}C and ^{43}Ca) NMR measurements supplemented with molecular modeling calculations". *J. Mol. Struct.* **2011**, *993(1-3)*, 336-340.

[137] *Biological compounds*: (a) Wong, A.; Howes, A.P.; Dupree, R.; Smith, M.E. "Natural abundance ^{43}Ca NMR study of calcium-containing organic solids: A model study for Ca-binding biomaterials". *Chem. Phys. Lett*. **2006**, *427*, 201-205. (b) Xu, J.; Zhu, P.; Gan, Z.; Sahar, N.; Tecklenburg, M.; Morris, M.D.; Kohn, D.H.; Ramamoorthy, A. "Natural-abundance ^{43}Ca solid-state NMR spectroscopy of bone". *J. Am. Chem. Soc.* **2010**,

132(33), 11504-11509. (c) Laurencin, D.; Wong, A.; Chrzanowski, W.; Knowles, J.C.; Qiu, D.; Pickup, D.M.; Newport, R.J.; Gan, Z.; Duer, M.J.; Smith, M.E. "Probing the calcium and sodium local environment in bones and teeth using multinuclear solid state NMR and X-ray absorption spectroscopy". *Phys. Chem. Chem. Phys.* **2010**, *12(5)*, 1081-1091.

[138] *Metalloproteins:* (a) Parello, J.; Lilja, H.; Cave, A.; Lindman, B. "A calcium-43 NMR study of the binding of calcium to parvalbumins" *FEBS Lett*. **1978**, *87*, 191–195. (b) Andersson, T.; Drakenberg, T.; Forsen, S.; Wieloch, T.; Lindstrom, M. "Calcium binding to porcine pancreatic prophospholipase A2 studied by calcium-43 NMR". *FEBS Lett*. **1981**, *123*, 115–117. (c) Andersson, T.; Drakenberg, T.; Forsen, S.; Thulin, E.; Swaerd, M. "Direct observation of the calcium-43 NMR signals from calcium(2+) bound to proteins". *J. Am. Chem. Soc*. **1982**, *104*, 576–580. (d) Shimizu, T.; Hatano, M.; Nagao, S.; Nozawa, Y. "Calcium-43 NMR studies of calcium(2+)-tetrahymena calmodulin complexes". *Biochem. Biophys. Res. Commun*. **1982**, *106*, 1112–1118. (e) Svaerd, M.; Drakenberg, T.; Anderson, T.; Fernlund, P. "Calcium binding to bone γ-carboxyglutamic acid protein from calf studied by calcium-43 NMR". *Eur. J. Biochem.* **1986**, *158(2)*, 373-378. (f) Drakenberg, T.; Andersson, T.; Forsen, S.; Wieloch, T. "Calcium ion binding to pancreatic phospholipase A2 and its zymogen: a calcium-43 NMR study". *Biochemistry.* **1984**, *23(11)*, 2387-2392. (g) Vogel, H.J.; Braunlin, W.H. "Shift reagents for calcium-43 NMR studies of calcium-binding proteins". *J. Magn. Reson*, **1985**, *62(1)*, 42-53. h) Ogoma, Y.; Shimizu, T.; Hatano, M.; Fujii, T.; Hachimori, A.; Kondo, Y. "Calcium-43 nuclear magnetic resonance spectra of calcium(2+)-S100 protein solutions". *Inorg. Chem.* **1988**, *27(11)*, 1853-1855. (h) Shimizu, T.; Hatano, M. "Calcium-43 nuclear magnetic resonance of calcium(2+)-calmodulin solutions: effects of trifluoperazine and peptides". *Inorganica Chimica Acta*, **1988**, *152(4)*, 257-260. (i) Martin, S.R.; Linse, S.; Johansson, C.; Bayley, P.M.; Forsen, S."Protein surface charges and Ca^{2+} binding to individual sites in calbindin D9k: stopped-flow studies". *Biochemistry*. **1990**, *29*, 4188–4193. (j) Aramini, J.M.; Drakenberg, T.; Hiraoki, T.; Ke, Y.; Nitta, K.; Vogel, H.J. "Calcium-43

NMR studies of calcium-binding lysozyms and α-lactalbumins". *Biochemistry*. **1992**, *31*, 6761–6768. (k) Ogoma, Y.; Kobayashi, H.; Fuiji, T.; Kondo, Y.; Hachimori, A.; Shimizu, T.; Hatano, M. "Binding study of metal ions of S100 protein: calcium-43, magnesium-25, zinc-65 and potassium-29 NMR". *Int. J. Biol. Macromol.* **1992**, *14(5)*, 279-286. (l) Wahlgren, N.; Dejmek, M.D.P.; Drakenberg, T. " Binding of magnesium and calcium to β-casein A1: a multi-nuclear magnetic resonance study". *J. Dairy Res.* **1993**, *60(1)*, 65-78. (m) Malmendal, A.; Linse, S.; Evenas, J.; Forsen, S.; Drakenberg, T. "Battle for the EF-Hands: Magnesium-calcium interference in calmodulin". *Biochemistry.* **1999**, *38(36)*, 11844-11850. (n) Ambrus, A.; Banyai, I.; Weiss, M.S.; Hilgenfeld, R.; Keresztessy, Z.; Muszbek, L.; Fesus, L. "calcium binding of transglutaminases: a ^{43}Ca NMR study combined with surface polarity analysis". *J. Biomol. Struct. Dyn.* **2001**, *19(1)*, 59-74.

[139] *Salts*: (a) Jacquinot, J.F.; Wenckebach, W.T.; Goldman, M.; Abragam, A. "Polarization and NMR observation of calcium-43 nuclei in calcium fluoride". *Phys. Rev. Lett.* **1974**, *32(20)*, 1096-1097. (b) Farmer, R.M.; Popov, A.I. "Calcium-43 NMR study of calcium salts in various solvents". *Inorg. Nucl. Chem. Lett*. **1981**, *123(1)*, 115-117.

[140] *Cement*: (a) Zanni, H.; Rassem-Bertolo, R.; Masse, S.; Fernandez, L.; Nieto, P.; Bresson, B. "A spectroscopic NMR investigation of the calcium silicate hydrates present in cement and concrete". *Magn. Reson. Imaging*, **1996**, *14(7/8)*, 827-831. (b) Bowers, G.M.; Kirkpatrick, R.J. "Natural abundance ^{43}Ca NMR spectroscopy of tobermorite and jennite: model compounds for C-S-H". *J. Am. Chem. Soc.* **2009**, *92(2)*, 545-548.

[141] *Glass*: (a) Angeli, F.; Gaillard, M.; Jollivet, P.; Charpentier, T. "Contribution of ^{43}Ca MAS NMR for probing the structural configuration of calcium in glass". *Chem. Phys. Lett.* **2007**, *440 (4-6)*, 324-328. (b) Shimoda, K.; Tobu, Y.; Kanehashi, K.; Saito, K.; Nemoto T. "First evidence of multiple Ca sites in amorphous slag structure. Multiple-quantum MAS NMR spectroscopy on calcium-43 at high magnetic field". *Solid State Nucl. Mag.* **2006**, *30*, 198.

[142] *Superconductors*: (a) Trokiner, A.; Le Noc, L.; Yakubovskii, A.; Mykhalyov, K.N.; Verkhovskii, S.V. "The ^{43}Ca NMR study of bismuth-based high-Tc superconductor". *Z.*

Naturforsch A. **1994**, *49(102)*, 373-378. (b) Bellot, P.-V.; Trokiner, A.; Zhdanov, Y.; Yakubovskii, A. "^{43}Ca NMR in solid state". *J. Chim. Phys. PCB*, **1998**, *95(2)*, 280-288. (c) Marchand, S.; Trokiner, A.; Yakubovskii, A.; Monod, P.; Knizhnik, A.; Eckstein, Y. "43Ca NMR study of the doping effects in the high temperature superconductor (La1-xCax)(Ba1.75-xLa0.25+x)Cu30y". *Cr. Acad. Sci. II C.* **2001**, *4(11)*, 819-824.

[143] *(Hydroxyl)apatite*: (a) Sahai, N.; Tossell, J.A. "Molecular orbital study of apatite ($Ca_5(PO_4)_3OH$) nucleation at silica bioceramic surfaces". *J. Phys. Chem. B*. **2000**, *104(18)*, 4322-4341. (b) Laurencin, D.; Wong, A.; Dupree, R.; Smith, M.E. "Natural abundance ^{43}Ca solid-state NMR characterization of hydroxyapatite: identification of the two calcium sites". *Magn. Reson. Chem.* **2008**, *46(4)*, 347-350. (c) Wong, A.; Laurencin, D.; Dupree, R.; Smith, M.E. "Two dimensional 43Ca-1H correlation solid-state NMR spectroscopy", *Solid State Nucl. Mag.*, **2009**, *35(1)*, 32-36.

[144] *Nucleic acids*: (a) Braunlin, W.H.; Drakenberg, T.; Nordenskioeld, L. "A calcium-43 NMR study of calcium(II)-DNA interactions". *Biopolymers.* **1987**, *26(7)*, 1047-1062. (b) Braunlin, W.H.; Nordenskioeld, L.; Drakenberg, T. "The interaction of calcium(II) with DNA probed by calcium-43 NMR is not influenced by terminal phosphate groups at ends and nicks". *Biopolymers*. **1989**, *28(7)*, 1339-1342. (c) Braunlin, W.H.; Drakenberg, T.; Nordenskioeld, L. "Calcium binding environments on natural and synthetic polymeric DNA's". *J. Biomol. Struct. Dyn.* **1992**, *10(2)*, 333-343.

[145] *Inorganics*: (a) Bryant, R.G.; Ganapathy, S.; Kennedy, S.D. "High-resolution calcium-43 NMR in solids". *J. Magn. Reson*. **1987**, *72*, 376–378. (b) Lin, Z.; Smith, M.E.; Sowrey, P.E.; Newport, R.J. "Probing the local structural envieonment of calcium by natural-abundance solid-state 43Ca NMR". *Phys. Rev. B: Condens. Matter Mater. Phys*. **2004**, *69(22)*, 224107/1-224107/7. (c) Dupree, R.; Howes, A.P.; Kohn, S.C. "Natural abundance solid state ^{43}Ca NMR". *Chem. Phys. Lett.* **1997**, *276*, 399–404. (d) Trokiner, A.; Bessière, A.; Thouvenot, R.; Hau, D.; Marko, J.; Nardello, V.; Pierlot, C.; Aubry, J.-M. "Solid state and solution ^{43}Ca NMR of calcium peroxides involved in the disproportionation of hydrogen peroxide by calcium hydroxide". *Solid State Nucl. Magn.*

Reson. 2004, **25**, 209. (e) Padro, D.; Jennings, V.; Smith, M.E.; Hoppe, R.; Thomas, P.A.; Dupree, R. Variations of titanium interactions in solid state NMR-correlations to local structure". *J. Phys. Chem. B*. 2002, **106**, 13176. (f) MacKenzie, K.J.D.; Schmucker, M.; Smith, M.E.; Poplett, I.J.F.; Kemmitt, T. "Evolution of crystalline aluminates from hybrid gel-derived precursors studied by XRD and multinuclear solid state MAS NMR IV: Calcium dialuminate, $CaAl_4O_7$ and calcium hexaluminate, $CaAl_{12}O_{19}$". *Thermochim. Acta*, 2000, **363**, 181. (g) MacKenzie, K.J.D.; Smith, M.E.; Wong, A. "A multinuclear MAS NMR study of calcium-containing aluminosilicate inorganic polymers". *J. Mater. Chem.* **2007,** *17*, 5090. (h) Gervais, C.; Laurencin, D.; Wong, A.; Pourpoint, F.; Labram, J.; Woodward, B.; Howes, A.P.; Pike, K.J.; Dupree, R.; Mauri, F.; Christian, B.; Smith, M.E. "New Perspectives on calcium environments in inorganic materials containing calcium-oxygen bonds: A combined computational-experimental ^{43}Ca NMR approach". *Chem. Phys. Lett.* **2008**, *464(103)*, 42-48.

[146] *Reviews*: (a) Forsen, S.; Johansson, C.; Linse, S. "Calcium nuclear magnetic resonance". *Method Enzymol.* **1993**, *227 (Metallobiochemistry, Pt. D)*, 107-118. (b) Aramini, J. M.; Vogel, H. J. "Quadrupolar metal ion NMR studies of metalloproteins". *Biochem. Cell Biol.* **1998**, *76(2/3)*, 210-222. (c) Drakenberg, T. "Calcium-43 NMR of calcium-binding proteins". *Methods Mol. Biol. (Totowa, NJ, US)*. **2002**, *173*, 217–230.

[147] Wong, A.; Agular, P.M.; Charpentier, T.; Sakellariou, D. "A low-cost strategy for ^{43}Ca solid-state NMR spectroscopy". *Chem. Sci.* **2011**, *2(4)*, 815-818.

[148] Bryce, D. L. "Calcium binding environments probed by ^{43}Ca NMR spectroscopy". *Dalton Trans.* **2010**, *39(37)*, 8593-8602.

[149] Shi, X.; Fettinger, J. C.; Davis, J. T. "Enantiomeric Self-Recognition: Cation-Templated Formation of Homochiral Isoguanosine Pentamers". *Angew. Chem. Int. Ed.* **2001**, *40*, 2827–2831.

[150] Akhshi, P.; Mosey, N.J.; Wu, G. "Free-energy landscapes of ion movement through a G-quadruplex DNA channel". *Angew. Chem. Int. Ed.*, **2012**, *51*, 2850-2854.

Appendix I: (Chapter 2)

Coordinates of the all-S and all-N G-quartets and channel Na^+ ions used in building the final Na_2(5'-GMP) G-quadruplex. Table 1 lists all proton-proton distances in the G-quadruplex including those observed in DOSY-NOESY and NOESY.

The following equations are used to build the 5'-GMP G-quadruplex:

$$x' = x(\cos\phi) - y(\sin\phi)$$

$$y' = y(\cos\phi) + x(\sin\phi)$$

$$z' = z + 6.8,$$

where x, y are the original coordinates from the calculated models, and ϕ is the twist angle (90°, 180°, and 270°) used in making a single all-S or all-N G-quartet. When building the stacking G-quadruplex, the next all-S layer is twisted 60° and 6.8 Å away from the previous all-S layer because of alternating all-S and all-N stacking. The same rules also apply to all-N quartets when stacking.

All-S (C2'-*endo*) quartet

HETATM	1	N	1	-2.194	-2.888	-19.843	N
HETATM	2	H	1	-2.460	-1.893	-19.843	H
HETATM	3	C	1	-3.216	-3.824	-19.843	C
HETATM	4	N	1	-4.453	-3.323	-19.843	N
HETATM	5	H	1	-4.594	-2.303	-19.843	H
HETATM	6	H	1	-5.265	-3.956	-19.843	H
HETATM	7	N	1	-3.010	-5.140	-19.843	N
HETATM	8	C	1	-1.677	-5.436	-19.843	C
HETATM	9	C	1	-0.608	-4.589	-19.843	C
HETATM	10	C	1	-0.827	-3.193	-19.843	C
HETATM	11	O	1	0.000	-2.280	-19.843	O
HETATM	12	N	1	0.591	-5.307	-19.843	N
HETATM	13	C	1	0.199	-6.557	-19.843	C
HETATM	14	H	1	0.814	-7.293	-19.843	H
HETATM	15	N	1	-1.170	-6.728	-19.843	N
HETATM	16	H	1	-3.219	-11.099	-19.569	H
HETATM	17	O	1	-2.185	-11.216	-19.562	O
HETATM	18	C	1	-1.600	-10.187	-18.776	C
HETATM	19	C	1	-2.567	-9.288	-17.969	C
HETATM	20	C	1	-0.902	-9.118	-19.633	C

HETATM	21	H	1	-0.937	-10.560	-18.189	H
HETATM	22	C	1	-2.013	-9.032	-16.575	C
HETATM	23	O	1	-2.689	-8.016	-18.634	O
HETATM	24	H	1	-3.429	-9.707	-17.926	H
HETATM	25	C	1	-1.912	-7.976	-19.811	C
HETATM	26	O	1	-0.494	-9.728	-20.846	O
HETATM	27	H	1	-0.137	-8.776	-19.165	H
HETATM	28	O	1	-0.595	-8.807	-16.623	O
HETATM	29	H	1	-2.446	-8.264	-16.195	H
HETATM	30	H	1	-2.199	-9.788	-16.013	H
HETATM	31	H	1	-2.474	-8.083	-20.582	H
HETATM	32	H	1	0.376	-9.340	-21.171	H
HETATM	33	P	1	0.249	-9.258	-15.306	P
HETATM	34	O	1	1.127	-8.109	-14.869	O
HETATM	35	O	1	1.123	-10.458	-15.577	O
HETATM	36	O	1	-0.645	-9.666	-14.134	O
HETATM	37	N	1	2.888	-2.194	-19.843	N
HETATM	38	H	1	1.893	-2.460	-19.843	H
HETATM	39	C	1	3.824	-3.216	-19.843	C
HETATM	40	N	1	3.323	-4.453	-19.843	N
HETATM	41	H	1	2.303	-4.594	-19.843	H
HETATM	42	H	1	3.956	-5.265	-19.843	H
HETATM	43	N	1	5.140	-3.010	-19.843	N
HETATM	44	C	1	5.436	-1.677	-19.843	C
HETATM	45	C	1	4.589	-0.608	-19.843	C
HETATM	46	C	1	3.193	-0.827	-19.843	C
HETATM	47	O	1	2.280	0.000	-19.843	O
HETATM	48	N	1	5.307	0.591	-19.843	N
HETATM	49	C	1	6.557	0.199	-19.843	C
HETATM	50	H	1	7.293	0.814	-19.843	H
HETATM	51	N	1	6.728	-1.170	-19.843	N
HETATM	52	H	1	11.099	-3.219	-19.569	H
HETATM	53	O	1	11.216	-2.185	-19.562	O
HETATM	54	C	1	10.187	-1.600	-18.776	C
HETATM	55	C	1	9.288	-2.567	-17.969	C
HETATM	56	C	1	9.118	-0.902	-19.633	C
HETATM	57	H	1	10.560	-0.937	-18.189	H
HETATM	58	C	1	9.032	-2.013	-16.575	C
HETATM	59	O	1	8.016	-2.689	-18.634	O
HETATM	60	H	1	9.707	-3.429	-17.926	H
HETATM	61	C	1	7.976	-1.912	-19.811	C
HETATM	62	O	1	9.728	-0.494	-20.846	O
HETATM	63	H	1	8.776	-0.137	-19.165	H
HETATM	64	O	1	8.807	-0.595	-16.623	O
HETATM	65	H	1	8.264	-2.446	-16.195	H
HETATM	66	H	1	9.788	-2.199	-16.013	H

HETATM	67	H	1	8.083	-2.474	-20.582	H
HETATM	68	H	1	9.340	0.376	-21.171	H
HETATM	69	P	1	9.258	0.249	-15.306	P
HETATM	70	O	1	8.109	1.127	-14.869	O
HETATM	71	O	1	10.458	1.123	-15.577	O
HETATM	72	O	1	9.666	-0.645	-14.134	O
HETATM	73	N	1	2.194	2.888	-19.843	N
HETATM	74	H	1	2.460	1.893	-19.843	H
HETATM	75	C	1	3.216	3.824	-19.843	C
HETATM	76	N	1	4.453	3.323	-19.843	N
HETATM	77	H	1	4.594	2.303	-19.843	H
HETATM	78	H	1	5.265	3.956	-19.843	H
HETATM	79	N	1	3.010	5.140	-19.843	N
HETATM	80	C	1	1.677	5.436	-19.843	C
HETATM	81	C	1	0.608	4.589	-19.843	C
HETATM	82	C	1	0.827	3.193	-19.843	C
HETATM	83	O	1	0.000	2.280	-19.843	O
HETATM	84	N	1	-0.591	5.307	-19.843	N
HETATM	85	C	1	-0.199	6.557	-19.843	C
HETATM	86	H	1	-0.814	7.293	-19.843	H
HETATM	87	N	1	1.170	6.728	-19.843	N
HETATM	88	H	1	3.219	11.099	-19.569	H
HETATM	89	O	1	2.185	11.216	-19.562	O
HETATM	90	C	1	1.600	10.187	-18.776	C
HETATM	91	C	1	2.567	9.288	-17.969	C
HETATM	92	C	1	0.902	9.118	-19.633	C
HETATM	93	H	1	0.937	10.560	-18.189	H
HETATM	94	C	1	2.013	9.032	-16.575	C
HETATM	95	O	1	2.689	8.016	-18.634	O
HETATM	96	H	1	3.429	9.707	-17.926	H
HETATM	97	C	1	1.912	7.976	-19.811	C
HETATM	98	O	1	0.494	9.728	-20.846	O
HETATM	99	H	1	0.137	8.776	-19.165	H
HETATM	100	O	1	0.595	8.807	-16.623	O
HETATM	101	H	1	2.446	8.264	-16.195	H
HETATM	102	H	1	2.199	9.788	-16.013	H
HETATM	103	H	1	2.474	8.083	-20.582	H
HETATM	104	H	1	-0.376	9.340	-21.171	H
HETATM	105	P	1	-0.249	9.258	-15.306	P
HETATM	106	O	1	-1.127	8.109	-14.869	O
HETATM	107	O	1	-1.123	10.458	-15.577	O
HETATM	108	O	1	0.645	9.666	-14.134	O
HETATM	109	N	1	-2.888	2.194	-19.843	N
HETATM	110	H	1	-1.893	2.460	-19.843	H
HETATM	111	C	1	-3.824	3.216	-19.843	C

HETATM	112	N	1	-3.323	4.453	-19.843	N
HETATM	113	H	1	-2.303	4.594	-19.843	H
HETATM	114	H	1	-3.956	5.265	-19.843	H
HETATM	115	N	1	-5.140	3.010	-19.843	N
HETATM	116	C	1	-5.436	1.677	-19.843	C
HETATM	117	C	1	-4.589	0.608	-19.843	C
HETATM	118	C	1	-3.193	0.827	-19.843	C
HETATM	119	O	1	-2.280	0.000	-19.843	O
HETATM	120	N	1	-5.307	-0.591	-19.843	N
HETATM	121	C	1	-6.557	-0.199	-19.843	C
HETATM	122	H	1	-7.293	-0.814	-19.843	H
HETATM	123	N	1	-6.728	1.170	-19.843	N
HETATM	124	H	1	-11.099	3.219	-19.569	H
HETATM	125	O	1	-11.216	2.185	-19.562	O
HETATM	126	C	1	-10.187	1.600	-18.776	C
HETATM	127	C	1	-9.288	2.567	-17.969	C
HETATM	128	C	1	-9.118	0.902	-19.633	C
HETATM	129	H	1	-10.560	0.937	-18.189	H
HETATM	130	C	1	-9.032	2.013	-16.575	C
HETATM	131	O	1	-8.016	2.689	-18.634	O
HETATM	132	H	1	-9.707	3.429	-17.926	H
HETATM	133	C	1	-7.976	1.912	-19.811	C
HETATM	134	O	1	-9.728	0.494	-20.846	O
HETATM	135	H	1	-8.776	0.137	-19.165	H
HETATM	136	O	1	-8.807	0.595	-16.623	O
HETATM	137	H	1	-8.264	2.446	-16.195	H
HETATM	138	H	1	-9.788	2.199	-16.013	H
HETATM	139	H	1	-8.083	2.474	-20.582	H
HETATM	140	H	1	-9.340	-0.376	-21.171	H
HETATM	141	P	1	-9.258	-0.249	-15.306	P
HETATM	142	O	1	-8.109	-1.127	-14.869	O
HETATM	143	O	1	-10.458	-1.123	-15.577	O
HETATM	144	O	1	-9.666	0.645	-14.134	O

All-N (C3'-*endo*) quartet

HETATM	145	N	1	-0.453	-3.603	-16.443	N
HETATM	146	H	1	-1.183	-2.876	-16.443	H
HETATM	147	C	1	-0.865	-4.926	-16.443	C
HETATM	148	N	1	-2.186	-5.115	-16.443	N
HETATM	149	H	1	-2.821	-4.305	-16.443	H
HETATM	150	H	1	-2.569	-6.071	-16.443	H
HETATM	151	N	1	-0.026	-5.961	-16.443	N
HETATM	152	C	1	1.265	-5.569	-16.443	C
HETATM	153	C	1	1.774	-4.276	-16.443	C
HETATM	154	C	1	0.883	-3.180	-16.443	C
HETATM	155	O	1	1.139	-1.974	-16.443	O

HETATM	156	N	1	3.172	-4.294	-16.443	N
HETATM	157	C	1	3.462	-5.571	-16.443	C
HETATM	158	H	1	4.365	-5.898	-16.443	H
HETATM	159	N	1	2.365	-6.407	-16.443	N
HETATM	160	C	1	2.297	-7.916	-16.433	C
HETATM	161	H	1	1.396	-8.192	-16.254	H
HETATM	162	C	1	2.782	-8.566	-17.728	C
HETATM	163	H	1	2.675	-7.988	-18.486	H
HETATM	164	C	1	4.249	-8.840	-17.417	C
HETATM	165	H	1	4.754	-8.029	-17.511	H
HETATM	166	C	1	4.193	-9.236	-15.961	C
HETATM	167	H	1	3.931	-10.157	-15.890	H
HETATM	168	C	1	5.484	-9.008	-15.163	C
HETATM	169	H	1	5.416	-8.191	-14.665	H
HETATM	170	H	1	6.226	-8.930	-15.767	H
HETATM	171	O	1	3.158	-8.395	-15.389	O
HETATM	172	O	1	2.067	-9.782	-17.878	O
HETATM	173	H	1	1.685	-10.081	-16.947	H
HETATM	174	O	1	4.822	-9.862	-18.233	O
HETATM	175	H	1	4.734	-9.595	-19.235	H
HETATM	176	O	1	5.703	-10.107	-14.266	O
HETATM	177	O	1	7.975	-9.954	-13.108	O
HETATM	178	O	1	6.264	-8.390	-12.435	O
HETATM	179	O	1	6.115	-10.872	-11.855	O
HETATM	180	P	1	6.490	-9.819	-12.872	P
HETATM	181	N	1	-3.603	0.453	-16.443	N
HETATM	182	H	1	-2.876	1.183	-16.443	H
HETATM	183	C	1	-4.926	0.865	-16.443	C
HETATM	184	N	1	-5.115	2.186	-16.443	N
HETATM	185	H	1	-4.305	2.821	-16.443	H
HETATM	186	H	1	-6.071	2.569	-16.443	H
HETATM	187	N	1	-5.961	0.026	-16.443	N
HETATM	188	C	1	-5.569	-1.265	-16.443	C
HETATM	189	C	1	-4.276	-1.774	-16.443	C
HETATM	190	C	1	-3.180	-0.883	-16.443	C
HETATM	191	O	1	-1.974	-1.139	-16.443	O
HETATM	192	N	1	-4.294	-3.172	-16.443	N
HETATM	193	C	1	-5.571	-3.462	-16.443	C
HETATM	194	H	1	-5.898	-4.365	-16.443	H
HETATM	195	N	1	-6.407	-2.365	-16.443	N
HETATM	196	C	1	-7.916	-2.297	-16.433	C
HETATM	197	H	1	-8.192	-1.396	-16.254	H
HETATM	198	C	1	-8.566	-2.782	-17.728	C
HETATM	199	H	1	-7.988	-2.675	-18.486	H
HETATM	200	C	1	-8.840	-4.249	-17.417	C
HETATM	201	H	1	-8.029	-4.754	-17.511	H

HETATM	202	C	1	-9.236	-4.193	-15.961	C
HETATM	203	H	1	-10.157	-3.931	-15.890	H
HETATM	204	C	1	-9.008	-5.484	-15.163	C
HETATM	205	H	1	-8.191	-5.416	-14.665	H
HETATM	206	H	1	-8.930	-6.226	-15.767	H
HETATM	207	O	1	-8.395	-3.158	-15.389	O
HETATM	208	O	1	-9.782	-2.067	-17.878	O
HETATM	209	H	1	-10.081	-1.685	-16.947	H
HETATM	210	O	1	-9.862	-4.822	-18.233	O
HETATM	211	H	1	-9.595	-4.734	-19.235	H
HETATM	212	O	1	-10.107	-5.703	-14.266	O
HETATM	213	O	1	-9.954	-7.975	-13.108	O
HETATM	214	O	1	-8.390	-6.265	-12.435	O
HETATM	215	O	1	-10.872	-6.115	-11.855	O
HETATM	216	P	1	-9.819	-6.490	-12.872	P
HETATM	217	N	1	0.453	3.603	-16.443	N
HETATM	218	H	1	1.183	2.876	-16.443	H
HETATM	219	C	1	0.865	4.926	-16.443	C
HETATM	220	N	1	2.186	5.115	-16.443	N
HETATM	221	H	1	2.821	4.305	-16.443	H
HETATM	222	H	1	2.569	6.071	-16.443	H
HETATM	223	N	1	0.026	5.961	-16.443	N
HETATM	224	C	1	-1.265	5.569	-16.443	C
HETATM	225	C	1	-1.774	4.276	-16.443	C
HETATM	226	C	1	-0.883	3.180	-16.443	C
HETATM	227	O	1	-1.139	1.974	-16.443	O
HETATM	228	N	1	-3.172	4.294	-16.443	N
HETATM	229	C	1	-3.462	5.571	-16.443	C
HETATM	230	H	1	-4.365	5.898	-16.443	H
HETATM	231	N	1	-2.365	6.407	-16.443	N
HETATM	232	C	1	-2.297	7.916	-16.433	C
HETATM	233	H	1	-1.396	8.192	-16.254	H
HETATM	234	C	1	-2.782	8.566	-17.728	C
HETATM	235	H	1	-2.675	7.988	-18.486	H
HETATM	236	C	1	-4.249	8.840	-17.417	C
HETATM	237	H	1	-4.754	8.029	-17.511	H
HETATM	238	C	1	-4.193	9.236	-15.961	C
HETATM	239	H	1	-3.931	10.157	-15.890	H
HETATM	240	C	1	-5.484	9.008	-15.163	C
HETATM	241	H	1	-5.416	8.190	-14.665	H
HETATM	242	H	1	-6.226	8.930	-15.767	H
HETATM	243	O	1	-3.158	8.395	-15.389	O
HETATM	244	O	1	-2.067	9.782	-17.878	O
HETATM	245	H	1	-1.685	10.081	-16.947	H
HETATM	246	O	1	-4.822	9.862	-18.233	O
HETATM	247	H	1	-4.734	9.595	-19.235	H

HETATM	248	O	1	-5.703	10.107	-14.266	O
HETATM	249	O	1	-7.975	9.954	-13.108	O
HETATM	250	O	1	-6.264	8.390	-12.435	O
HETATM	251	O	1	-6.115	10.872	-11.855	O
HETATM	252	P	1	-6.490	9.819	-12.872	P
HETATM	253	N	1	3.603	-0.453	-16.443	N
HETATM	254	H	1	2.876	-1.183	-16.443	H
HETATM	255	C	1	4.926	-0.865	-16.443	C
HETATM	256	N	1	5.115	-2.186	-16.443	N
HETATM	257	H	1	4.305	-2.821	-16.443	H
HETATM	258	H	1	6.071	-2.569	-16.443	H
HETATM	259	N	1	5.961	-0.026	-16.443	N
HETATM	260	C	1	5.569	1.265	-16.443	C
HETATM	261	C	1	4.276	1.774	-16.443	C
HETATM	262	C	1	3.180	0.883	-16.443	C
HETATM	263	O	1	1.974	1.139	-16.443	O
HETATM	264	N	1	4.294	3.172	-16.443	N
HETATM	265	C	1	5.571	3.462	-16.443	C
HETATM	266	H	1	5.898	4.365	-16.443	H
HETATM	267	N	1	6.407	2.365	-16.443	N
HETATM	268	C	1	7.916	2.297	-16.433	C
HETATM	269	H	1	8.192	1.396	-16.254	H
HETATM	270	C	1	8.566	2.782	-17.728	C
HETATM	271	H	1	7.988	2.675	-18.486	H
HETATM	272	C	1	8.840	4.249	-17.417	C
HETATM	273	H	1	8.029	4.754	-17.511	H
HETATM	274	C	1	9.236	4.193	-15.961	C
HETATM	275	H	1	10.157	3.931	-15.890	H
HETATM	276	C	1	9.008	5.484	-15.163	C
HETATM	277	H	1	8.191	5.415	-14.665	H
HETATM	278	H	1	8.930	6.226	-15.767	H
HETATM	279	O	1	8.395	3.158	-15.389	O
HETATM	280	O	1	9.782	2.067	-17.878	O
HETATM	281	H	1	10.081	1.685	-16.947	H
HETATM	282	O	1	9.862	4.822	-18.233	O
HETATM	283	H	1	9.595	4.734	-19.235	H
HETATM	284	O	1	10.107	5.703	-14.266	O
HETATM	285	O	1	9.954	7.975	-13.108	O
HETATM	286	O	1	8.390	6.264	-12.435	O
HETATM	287	O	1	10.872	6.115	-11.855	O
HETATM	288	P	1	9.819	6.490	-12.872	P

Channel Na^+ ions

HETATM	1729	Na	1	0.000	0.000	-18.143	Na
HETATM	1730	Na	1	0.000	0.000	-14.743	Na

Table A1. Intra-molecule, intra-quartet, and inter-quartet distances between hydrogens in the right-handed 5'-GMP G-quadruplex model.

Intra-molecule

C2'-*endo*	N1H	N2HA	N2HB	H8	H1'	H2'	H3'	H4'	H5'	H5''	2'OH	3'OH
N1H		2.17	3.48									
N2HA	2.17		1.78									
N2HB	3.48	1.78										
H8												
H1'				3.46							3.16	
H2'				1.86	2.88						2.16	3.95
H3'				4.06	3.77	2.21					2.21	2.72
H4'				5.25	3.26	3.65	2.65					2.16
H5'				5.05	4.42	3.77	3.40	2.43		1.55		4.46
H5''				5.44	4.88	3.81	2.58	2.30	1.55			3.91
2'-OH				2.25	3.16	2.16	3.54	5.06	5.81	5.74		4.45
3'OH				5.55	3.27	3.95	2.72	2.16	4.46	3.91		

C3'-*endo*	N1H	N2HA	N2HB	H8	H1'	H2'	H3'	H4'	H5'	H5''	2'OH	3'OH
N1H		2.17	3.48									
N2HA	2.17		1.78									
N2HB	3.48	1.78										
H8												
H1'				3.76							2.03	
H2'				3.38	2.58						2.78	3.65
H3'				2.42	3.59	2.30					3.73	2.18
H4'				4.32	3.23	3.61	2.80				2.48	3.07
H5'				2.92	4.37	4.58	2.71	2.81		1.56	4.80	3.73
H5''				3.90	4.99	4.69	2.63	2.50	1.56		4.80	2.62
2'-OH				4.99	2.03	2.78	3.73	2.48	4.80	4.80		4.38
3'OH				4.51	5.13	3.65	2.18	3.07	3.73	2.62	4.38	

Table A1. (continued)

Intra-quartet

C2'-*endo*	N1H	N2HA	N2HB	H8	H1'	H2'	H3'	H4'	H5'	H5''	2'OH	3'OH
N1H				4.94								
N2HA				3.07								
N2HB				3.73								
H8												
H1'												
H2'		4.82	5.37									
H3'												
H4'												
H5'												
H5''												
2'-OH		5.03										
3'OH												

C3'-*endo*	N1H	N2HA	N2HB	H8	H1'	H2'	H3'	H4'	H5'	H5''	2'OH	3'OH
N1H				4.95								
N2HA				3.08								
N2HB				3.74								
H8												
H1'												
H2'												
H3'												
H4'												
H5'												
H5''												
2'-OH												
3'OH												

Table A1. (continued)

Inter-quartet

C2'-*endo* → C3'-*endo* ↓	N1H	N2HA	N2HB	H8	H1'	H2'	H3'	H4'	H5'	H5''	2'OH	3'OH
N1H	3.76	4.17										
N2HA	4.84, 4.19	4.31		4.17					4.02			
N2HB		4.19	4.80	3.48				4.01	2.25, 4.86*			
H8		4.19			3.02				3.53*	4.37*	4.66	
H1'				3.75		3.23	3.84		3.89	3.89		
H2'			3.30	2.41		2.93	4.44		4.44*		3.61	
H3'			3.71	4.64								
H4'					4.86						4.02*	
H5'			4.86*	4.37*	2.23	4.44*		3.97			2.50*, 4.37	3.26
H5''				3.53*	3.64	4.99*		4.81	2.50*		3.15*	3.54
2'-OH				4.12		3.10	2.94		4.61	3.94, 3.15*	4.44	
3'OH												

Legend: * = two quartets away (i.e., C2'-*endo* to C2'-*endo*)
Underline = from the quartet below (non-underline = quartet above)
Grey box = cross peaks observed in DOSY-NOESY and NOESY

Appendix II: (Chapter 3)

Coordinates of the acidic, right-handed Na_2(5'-GMP) G-quadruplex model.

HETATM	1	N	1	1.665	2.907	-4.000	N
HETATM	2	H	1	0.788	2.775	-3.848	H
HETATM	3	C	1	2.140	4.218	-3.900	C
HETATM	4	N	1	3.500	4.512	-3.940	N
HETATM	5	C	1	4.197	3.398	-4.200	C
HETATM	6	C	1	3.893	2.114	-4.340	C
HETATM	7	C	1	2.421	1.805	-4.310	C
HETATM	8	N	1	4.949	1.234	-4.550	N
HETATM	9	C	1	5.963	2.065	-4.600	C
HETATM	10	H	1	6.854	1.780	-4.815	H
HETATM	11	N	1	5.639	3.429	-4.310	N
HETATM	12	O	1	1.930	0.661	-4.340	O
HETATM	13	N	1	1.274	5.186	-3.520	N
HETATM	14	H	1	0.417	4.977	-3.339	H
HETATM	15	H	1	1.554	6.038	-3.448	H
HETATM	16	C	1	6.602	4.623	-4.150	C
HETATM	17	H	1	6.182	5.377	-4.571	H
HETATM	18	C	1	7.897	4.359	-4.910	C
HETATM	19	H	1	8.129	3.429	-4.870	H
HETATM	20	C	1	8.901	5.222	-4.050	C
HETATM	21	H	1	9.742	4.763	-3.990	H
HETATM	22	C	1	8.273	5.291	-2.680	C
HETATM	23	H	1	8.376	6.181	-2.335	H
HETATM	24	C	1	8.913	4.309	-1.710	C
HETATM	25	H	1	9.864	4.312	-1.839	H
HETATM	26	H	1	8.737	4.593	-0.810	H
HETATM	27	O	1	6.893	5.008	-2.810	O
HETATM	28	O	1	7.810	4.786	-6.230	O
HETATM	29	H	1	7.260	4.294	-6.652	H
HETATM	30	O	1	9.087	6.410	-4.650	O
HETATM	31	H	1	9.627	6.878	-4.190	H
HETATM	32	O	1	8.414	2.963	-1.890	O
HETATM	33	P	1	9.009	1.866	-1.050	P
HETATM	34	O	1	9.129	2.242	0.390	O
HETATM	35	H	1	9.632	2.923	0.464	H
HETATM	36	O	1	10.359	1.585	-1.750	O
HETATM	37	H	1	10.850	2.278	-1.706	H
HETATM	38	O	1	8.058	0.592	-1.110	O
HETATM	39	H	1	8.387	0.018	-1.644	H
HETATM	40	N	1	2.717	-1.960	-4.883	N
HETATM	41	H	1	2.677	-1.073	-4.731	H
HETATM	42	C	1	3.971	-2.569	-4.783	C
HETATM	43	N	1	4.121	-3.952	-4.823	N

HETATM	44	C	1	2.941	-4.529	-5.083	C
HETATM	45	C	1	1.695	-4.093	-5.223	C
HETATM	46	C	1	1.542	-2.597	-5.193	C
HETATM	47	N	1	0.710	-5.050	-5.433	N
HETATM	48	C	1	1.430	-6.146	-5.483	C
HETATM	49	H	1	1.053	-7.002	-5.698	H
HETATM	50	N	1	2.821	-5.967	-5.193	N
HETATM	51	O	1	0.455	-1.989	-5.223	O
HETATM	52	N	1	5.024	-1.809	-4.403	N
HETATM	53	H	1	4.906	-0.935	-4.222	H
HETATM	54	H	1	5.842	-2.177	-4.331	H
HETATM	55	C	1	3.908	-7.049	-5.033	C
HETATM	56	H	1	4.701	-6.710	-5.454	H
HETATM	57	C	1	3.510	-8.309	-5.793	C
HETATM	58	H	1	2.560	-8.443	-5.753	H
HETATM	59	C	1	4.263	-9.398	-4.933	C
HETATM	60	H	1	3.719	-10.187	-4.873	H
HETATM	61	C	1	4.397	-8.781	-3.563	C
HETATM	62	H	1	5.271	-8.977	-3.218	H
HETATM	63	C	1	3.354	-9.315	-2.593	C
HETATM	64	H	1	3.258	-10.261	-2.722	H
HETATM	65	H	1	3.655	-9.169	-1.693	H
HETATM	66	O	1	4.260	-7.379	-3.693	O
HETATM	67	O	1	3.943	-8.268	-7.113	O
HETATM	68	H	1	3.511	-7.669	-7.535	H
HETATM	69	O	1	5.425	-9.707	-5.533	O
HETATM	70	H	1	5.834	-10.293	-5.073	H
HETATM	71	O	1	2.067	-8.677	-2.773	O
HETATM	72	P	1	0.914	-9.155	-1.933	P
HETATM	73	O	1	1.276	-9.313	-0.493	O
HETATM	74	H	1	1.900	-9.885	-0.419	H
HETATM	75	O	1	0.494	-10.468	-2.633	O
HETATM	76	H	1	1.131	-11.029	-2.589	H
HETATM	77	O	1	-0.254	-8.076	-1.993	O
HETATM	78	H	1	-0.859	-8.343	-2.527	H
HETATM	79	N	1	-2.233	-2.497	-5.766	N
HETATM	80	H	1	-1.347	-2.550	-5.614	H
HETATM	81	C	1	-2.970	-3.681	-5.666	C
HETATM	82	N	1	-4.361	-3.686	-5.706	N
HETATM	83	C	1	-4.811	-2.452	-5.966	C
HETATM	84	C	1	-4.248	-1.258	-6.106	C
HETATM	85	C	1	-2.744	-1.262	-6.076	C
HETATM	86	N	1	-5.097	-0.178	-6.316	N
HETATM	87	C	1	-6.262	-0.780	-6.366	C
HETATM	88	H	1	-7.074	-0.316	-6.581	H
HETATM	89	N	1	-6.229	-2.181	-6.076	N
HETATM	90	O	1	-2.025	-0.245	-6.106	O

HETATM	91	N	1	-2.324	-4.808	-5.286	N
HETATM	92	H	1	-1.443	-4.782	-5.105	H
HETATM	93	H	1	-2.776	-5.583	-5.214	H
HETATM	94	C	1	-7.419	-3.149	-5.916	C
HETATM	95	H	1	-7.165	-3.974	-6.337	H
HETATM	96	C	1	-8.630	-2.622	-6.676	C
HETATM	97	H	1	-8.665	-1.664	-6.636	H
HETATM	98	C	1	-9.792	-3.258	-5.816	C
HETATM	99	H	1	-10.519	-2.634	-5.756	H
HETATM	100	C	1	-9.192	-3.455	-4.446	C
HETATM	101	H	1	-9.478	-4.304	-4.101	H
HETATM	102	C	1	-9.614	-2.361	-3.476	C
HETATM	103	H	1	-10.545	-2.167	-3.605	H
HETATM	104	H	1	-9.501	-2.677	-2.576	H
HETATM	105	O	1	-7.783	-3.465	-4.576	O
HETATM	106	O	1	-8.635	-3.058	-7.996	O
HETATM	107	H	1	-7.994	-2.690	-8.418	H
HETATM	108	O	1	-10.221	-4.381	-6.416	O
HETATM	109	H	1	-10.847	-4.726	-5.956	H
HETATM	110	O	1	-8.846	-1.149	-3.656	O
HETATM	111	P	1	-9.200	0.048	-2.816	P
HETATM	112	O	1	-9.395	-0.295	-1.376	O
HETATM	113	H	1	-10.029	-0.857	-1.302	H
HETATM	114	O	1	-10.463	0.603	-3.516	O
HETATM	115	H	1	-11.087	0.028	-3.472	H
HETATM	116	O	1	-8.005	1.097	-2.876	O
HETATM	117	H	1	-8.208	1.726	-3.410	H
HETATM	118	N	1	-2.250	2.482	-6.649	N
HETATM	119	H	1	-2.395	1.607	-6.497	H
HETATM	120	C	1	-3.350	3.339	-6.549	C
HETATM	121	N	1	-3.210	4.723	-6.589	N
HETATM	122	C	1	-1.935	5.041	-6.849	C
HETATM	123	C	1	-0.807	4.356	-6.989	C
HETATM	124	C	1	-0.968	2.861	-6.959	C
HETATM	125	N	1	0.356	5.088	-7.199	N
HETATM	126	C	1	-0.121	6.309	-7.249	C
HETATM	127	H	1	0.425	7.068	-7.464	H
HETATM	128	N	1	-1.518	6.423	-6.959	N
HETATM	129	O	1	-0.032	2.040	-6.989	O
HETATM	130	N	1	-4.538	2.814	-6.169	N
HETATM	131	H	1	-4.605	1.935	-5.988	H
HETATM	132	H	1	-5.262	3.344	-6.097	H
HETATM	133	C	1	-2.357	7.708	-6.799	C
HETATM	134	H	1	-3.203	7.541	-7.220	H
HETATM	135	C	1	-1.706	8.857	-7.559	C
HETATM	136	H	1	-0.749	8.791	-7.519	H
HETATM	137	C	1	-2.216	10.079	-6.699	C

HETATM	138	H	1	-1.519	10.737	-6.639	H
HETATM	139	C	1	-2.475	9.503	-5.329	C
HETATM	140	H	1	-3.290	9.876	-4.984	H
HETATM	141	C	1	-1.344	9.808	-4.359	C
HETATM	142	H	1	-1.053	10.714	-4.488	H
HETATM	143	H	1	-1.669	9.728	-3.459	H
HETATM	144	O	1	-2.633	8.103	-5.459	O
HETATM	145	O	1	-2.138	8.907	-8.879	O
HETATM	146	H	1	-1.840	8.232	-9.301	H
HETATM	147	O	1	-3.288	10.623	-7.299	O
HETATM	148	H	1	-3.567	11.281	-6.839	H
HETATM	149	O	1	-0.218	8.917	-4.539	O
HETATM	150	P	1	1.010	9.144	-3.699	P
HETATM	151	O	1	0.688	9.375	-2.259	O
HETATM	152	H	1	0.196	10.064	-2.185	H
HETATM	153	O	1	1.694	10.342	-4.399	O
HETATM	154	H	1	1.187	11.023	-4.355	H
HETATM	155	O	1	1.927	7.847	-3.759	O
HETATM	156	H	1	2.575	7.982	-4.293	H
HETATM	157	N	1	2.703	1.979	-7.532	N
HETATM	158	H	1	1.848	2.214	-7.380	H
HETATM	159	C	1	3.671	2.983	-7.432	C
HETATM	160	N	1	5.032	2.698	-7.472	N
HETATM	161	C	1	5.216	1.398	-7.732	C
HETATM	162	C	1	4.416	0.348	-7.872	C
HETATM	163	C	1	2.946	0.664	-7.842	C
HETATM	164	N	1	5.023	-0.886	-8.082	N
HETATM	165	C	1	6.287	-0.539	-8.132	C
HETATM	166	H	1	6.985	-1.162	-8.347	H
HETATM	167	N	1	6.547	0.839	-7.842	N
HETATM	168	O	1	2.032	-0.181	-7.872	O
HETATM	169	N	1	3.273	4.219	-7.052	N
HETATM	170	H	1	2.406	4.377	-6.871	H
HETATM	171	H	1	3.876	4.884	-6.980	H
HETATM	172	C	1	7.912	1.538	-7.682	C
HETATM	173	H	1	7.835	2.397	-8.103	H
HETATM	174	C	1	8.987	0.770	-8.442	C
HETATM	175	H	1	8.821	-0.174	-8.402	H
HETATM	176	C	1	10.256	1.150	-7.582	C
HETATM	177	H	1	10.837	0.389	-7.522	H
HETATM	178	C	1	9.710	1.468	-6.212	C
HETATM	179	H	1	10.166	2.239	-5.867	H
HETATM	180	C	1	9.895	0.311	-5.242	C
HETATM	181	H	1	10.766	-0.073	-5.371	H
HETATM	182	H	1	9.850	0.643	-4.342	H
HETATM	183	O	1	8.334	1.771	-6.342	O
HETATM	184	O	1	9.082	1.196	-9.762	O

HETATM	185	H	1	8.379	0.970	-10.184	H
HETATM	186	O	1	10.908	2.160	-8.182	O
HETATM	187	H	1	11.592	2.368	-7.722	H
HETATM	188	O	1	8.891	-0.715	-5.422	O
HETATM	189	P	1	8.989	-1.960	-4.582	P
HETATM	190	O	1	9.251	-1.665	-3.142	O
HETATM	191	H	1	8.777	-1.003	-2.897	H
HETATM	192	O	1	10.109	-2.765	-5.282	O
HETATM	193	H	1	10.839	-2.333	-5.238	H
HETATM	194	O	1	7.602	-2.737	-4.642	O
HETATM	195	H	1	7.669	-3.395	-5.176	H
HETATM	196	N	1	1.685	-2.895	-8.415	N
HETATM	197	H	1	2.009	-2.069	-8.263	H
HETATM	198	C	1	2.583	-3.962	-8.315	C
HETATM	199	N	1	2.157	-5.287	-8.355	N
HETATM	200	C	1	0.845	-5.334	-8.615	C
HETATM	201	C	1	-0.116	-4.428	-8.755	C
HETATM	202	C	1	0.352	-2.999	-8.725	C
HETATM	203	N	1	-1.406	-4.902	-8.965	N
HETATM	204	C	1	-1.193	-6.196	-9.015	C
HETATM	205	H	1	-1.886	-6.825	-9.230	H
HETATM	206	N	1	0.150	-6.598	-8.725	N
HETATM	207	O	1	-0.393	-2.002	-8.755	O
HETATM	208	N	1	3.854	-3.696	-7.935	N
HETATM	209	H	1	4.102	-2.850	-7.754	H
HETATM	210	H	1	4.452	-4.365	-7.863	H
HETATM	211	C	1	0.702	-8.029	-8.565	C
HETATM	212	H	1	1.565	-8.042	-8.986	H
HETATM	213	C	1	-0.173	-9.018	-9.325	C
HETATM	214	H	1	-1.095	-8.755	-9.285	H
HETATM	215	C	1	0.072	-10.320	-8.465	C
HETATM	216	H	1	-0.746	-10.818	-8.405	H
HETATM	217	C	1	0.445	-9.810	-7.095	C
HETATM	218	H	1	1.164	-10.345	-6.750	H
HETATM	219	C	1	-0.725	-9.873	-6.125	C
HETATM	220	H	1	-1.198	-10.699	-6.254	H
HETATM	221	H	1	-0.390	-9.863	-5.225	H
HETATM	222	O	1	0.891	-8.473	-7.225	O
HETATM	223	O	1	0.240	-9.157	-10.645	O
HETATM	224	H	1	0.088	-8.434	-11.067	H
HETATM	225	O	1	1.008	-11.074	-9.065	O
HETATM	226	H	1	1.143	-11.776	-8.605	H
HETATM	227	O	1	-1.641	-8.768	-6.305	O
HETATM	228	P	1	-2.889	-8.735	-5.465	P
HETATM	229	O	1	-2.623	-9.027	-4.025	O
HETATM	230	H	1	-1.915	-8.624	-3.780	H
HETATM	231	O	1	-3.807	-9.764	-6.165	O

HETATM	232	H	1	-3.453	-10.536	-6.121	H
HETATM	233	O	1	-3.517	-7.275	-5.525	O
HETATM	234	H	1	-4.178	-7.272	-6.059	H
HETATM	235	N	1	-3.056	-1.373	-9.298	N
HETATM	236	H	1	-2.268	-1.782	-9.146	H
HETATM	237	C	1	-4.211	-2.155	-9.198	C
HETATM	238	N	1	-5.483	-1.593	-9.238	N
HETATM	239	C	1	-5.393	-0.283	-9.498	C
HETATM	240	C	1	-4.392	0.578	-9.638	C
HETATM	241	C	1	-3.020	-0.037	-9.608	C
HETATM	242	N	1	-4.729	1.910	-9.848	N
HETATM	243	C	1	-6.037	1.834	-9.898	C
HETATM	244	H	1	-6.591	2.589	-10.113	H
HETATM	245	N	1	-6.578	0.541	-9.608	N
HETATM	246	O	1	-1.950	0.600	-9.638	O
HETATM	247	N	1	-4.079	-3.447	-8.818	N
HETATM	248	H	1	-3.263	-3.782	-8.637	H
HETATM	249	H	1	-4.806	-3.971	-8.746	H
HETATM	250	C	1	-8.059	0.141	-9.448	C
HETATM	251	H	1	-8.162	-0.716	-9.869	H
HETATM	252	C	1	-8.951	1.115	-10.208	C
HETATM	253	H	1	-8.592	2.004	-10.168	H
HETATM	254	C	1	-10.271	1.007	-9.348	C
HETATM	255	H	1	-10.681	1.873	-9.288	H
HETATM	256	C	1	-9.803	0.582	-7.978	C
HETATM	257	H	1	-10.410	-0.077	-7.633	H
HETATM	258	C	1	-9.744	1.753	-7.008	C
HETATM	259	H	1	-10.515	2.309	-7.137	H
HETATM	260	H	1	-9.768	1.419	-6.108	H
HETATM	261	O	1	-8.520	0.000	-8.108	O
HETATM	262	O	1	-9.132	0.719	-11.528	O
HETATM	263	H	1	-8.397	0.794	-11.950	H
HETATM	264	O	1	-11.119	0.155	-9.948	O
HETATM	265	H	1	-11.831	0.094	-9.488	H
HETATM	266	O	1	-8.548	2.548	-7.188	O
HETATM	267	P	1	-8.385	3.786	-6.348	P
HETATM	268	O	1	-8.703	3.552	-4.908	O
HETATM	269	H	1	-8.376	2.806	-4.663	H
HETATM	270	O	1	-9.313	4.807	-7.048	O
HETATM	271	H	1	-10.117	4.535	-7.004	H
HETATM	272	O	1	-6.867	4.258	-6.408	O
HETATM	273	H	1	-6.796	4.915	-6.942	H
HETATM	274	N	1	-1.046	3.182	-10.181	N
HETATM	275	H	1	-1.535	2.442	-10.029	H
HETATM	276	C	1	-1.703	4.413	-10.081	C
HETATM	277	N	1	-1.011	5.620	-10.121	N
HETATM	278	C	1	0.283	5.393	-10.381	C

HETATM	279	C	1	1.034	4.308	-10.521	C
HETATM	280	C	1	0.279	3.007	-10.491	C
HETATM	281	N	1	2.394	4.503	-10.731	N
HETATM	282	C	1	2.455	5.813	-10.781	C
HETATM	283	H	1	3.264	6.284	-10.996	H
HETATM	284	N	1	1.225	6.485	-10.491	N
HETATM	285	O	1	0.800	1.876	-10.521	O
HETATM	286	N	1	-3.002	4.417	-9.701	N
HETATM	287	H	1	-3.420	3.640	-9.520	H
HETATM	288	H	1	-3.447	5.195	-9.629	H
HETATM	289	C	1	0.982	8.000	-10.331	C
HETATM	290	H	1	0.141	8.192	-10.752	H
HETATM	291	C	1	2.044	8.785	-11.091	C
HETATM	292	H	1	2.892	8.336	-11.051	H
HETATM	293	C	1	2.075	10.109	-10.231	C
HETATM	294	H	1	2.979	10.427	-10.171	H
HETATM	295	C	1	1.604	9.688	-8.861	C
HETATM	296	H	1	1.012	10.361	-8.516	H
HETATM	297	C	1	2.762	9.507	-7.891	C
HETATM	298	H	1	3.396	10.216	-8.020	H
HETATM	299	H	1	2.432	9.566	-6.991	H
HETATM	300	O	1	0.891	8.473	-8.991	O
HETATM	301	O	1	1.669	9.007	-12.411	O
HETATM	302	H	1	1.667	8.269	-12.833	H
HETATM	303	O	1	1.317	11.042	-10.831	O
HETATM	304	H	1	1.330	11.757	-10.371	H
HETATM	305	O	1	3.428	8.235	-8.071	O
HETATM	306	P	1	4.642	7.943	-7.231	P
HETATM	307	O	1	4.442	8.284	-5.791	O
HETATM	308	H	1	3.666	8.037	-5.546	H
HETATM	309	O	1	5.754	8.759	-7.931	O
HETATM	310	H	1	5.568	9.588	-7.887	H
HETATM	311	O	1	4.952	6.384	-7.291	O
HETATM	312	H	1	5.599	6.245	-7.825	H
HETATM	313	N	1	3.274	0.708	-11.064	N
HETATM	314	H	1	2.589	1.271	-10.912	H
HETATM	315	C	1	4.567	1.232	-10.964	C
HETATM	316	N	1	5.695	0.418	-11.004	N
HETATM	317	C	1	5.334	-0.845	-11.264	C
HETATM	318	C	1	4.176	-1.479	-11.404	C
HETATM	319	C	1	2.961	-0.592	-11.374	C
HETATM	320	N	1	4.228	-2.852	-11.614	N
HETATM	321	C	1	5.524	-3.050	-11.664	C
HETATM	322	H	1	5.909	-3.903	-11.879	H
HETATM	323	N	1	6.322	-1.897	-11.374	N
HETATM	324	O	1	1.783	-0.992	-11.404	O
HETATM	325	N	1	4.706	2.523	-10.584	N

HETATM	326	H	1	3.978	3.021	-10.403	H
HETATM	327	H	1	5.527	2.885	-10.512	H
HETATM	328	C	1	7.853	-1.813	-11.214	C
HETATM	329	H	1	8.132	-0.996	-11.635	H
HETATM	330	C	1	8.523	-2.952	-11.974	C
HETATM	331	H	1	7.988	-3.747	-11.934	H
HETATM	332	C	1	9.837	-3.120	-11.114	C
HETATM	333	H	1	10.058	-4.053	-11.054	H
HETATM	334	C	1	9.467	-2.608	-9.744	C
HETATM	335	H	1	10.198	-2.089	-9.399	H
HETATM	336	C	1	9.166	-3.741	-8.774	C
HETATM	337	H	1	9.805	-4.445	-8.903	H
HETATM	338	H	1	9.259	-3.419	-7.874	H
HETATM	339	O	1	8.334	-1.771	-9.874	O
HETATM	340	O	1	8.783	-2.602	-13.294	O
HETATM	341	H	1	8.049	-2.522	-13.716	H
HETATM	342	O	1	10.844	-2.464	-11.714	O
HETATM	343	H	1	11.553	-2.552	-11.254	H
HETATM	344	O	1	7.832	-4.270	-8.954	O
HETATM	345	P	1	7.415	-5.447	-8.114	P
HETATM	346	O	1	7.775	-5.284	-6.674	O
HETATM	347	H	1	7.610	-4.486	-6.429	H
HETATM	348	O	1	8.110	-6.638	-8.814	O
HETATM	349	H	1	8.953	-6.539	-8.770	H
HETATM	350	O	1	5.832	-5.593	-8.174	O
HETATM	351	H	1	5.625	-6.221	-8.708	H
HETATM	352	N	1	0.362	-3.330	-11.947	N
HETATM	353	H	1	0.994	-2.708	-11.795	H
HETATM	354	C	1	0.748	-4.670	-11.847	C
HETATM	355	N	1	-0.179	-5.707	-11.887	N
HETATM	356	C	1	-1.398	-5.216	-12.147	C
HETATM	357	C	1	-1.907	-3.998	-12.287	C
HETATM	358	C	1	-0.898	-2.883	-12.257	C
HETATM	359	N	1	-3.278	-3.907	-12.497	N
HETATM	360	C	1	-3.610	-5.175	-12.547	C
HETATM	361	H	1	-4.499	-5.468	-12.762	H
HETATM	362	N	1	-2.547	-6.089	-12.257	N
HETATM	363	O	1	-1.173	-1.669	-12.287	O
HETATM	364	N	1	2.018	-4.944	-11.467	N
HETATM	365	H	1	2.588	-4.272	-11.286	H
HETATM	366	H	1	2.292	-5.798	-11.395	H
HETATM	367	C	1	-2.624	-7.621	-12.097	C
HETATM	368	H	1	-1.841	-7.984	-12.518	H
HETATM	369	C	1	-3.826	-8.168	-12.857	C
HETATM	370	H	1	-4.561	-7.552	-12.817	H
HETATM	371	C	1	-4.132	-9.457	-11.997	C
HETATM	372	H	1	-5.082	-9.580	-11.937	H

HETATM	373	C	1	-3.583	-9.143	-10.627	C
HETATM	374	H	1	-3.144	-9.924	-10.282	H
HETATM	375	C	1	-4.678	-8.725	-9.657	C
HETATM	376	H	1	-5.446	-9.287	-9.786	H
HETATM	377	H	1	-4.368	-8.851	-8.757	H
HETATM	378	O	1	-2.633	-8.103	-10.757	O
HETATM	379	O	1	-3.505	-8.463	-14.177	O
HETATM	380	H	1	-3.350	-7.741	-14.599	H
HETATM	381	O	1	-3.584	-10.527	-12.597	O
HETATM	382	H	1	-3.745	-11.223	-12.137	H
HETATM	383	O	1	-5.065	-7.342	-9.837	O
HETATM	384	P	1	-6.192	-6.805	-8.997	P
HETATM	385	O	1	-6.067	-7.180	-7.557	O
HETATM	386	H	1	-5.257	-7.099	-7.312	H
HETATM	387	O	1	-7.449	-7.372	-9.697	O
HETATM	388	H	1	-7.439	-8.220	-9.653	H
HETATM	389	O	1	-6.171	-5.215	-9.057	O
HETATM	390	H	1	-6.775	-4.944	-9.591	H
HETATM	391	N	1	-3.350	-0.012	-12.830	N
HETATM	392	H	1	-2.797	-0.705	-12.678	H
HETATM	393	C	1	-4.723	-0.256	-12.730	C
HETATM	394	N	1	-5.657	0.775	-12.770	N
HETATM	395	C	1	-5.041	1.935	-13.030	C
HETATM	396	C	1	-3.777	2.315	-13.170	C
HETATM	397	C	1	-2.774	1.195	-13.140	C
HETATM	398	N	1	-3.543	3.669	-13.380	N
HETATM	399	C	1	-4.769	4.131	-13.430	C
HETATM	400	H	1	-4.968	5.046	-13.645	H
HETATM	401	N	1	-5.789	3.169	-13.140	N
HETATM	402	O	1	-1.537	1.341	-13.170	O
HETATM	403	N	1	-5.128	-1.490	-12.350	N
HETATM	404	H	1	-4.519	-2.127	-12.169	H
HETATM	405	H	1	-6.006	-1.673	-12.278	H
HETATM	406	C	1	-7.305	3.406	-12.980	C
HETATM	407	H	1	-7.748	2.666	-13.401	H
HETATM	408	C	1	-7.724	4.659	-13.740	C
HETATM	409	H	1	-7.034	5.326	-13.700	H
HETATM	410	C	1	-8.973	5.097	-12.880	C
HETATM	411	H	1	-8.996	6.055	-12.820	H
HETATM	412	C	1	-8.718	4.519	-11.510	C
HETATM	413	H	1	-9.541	4.164	-11.165	H
HETATM	414	C	1	-8.188	5.565	-10.540	C
HETATM	415	H	1	-8.667	6.387	-10.669	H
HETATM	416	H	1	-8.346	5.269	-9.640	H
HETATM	417	O	1	-7.783	3.465	-11.640	O
HETATM	418	O	1	-8.050	4.371	-15.060	O
HETATM	419	H	1	-7.349	4.141	-15.482	H

HETATM	420	O	1	-10.094	4.664	-13.480	O
HETATM	421	H	1	-10.770	4.898	-13.020	H
HETATM	422	O	1	-6.773	5.805	-10.720	O
HETATM	423	P	1	-6.120	6.869	-9.880	P
HETATM	424	O	1	-6.506	6.785	-8.440	O
HETATM	425	H	1	-6.511	5.971	-8.195	H
HETATM	426	O	1	-6.553	8.179	-10.580	O
HETATM	427	H	1	-7.398	8.258	-10.536	H
HETATM	428	O	1	-4.542	6.683	-9.940	O
HETATM	429	H	1	-4.209	7.255	-10.474	H
HETATM	430	N	1	0.339	3.333	-13.713	N
HETATM	431	H	1	-0.409	2.855	-13.561	H
HETATM	432	C	1	0.239	4.724	-13.613	C
HETATM	433	N	1	1.362	5.545	-13.653	N
HETATM	434	C	1	2.452	4.811	-13.913	C
HETATM	435	C	1	2.697	3.515	-14.053	C
HETATM	436	C	1	1.478	2.634	-14.023	C
HETATM	437	N	1	4.019	3.140	-14.263	N
HETATM	438	C	1	4.607	4.311	-14.313	C
HETATM	439	H	1	5.537	4.413	-14.528	H
HETATM	440	N	1	3.757	5.426	-14.023	N
HETATM	441	O	1	1.494	1.389	-14.053	O
HETATM	442	N	1	-0.946	5.256	-13.233	N
HETATM	443	H	1	-1.643	4.717	-13.052	H
HETATM	444	H	1	-1.036	6.148	-13.161	H
HETATM	445	C	1	4.151	6.909	-13.863	C
HETATM	446	H	1	3.461	7.426	-14.284	H
HETATM	447	C	1	5.441	7.194	-14.623	C
HETATM	448	H	1	6.032	6.439	-14.583	H
HETATM	449	C	1	6.008	8.391	-13.763	C
HETATM	450	H	1	6.963	8.314	-13.703	H
HETATM	451	C	1	5.406	8.198	-12.393	C
HETATM	452	H	1	5.138	9.053	-12.048	H
HETATM	453	C	1	6.390	7.562	-11.423	C
HETATM	454	H	1	7.258	7.952	-11.552	H
HETATM	455	H	1	6.113	7.750	-10.523	H
HETATM	456	O	1	4.260	7.379	-12.523	O
HETATM	457	O	1	5.188	7.549	-15.943	O
HETATM	458	H	1	4.886	6.876	-16.365	H
HETATM	459	O	1	5.694	9.552	-14.363	O
HETATM	460	H	1	5.997	10.199	-13.903	H
HETATM	461	O	1	6.481	6.129	-11.603	O
HETATM	462	P	1	7.471	5.369	-10.763	P
HETATM	463	O	1	7.427	5.761	-9.323	O
HETATM	464	H	1	6.618	5.851	-9.078	H
HETATM	465	O	1	8.819	5.662	-11.463	O
HETATM	466	H	1	8.986	6.494	-11.419	H

HETATM	467	O	1	7.121	3.818	-10.823	O
HETATM	468	H	1	6.378	3.680	-10.433	H
HETATM	469	N	1	3.279	-0.685	-14.596	N
HETATM	470	H	1	2.882	0.108	-14.444	H
HETATM	471	C	1	4.673	-0.732	-14.496	C
HETATM	472	N	1	5.372	-1.934	-14.536	N
HETATM	473	C	1	4.529	-2.941	-14.796	C
HETATM	474	C	1	3.213	-3.049	-14.936	C
HETATM	475	C	1	2.465	-1.745	-14.906	C
HETATM	476	N	1	2.703	-4.325	-15.146	N
HETATM	477	C	1	3.806	-5.033	-15.196	C
HETATM	478	H	1	3.810	-5.968	-15.411	H
HETATM	479	N	1	5.004	-4.304	-14.906	N
HETATM	480	O	1	1.225	-1.631	-14.936	O
HETATM	481	N	1	5.326	0.391	-14.116	N
HETATM	482	H	1	4.863	1.141	-13.935	H
HETATM	483	H	1	6.223	0.388	-14.044	H
HETATM	484	C	1	6.437	-4.851	-14.746	C
HETATM	485	H	1	7.024	-4.218	-15.167	H
HETATM	486	C	1	6.586	-6.163	-15.506	C
HETATM	487	H	1	5.773	-6.672	-15.466	H
HETATM	488	C	1	7.717	-6.852	-14.646	C
HETATM	489	H	1	7.540	-7.793	-14.586	H
HETATM	490	C	1	7.588	-6.233	-13.276	C
HETATM	491	H	1	8.467	-6.057	-12.931	H
HETATM	492	C	1	6.852	-7.145	-12.306	C
HETATM	493	H	1	7.150	-8.049	-12.435	H
HETATM	494	H	1	7.068	-6.890	-11.406	H
HETATM	495	O	1	6.893	-5.008	-13.406	O
HETATM	496	O	1	6.965	-5.949	-16.826	O
HETATM	497	H	1	6.327	-5.578	-17.248	H
HETATM	498	O	1	8.904	-6.661	-15.246	O
HETATM	499	H	1	9.516	-7.030	-14.786	H
HETATM	500	O	1	5.418	-7.086	-12.486	O
HETATM	501	P	1	4.558	-7.991	-11.646	P
HETATM	502	O	1	4.953	-7.989	-10.206	O
HETATM	503	H	1	5.127	-7.194	-9.961	H
HETATM	504	O	1	4.709	-9.363	-12.346	O
HETATM	505	H	1	5.519	-9.616	-12.302	H
HETATM	506	O	1	3.053	-7.481	-11.706	O
HETATM	507	H	1	2.993	-6.728	-11.316	H
HETATM	508	N	1	-1.024	-3.190	-15.479	N
HETATM	509	H	1	-0.194	-2.878	-15.327	H
HETATM	510	C	1	-1.216	-4.571	-15.379	C
HETATM	511	N	1	-2.485	-5.141	-15.419	N
HETATM	512	C	1	-3.398	-4.197	-15.679	C
HETATM	513	C	1	-3.369	-2.877	-15.819	C

HETATM	514	C	1	-1.993	-2.269	-15.789	C
HETATM	515	N	1	-4.584	-2.236	-16.029	N
HETATM	516	C	1	-5.403	-3.259	-16.079	C
HETATM	517	H	1	-6.334	-3.166	-16.294	H
HETATM	518	N	1	-4.803	-4.526	-15.789	N
HETATM	519	O	1	-1.750	-1.048	-15.819	O
HETATM	520	N	1	-0.168	-5.337	-14.999	N
HETATM	521	H	1	0.627	-4.955	-14.818	H
HETATM	522	H	1	-0.265	-6.229	-14.927	H
HETATM	523	C	1	-5.497	-5.895	-15.629	C
HETATM	524	H	1	-4.929	-6.545	-16.050	H
HETATM	525	C	1	-6.818	-5.906	-16.389	C
HETATM	526	H	1	-7.239	-5.044	-16.349	H
HETATM	527	C	1	-7.621	-6.959	-15.529	C
HETATM	528	H	1	-8.539	-6.684	-15.469	H
HETATM	529	C	1	-6.992	-6.895	-14.159	C
HETATM	530	H	1	-6.908	-7.787	-13.814	H
HETATM	531	C	1	-7.823	-6.068	-13.189	C
HETATM	532	H	1	-8.752	-6.269	-13.318	H
HETATM	533	H	1	-7.591	-6.309	-12.289	H
HETATM	534	O	1	-5.701	-6.332	-14.289	O
HETATM	535	O	1	-6.644	-6.305	-17.709	O
HETATM	536	H	1	-6.209	-5.709	-18.131	H
HETATM	537	O	1	-7.555	-8.159	-16.129	O
HETATM	538	H	1	-7.987	-8.729	-15.669	H
HETATM	539	O	1	-7.614	-4.647	-13.369	O
HETATM	540	P	1	-8.424	-3.698	-12.529	P
HETATM	541	O	1	-8.463	-4.091	-11.089	O
HETATM	542	H	1	-7.690	-4.347	-10.844	H
HETATM	543	O	1	-9.803	-3.704	-13.229	O
HETATM	544	H	1	-10.140	-4.484	-13.185	H
HETATM	545	O	1	-7.759	-2.254	-12.589	O
HETATM	546	H	1	-7.004	-2.274	-12.199	H
HETATM	547	N	1	-3.065	1.352	-16.362	N
HETATM	548	H	1	-2.842	0.493	-16.210	H
HETATM	549	C	1	-4.419	1.687	-16.262	C
HETATM	550	N	1	-4.853	3.009	-16.302	N
HETATM	551	C	1	-3.818	3.818	-16.562	C
HETATM	552	C	1	-2.509	3.651	-16.702	C
HETATM	553	C	1	-2.048	2.219	-16.672	C
HETATM	554	N	1	-1.744	4.792	-16.912	N
HETATM	555	C	1	-2.677	5.714	-16.962	C
HETATM	556	H	1	-2.486	6.630	-17.177	H
HETATM	557	N	1	-4.000	5.250	-16.672	N
HETATM	558	O	1	-0.859	1.850	-16.702	O
HETATM	559	N	1	-5.291	0.725	-15.882	N
HETATM	560	H	1	-4.994	-0.105	-15.701	H

HETATM	561	H	1	-6.167	0.915	-15.810	H
HETATM	562	C	1	-5.288	6.083	-16.512	C
HETATM	563	H	1	-5.994	5.586	-16.933	H
HETATM	564	C	1	-5.161	7.398	-17.272	C
HETATM	565	H	1	-4.260	7.726	-17.232	H
HETATM	566	C	1	-6.124	8.307	-16.412	C
HETATM	567	H	1	-5.755	9.191	-16.352	H
HETATM	568	C	1	-6.127	7.675	-15.042	C
HETATM	569	H	1	-7.022	7.685	-14.697	H
HETATM	570	C	1	-5.217	8.414	-14.072	C
HETATM	571	H	1	-5.320	9.360	-14.201	H
HETATM	572	H	1	-5.481	8.209	-13.172	H
HETATM	573	O	1	-5.701	6.332	-15.172	O
HETATM	574	O	1	-5.576	7.267	-18.592	O
HETATM	575	H	1	-5.029	6.772	-19.014	H
HETATM	576	O	1	-7.325	8.367	-17.012	O
HETATM	577	H	1	-7.847	8.855	-16.552	H
HETATM	578	O	1	-3.826	8.058	-14.252	O
HETATM	579	P	1	-2.797	8.764	-13.412	P
HETATM	580	O	1	-3.184	8.844	-11.972	O
HETATM	581	H	1	-3.519	8.103	-11.727	H
HETATM	582	O	1	-2.659	10.137	-14.112	O
HETATM	583	H	1	-3.399	10.553	-14.068	H
HETATM	584	O	1	-1.431	7.952	-13.472	O
HETATM	585	H	1	-1.529	7.203	-13.082	H

Appendix III: (Chapter 5)

Supplementary data for ESI-MS spectral analyses. G = monomeric TAG with 409.35 a.m.u.

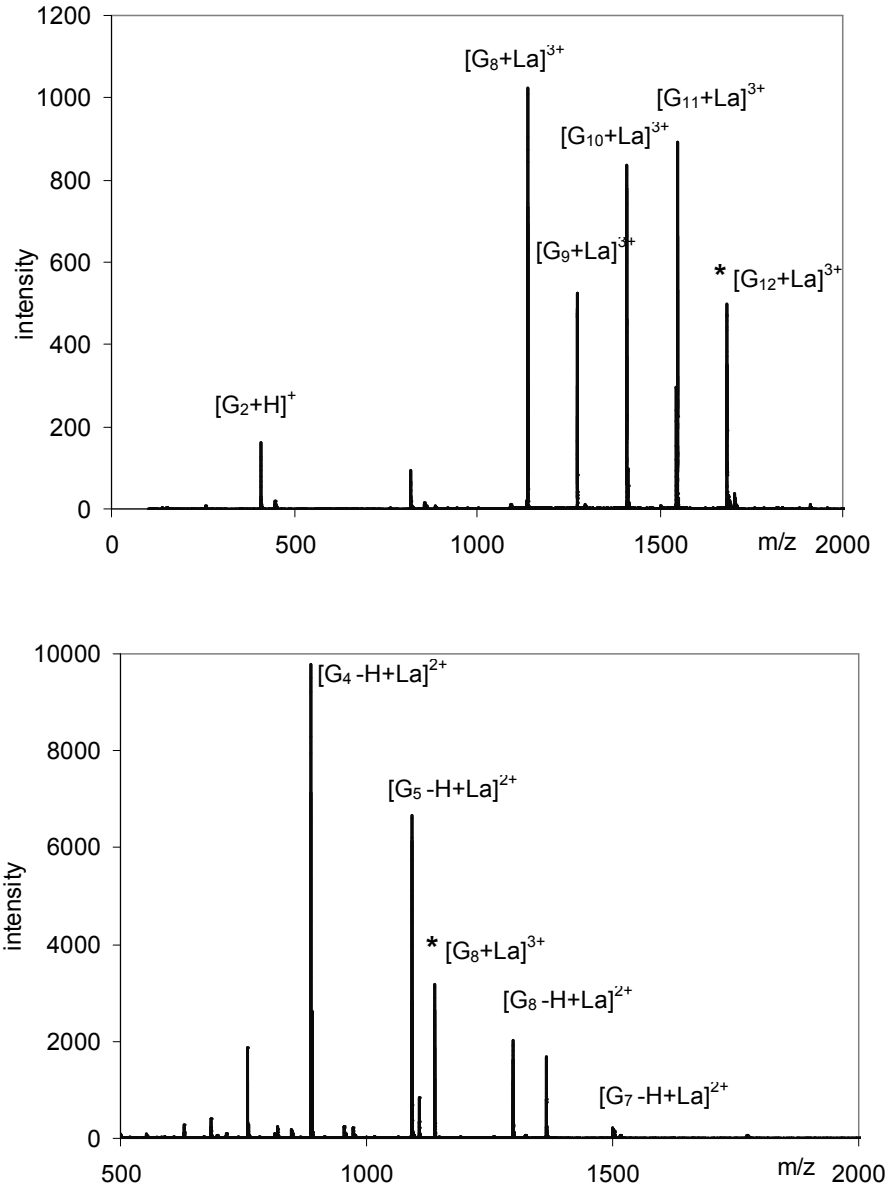

Figure 1. ESI-MS/MS spectra of the $[TAG]La^{3+}$ complex: $[TAG_{12} + La]^{3+}$ (top) and $[TAG_8 + La]^{3+}$ (bottom). The parent ion is marked by an asterisk *.

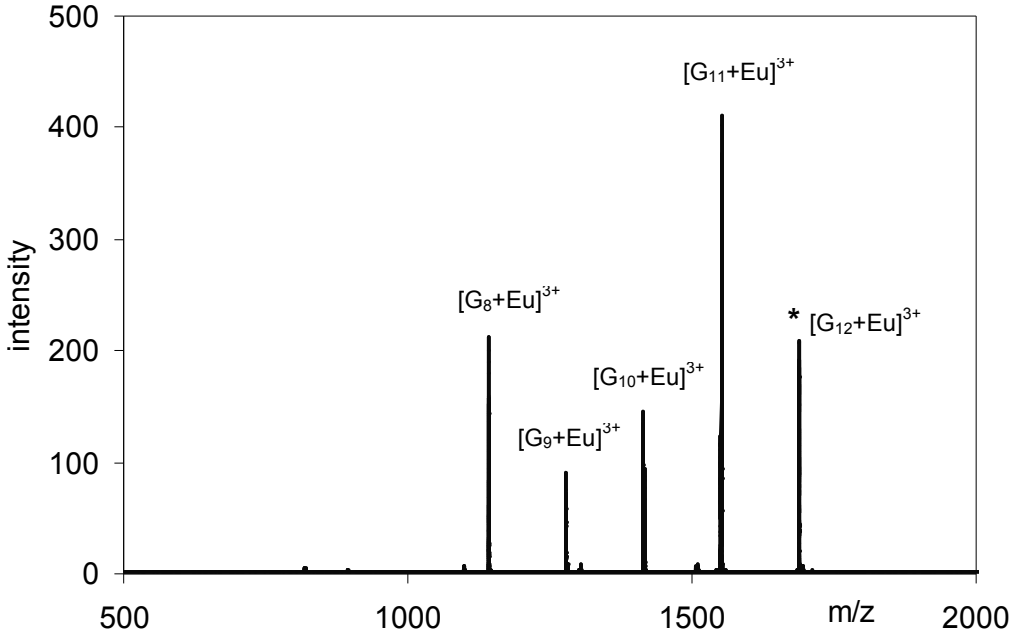

Figure 2. ESI-MS/MS spectra of the [TAG]Eu^{3+} complex: : $[TAG_{12} + Eu]^{3+}$. The parent ion is marked by an asterisk *.

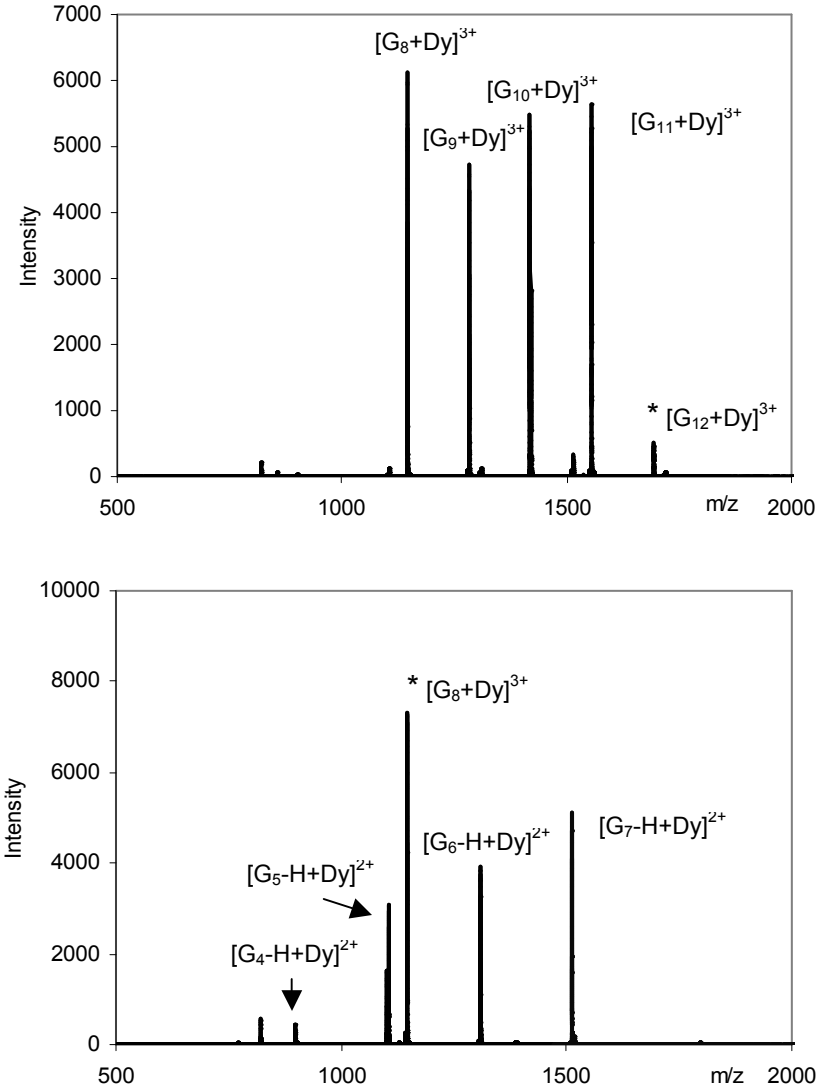

Figure 3. ESI-MS/MS spectra of the [TAG]Dy^{3+} complex: $[TAG_{12} + Dy]^{3+}$ (top) and $[TAG_8 + Dy]^{3+}$ (bottom). The parent ion is marked by an asterisk *.

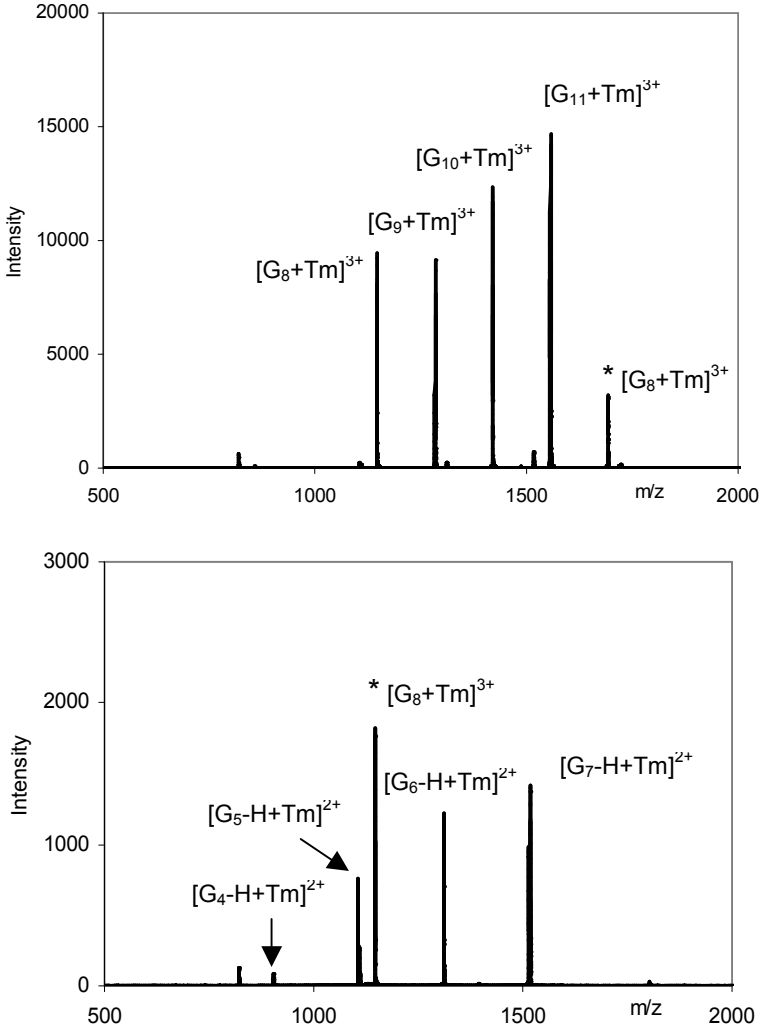

Figure 4. ESI-MS/MS spectra of the $[TAG]Tm^{3+}$ complex: $[TAG_{12} + Tm]^{3+}$ (top) and $[TAG_8 + Tm]^{3+}$ (bottom). The parent ion is marked by an asterisk *.

Table 1a. TANDEM MS of $[M12+La]^{3+}$ (1683.1 m/z) at DP80. G = monomeric TAG with 409.36 a.m.u.

$[TAG]_nLa^{3+}{}_n$	*m/z*	Rel. intensity
$[G+H]^+$	410.1	15.8
$[G2+H]^+$	819.2	8.2
$[G8+La]^{3+}$	1137.3	100.0
$[G9+La]^{3+}$	1273.7	51.3
$[G10+La]^{3+}$	1410.1	81.8
$[G11+La]^{3+}$	1546.4	86.9
$[G12+La]^{3+}$	1683.1	48.5

Table 1b. TANDEM MS of $[M8+La]^{3+}$ (1137.7 m/z) at DP80. G = monomeric TAG with 409.36 a.m.u.

$[TAG]_nLa^{3+}{}_n$	*m/z*	Rel. intensity
monoacetyl sugar	139.0	43.3
guanine	152.0	24.5
triacetyl sugar	250.1	76.3
$[G+H]^+$	410.1	100.0
$[G3-3H+La+Eu]^{2+}$	758.2	6.9
$[G4-H+La]^{2+}$	887.2	44.6
$[G5-H+La]^{2+}$	1091.8	30.1
$[G8+La]^{3+}$	1137.7	14.2
$[G6-H+La]^{2+}$	1296.9	8.2
$[G3-2H+La]^+$	1364.3	6.2

Table 2. TANDEM MS of $[M12+Eu]^{3+}$ (1687.8 m/z) at DP80. G = monomeric TAG with 409.36 a.m.u.

$[TAG]_nEu^{3+}{}_n$	*m/z*	Rel. intensity
$[G+H]^+$	410.1	5.8
$[G8+Eu]^{3+}$	1142.3	51.8
$[G9+Eu]^{3+}$	1278.7	21.9
$[G10+Eu]^{3+}$	1415.1	35.5
$[G11+Eu]^{3+}$	1551.7	100.0
$[G12+Eu]^{3+}$	1687.8	50.9

Table 3a. TANDEM MS of $[M12+Tb]^{3+}$ (1689.4 m/z) at DP80. G = monomeric TAG with 409.36 a.m.u.

$[TAG]_nTb^{3+}{}_n$	*m/z*	Rel. intensity
$[G+H]^+$	410.2	0.9
$[G8+Tb]^{3+}$	1144.3	33.4
$[G9+Tb]^{3+}$	1280.7	24.8
$[G10+Tb]^{3+}$	1417.4	36.8
$[G11+Tb]^{3+}$	1553.4	100.0
$[G12+Tb]^{3+}$	1689.4	77.5

Table 3b. TANDEM MS of $[M8+Tb]^{3+}$ (1143.9 m/z) at DP80. G = monomeric TAG with 409.36 a.m.u.

$[TAG]_nTb^{3+}{}_n$	*m/z*	Rel. intensity
guanine	152.1	12.9
triacetyl sugar	259.1	48.1
$[G+H]^+$	410.1	100.0
$[G2+H]^+$	819.3	1.6
$[G4-H+Tb]^{2+}$	897.7	3.7
$[G5-H+Tb]^{2+}$	1101.8	27.1
$[G6-H+Tb]^{2+}$	1306.8	26.5
$[G7-H+Tb]^{2+}$	1511.4	32.4
$[G8+Tb]^{3+}$	1143.9	60.6

Table 4a. TANDEM MS of [M12+Dy]3+ (1691.4 m/z) at DP80. G = monomeric TAG with 409.36 a.m.u.

$[TAG]_nDy^{3+}{}_n$	*m/z*	Rel. intensity
$[G+H]^+$	410.1	10.4
$[G2+H]^+$	819.7	2.3
$[G8+Dy]^{3+}$	1145.6	108.5
$[G9+Dy]^{3+}$	1282.0	83.9
$[G10+Dy]^{3+}$	1418.7	97.0
$[G11+Dy]^{3+}$	1555.1	100.0
$[G12+Dy]^{3+}$	1691.4	7.7
$[G5-H+Dy]^{2+}$	1104.3	2.4
$[G6-H+Dy]^{2+}$	1308.9	2.4
$[G7-H+Dy]^{2+}$	1513.4	5.7

$[G8\text{-}H+Dy]^{2+}$	1718.0	1.3

Table 4b. TANDEM MS of [M8+Dy]3+ (1144.6 m/z) at DP80. G = monomeric TAG with 409.36 a.m.u.

$\mathbf{[TAG]_nDy^{3+}{}_n}$	*m/z*	Rel. intensity
guanine	152	12.9
triacetyl sugar	259	31.0
$[G+H]^+$	410.1	100.0
$[G2+H]^+$	819.3	2.8
$[G4\text{-}H+Dy]^{2+}$	899.2	2.7
$[G5\text{-}H+Dy]^{2+}$	1103.8	19.6
$[G6\text{-}H+Dy]^{2+}$	1308.3	24.4
$[G7\text{-}H+Dy]^{2+}$	1512.9	32.5
$[G8+Dy]^{3+}$	1144.6	46.4

Table 5a. TANDEM MS of [M12+Tm]3+ (1692.8 m/z) at DP80. G = monomeric TAG with 409.36 a.m.u.

$\mathbf{[TAG]_nTm^{3+}{}_n}$	*m/z*	Rel. intensity
$[G+H]^+$	410.1	8.5
$[G2+H]^+$	819.3	3.1
$[G5\text{-}H+Tm]^{2+}$	1106.8	1.6
$[G6\text{-}H+Tm]^{2+}$	1311.4	1.8
$[G7\text{-}H+Tm]^{2+}$	1516.4	4.8
$[G8\text{-}H+Tm]^{2+}$	1720.9	0.9
$[G8+Tm]^{3+}$	1147.7	64.4
$[G9+Tm]^{3+}$	1284.0	62.2
$[G10+Tm]^{3+}$	1420.4	83.7
$[G11+Tm]^{3+}$	1556.8	100
$[G12+Tm]^{3+}$	1692.8	21.1

Table 5b. TANDEM MS of [M8+Tm]3+ (1147.3 m/z) at DP80. G = monomeric TAG with 409.36 amu.

$[TAG]_nTm^{3+}{}_n$	*m/z*	Rel. intensity
guanine	152.1	6
triacetyl sugar	259.1	17.1
$[G+H]^+$	410.1	100.0
$[G5-H+Tm]^{2+}$	1106.8	11.4
$[G6-H+Tm]^{2+}$	1311.9	20.5
$[G7-H+Tm]^{2+}$	1516.4	24.8
$[G8+Tm]^{3+}$	1147.3	31.3

ESI-MS spectra of both theoretical and experimental data of $[TAG]_n$-(cation-picrate)$_n$ species. TAG = monomeric 2′,3′-5′-*O*-triacetylguanosine with 409.35 a.m.u.

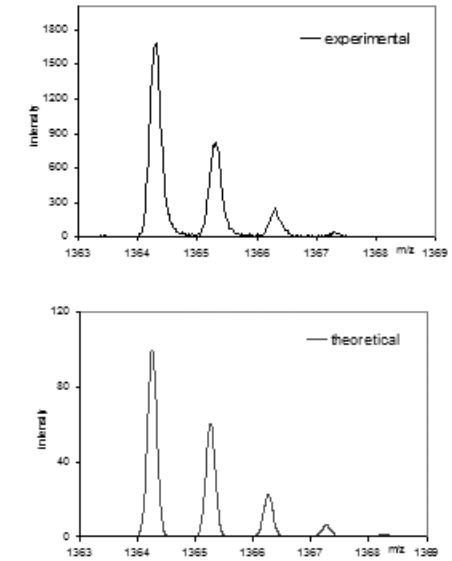

$[TAG_3\text{-}2H+La]^+$

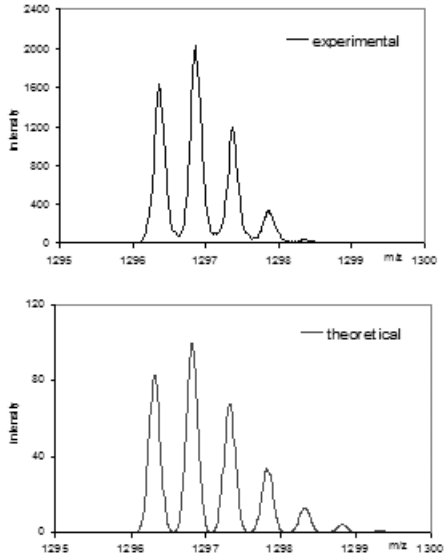

$[TAG_6\text{-}H+La]^{2+}$

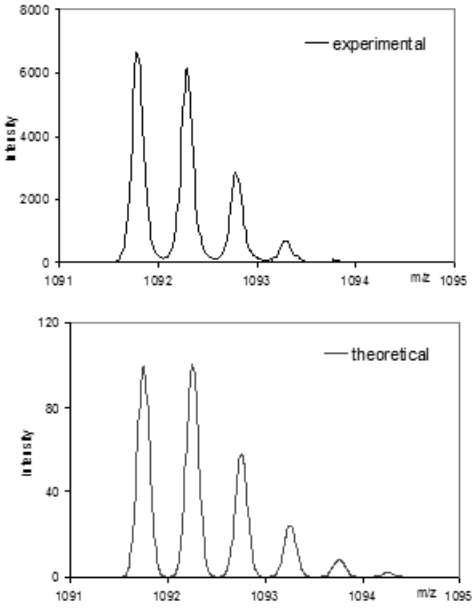

$[TAG_5\text{-}H+La]^{2+}$

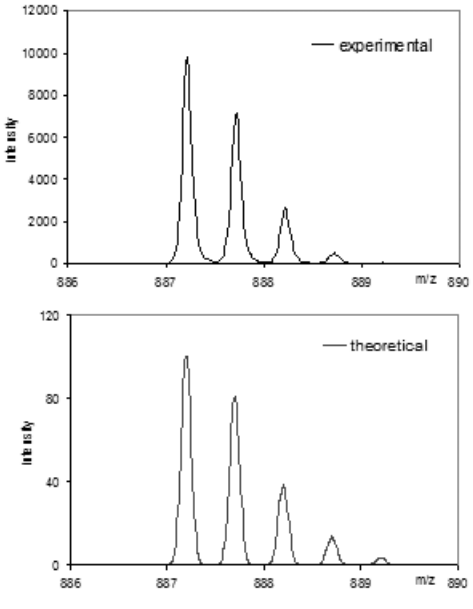

$[TAG_4\text{-}H+La]^{2+}$

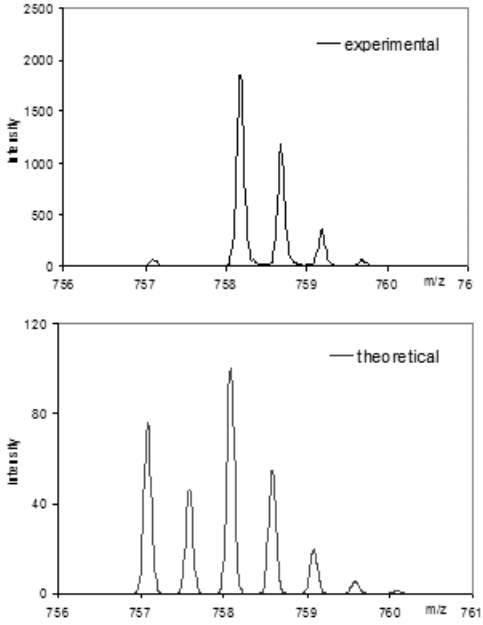

$[TAG_3\text{-}3H+La+Eu]^{2+}$

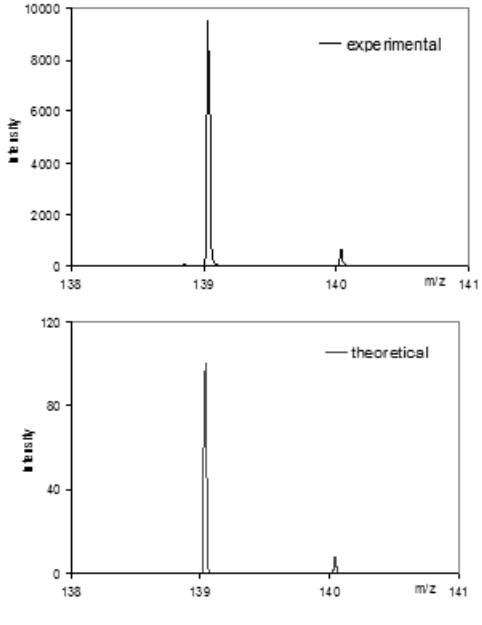

[monoacetyl sugar]$^{+}$

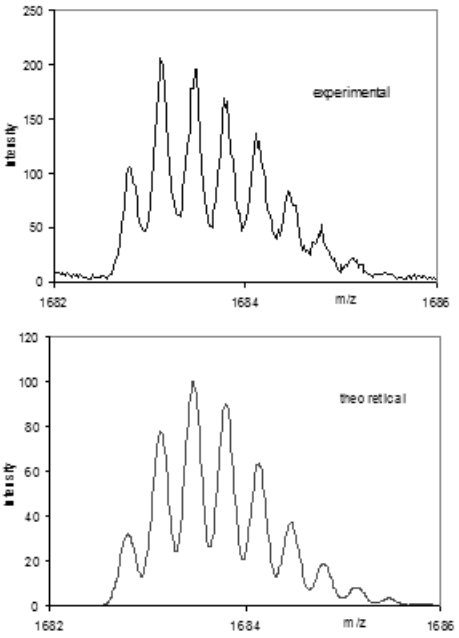

$[TAG_{12}+La]^{3+}$

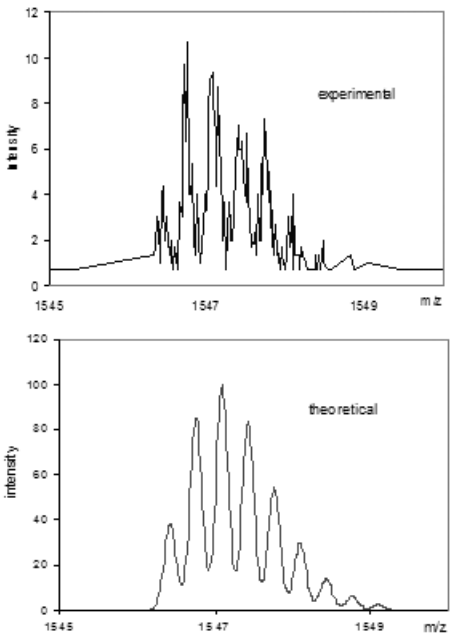

$[TAG_{11}+La]^{3+}$

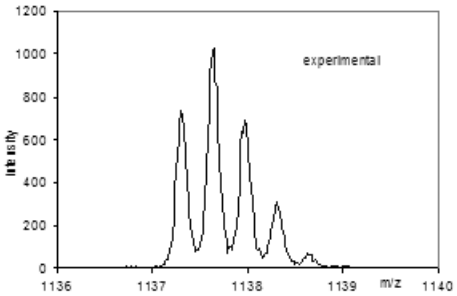

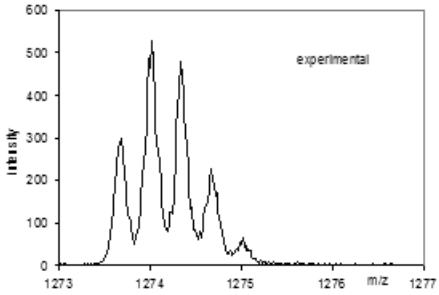

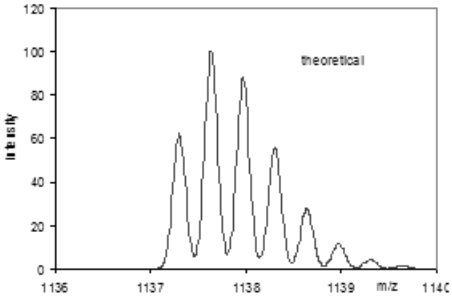

$[TAG_8+La]^{3+}$

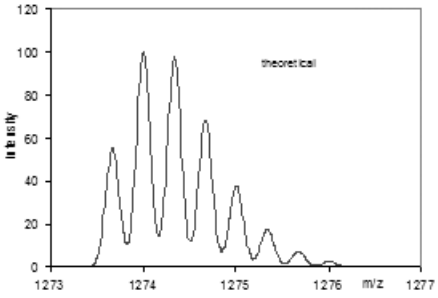

$[TAG_9+La]^{3+}$

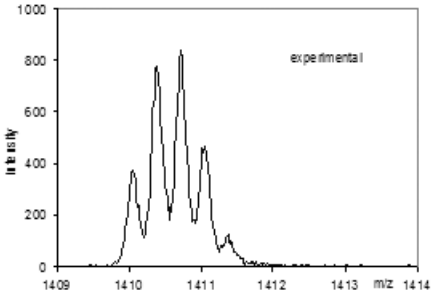

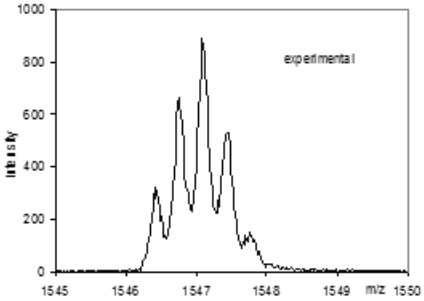

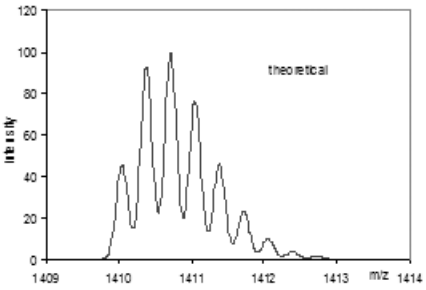

$[TAG_{10}+La]^{3+}$

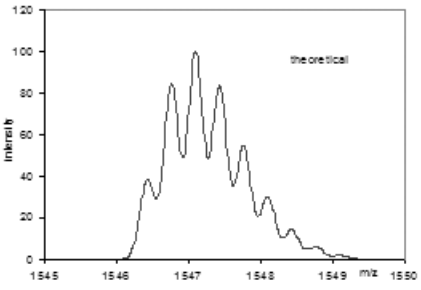

$[TAG_{11}+La]^{3+}$

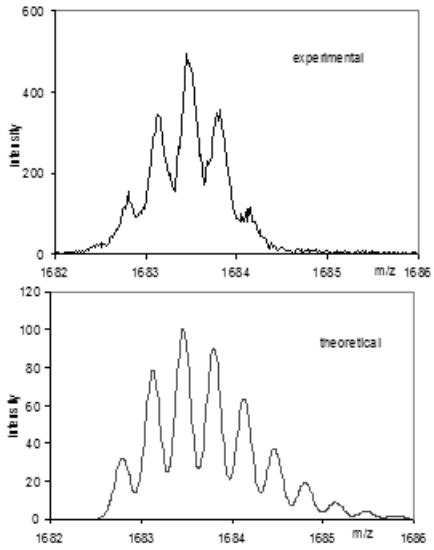

$[TAG_{12}+La]^{3+}$

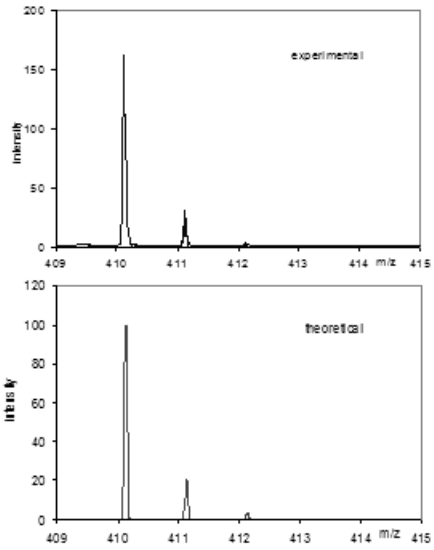

$[TAG]^{+}$

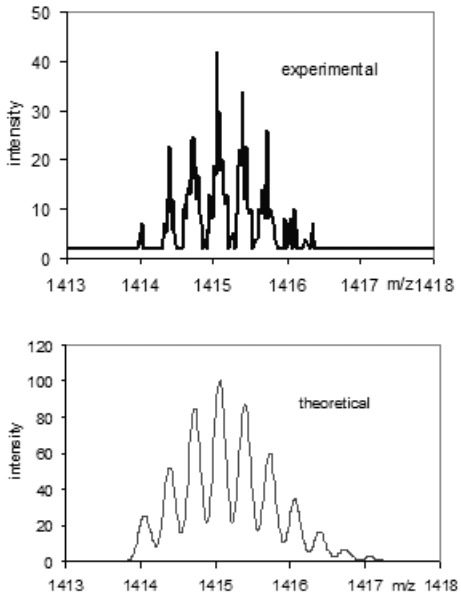

$[TAG_{10}+Eu]^{3+}$

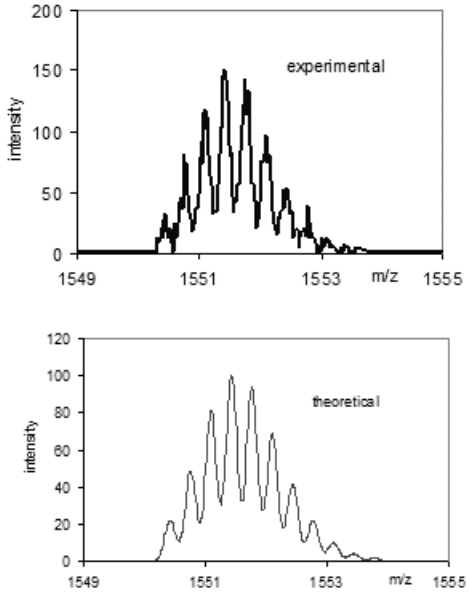

$[TAG_{11}+Eu]^{3+}$

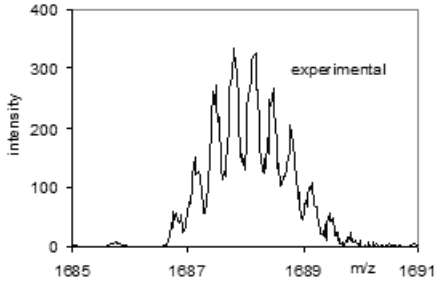

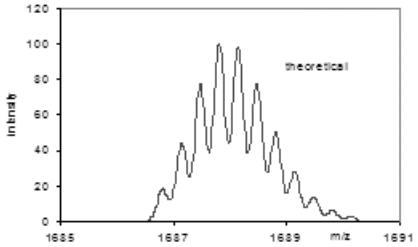

$[TAG_{12}+Eu]^{3+}$

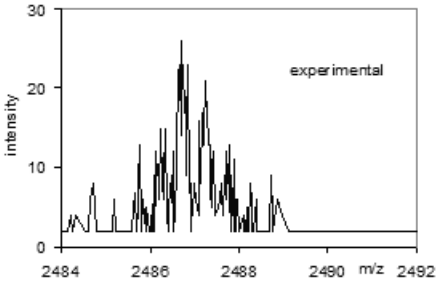

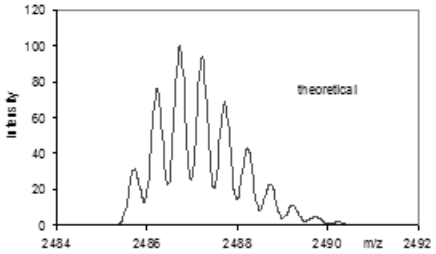

$[TAG_{12}+Na+K]^{2+}$

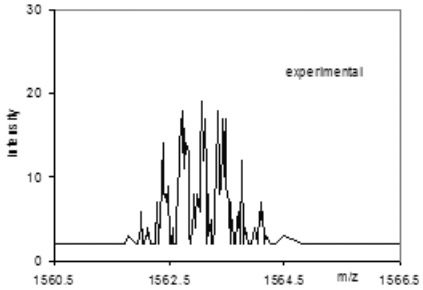

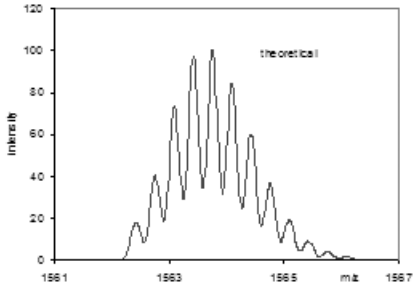

$[TAG_{11}+Eu+HCl]^{3+}$
(different scales)

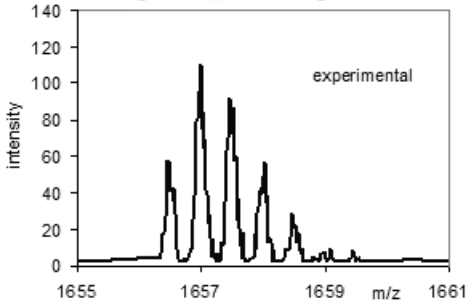

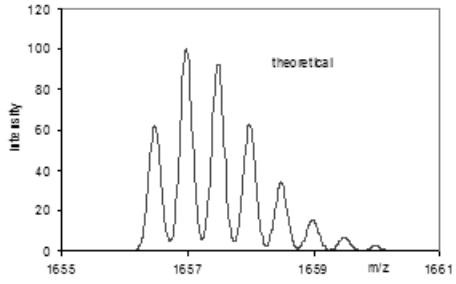

$[TAG_8+K+H]^{2+}$

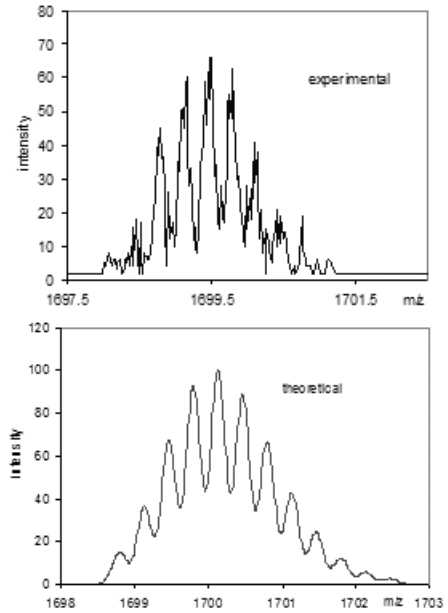

$[TAG_{12}+Eu+HCl]^{3+}$
(different scales)

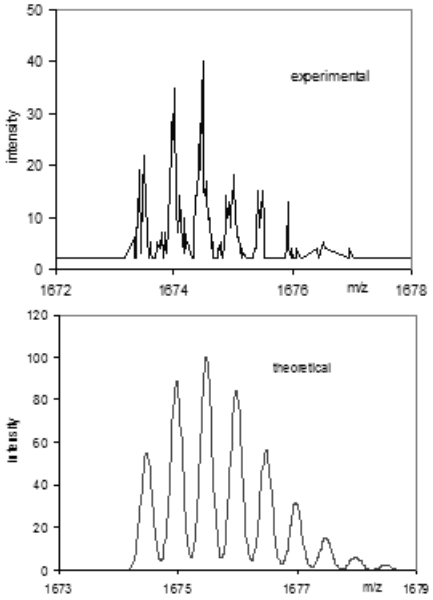

$[TAG_{8}+K+H+HCl]^{2+}$
(different scales)

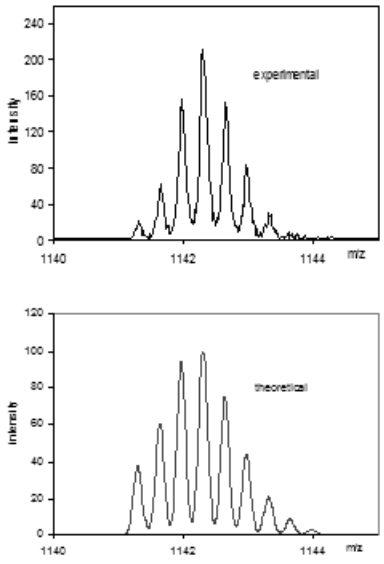

$[TAG_{8}+Eu]^{3+}$

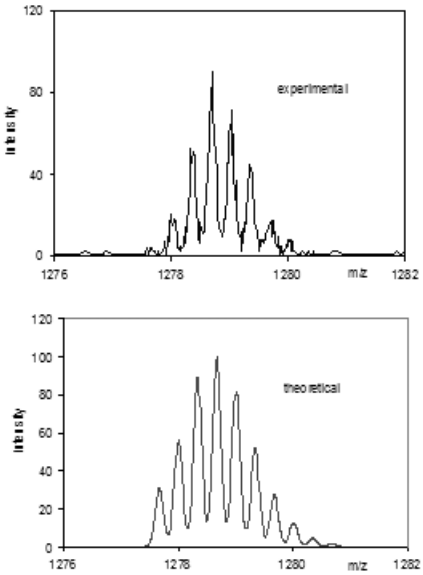

$[TAG_{9}+Eu]^{3+}$

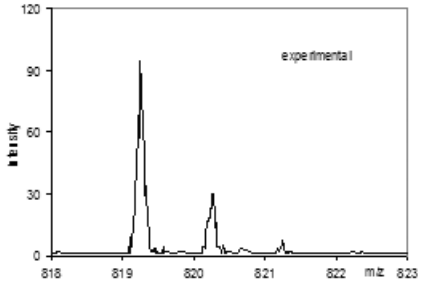

$[TAG]_2^+$

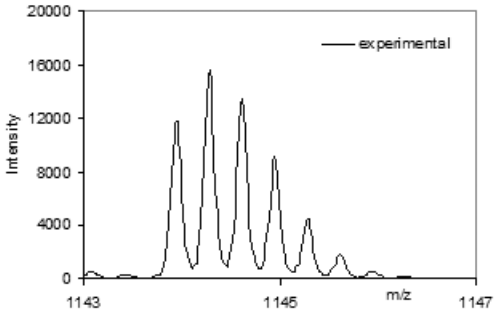

$[TAG_8+Tb]^{3+}$

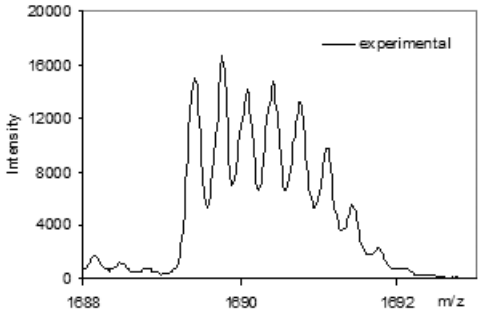

$[TAG_{12}+Tb]^{3+}$

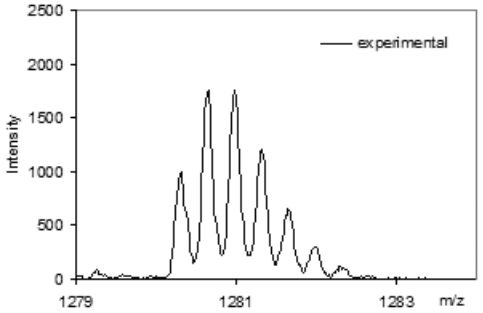

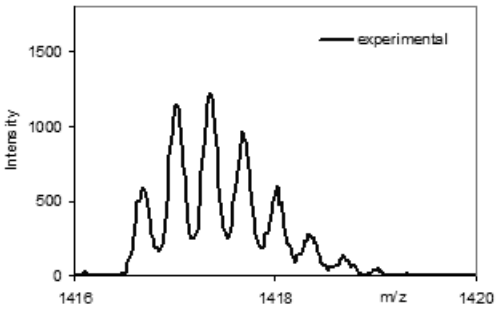

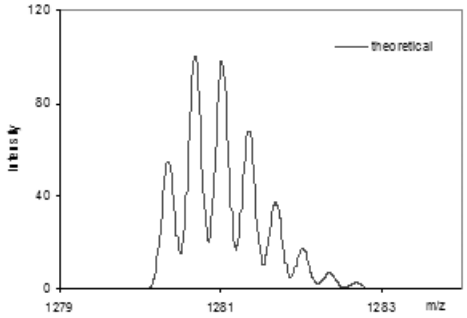

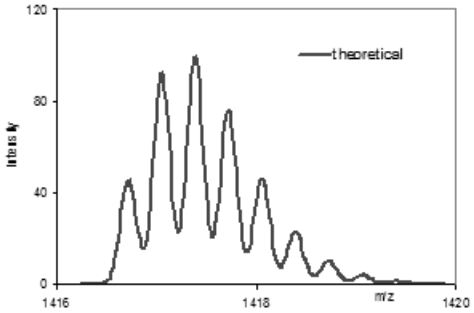

$[TAG_n+Tb]^{3+}$

$[TAG_{10}+Tb]^{3+}$

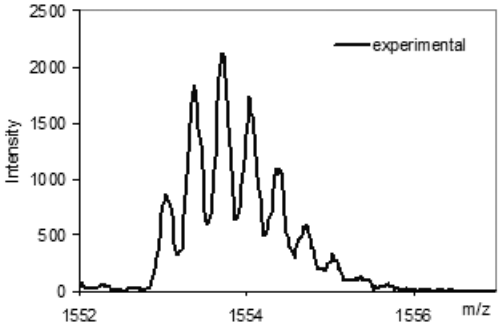

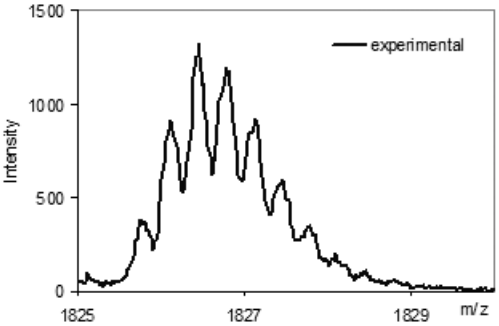

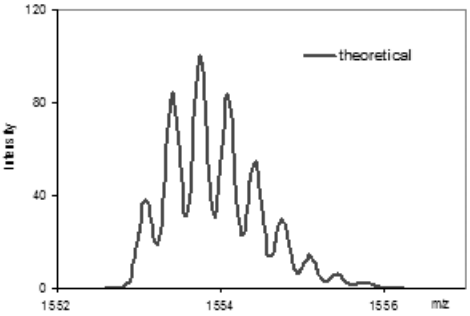

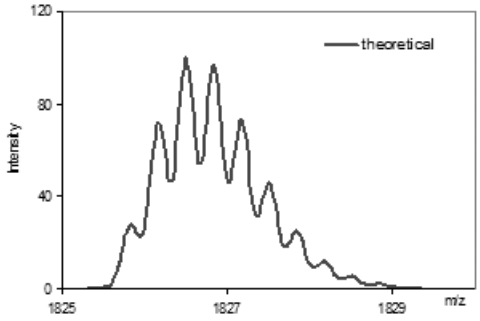

$[TAG_{11}+Tb]^{3+}$

$[TAG_{13}+Tb]^{3+}$

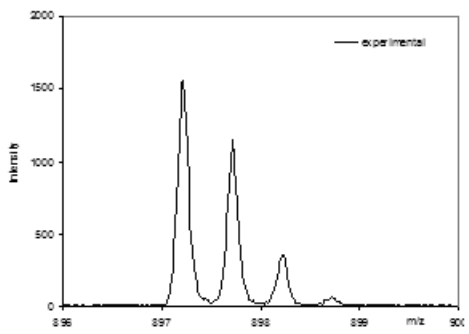

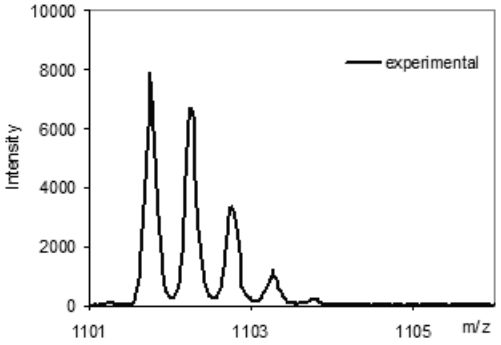

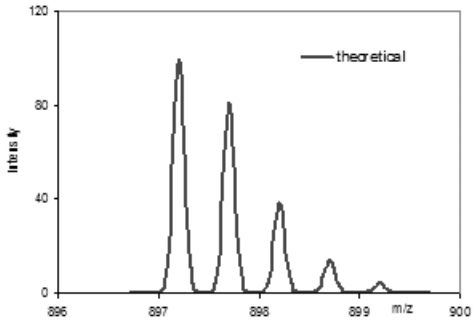

$[TAG_4\text{-}H+Tb]^{2+}$

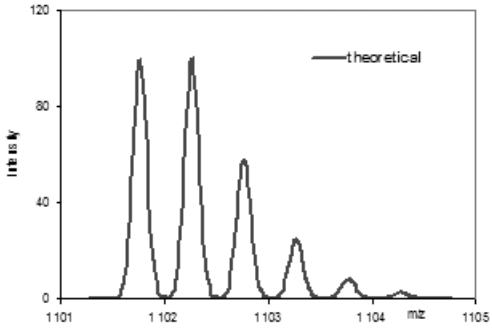

$[TAG_5\text{-}H+Tb]^{2+}$

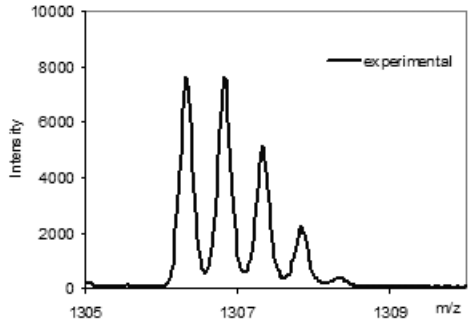

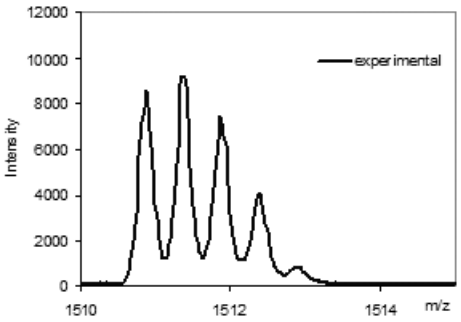

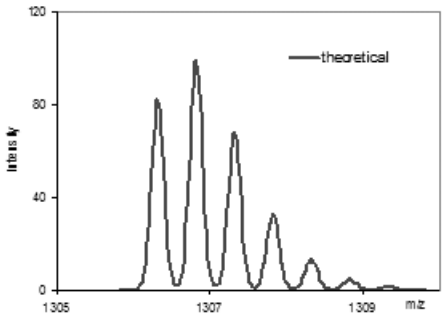

$[TAG_6\text{-}H+Tb]^{2+}$

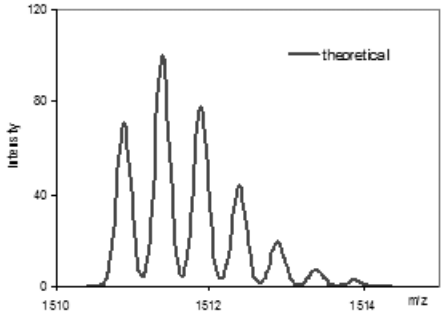

$[TAG_7\text{-}H+Tb]^{2+}$

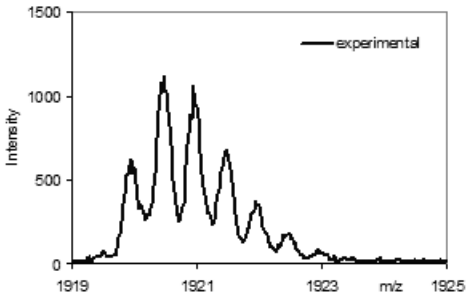

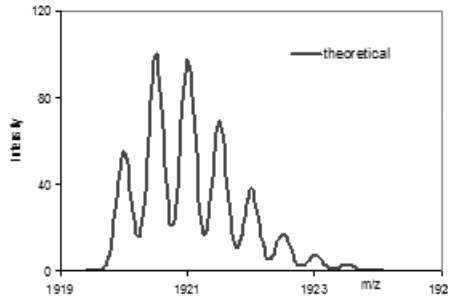

$[TAG_9\text{-}H+Tb]^{2+}$

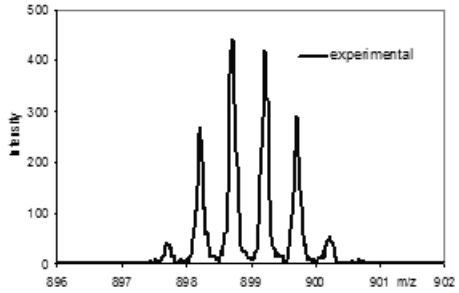

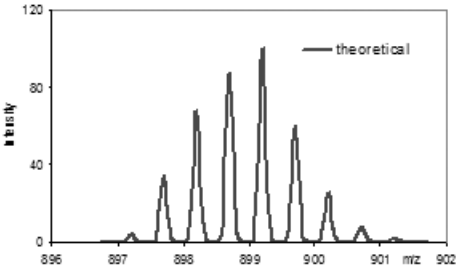

$[(TAG\text{-}H)_4+Dy]^{2+}$

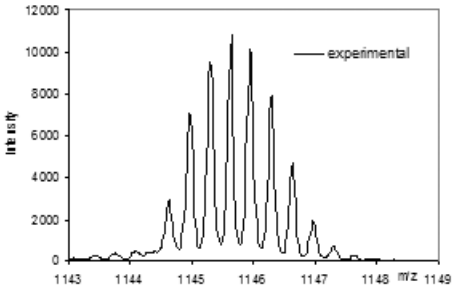

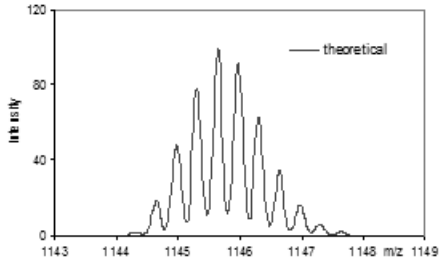

$[TAG_8+Dy]^{3+}$

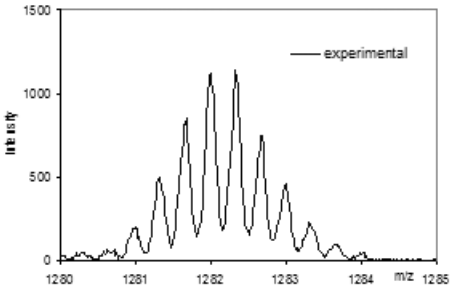

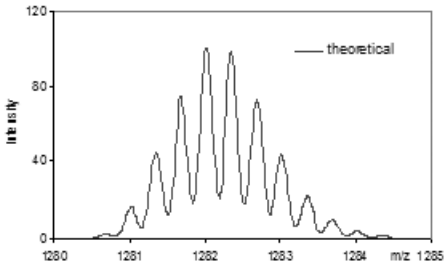

$[TAG_9+Dy]^{3+}$

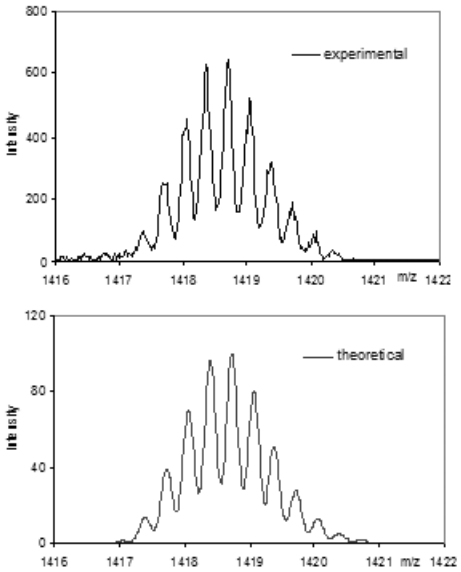

$[TAG_{10}+Dy]^{3+}$

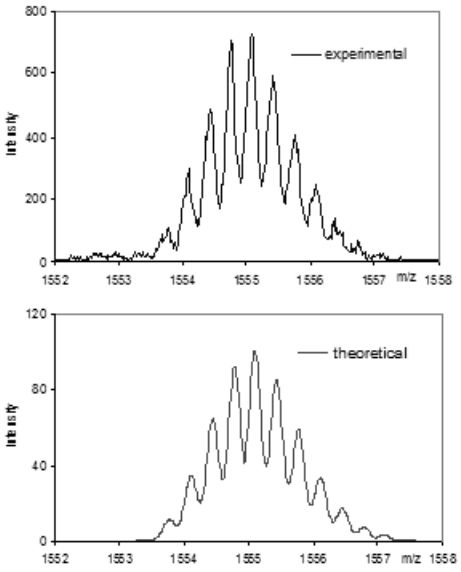

$[TAG_{11}+Dy]^{3+}$

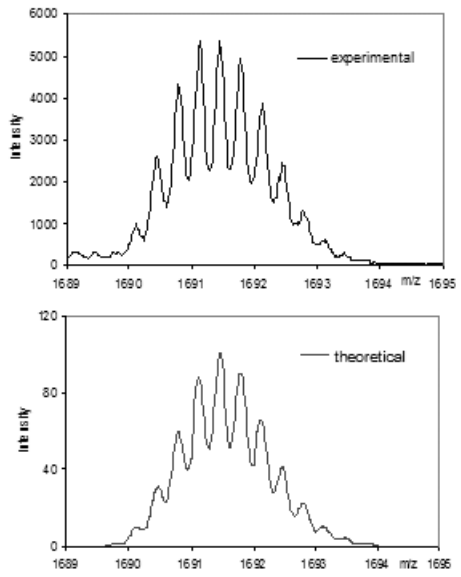

$[TAG_{12}+Dy]^{3+}$

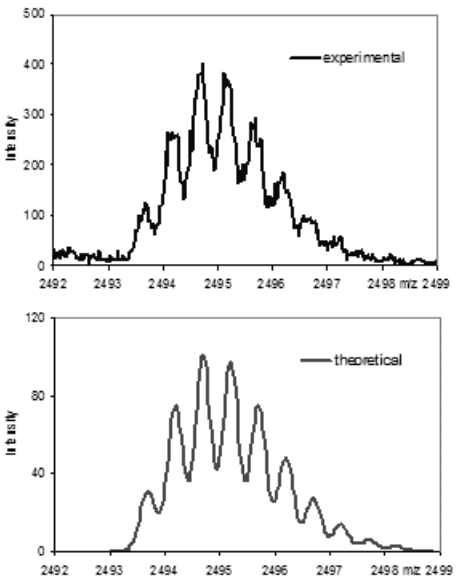

$[TAG_{12}+K]^{2+}$

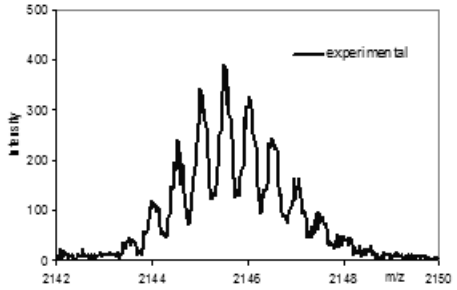

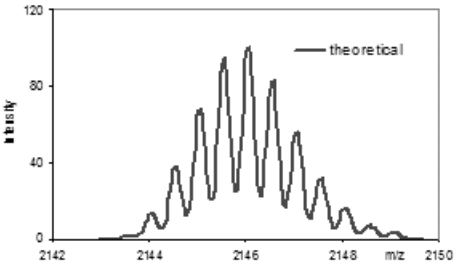

$[(TAG\text{-}3H)_{10}+K+Dy]^{2+}$

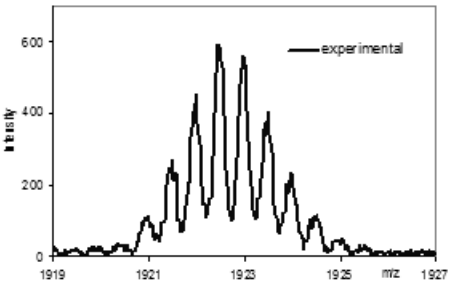

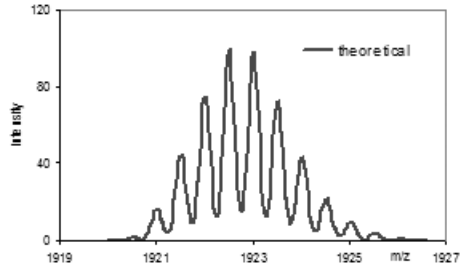

$[(TAG\text{-}H)_{9}+Dy]^{2+}$

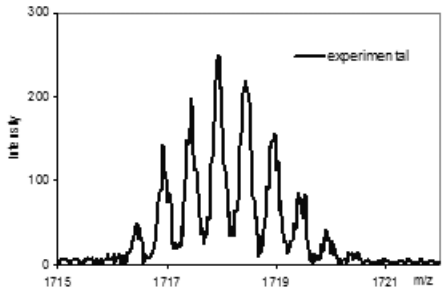

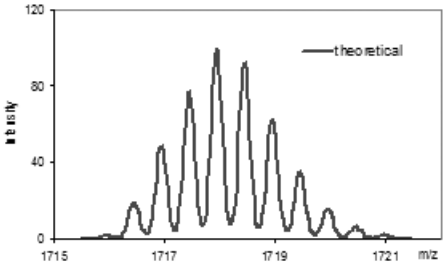

$[(TAG\text{-}H)_{8}+Dy]^{2+}$

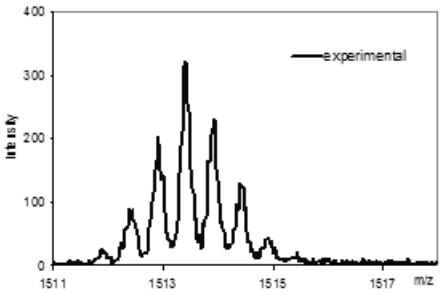

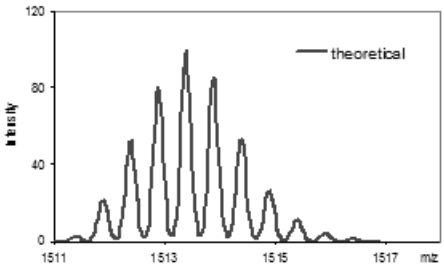

$[(TAG\text{-}H)_{7}+Dy]^{2+}$

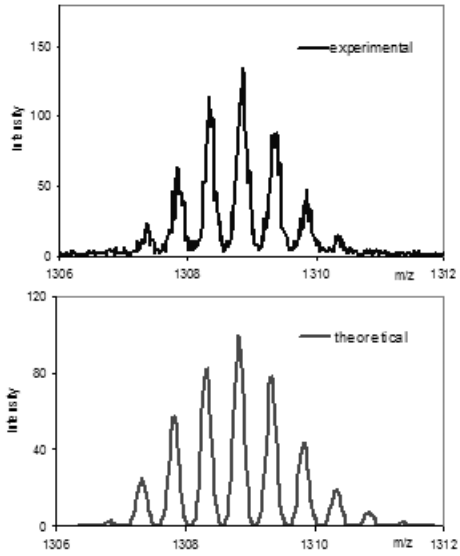

$[(TAG\text{-}H)_6+Dy]^{2+}$

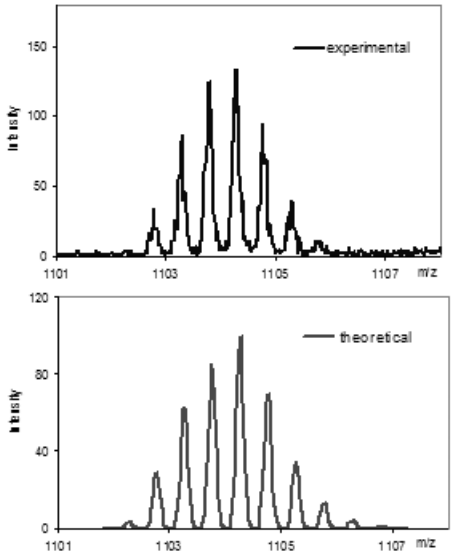

$[(TAG\text{-}H)_5Dy]^{2+}$

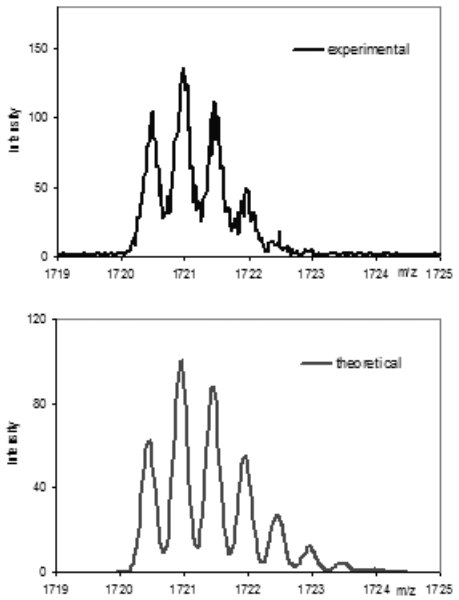

$[TAG_8\text{-}H+Tm]^{2+}$

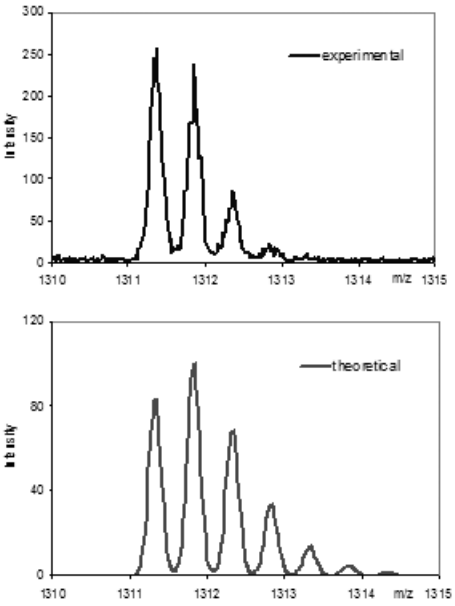

$[TAG_6\text{-}H+Tm]^{2+}$

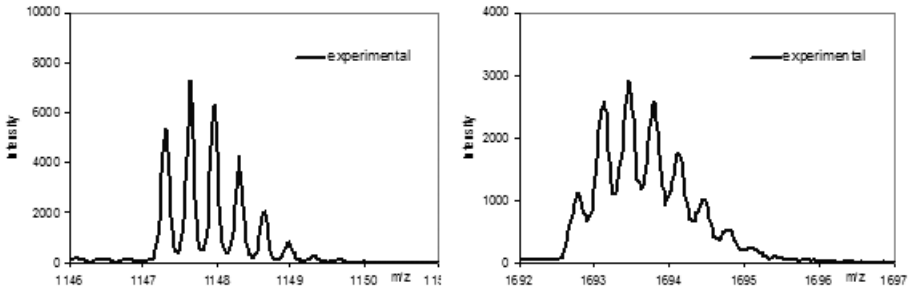

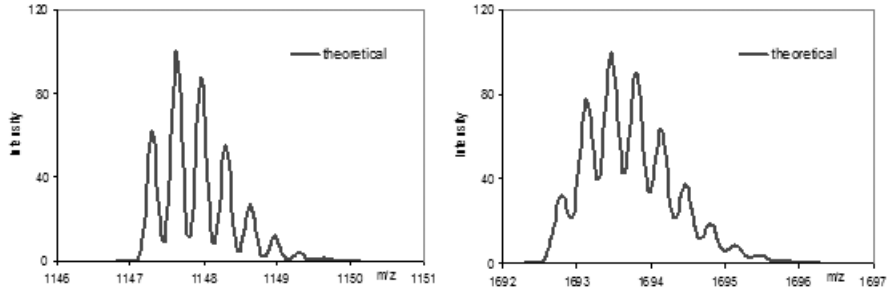

$[TAG_8+Tm]^{3+}$ $[TAG_{12}+Tm]^{3+}$

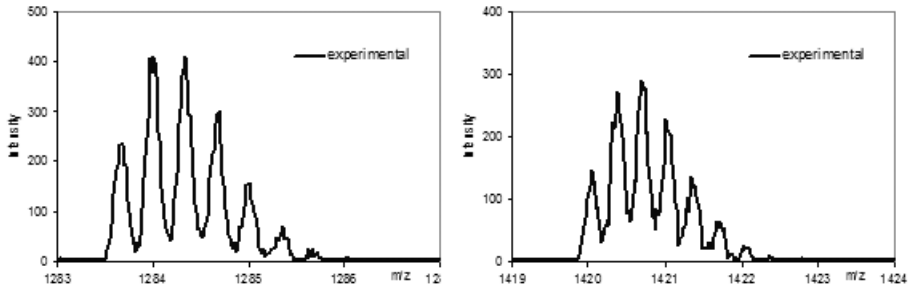

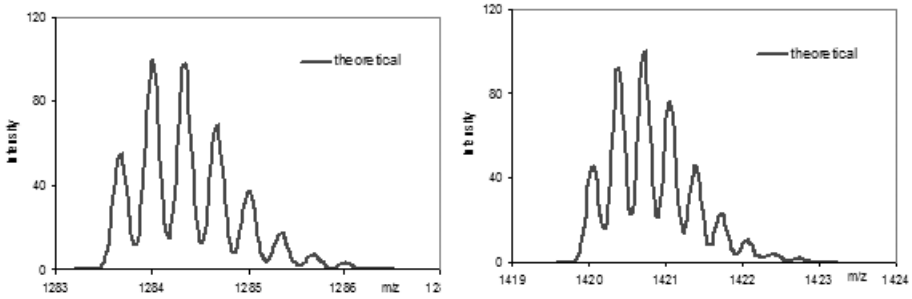

$[TAG_9+Tm]^{3+}$ $[TAG_{10}+Tm]^{3+}$

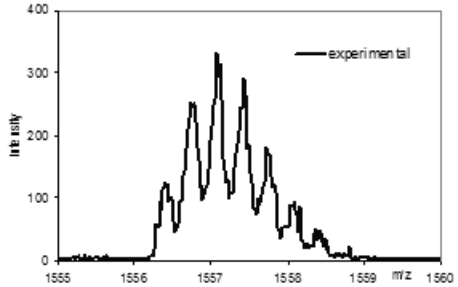

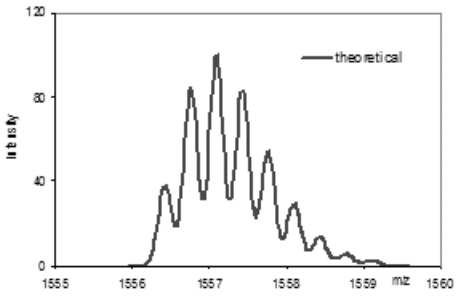

$[TAG_{11}+Tm]^{3+}$

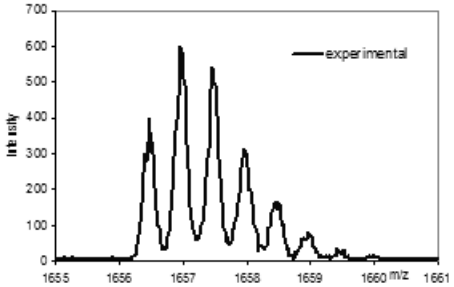

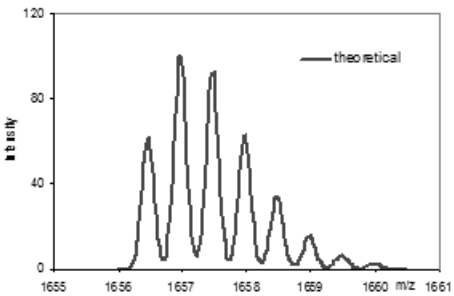

$[TAG_{9}+K+H]^{2+}$

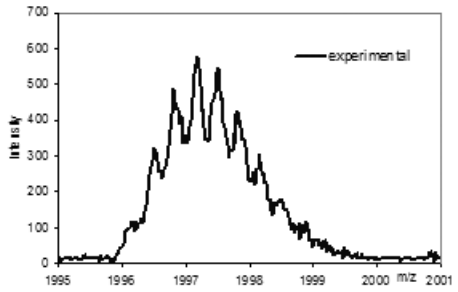

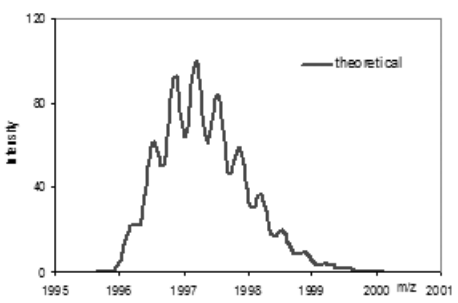

$[TAG_{14}-H+La+K+Na+CH_3NO_2H]^{3+}$

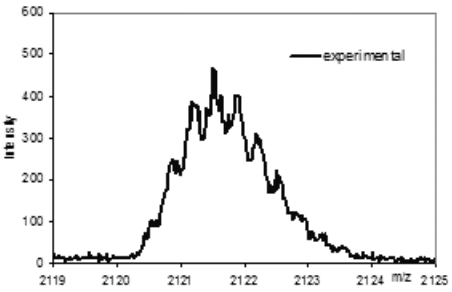

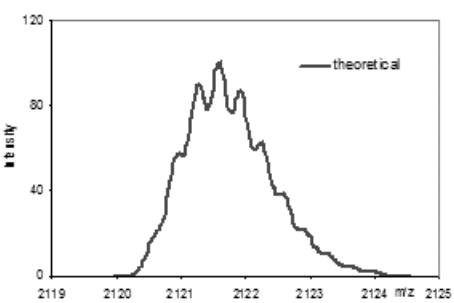

$[TAG_{15}+La+Na+CH_3NO_2H_2]^{3+}$

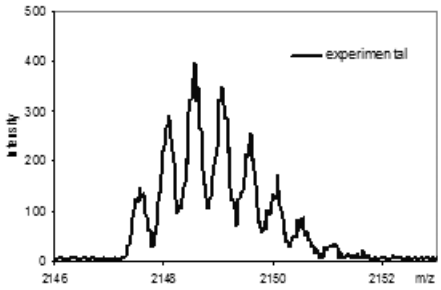

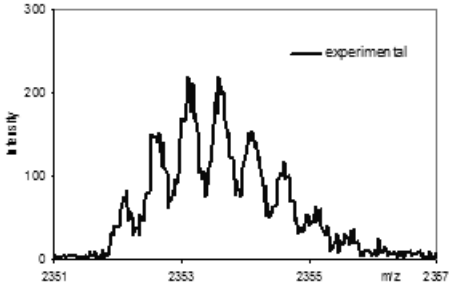

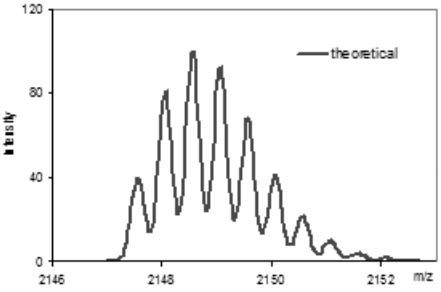

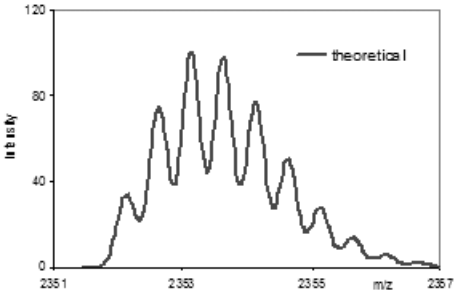

$[TAG_{10}\text{-}H+Tm+HCl]^{2+}$

$[TAG_{11}\text{-}H+Tm+HCl]^{2+}$

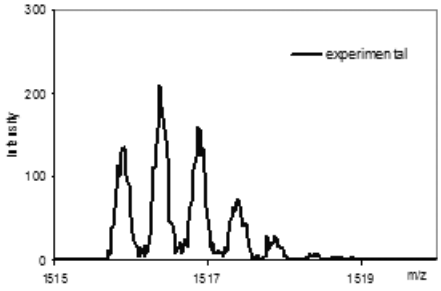

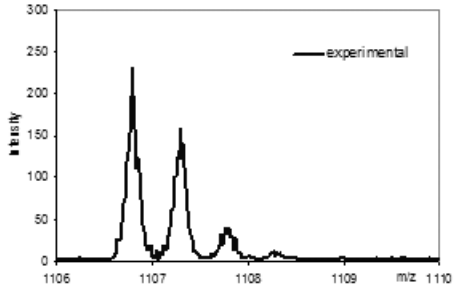

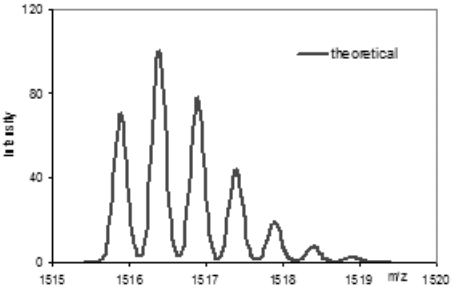

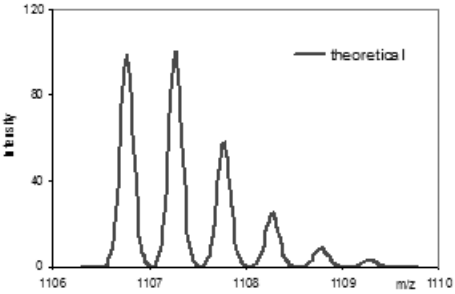

$[TAG_{7}\text{-}H+Tm]^{2+}$

$[TAG_{5}\text{-}H+Tm]^{2+}$

Appendix IX: (Chapter 5)

ESI-MS spectra of both theoretical and experimental data of $[TAG]_n$-$(Ca^{2+}picrate)_n$ species. TAG = monomeric 2′,3′-5′-*O*-triacetylguanosine with 409.35 a.m.u.

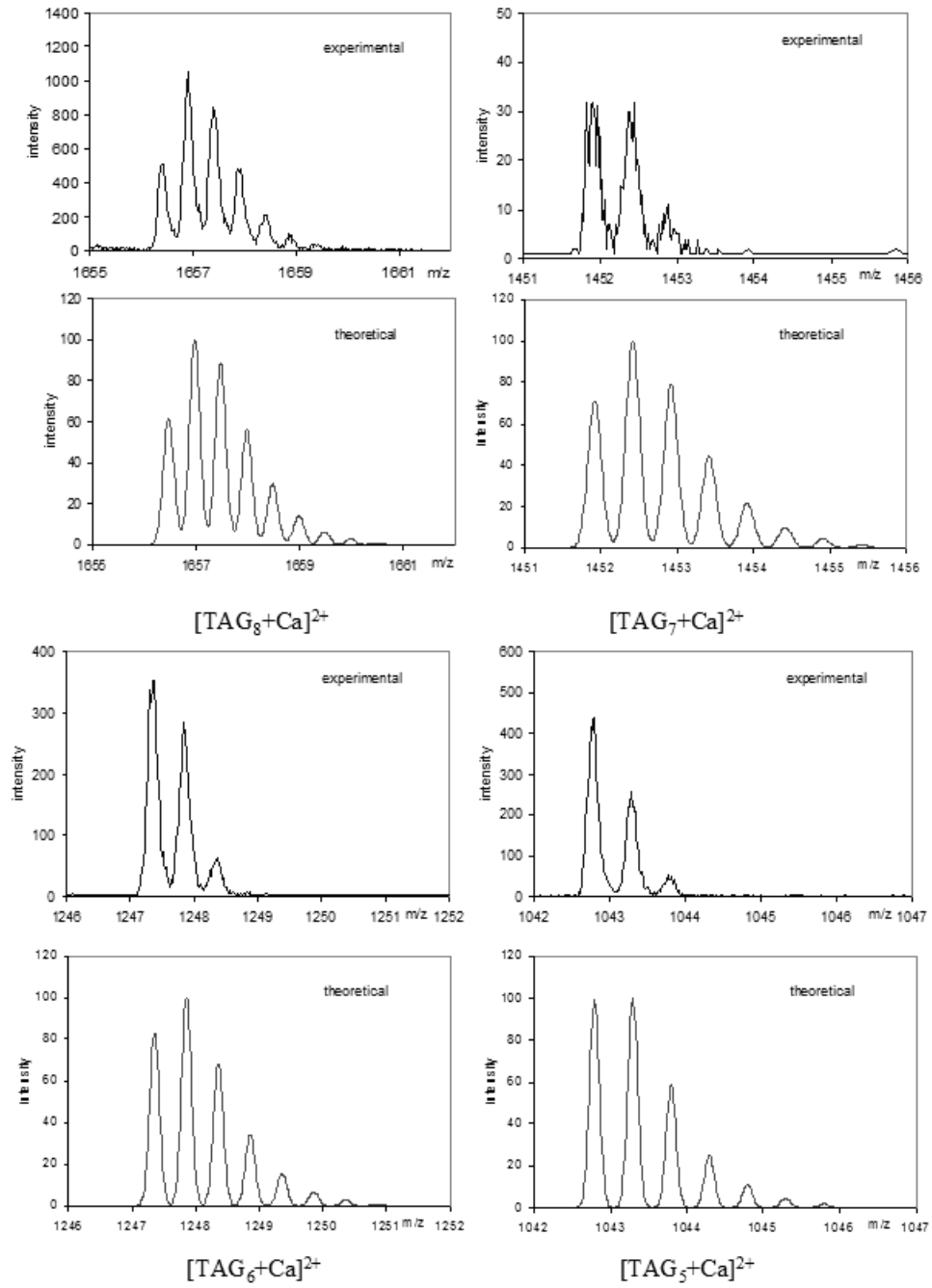

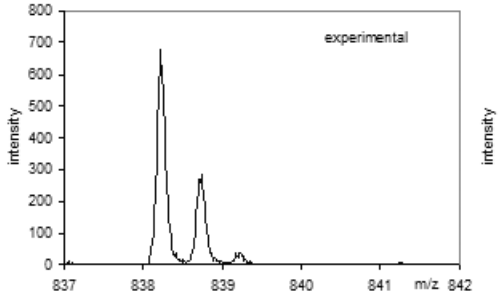

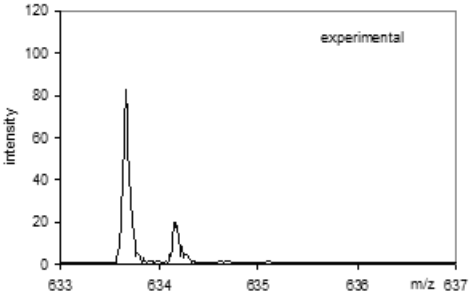

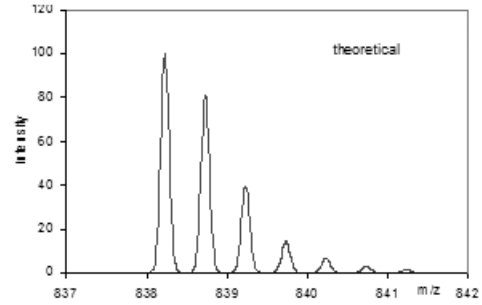

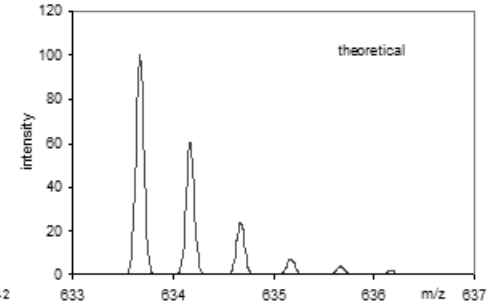

$[TAG_4+Ca]^{2+}$ $[TAG_3+Ca]^{2+}$

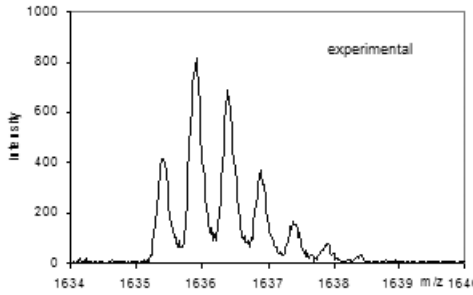

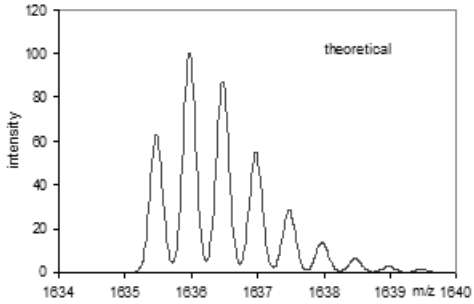

$[TAG_8\text{-acetyl+H}+Ca]^{2+}$